

Universität  
Rostock



---

**Hydrogen generation from the chemical energy carrier  
methanol**

Mechanistic insights into the ruthenium-catalysed  
dehydrogenation reaction and the implementation of a novel  
base-metal catalyst system

---

Dissertation  
to obtain the academic degree  
"Doktor der Naturwissenschaften" (Dr. rer. nat.)  
submitted at the Mathematisch-Naturwissenschaftlichen Fakultät  
der Universität Rostock

Submitted by  
M. Sc. Lydia Katharina Vogt (née Neumann)  
Born September 4<sup>th</sup> 1989 in Berlin

Rostock, 21 February 2017

---

The work of this thesis was conducted between November 2014 and February 2017 under the supervision of Dr. Henrik Junge and Professor Dr. Matthias Beller at the Leibniz-Institut für Katalyse an der Universität Rostock.

1. Gutachter:

Prof. Dr. Matthias Beller

Leibniz-Institut für Katalyse e. V. an der Universität Rostock

2. Gutachter:

Prof. Dr. Gabor Laurency

Institut des sciences et ingénierie chimiques, Ecole polytechnique fédérale de Lausanne

**Datum der Einreichung:** 21. Februar 2017

**Datum der Verteidigung:** 16. Mai 2017

---

## Erklärung

Ich versichere hiermit an Eides statt, dass ich die vorliegende Arbeit selbstständig angefertigt und ohne fremde Hilfe verfasst habe, keine außer den von mir angegebenen Hilfsmitteln und Quellen dazu verwendet habe und die den benutzten Werken inhaltlich und wörtlich entnommenen Stellen als solche kenntlich gemacht habe.

Diese Dissertation wurde bisher an keiner anderen Hochschule oder Universität vorgelegt.

Rostock, den 21.02.2017



.....  
Lydia Vogt

---

## Acknowledgements

I sincerely thank my PhD supervisor *Prof. Matthias Beller* for his support and guidance during the last three years. I will always remember his brilliant ideas and remarkable enthusiasm, which was a great source of motivation throughout this journey. Furthermore I am thankful for the excellent working conditions, the possibility of participating at various conferences, and the opportunity of going on a research stay for three months.

I also would like to express my thanks to my project leader, *Dr. Henrik Junge*, for the cordial working atmosphere in his group and the many valuable discussions, which have significantly contributed to the successful completion of my PhD thesis.

Furthermore, I am grateful to *Prof. Ian Fairlamb* for his very welcoming reception into his working group at the University of York and the very interesting research topic. I have had a wonderful time in York, which is to a great extent because of *Dr. Alan Reay*, who has not only been an excellent lab partner, but even more so has become a very good friend.

Two people have been very important during my studies at the LIKAT, without whom the investigations on the ruthenium catalyst would have not been possible: *Dr. Elisabetta Alberico* and *Dr. Alastair Lennox*. Thanks to their chemical expertise and profound knowledge in mechanistic investigations and the many intensive discussions, this project has been highly rewarding and has taught me how to equally appreciate the joys and challenges of doing chemical research.

I would also like to thank *Maria Anderez-Fernandez* and *Steffen Fischer*, with whom I have worked together on the manganese project. It was a very fruitful cooperation, which I enjoyed very much. I wish them good luck with their further scientific projects and all the best for the future.

I am also grateful for the cooperation with *Dr. Marco Haumann* and *Vinzent Strobel* from the Friedrich-Alexander Universität Erlangen-Nürnberg, which led to very interesting insights into our ruthenium system.

Furthermore, I thank *Dr. Haijun Jiao* for his extensive theoretical calculations.

A big thank you to all the people of the "Catalysis for Energy" group, together with whom I shared the ups and downs of lab work and enjoyed many entertaining out-of-lab activities: *Alonso Rosas*, *Christoph Steinlechner*, *Christoph Prichartz*, *Anja Kammer*, *Steffi Kreft*, *Dr. Conghui Tang*, *Wei Zhou*, *Jacob Schneidewind*, *Anastasyia Agapova* and *Jenny Kuziola*.

Thanks as well to the other former and current group members *Annette-Enrica Surkus*, *Petra Bartels*, *Nils Rockstroh* and *Jagadeesh Rajenahally* for the very pleasant working atmosphere and helpful discussions.

---

Many other friends and colleagues from the LIKAT made me enjoy my time at the institute and I would like to thank especially *Martha Höhne, Markus Joksch, Dr. Bernd Müller, Dr. Anja König, Saskia Möller, Prof. Marko Hapke* and *Dr. Jola Pospech*.

Another thank you to the excellent staff of the analytical department and particularly *Andreas Koch, Dr. Christine Fischer* and *Dr. Wolfgang Baumann*, who found solutions to almost all analytical problems and who made even unusual analytical experiment possible.

I also thank the Fonds der chemischen Industrie (FCI) for the financial support of my PhD thesis.

A big thank you to all of my friends, who made my university and PhD studies to the unforgettable and unique time of my life that it was.

I cannot adequately express how fortunate I feel to be part of the wonderful Neumann and Vogt families. A heartfelt thank you to my *parents, Vati, Mutti, Luis* and *Oma* and all the others, who make Berlin and Rostock to my two hometowns.

Last but not least I thank *Robi*. Without you, all this would not have been possible.

---

## Publications based on the work of this thesis

- 1) E. Alberico\*, A. J. J. Lennox\*, L. K. Vogt, H. Jiao, W. Baumann, H.-J. Drexler, M. Nielsen, A. Spannenberg, M. P. Checinski, H. Junge, M. Beller, *J. Am. Chem. Soc.* **2016**, *138*, 14890–14904.
- 2) M. Anderez-Fernandez\*, L. K. Vogt\*, S. Fischer, W. Zhou, H. Jiao, M. Garbe, S. Elangovan, K. Junge, H. Junge, R. Ludwig, M. Beller, *Angew. Chem. Int. Ed.* **2017**, *56*, 559–562.
- 3) V. Strobel, J. J. Schuster, A. S. Braeuer, L. K. Vogt, H. Junge, M. Haumann, *React. Chem. Eng.*, **2017**, Accepted Manuscript.

\* These authors contributed equally.

## Further publications

- 1) A. J. Reay, L. K. Neumann, I. J. S. Fairlamb, *Synlett* **2016**, *27*, 1211–1216.
- 2) E. Alberico, L. K. Neumann, N. Rockstroh, H. Junge in *Non-Noble Metal Catalysis: Molecular Approaches and Reactions* (Eds.: M.-E. Moret, B. K. Gebbink), Wiley-VCH, Weinheim, currently edited.

---

## Presentations at national and international conferences

### Oral presentations

- 1) L. Neumann, E. Alberico, M. Nielsen, C. Cordes, H. Junge, M. Beller, *Novel catalysts for the selective dehydrogenation of methanol as chemical energy carrier*, REGWA Symposium, Stralsund, Germany, November 6–8 2014.
- 2) L. Neumann, E. Alberico, A. Lennox, H. Junge, M. Beller, *Mechanism of the aqueous-phase reforming of methanol - Understanding the role of the base*, 115<sup>th</sup> General Assembly of the German Bunsen Society for Physical Chemistry, Rostock, Germany, May 6–7 2016.
- 3) L. Neumann, E. Alberico, A. Lennox, H. Junge, M. Beller, *Insights into the mechanism of the aqueous-phase dehydrogenation of methanol*, World Energy Hydrogen Conference, Zaragoza, Spain, June 13–16 2016.
- 4) L. Vogt, E. Alberico, A. Lennox, H. Junge, M. Beller, *Unravelling the mechanism of methanol reforming catalysed by Ru- and Mn-PNP pincer complexes*, XVIII<sup>th</sup> Netherlands' Catalysis and Chemistry Conference, Noordwijkerhout, the Netherlands, March 6–8 2017.

### Poster presentations

- 1) L. Neumann, E. Alberico, A. Lennox, H. Junge, M. Beller, *Ruthenium and iron catalysts for the high-efficient decomposition of methanol*, EuCOMC XXI, Bratislava, Slovakia, July 5–9 2015.
- 2) L. Neumann, E. Alberico, A. Lennox, H. Junge, M. Beller, *Ru-PNP catalyzed aqueous-phase reforming of methanol*, 49. Jahrestreffen Deutscher Katalytiker, Weimar, Germany, March 16–18 2016.

---

## Abstract

The aim of this work was to acquire comprehensive understanding of the mechanism of the homogeneously Ru-PNP catalysed aqueous-phase reforming of methanol. This was accomplished by employing a variety of experimental, spectroscopic and theoretical tools. Based on the results of the performed labelling experiments, spectroscopic investigations under stoichiometric and catalytic conditions, comprehensive kinetic investigations and supporting theoretical calculations, a complete mechanistic cycle could be proposed for both the original Ru-pincer catalyst **1** and its methylated derivative **Me-1**.

The focus of the second part of this thesis was the development of an efficient catalyst system based on the base metal manganese for the aqueous-phase reforming of methanol at low temperatures. By combining methodology for optimising reaction parameters, investigations on the long-term activity and the analysis of reactive catalytic species, a stable Mn-pincer complex was successfully applied for the hydrogen generation from methanol. Furthermore, mechanistic aspects were elucidated, which are crucial in advancing specific catalyst designs tailored to the distinct reaction conditions.



---

## Table of contents

<b>OBJECTIVE OF THIS THESIS.....</b>	<b>1</b>
<b>1. INTRODUCTION.....</b>	<b>2</b>
1.1. OUR CURRENT ENERGY SYSTEM .....	2
1.2. HYDROGEN AS ENERGY VECTOR.....	5
1.3. CHEMICAL ENERGY CARRIERS.....	5
1.4. METHANOL AS CHEMICAL ENERGY CARRIER.....	6
1.4.1. <i>Heterogeneously catalysed methanol dehydrogenation</i> .....	8
1.4.2. <i>Homogeneously catalysed alcohol dehydrogenation</i> .....	9
<b>2. PART I: RUTHENIUM-CATALYSED DEHYDROGENATION OF METHANOL.....</b>	<b>14</b>
2.1. INTRODUCTION.....	14
2.2. OBJECTIVE OF PROJECT I.....	16
2.3. RESULTS AND DISCUSSION .....	17
2.3.1. <i>Inner-sphere vs. outer-sphere mechanism</i> .....	17
2.3.2. <i>Investigations for catalyst <b>1</b></i> .....	20
2.3.3. <i>Mechanistic proposal</i> .....	40
2.3.4. <i>Investigations for catalyst <b>Me-1</b></i> .....	46
2.3.5. <i>Mechanistic proposal</i> .....	52
2.4. SUMMARY AND OUTLOOK FOR THE RUTHENIUM-CATALYSED DEHYDROGENATION OF METHANOL.....	57
<b>3. PART II: MANGANESE-CATALYSED DEHYDROGENATION OF METHANOL.....</b>	<b>62</b>
3.1. INTRODUCTION.....	62
3.2. OBJECTIVES OF PROJECT II.....	65
3.3. RESULTS AND DISCUSSION .....	66
3.3.1. <i>Preliminary tests</i> .....	66
3.3.2. <i>Optimisation reactions</i> .....	67
3.3.3. <i>Longterm investigations</i> .....	69
3.3.4. <i>NMR investigations: Difference between defined Mn-catalyst and precursor</i> .....	71
3.3.5. <i>IR and NMR investigations on the defined Mn-catalyst <b>9</b></i> .....	74
3.3.6. <i>Mechanistic proposal</i> .....	81
3.3.7. <i>Dehydrogenation of further relevant substrates</i> .....	82
3.4. SUMMARY AND OUTLOOK FOR THE MANGANESE-CATALYSED DEHYDROGENATION OF METHANOL .....	83
<b>4. CONCLUSION AND OUTLOOK.....</b>	<b>85</b>
<b>5. BIBLIOGRAPHY .....</b>	<b>86</b>
<b>6. APPENDIX.....</b>	<b>I</b>

---

## List of figures, schemes and tables

### Figures

Figure 1: World's primary energy consumption by fuel 2015 in Mtoe .....	2
Figure 2: Annual global land and ocean temperature anomalies over the last 150 years... ..	3
Figure 3: Monthly atmospheric carbon dioxide levels (1950 until today) .....	3
Figure 4: Share of renewable energies of the primary energy consumption and the gross electricity production. ....	4
Figure 5: Activities of <b>1</b> and <b>Me-1</b> .....	18
Figure 6: Arrhenius plot .....	20
Figure 7: Influence of H <sub>2</sub> and N <sub>2</sub> pressure on the catalytic activity of <b>1</b> .....	22
Figure 8: Modified autoclave setup .....	22
Figure 9: The influence of KOH concentration on the activity of catalyst <b>1</b> in methanol reforming at 60 °C and 90 °C.....	23
Figure 10: Catalytic activity of <b>1</b> vs. catalyst concentration .....	24
Figure 11: Dependency of hydrogen gas evolution on the stirring rate.....	25
Figure 12: Comparison of hydrogen gas evolution under standard conditions and in the presence of 10 eq. of KCl .....	27
Figure 13: <sup>31</sup> P NMR of the reaction solution containing <b>1</b> .....	32
Figure 14: <sup>1</sup> H NMR of the reaction solution containing <b>1</b> .....	32
Figure 15: Comparison of hydrogen gas evolution caused by basic and thermal decomposition of formaldehyde with the standard gas evolution rate .....	34
Figure 16: <sup>31</sup> P NMR of the reaction solution containing <b>1</b> . Addition of increasing amounts of KOH .....	35
Figure 17: An exemplary Raman spectrum of the reaction solution recorded for a duration of 7.5 hours .....	38
Figure 18: Coating of the inner wall of the reaction vessel with potassium carbonate .....	38
Figure 19: All experimental data obtained from a single run in the GC-Raman setup.....	39
Figure 20: Potential energy surface for the anionic, inner-sphere pathway for the C-H cleavage step and Ru-dihydride formation .....	42
Figure 21: The influence of KOH concentration on the activity of catalyst <b>Me-1</b> at 60 °C and 90 °C..	46
Figure 22: <sup>31</sup> P NMR of the reaction solution at room temperature containing <b>Me-1</b> .....	48
Figure 23: <sup>1</sup> H{ <sup>31</sup> P} NMR of the reaction solution containing <b>Me-1</b> .....	49
Figure 24: <sup>31</sup> P NMR of the reaction solution containing Me-1. Addition of increasing amounts of KOH	50
Figure 25: Potential energy surface for the inner-sphere pathway for the C-H cleavage step and Ru-dihydride formation .....	54
Figure 26: Modified autoclave setup .....	58
Figure 27: Coating of the inner wall of the reaction vessel with potassium carbonate .....	59
Figure 28: Influence of light on the catalytic activity of the Mn complex <b>9</b> .....	66

---

Figure 29: Testing of the long-term effects of the addition of solvents.....	69
Figure 30: Longterm measurements .....	700
Figure 31: <sup>31</sup> P NMR of the reaction solution containing catalyst <b>9</b> .....	71
Figure 32: Influence of temperature on the active catalytic species of complex <b>9</b> .....	72
Figure 33: Influence of temperature on the active catalytic species of the in-situ system. ....	73
Figure 34: IR measurements of the active catalytic species in dependence on base molarity. ....	74
Figure 35: Addition of 10 eq. of H <sub>2</sub> O to amido species <b>11</b> .....	75
Figure 36: Addition of 10 eq. of MeOH to amido species <b>11</b> .....	75
Figure 37: Addition of 10 eq. of formic acid to amido species <b>11</b> .....	76
Figure 38: <sup>13</sup> C NMR. Addition of 10 eq. of <sup>13</sup> C-MeOH to amido species <b>11</b> .....	76
Figure 39: <sup>31</sup> P NMR. Addition of 10 eq. of <sup>13</sup> C-MeOH to amido species <b>11</b> .....	77
Figure 40: <sup>13</sup> C NMR. Dissolution of pre-catalyst <b>9</b> in a basic methanol-water solution.....	77
Figure 41: DFT-calculated IR spectra for a range of Mn species.....	78
Figure 42: DFT-calculated IR spectra for a range of Mn species with an extended scaling of the x-axis up to 1500 cm <sup>-1</sup> .....	79
Figure 43: Reaction monitoring by IR .....	80
Figure 44: GC spectrum for the dehydrogenation of methanol.....	V
Figure 45: GC spectrum for the dehydrogenation of ethanol .....	VI
Figure 46: GC spectrum for the dehydrogenation of formic acid .....	VII
Figure 47: GC spectrum for the dehydrogenation of paraformaldehyde.....	VIII
Figure 48: Setup of the manual burette equipment.....	IX
Figure 49: Setup of the automatic burette equipment. ....	X
Figure 50: Setup of the autoclave equipment .....	XI
Figure 51: Correlation between catalytic activity and temperature .....	XIV
Figure 52: Testing of different solvents for reduction of base .....	XVI
Figure 53: Testing of pH-buffered solutions for the reduction of base .....	XVI
Figure 54: Correlation between base molarity and boiling temperature of the 9:1 MeOH:H <sub>2</sub> O reaction solution. ....	XVII
Figure 55: Difference in catalytic activity between manual burette and autoclave setup .....	XVII
Figure 56: Measurements of increase in pressure by the evolution of hydrogen gas .....	XIX
Figure 57: Calculated TOF based on the increase in pressure measured in the closed autoclave setup .....	XX
Figure 58: <sup>31</sup> P NMR spectra of the reaction mixture arising from aqueous methanol reforming with <b>1</b> .....	XXII
Figure 59: <sup>13</sup> C NMR of the precipitate formed during aqueous methanol reforming with <b>1</b> .....	XXIII
Figure 60: DFT calculated energies (kcal mol <sup>-1</sup> ) for the formation of anionic complexes .....	XXIV
Figure 61: Setup for the operando Raman and GC investigation .....	XXV
Figure 62: Recording of the operando Raman spectra.....	XXVI

---

---

Figure 63: Comparison of Raman spectra for formaldehyde, methanol and the reaction solution. .	XXVII
Figure 64: <sup>31</sup> P NMR of the reaction solution containing <b>Me-1</b> .....	XXVIII
Figure 65: <sup>31</sup> P NMR of the reaction solution containing <b>Me-1</b> in 5 mL 9/1 MeOH/H <sub>2</sub> O, 8 M KOH. ....	XXIX
Figure 66: <sup>13</sup> C NMR. Solid dissolved in D <sub>2</sub> O.....	XXIX
Figure 67: Testing of the IL Ecoeng 212 as additional solvent .....	XXX
Figure 68: Testing of a bicatalytic system .....	XXX
Figure 69: Replacement of KOH by K <sub>2</sub> CO <sub>3</sub> .....	XXXI
Figure 70: Activity measurements using a variation of Milstein's catalyst <b>15</b> .....	XXXIV
Figure 71: Activity measurements using Ru-Pr catalyst <b>9</b> .....	XXXIV
Figure 72: Correlation between catalyst concentration and productivity of <b>9</b> .....	XXXV
Figure 73: <sup>1</sup> H NMR of the reaction solution containing catalyst <b>9</b> .....	XXXVI
Figure 74: <sup>1</sup> H NMR of the reaction solution containing Mn(CO) <sub>5</sub> Br with 10 eq. HPNP/Pr ligand .....	XXXVI

## Schemes

Scheme 1: One of the essential questions that still have to be elucidated for the Ru-PNP catalyst system .....	1
Scheme 2: Extending the scope to manganese-based catalyst systems.....	1
Scheme 3: Combined methanol and hydrogen economy .....	7
Scheme 4: Pathways for the transfer of hydrogen. ....	9
Scheme 5: Two examples for the Noyori-type of catalyst. ....	10
Scheme 6: Non-innocent pyridine-PNP pincer catalysts introduced by Milstein and co-workers. ....	11
Scheme 7: Aliphatic PNP-pincer complex by Schneider and co-workers. ....	11
Scheme 8: First homogeneous catalyst system for the aqueous-phase dehydrogenation of methanol	12
Scheme 9: Examples of homogeneous catalysts employed for the methanol dehydrogenation .....	13
Scheme 10: Overview of the steps of the complete methanol dehydrogenation reaction .....	14
Scheme 11: Complete mechanistic cycle proposed for the methanol dehydrogenation by catalyst <b>1</b> ..	15
Scheme 12: Ru-PNP parent catalyst <b>1</b> and its methylated derivative <b>Me-1</b> . ....	17
Scheme 13: Overview of the KIEs determined for catalysts <b>1</b> and <b>Me-1</b> .....	19
Scheme 14: Dehydrochlorination of precursor <b>1</b> with base .....	26
Scheme 15: Overview of related complexes of parent catalyst <b>1</b> .....	27
Scheme 16: Equilibrium between <b>3</b> and <b>4</b> considering solvent-assisted H <sub>2</sub> evolution.....	29
Scheme 17: Theoretical energies for the addition of protic species across the Ru-N bond .....	30
Scheme 18: Schematic overview of the experimental setup for operando monitoring.....	37
Scheme 19: Possible mechanistic pathways for the key C-H cleavage step involving catalyst <b>1</b> .....	41
Scheme 20: Proposed mechanistic cycle for the complete dehydrogenation of methanol employing Ru-pincer complex <b>1</b> .....	44
Scheme 21: Protonation of <i>trans</i> <b>Me-3</b> by CH <sub>3</sub> OD .....	47

---

---

Scheme 22: Possible mechanistic pathways for the key C-H cleavage step involving catalyst <b>Me-1</b> ...	53
Scheme 23: Proposed mechanistic cycle for the complete dehydrogenation of methanol employing Ru-pincer complex <b>Me-1</b> .....	55
Scheme 24: Ru-PNP parent catalyst <b>1</b> and its methylated derivative <b>Me-1</b> . .....	57
Scheme 25: Combination of possible catalysts that can be combined for a bicatalytic system .....	60
Scheme 26: Structure of the basic IL Ecoeng 212 (1-ethyl-3-methyl-imidazolium-ethylsulfate) .....	61
Scheme 27: Overview of manganese-based pincer catalysts. ....	62
Scheme 28: Hydrogenation of nitriles, ketones and aldehydes using Mn-catalyst <b>9</b> .....	63
Scheme 29: Transfer hydrogenation of ketones with Mn-catalyst <b>17</b> . ....	63
Scheme 30: Dehydrogenative coupling of alcohols and amines to imines using Mn-catalyst <b>18</b> .....	64
Scheme 31: 1,2-Addition of formic acid and oxalic acid to the Mn-amido complex <b>11</b> . .....	64
Scheme 32: Structure of the Mn-porphyrine complex <b>20</b> . ....	66
Scheme 33: Overview of related complexes of Mn-parent catalyst <b>9</b> .....	71
Scheme 34: Proposed mechanistic cycle for the complete dehydrogenation of methanol employing Mn-pincer complex <b>9</b> . ....	81
Scheme 35: Optimised conditions for the methanol dehydrogenation using Mn catalyst <b>9</b> .....	83
Scheme 36: Experiments performed to investigate different catalytic activities between burette and autoclave setup. ....	XVIII

## **Tables**

Table 1: Testing of different Mn catalysts for the dehydrogenation of methanol .....	67
Table 2: Influence of the different conditions on the activity of the Mn-catalyst <b>9</b> .....	68
Table 3: Dehydrogenation of C <sub>1</sub> - and C <sub>2</sub> -substrates with Mn complex <b>9</b> .....	82
Table 4: NMR data for the PNP-pincer complex <b>1</b> and related complexes in deuterated solvents .....	XXI
Table 5: NMR data for the PNP-pincer complex <b>1</b> and related complexes in the 9:1 MeOH:H <sub>2</sub> O reaction solution containing 8 M KOH. ....	XXI
Table 6: NMR data for the methylated PNP-pincer complex <b>Me-1</b> and related complexes in deuterated solvents.....	XXVIII
Table 7: B3PW91 Computed Cartesian Coordinates. ....	XXXIX

---

## Abbreviations

### Symbols, Units and Variables

°C	Degree Celsius
GWh	Gigawatt-hour
h	Hour
H	Enthalpy
kcal	Kilocalories
kg	Kilogram
kJ	Kilojoule
km	Kilometer
kWh	Kilowatt hour
L	Liter
M	Molarity
m <sup>3</sup>	Cubic metres
mL	Milliliter
Mtoe	Million tonnes of oil equivalent = 41.87 GJ
μmol	Micromol
MWh	Megawatt hour
p	Pressure
ppm	Parts per million
R	Gas constant
rpm	Rounds per minute
s	Second
T	Temperature
TWh	Terra watt hour
η	Efficiency
wt%	Weight percent

### Abbreviations

Bu	Butyl
DFT	Density Functional Theory
DH	Dehydrogenation
dppe	1,2-Bis-(diphenylphosphino)ethane
EtOH	Ethanol

<i>et al.</i>	<i>et alii, et aliae</i> or <i>et alia</i>
eq.	Equivalent
<i>ex situ</i>	Here: after the reaction
GC	Gas chromatography
<i>i</i>	<i>iso-</i>
i.a.	inter allia (amongst others)
<i>in situ</i>	During the reaction
IL	Ionic liquid
<i>i</i> Pr	<i>Iso</i> -propyl group
IR	Infrared (spectroscopy)
KIE	Kinetic isotope effect
L	Ligand
LOHC	Liquid Organic Hydrogen Carrier
M	Metal
Me	Methyl
MeOH	Methanol
<i>m, p, o</i>	<i>Meta, Para, Ortho</i>
MOF	Metal-Organic Framework
MS	Mass Spectrometry
NMR	Nuclear Magnetic Resonance (Spectroscopy)
NMP	N-Methylpyrrolidone
<i>operando</i>	Simultaneous measurement of catalytic activity and selectivity
PEMFC	Proton Exchange Membrane Fuel Cell
pH	Negative decimal logarithm of the free H <sup>+</sup> ion concentration
Ph	Phenyl group
PhD	<i>Philosophiae Doctor</i>
PNP	Ligand based on a phosphor- nitrogen-phosphor scaffold
<i>t</i>	<i>tertiary-</i>
TOF	Turnover frequency
TON	Turnover number
Ts	Tosyl group
UK	United Kingdom

---

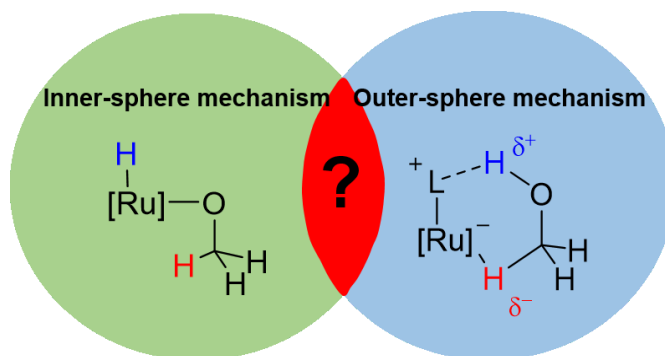
## Objective of this thesis

---

### Objective of this thesis

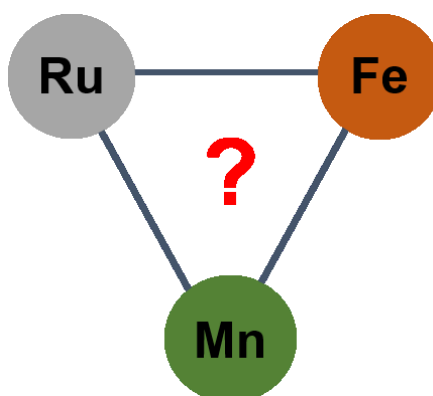
The homogeneously catalysed dehydrogenation of methanol for the generation of hydrogen as a viable energy carrier has become increasingly attractive since significant progress concerning catalyst efficiency and stability has been made. Especially the system based on an aliphatic Ru-PNP catalyst used in a highly basic aqueous methanol solution has reached unprecedented high activities. Nevertheless, so far no conclusive mechanism was postulated for this catalyst, nor was the key question regarding the type of pathway for the C-H cleavage step sufficiently answered (Scheme 1). Thus, the first part of this thesis aims to elucidate these essential aspects by using a range of kinetic and spectroscopic methods, combined with theoretical studies.

**Scheme 1:** One of the essential questions that still have to be elucidated for the Ru-PNP catalyst system.



The second part of this thesis deals with the application of a suitable catalyst based on manganese, which would be the first catalyst system based on this base metal for the homogeneously catalysed aqueous-phase reforming of methanol. So far, active catalysts have been limited to the use of the noble metals ruthenium and iridium, as well as iron as the only example of a base metal (Scheme 2). In the course of this work, it is envisioned to transfer the expertise gained by the intensive mechanistic investigations on the ruthenium complex to this novel type of manganese catalyst system.

**Scheme 2:** Extending the scope to manganese-based catalyst systems.





## 1. Introduction

### 1.1. Our current energy system

A reliable energy supply is one of the major pillars of the modern society.<sup>[1]</sup> Nowadays, this awareness is widely prevalent and even a decade ago, the then-Senator Barack Obama emphasized that “a nation that can't control its energy sources can't control its future.”<sup>[2]</sup>

Generally, the magnitude of energy consumption is linked with both the prosperity of a society and its size of population.<sup>[3]</sup> For the last two centuries, a seven-fold increase of the latter has caused an increase in energy need by a factor of 27, leading to a global annual primary energy consumption of 13,147 Mtoe in 2015.<sup>[4-5]</sup> This amount of energy equals the energy output of more than 1,700 times the world's largest capacity hydroelectric power station, the three-gorges dam in China.<sup>[6-7]</sup>

During the last decades, wind, solar, geothermal and biomass-based energies have been increasingly implemented and have seen a rise from less than 1% to almost 3% of the global primary energy sources.<sup>[5]</sup> Nevertheless, this value also means that the majority of the world's energy demand is still met by the main fossil fuels oil, natural gas and coal (Figure 1).

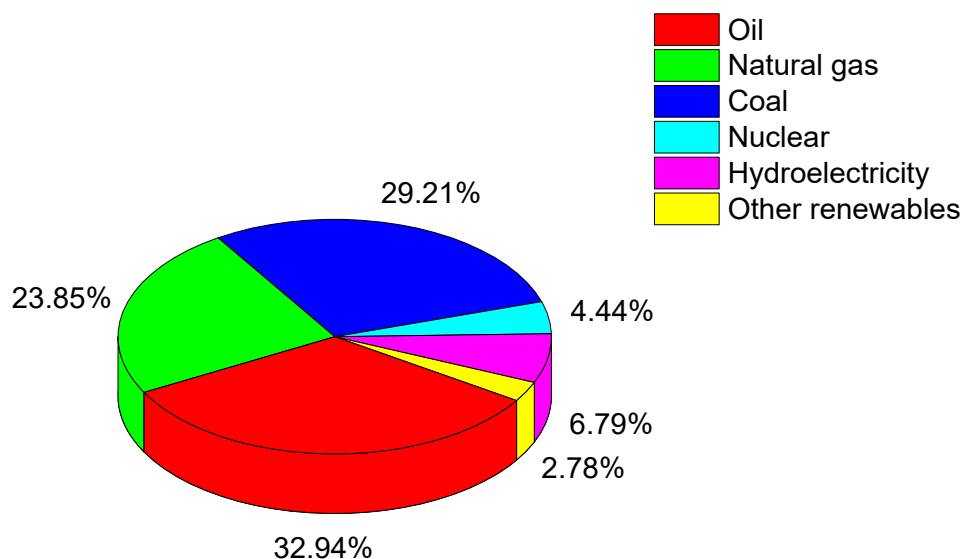


**Figure 1:** World's primary energy consumption by fuel 2015 in Mtoe.<sup>[5]</sup>

Today two fundamental reasons are mainly regarded for the urgent need for the transition to a non-fossil based energy economy: Firstly, the limited availability of oil, natural gas and coal and their growing depletion<sup>[8]</sup> and secondly, the effect of the produced greenhouse gas CO<sub>2</sub> by the burning of these fossil fuels on the world's climate.<sup>[9-13]</sup> During the last 150 years, the atmospheric

## Introduction

---

concentration of carbon dioxide has increased from circa 280 ppm to 405 ppm today with the concomitant rise of the global temperature of approx. 1 °C (Figures 2 and 3).<sup>[14-16]</sup>

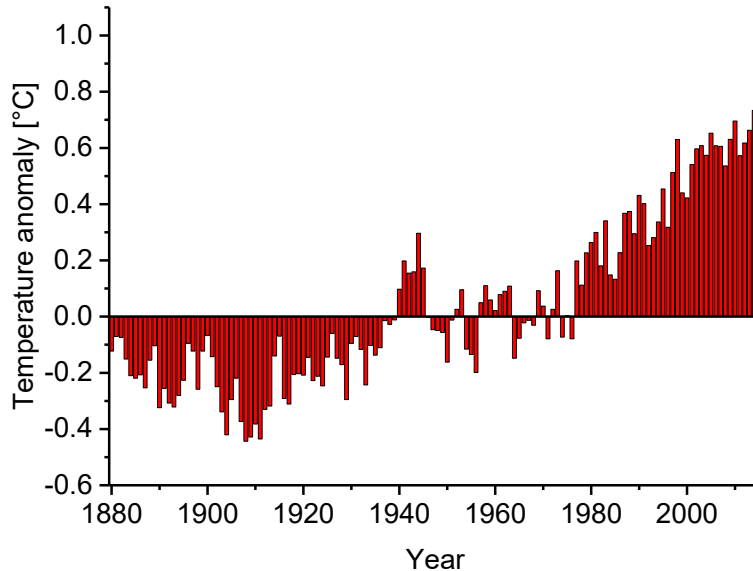


**Figure 2:** Annual global land and ocean temperature anomalies over the last 150 years.<sup>[15-16]</sup>

Nowadays, it is scientifically accepted that this rise in temperature, which effects the earth's climate substantially, is man-made.<sup>[17-18]</sup> To emphasize how critical the situation is, David King, the UK Government's Chief Science Advisor until 2007, called climate change "the single biggest challenge our civilization has ever had to face."<sup>[14]</sup>

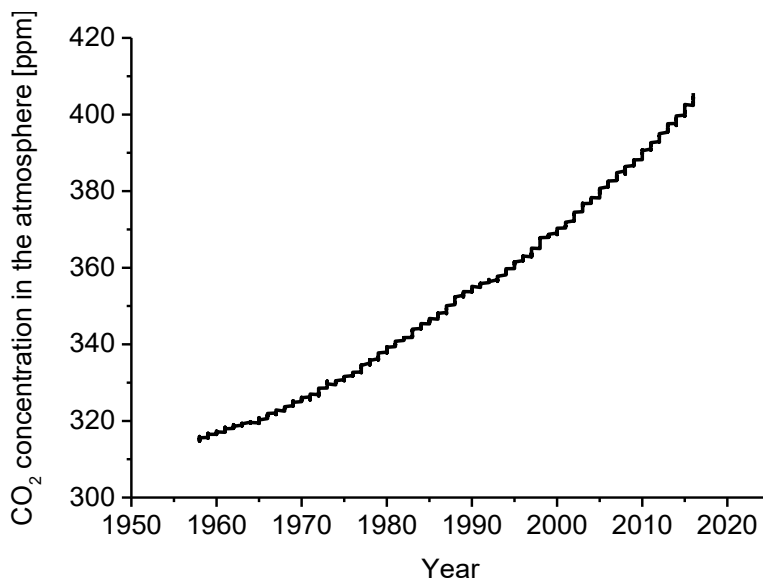


**Figure 3:** Monthly atmospheric carbon dioxide levels (1950 until today).<sup>[15]</sup>

## Introduction

---

The international community has made increasing efforts to take countermeasures against this trend, which led to the adoption of the Kyoto protocol in 1997 and the successive proceedings of the yearly United Nations Climate Change Conferences. One of the aims of the Paris Agreement, which was negotiated at the last convention in 2015, is to limit the global warming to 2 °C compared to pre-industrial levels. This means that global emissions have to decline before 2020 and by 2050 have to be cut by half with regard to the levels of 1990.<sup>[19]</sup> This in turn entails the stabilization of greenhouse gas emissions to a value of 450 ppm CO<sub>2</sub> equivalents.<sup>[20]</sup>

A number of examples exist for the beginning of a steady transition to a non-fossil based energy supply.<sup>[21-22]</sup> Also the German energy policy has been a role model for other countries due to the implementation of the so called "German Energiewende" and the regulation of the feed-in of electricity generated from renewables into the existing grid structures.<sup>[23]</sup> Since the 1990s, the share of renewable energies has exponentially increased to ca. 12% of the primary energy consumption and has even reached around 30% of the gross electricity production last year (Figure 4).<sup>[24]</sup>

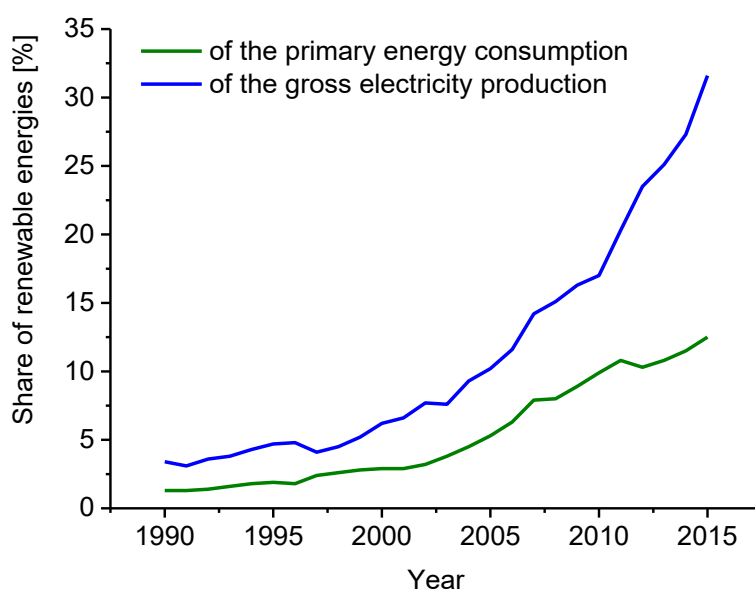


**Figure 4:** Share of renewable energies of the primary energy consumption and the gross electricity production.<sup>[24]</sup>

The significant difference between the share of renewables on the electricity production and the general primary energy consumption can be explained by the energy form delivered by wind and solar power, which is electricity. This is different to the traditional energy form of heat produced by the burning of coal, oil and natural gas. Thus, with an increasing share of renewables, the main form of energy is shifted from heat to electricity. Another major difference between traditional and renewable energy sources is the fluctuation of energy supply and the non-conformity between offer and demand as wind and sun are fluctuating and do not comply with the day-to-day peaks and

---

## Introduction

---

lows.<sup>[25]</sup> These factors lead to the urgent need of reliable energy storing systems in the case of overproduction and in general for the warranty of a stable energy supply. Hereby, the factors time scale of availability, e.g. discharge time, and storage capacity play important roles. For example, the flywheel technology offers a very rapid provision of energy, whereby the storage capacity is limited to max. 100 kWh. Batteries are more versatile and can provide electric energy in the range of 5 kWh to 10 MWh, which is comparable to the energy output of a cogeneration unit used for family homes to residential areas.<sup>[26]</sup> For providing mid- to longterm storage capacities from 1 GWh to 1 TWh the power-to-gas process is a feasible option. With this technology, excess electric energy is used to electrolyze water for generating hydrogen and oxygen, whereby the hydrogen gas is the energy carrier of interest.<sup>[27]</sup>

### 1.2. Hydrogen as energy vector

Hydrogen is seen as a viable energy vector, as it is a non-toxic, environmentally benign gas, which can be stored in tanks and can be either used in a fuel cell or be burned when energy is needed.<sup>[12, 28]</sup> Hereby, the combustion of H<sub>2</sub> in internal combustion engines features a higher efficiency ( $\eta = 38.2\%$ ) compared to diesel ( $\eta = 35.1\%$ ) or gasoline ( $\eta = 30.1\%$ ).<sup>[29-31]</sup> Especially H<sub>2</sub>/O<sub>2</sub> polymer electrolyte membrane (PEM) fuel cells are a more efficient and cleaner alternative as they reach a very high efficiency of up to a theoretical value of 85% for the conversion to electricity and produce water as the sole by-product.<sup>[32]</sup>

With 33.33 kWh kg<sup>-1</sup> hydrogen has a comparably high gravimetric energy density, which is more than two times higher than that of gasoline with 12.4 kWh kg<sup>-1</sup>.<sup>[28]</sup> Another positive effect is its high diffusion rate and its excellent miscibility with air, preventing a high local concentration in case of a leak.<sup>[33]</sup> Nevertheless, high safety and material standards have to be ensured because of its highly flammable and volatile properties.<sup>[34-35]</sup> Furthermore, in terms of volumetric energy density, hydrogen gas at ambient pressure features a very low value of 3.00 kWh m<sup>-3</sup>, which is approx. 3,000 times lower than that of petrol.<sup>[33]</sup> This means that either big storage volumes or additional means of volume reduction have to be taken into account.

Generally, physical and chemical methods for the storage of hydrogen gas exist.<sup>[36-37]</sup> For physical storage, gaseous hydrogen can be either compressed at 350–700 bar at room temperature or liquefied at –253 °C. Especially for mobile applications the technical methods of cryoadsorption on high-surface materials such as zeolites, MOFs or carbon nanofibers or cryocompression are considered. For the first two technologies, energy losses in the range of 10–15% and 30–40% of the stored energy for pressurising or cooling the system have to be considered. Also hydrogen losses by either diffusion of the volatile gas or by the so called boil-off decrease the efficiency.<sup>[38]</sup>

### 1.3. Chemical energy carriers

The chemical storage is based on the bonding, complexation or the incorporation of hydrogen into small molecules.<sup>[36]</sup> The benefits of this method are the safer and easier handling and transporting without significant loss of energy, which compensate for the additional energy that has to be

## Introduction

---

invested for the reversible formation/breaking of the chemical bonds. When needed, the hydrogen gas is released by hydrolysis, thermolysis or dehydrogenation using metal, acid or base catalysts.<sup>[39-40]</sup>

Chemical carriers can be either solids, such as hydrides, or (in)organic liquids. Hydrides feature some intrinsic unfavourable properties, as metal hydrides can only store a comparably low hydrogen content of max. 2 wt% and complex or borohydrides need high temperatures for the thermodynamically unfavourable release of hydrogen.<sup>[41-42]</sup> Also amine-borane adducts have been intensively investigated, as they can store high hydrogen contents up to nearly 20 wt%, although their technical application is diminished by the intrinsic risk of releasing ammonia.<sup>[43-44]</sup> Another class that has been increasingly in the focus of interest are liquid organic hydrogen carriers (LOHC), which include cyclic and heterocyclic compounds.<sup>[45-48]</sup> They can incorporate theoretical hydrogen contents in the range of 5–7 wt%, e.g. benzene (7.1 wt%), naphthalene (6.2 wt%), N-ethylcarbazole (5.8 wt%) or pyridine (7.1 wt%).<sup>[49]</sup> Technical storage solutions based on LOHCs have already been launched.<sup>[50]</sup> For the efficient dehydrogenation of these compounds heterogeneous catalysts based on the noble metals Pd or Pt at temperatures from 373–523 K are employed.<sup>[51]</sup>

Other interesting liquid carriers are hydrazine (12.5 wt%), alkanes (methane 25.2 wt%), formic acid (4.4 wt%) and alcohols (ethanol 13.2 wt%, methanol 12.6 wt%). Especially alcohols are a very interesting and promising class of energy carriers due to their often liquid state under ambient conditions and low dehydrogenation temperatures.<sup>[52]</sup>

### 1.4. Methanol as chemical energy carrier

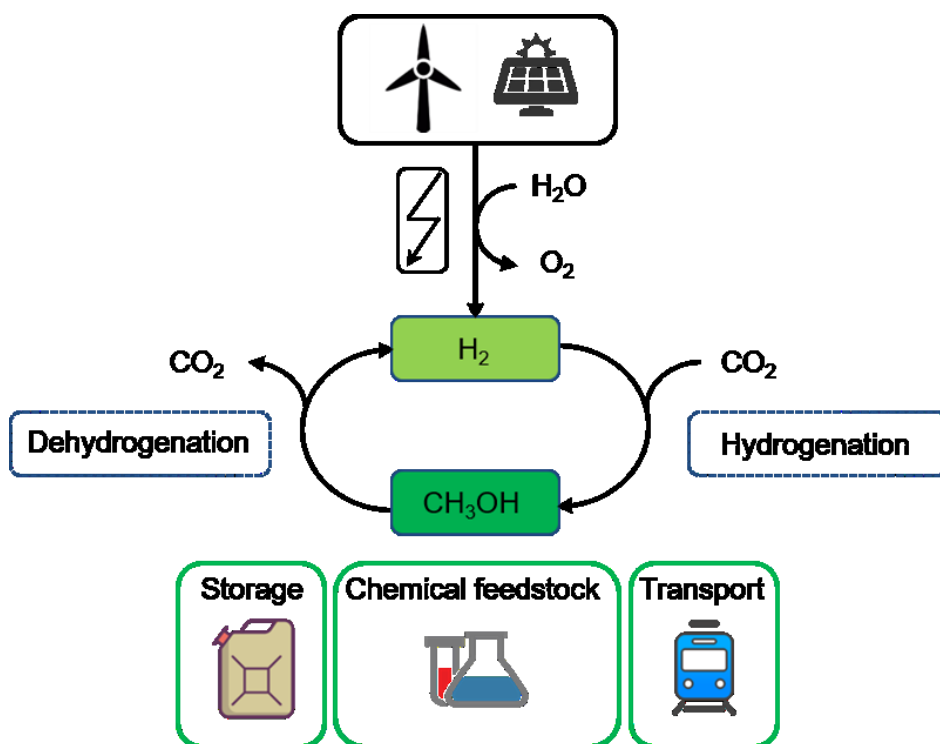
As the release is limited to one equivalent of hydrogen per hydroxyl group of the alcohol, the three simplest alcohols propanol, ethanol and especially methanol have been the desired target of research and notable progress has been made in recent years. The simplest alcohol is considered as the most viable choice because of the highest hydrogen-to-carbon ratio, which means minimum carbon waste and the generation of CO<sub>2</sub> as the sole by-product of the full dehydrogenation reaction.<sup>[52]</sup> Other favourable properties are its comparably low volatility under ambient conditions and the possibility of using already existing structures for storage, transportation and distribution.<sup>[53]</sup> Already in 1968 by F. A. S. and more recently also by G. Olah the idea of a methanol economy has been propagated, which is based on methanol as raw material for synthetic hydrocarbons, such as ethylene or propylene (methanol-to-olefin process), storage medium and fuel.<sup>[28, 34, 54]</sup>

## Introduction

---

A modified version of the methanol economy, which combines the advantages of both the methanol and the hydrogen system and uses catalysis as key technology, is depicted in Scheme 3.

**Scheme 3:** Combined methanol and hydrogen economy.<sup>[55]</sup>



Excess electric energy is utilised to generate hydrogen that reacts in the concomitant hydrogenation step with carbon dioxide to methanol, which can be easily stored and transported. In case of energy need, the reverse process, the dehydrogenation of methanol, is performed and the produced hydrogen can be used in fuel cells for the generation of electric energy. The advantage is that catalysed dehydrogenation reactions are able to produce high-purity  $H_2$ , which does not need to be further purified in an additional step, as this would mean a decrease in efficiency and increase in costs.<sup>[56-59]</sup> The combination of an efficient catalytic system with a PEMF cell leads to an overall high productivity.

To render this envisioned model a realistic alternative to our current fossil-based energy supply and storage system, every single step has to be optimised in terms of energetic efficiency, safety standards and technical practicability.

The focus of this work lies on the catalysed dehydrogenation of methanol for the efficient generation of hydrogen. The following section gives an overview of the development of the heterogeneous and homogeneous catalysts and informs about the state-of-the-art catalyst system for this process.

---

## Introduction

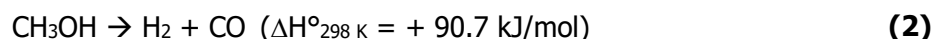
---

### 1.4.1. Heterogeneously catalysed methanol dehydrogenation

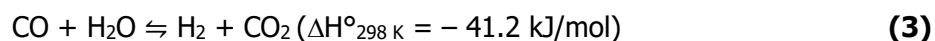
As hot vapour is reacted with methanol, the heterogeneously catalysed dehydrogenation of methanol for hydrogen generation is termed methanol steam reforming. Due to its comparably easy activation this reaction is performed at temperatures from 150 to 350 °C, which is significantly lower than the temperature range of 800–1000 °C for methane reforming.<sup>[60-61]</sup>



An undesired reaction that takes place during the reforming process is the decomposition of methanol to H<sub>2</sub> and CO. As carbon monoxide is a strong fuel cell poison, it is aimed to optimise catalyst selectivity and thereby reduce the amount of carbon monoxide production.<sup>[62]</sup>



Generally, CO can react with water to form hydrogen and carbon dioxide according to the water-gas shift reaction:



As catalysts, copper-containing systems such as Cu/ZnO and Cu/ZnO/Al<sub>2</sub>O<sub>3</sub>, have been applied for the steam reforming reaction since they are successfully used for the synthesis of methanol and the low-temperature water-gas-shift reaction.<sup>[63]</sup> These base-metal based catalysts show high activity at low material costs, although pyrophoric properties and a comparably low selectivity towards CO generation have to be taken into account.<sup>[62]</sup> Notably palladium- and platinum-containing catalysts feature higher stability. For these noble-metal based catalysts, highest activity was reached with bimetallic Pd/ZnO, whereas the use of Pd/Cd resulted in best selectivity.<sup>[64]</sup>

At the beginning of the 21<sup>st</sup> century, Dumesic et al. made a pioneering contribution to the heterogeneously catalysed generation of hydrogen from alcohols and sugars by introducing the aqueous-phase reforming process during which the substrates are reacted with liquid water at temperatures in the range of 200 °C and pressures of 25–50 bar using Pt/Al<sub>2</sub>O<sub>3</sub> as catalyst.<sup>[65-66]</sup> Since then, extensive research has been performed on advancing the aqueous-phase reforming process for a variety of substrates, such as alcohols, sugars and biomass-derived hydrocarbons.<sup>[67-71]</sup>

## Introduction

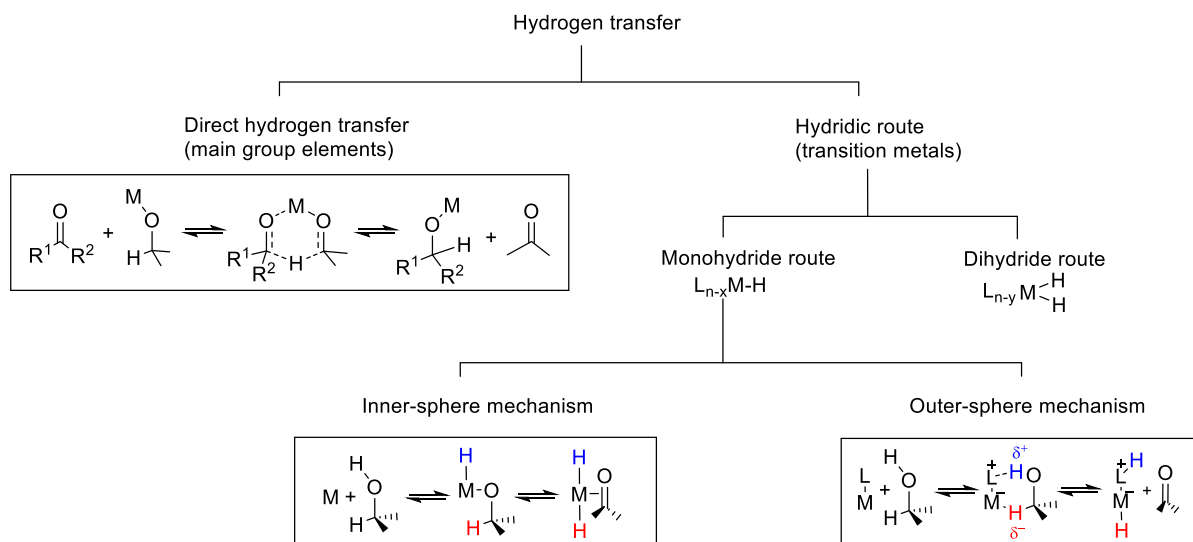
### 1.4.2. Homogeneously catalysed alcohol dehydrogenation

In case of homogeneously catalysed reactions reactants, solvent and catalyst are all in one phase, which is the main difference to heterogeneous systems. Generally, homogeneous catalysis is operated at lower temperatures and better selectivities are obtained, whereas catalyst recovery is more challenging.<sup>[72]</sup>

#### 1.4.2.1 Basic principles

Classically, alcohol dehydrogenations were performed under synthetic considerations and the goal of the oxidation reaction was to obtain maximum yield of the desired carbonyl product. By using a sacrificial reagent, which is concomitantly hydrogenated, an efficient method for reaching higher conversions was developed (transfer hydrogenation). In contrast, the more recent approach of the acceptorless dehydrogenation focuses on the generation of hydrogen as a valuable product.<sup>[73-74]</sup> One of the key steps of the homogeneously catalysed dehydrogenation of alcohols is the hydrogen transfer from reactant to the metal or the acceptor in case of transfer hydrogenation. For main group elements, such as  $\text{Al}(\text{O}^i\text{Pr})_3$ , which is used for the Meerwein-Ponndorf-Verley reduction, the hydrogen atom is directly transferred to the acceptor molecule through a six-membered transition state without the formation of a metal hydride (Scheme 4).<sup>[75-77]</sup>

**Scheme 4:** Pathways for the transfer of hydrogen.



For transition metals, the hydridic route prevails, and both inner-sphere and outer-sphere mechanisms have been proposed as viable pathways. The inner-sphere route involves the direct coordination of the metal to the alcohol in the form of a metal alkoxide, to which the hydride is transferred. In the outer-sphere mechanism, no direct bonding between metal and alcohol exists, instead the coordination to a so-called non-innocent ligand takes place. They are termed non-innocent because they are not merely spectator ligands, which modify the electronic and steric

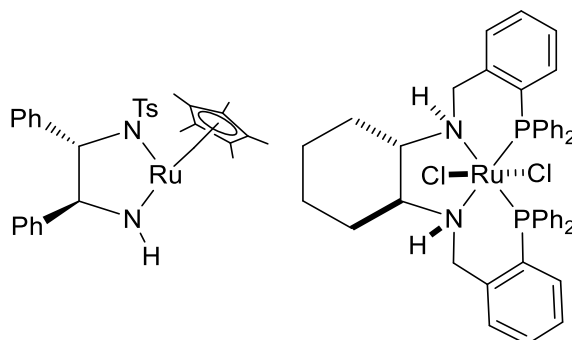


## Introduction

---

properties of the metal, but are directly involved in substrate activation.<sup>[78]</sup> In the following step, the hydride is transferred to the metal centre and the proton to the ligand moiety, which is reminiscent of the reactivity of a frustrated Lewis-base and -acid pair.<sup>[79-80]</sup> This transformation can either proceed via a concerted or a stepwise, ionic pathway.<sup>[76, 81-84]</sup> These novel types of catalysts were introduced by Fryzuk, Shvo and Noyori in the 1980s, for which Noyori postulated the elemental mechanism of metal-ligand bifunctional catalysis.<sup>[85-88]</sup> Typical structures of the Noyori type of catalysts based on ligands featuring N-H moieties are shown in Scheme 5.<sup>[89-90]</sup>

**Scheme 5:** Two examples for the Noyori-type of catalyst.



### 1.4.2.2 Historic development

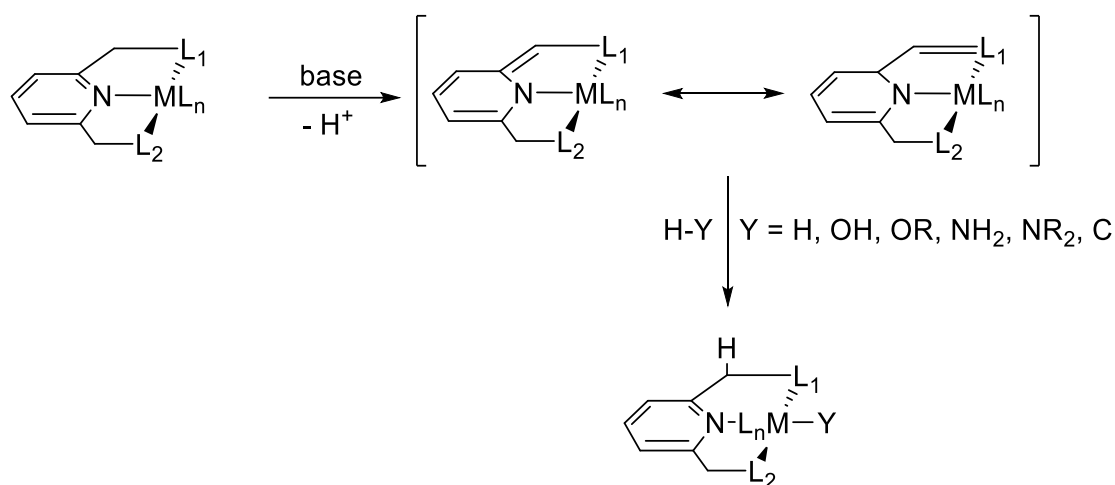
First acceptorless alcohol dehydrogenation reactions were already reported in the 1960s by Charman, using Rh(III)-tin-complexes and *iso*-propanol as substrate.<sup>[91-93]</sup> In the late 1970s Robinson employed the ruthenium and osmium complexes  $[M(\text{COOR}_F)_2(\text{CO})(\text{PPh}_3)_2]$  in combination with trifluoroacetic acid for the dehydrogenation of primary and secondary alcohols.<sup>[94]</sup> A decade later, the group of Cole-Hamilton was one of the first ones to shift the focus from synthetic applications to the production of hydrogen from methanol and higher alcohols. By employing  $[\text{RuH}_2(\text{N}_2)(\text{PPh}_3)_3]$  under irradiation of light at 150 °C catalytic activities of 210 h<sup>-1</sup> and 1185 h<sup>-1</sup> for the acceptorless dehydrogenation of ethanol and ethylene glycol, respectively, were reached.<sup>[95-96]</sup> For the following decades, it remained one of the most active systems.

At the beginning of the 21<sup>st</sup> century, a new type of catalyst based on non-innocent pyridine-PNP pincer ligands was introduced by Milstein and co-workers and was shown to successfully catalyse the dehydrogenation of *iso*-propanol and higher alcohols.<sup>[97]</sup> The name of these type of ligands is based on the meridional manner they coordinate around the metal centre.<sup>[98]</sup> Their ligand cooperation can be attributed to the reversible process of ligand backbone aromatization and de-aromatization (Scheme 6).

## Introduction

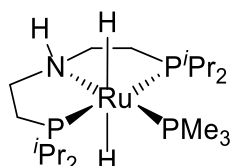
---

**Scheme 6:** Non-innocent pyridine-PNP pincer catalysts introduced by Milstein and co-workers.



With similar scaffolds of bifunctional pincer catalysts the dehydrogenation of primary alcohols to esters and acids were performed.<sup>[99-100]</sup> In 2009 Schneider and co-workers broadened the spectrum of non-innocent complexes by applying a ruthenium catalyst bearing an aliphatic PNP pincer ligand for the dehydrogenation of ammonia borane.<sup>[101]</sup>

**Scheme 7:** Aliphatic PNP-pincer complex by Schneider and co-workers.



This catalyst motif was readily picked up by other groups and a couple of years later Beller and co-workers used the *in-situ* generated system based on the pre-catalyst [RuH<sub>2</sub>(PPh<sub>3</sub>)<sub>3</sub>(CO)] and the cooperative bis-[(2-di*iso*propylphosphino)ethyl] amine pincer ligand HN(CH<sub>2</sub>CH<sub>2</sub>)P(CH(CH<sub>3</sub>)<sub>2</sub>)<sub>2</sub> (from here on termed HPNP<sup>*i*</sup>Pr ligand) for the low-temperature dehydrogenation of *iso*-propanol and ethanol. Under neutral conditions, remarkable activities of 8,000 h<sup>-1</sup> and 1,400 h<sup>-1</sup>, respectively, were achieved.<sup>[102]</sup>

Only two years later, the same group performed the 1<sup>st</sup> homogeneously catalysed aqueous-phase reforming of methanol. This meant a great breakthrough in the field of alcohol dehydrogenation for energy purposes as the addition of water allowed the complete conversion to hydrogen and carbon dioxide.<sup>[103]</sup>

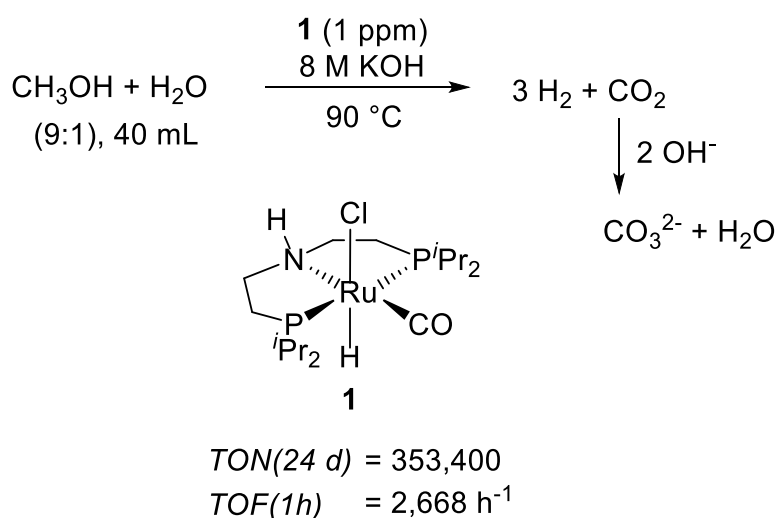
---

## Introduction

---

Hereby, the aliphatic Ru-pincer complex **1** was employed. Under highly basic conditions and using less than 1 ppm of **1**, a productivity of over 350,000 was achieved, which represents the most active system developed to date at a temperature below 100 °C (Scheme 8). Besides, the long-term stability was demonstrated, as the catalyst remained active for more than 23 days. The catalyst's productivity is depicted as turnover number (TON) and its activity as turnover frequency (TOF), for which the detailed calculations can be found in the Appendix Section 6.3.1.3.

**Scheme 8:** First homogeneous catalyst system for the aqueous-phase dehydrogenation of methanol.



At the same time, Trincado, Grützmacher and co-workers employed the  $[\text{K}(\text{dme})_2][\text{Ru}(\text{H})(\text{trop}_2\text{dad})]$  catalyst based on the chelating bis(olefin) diazadiene ligand for the successful conversion of methanol. Under neutral conditions and with THF as solvent, a productivity of 540 generated moles of hydrogen for each mole of catalyst was reached after ten hours.<sup>[104]</sup> Other catalyst systems based on the noble metals ruthenium and iridium, but also the base metal iron were subsequently developed and applied for the generation of hydrogen from methanol by Crabtree, Holthausen, Fujita, Yamaguchi and others.<sup>[105-111]</sup> The variety of catalyst systems and their productivities are shown in Scheme 9.

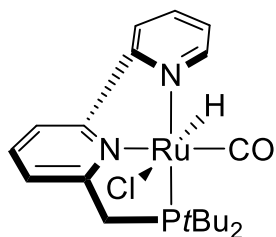
---

## Introduction

---

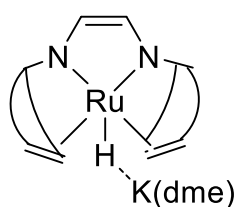
**Scheme 9:** Examples of homogeneous catalysts employed for the methanol dehydrogenation.

**Milstein**

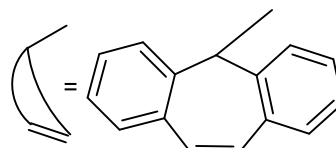


$TON(27\text{ d}) = 28,700$

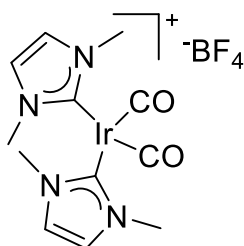
**Grützmacher**



$TON(10\text{ h}) = 540$

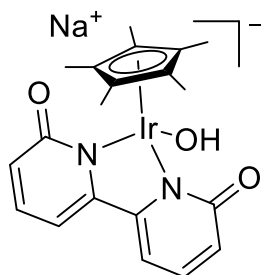


**Crabtree**



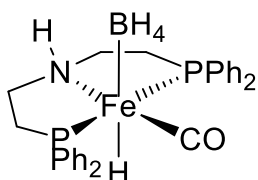
$TON(24\text{ h}) = 3,600$

**Fujita, Yamaguchi**



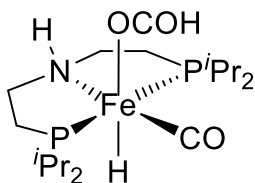
$TON(150\text{ h}) = 10,500$

**Beller**



$TON(111\text{ h}) = 9,184$

**Bernskoetter, Hazari & Holthausen**



$TON(52\text{ h}) = 30,000$

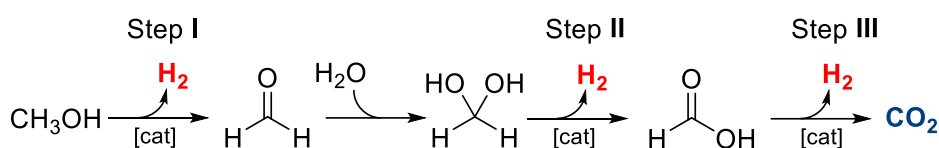
## 2. Part I: Ruthenium-catalysed dehydrogenation of methanol

### 2.1. Introduction

For the state-of-the-art system based on the aliphatic Ru-PNP complex **1**<sup>[103]</sup>, it was shown that the nature of the base, its concentration and the reaction temperature had significant influence on the catalytic activity. Generally, the combination of a 9:1 MeOH:H<sub>2</sub>O solution with 8 M KOH resulted in best catalytic performance for the aqueous-phase reforming of methanol. It was assumed that the increase in activity at this high base concentration was mainly caused by the increase of temperature from 65 °C to 90 °C by the effect of boiling-point elevation than by the effect of the base itself.

Full methanol reforming proceeds through three consecutive steps, leading to the release of three equivalents of hydrogen. Hereby, the dehydrogenation of methanol induces the formation of formaldehyde, which reacts in the subsequent step in the form of a gem-diol to formic acid. Then, during the last step, the formic acid is dehydrogenated to carbon dioxide (Scheme 10).

**Scheme 10:** Overview of the steps of the complete methanol dehydrogenation reaction.<sup>[103]</sup>

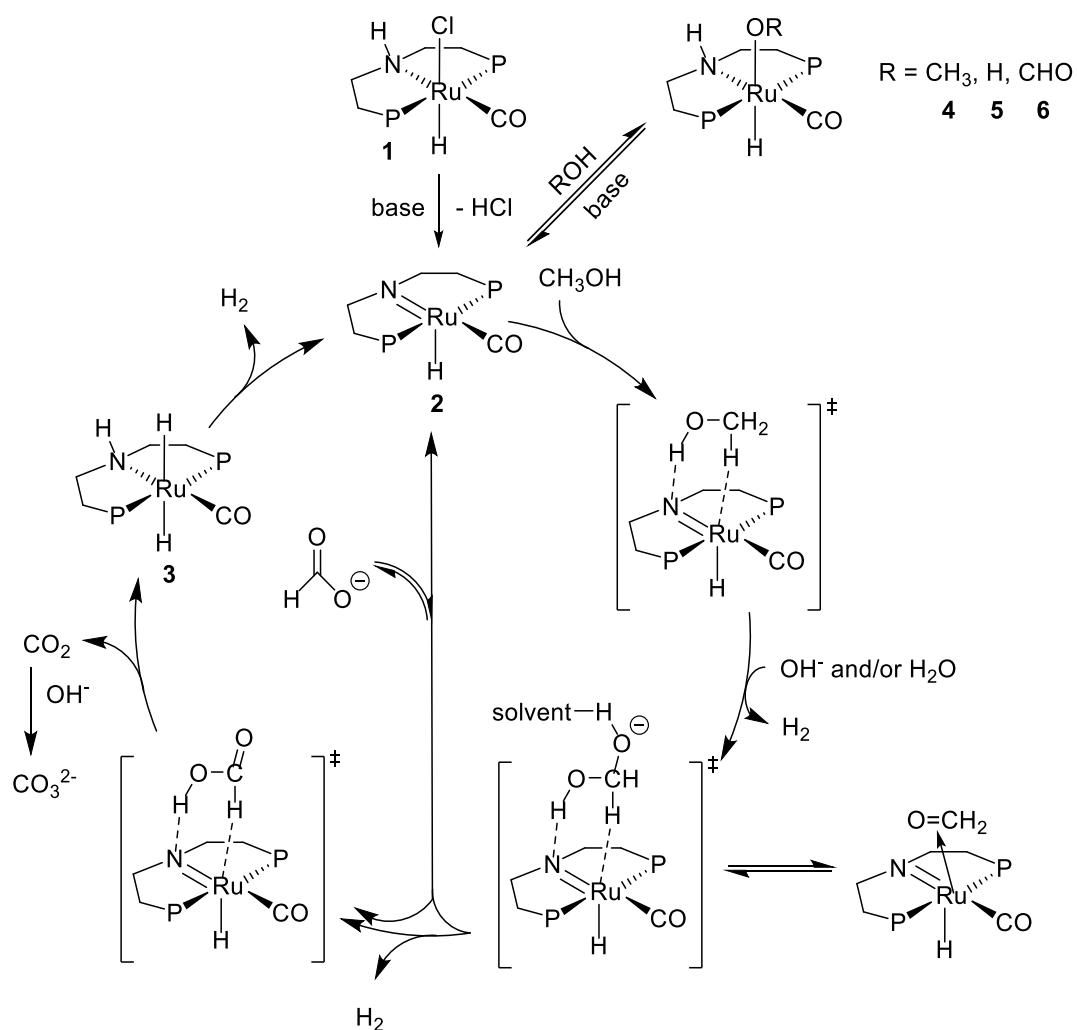


An overall mechanistic cycle was proposed, which starts with the dehydrochlorination of the precursor **1** to give the amido species **2** (Scheme 11). This complex features a Lewis-basic amido functionality and a partial metal-nitrogen double bond exists between the Lewis-acidic ruthenium and the amido group.<sup>[78]</sup> Onto this coordinatively unsaturated species, the outer-sphere coordination of methanol takes place and the key C-H cleavage step is performed by the simultaneous transfer of a hydride to the ruthenium centre and a proton to the nitrogen moiety, which leads to the generation of one equivalent of H<sub>2</sub>.

It was assumed that the formed formaldehyde undergoes further reactions while still being coordinated to the catalyst species as it could not be detected in solution. Subsequently, by the addition of water and/or hydroxide the gem-diolate is formed, which is again dehydrogenated to give formic acid and the next equivalent of hydrogen. Free formate is actually detected in solution, which means two pathways can be followed at this point. One option is the restarting of the catalytic cycle by the release of formate and the formation of the amido species **2**, onto which methanol can coordinate again. The second possibility is the completion of the cycle by the release of CO<sub>2</sub> and the last equivalent of H<sub>2</sub>.

## Part I - Introduction

**Scheme 11:** Complete mechanistic cycle proposed for the methanol dehydrogenation by catalyst **1**. P = P'Pr<sub>2</sub>.<sup>[103]</sup>



During the reaction process monohydride species were observed, which were assumed to be either the methoxide species **4**, hydroxide species **5** or the formate species **6**. In this regard it was speculated that the role of the base is to regenerate the active amido species from these resting states instead of the deprotonation of methanol and formic acid. Nevertheless, it was mused that the reactivity might be increased by the deprotonation of methanol, though that would rather hint at an inner-sphere mechanism.

The theoretical work by Yang in 2014 and Ma and co-workers in 2015 supported the proposal of an outer-sphere mechanism.<sup>[112-113]</sup> Yang postulated that the transfer of the hydride and the proton takes place in a stepwise process, whereby Ma proposed the co-existence of the outer-sphere and the inner-sphere pathways in the case of the formate dehydrogenation.

### 2.2. Objective of project I

Based on the results summarised in the introduction, it can be concluded that a very effective catalytic system based on the Ru-PNP complex **1** was established. Nevertheless, a range of important aspects have not been clarified and some assumptions have been made without further clarification as no conclusive mechanistic investigations have been performed so far.

The most important questions that still have to be answered and are crucial for the overall understanding of this catalyst system are summarised below:

- Is the high concentration of base solely needed to increase the temperature of the reaction solution, which leads to enhanced activity? Or does it also play an active role in the mechanism?
- What kind of mechanistic pathway does the Ru-PNP complex follow? Is it an inner-sphere or an outer-sphere mechanism and how can this be verified?
- Which complexes are the active catalytic species that take part in the mechanistic cycle and how do they interact with each other?

It is hoped that by answering these questions, a comprehensive mechanistic cycle can be developed, which is a crucial step towards improving and implementing novel catalyst scaffolds. In order to reach this goal, a range of experimental, spectroscopic and theoretical tools are envisioned to be employed. This includes performing kinetic investigations, stoichiometric and catalytic NMR measurements and reaction monitoring by a combined Raman and GC setup. Furthermore, it is planned to support the results by theoretical DFT calculations.

### 2.3. Results and discussion<sup>[114]</sup>

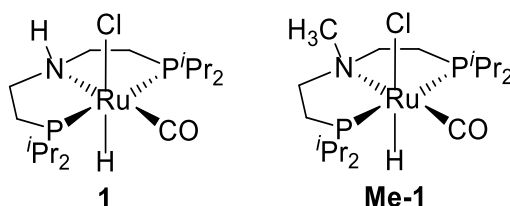
#### 2.3.1. Inner-sphere vs. outer-sphere mechanism<sup>[115]</sup>

In order to be able to answer the essential question whether the key C-H cleavage step occurs via an inner-sphere or an outer-sphere pathway, the methylated derivative **Me-1** was synthesized by Dr. Elisabetta Alberico (Scheme 12). This strategy to replace the N-H moiety by a N-Me moiety is common to test for ligand cooperativity and to assess if the ligand is non-innocent.<sup>[116-117]</sup>

##### 2.3.1.1. Activity of **1** and **Me-1**

The activity of the methylated Ru-pincer catalyst for the methanol dehydrogenation was investigated under optimised conditions and to our surprise it resulted in significant hydrogen evolution of approx. 40% of the state-of-the-art catalyst **1** (Figure 5).

**Scheme 12:** Ru-PNP parent catalyst **1** and its methylated derivative **Me-1**.



A contrasting result was obtained in the case of ammonia-borane dehydrocoupling catalysed by [Ru(H)<sub>2</sub>(PMe<sub>3</sub>)(HNPNP)] as Schneider and co-workers measured a lower activity for the N-methylated backbone derivative of almost two orders of magnitude. Hereby, calculations showed that for both catalysts the same mechanistic pathway is undergone, though with higher energy barriers in the case of the latter.<sup>[117]</sup>



## Part I - Inner-sphere vs. outer-sphere mechanism

---

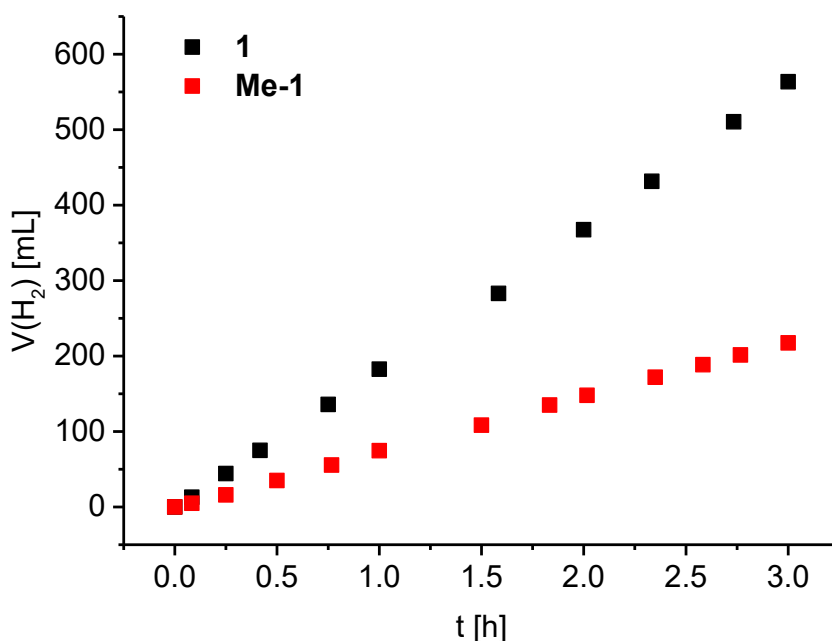


**Figure 5:** Activities of **1** and **Me-1**. Conditions: 8 M KOH, MeOH:H<sub>2</sub>O (9:1, 10 mL), 4.2 μmol **1** or **Me-1**, 90 °C.<sup>[118]</sup>

The outcome of the methylation experiment has shown that the N-H moiety does not seem to be essential for catalytic activity. The question, which consecutively arises, is whether the same mechanism is operating for both types of catalysts or if indeed significantly different pathways are followed.

### 2.3.1.2. KIEs

In order to get a better understanding of the reasons causing the differences in activities, the kinetic isotope effects (KIEs) were determined for both catalysts. The KIE is based on the substitution of the substrates' atoms by one of their isotopes, which can lead to a change of the reaction rate due to the breaking of bonds of the isotopes, hyperconjugation effects or changes in hybridization during the rate-determining step. Hereby, the definition of the KIE is the proportion of the rate constant for the reactant containing light isotopes ( $k_L$ ) and the rate constant for the reactant consisting of heavy isotopes ( $k_H$ ).<sup>[119-120]</sup>

$$KIE = \frac{k_L}{k_H} \quad (4)$$

For this set of experiments, activities for both **1** and **Me-1** were measured using deuterated methanol, water and base and then compared to the activities under standard conditions. In the

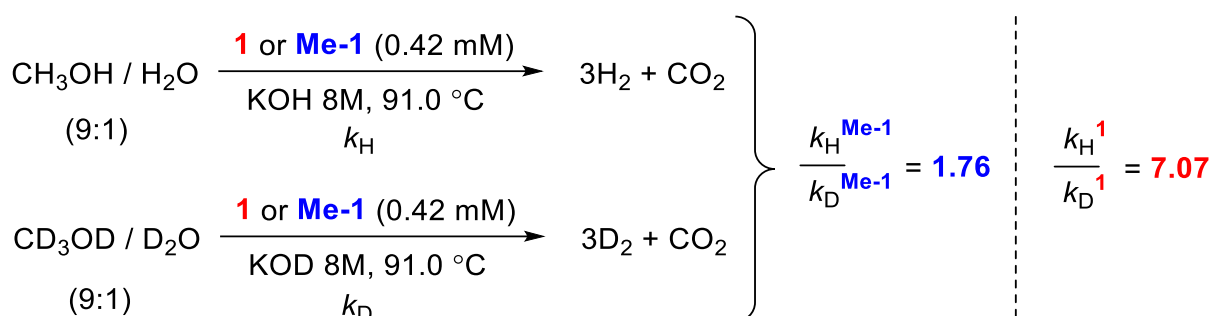
---

## Part I - Inner-sphere vs. outer-sphere mechanism

---

case of the state-of-the-art Ru-pincer catalyst, deuteration of the substrates led to a decrease in activity by a sevenfold, whereas the activity of **Me-1** was not even diminished by a factor of two (Scheme 13).

**Scheme 13:** Overview of the KIEs determined for catalysts **1** and **Me-1**.



The implications of this striking difference in KIE cannot be easily assessed, as the measured rate of the reaction is composed of three entangled steps, thus the product of the preceding is the starting material for the following step. Nevertheless, based on the magnitude of the difference in KIE for both catalysts, it is possible to assume that they likely follow different mechanistic pathways. With a value of 1.71 for the methylated derivative, the KIE is only slightly higher than one, which means that no significant cleavage of C-H, O-H or Ru-H bonds take place during the rate-limiting step(s).

These results were already promising and meant a step closer to improved comprehension of the mechanistic pathway. For a better understanding of the differences between the two catalysts, subsequent investigations concentrating on the parent catalyst **1** were performed. The results are described in detail in the following section.

## Part I - Investigations for catalyst 1

### 2.3.2. Investigations for catalyst 1

#### 2.3.2.1. Base- and temperature-activity dependency

One of the unsolved challenges was to find out the role of the base for the mechanism. The first step towards this goal was to entangle the reciprocal correlation of base and reaction temperature. Thus, to test for the salt effect, it was tried to replace the base by innocent types of salt, such as  $\text{KNO}_3$  or  $\text{KPF}_6$ . Unluckily, this approach proved to be unsuccessful due to the reduced solubility of these particles. The use of pH-buffered solutions was not futile either. A third attempt was the addition of high-boiling solvents, e.g. *t*-BuOH or NMP, to the reaction mixture, which caused the complete seizure of activity (For details on the experiments see Appendix Section 6.4.1.1.).

#### Temperature-activity measurements

Since these strategies were not fruitful, the focus shifted to the investigation of the correlation between base amount and reaction temperature. The first step was to measure the rate of the methanol dehydrogenation at a temperature range between 50–90 °C, which resulted in the Arrhenius plot shown in Figure 6. Based on the linear extrapolation it can be concluded that the inflation of the temperature above the boiling point of the methanol-water mixture does not alter the mechanism as it does not lead to a higher activity than caused by the rise in temperature. Consequently, it is possible to perform mechanistic investigations at lower temperatures. Additionally, this result means that the base does not solely increase the reaction temperature, but that it indeed plays an essential part in the mechanism.

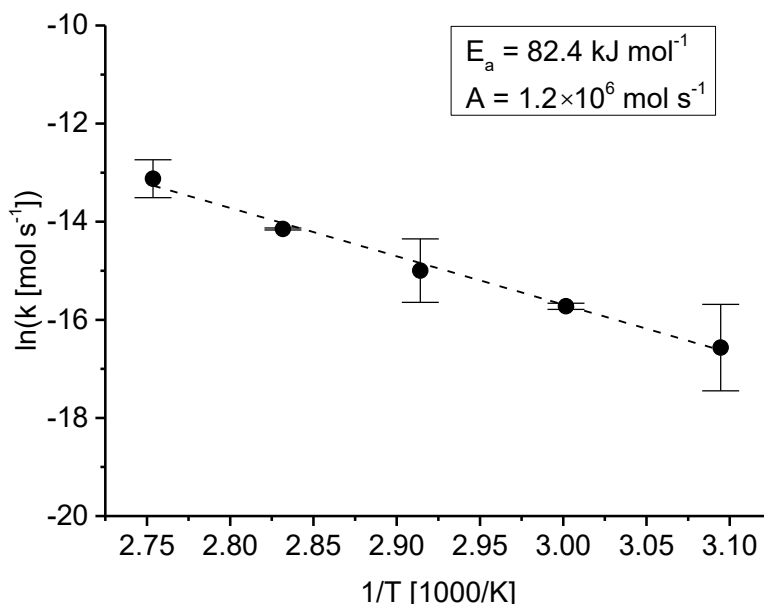


**Figure 6:** Arrhenius plot. Conditions: 8 M KOH, MeOH:H<sub>2</sub>O (9:1, 10 mL), 4.2 μmol **1**, 90 °C, 3 h.<sup>[118]</sup>

## Part I - Investigations for catalyst 1

---

### Base molarity-activity measurements

Based on the results of the temperature-activity measurements, the next investigation concentrated on the influence of base molarity on the activity. A promising plan of action was to use an autoclave to overpressurize the system for enabling a higher boiling point. Thus, it would be possible to vary the amount of base while leaving the reaction temperature at 90 °C. To determine the value of the overpressure, the Clausius-Clapeyron equation was used:

$$\ln\left(\frac{p_2}{p_1}\right) = -\frac{\Delta H}{R}\left(\frac{1}{T_1} - \frac{1}{T_2}\right) \quad (5)$$

Before starting with the actual measurements, the temperature of reaction solutions containing different base molarities were determined in order to know the amount of base needed in the system to reach a certain boiling point. The resulting linear correlation is shown below:

$$T = 3.3 \frac{^{\circ}\text{C}}{\text{mol L}^{-1}} \cdot M(\text{KOH}) + 65.3 \text{ }^{\circ}\text{C} \quad (6)$$

The reactions were performed in a completely sealed autoclave containing KOH, reaction solution and catalyst. Once the desired inner temperature was reached, the activity was measured by the increase of pressure in the autoclave caused by the formation of hydrogen gas. During the measured reaction times, the generated carbon dioxide was trapped as carbonate and thus did not have to be taken into account. For calculating the generated amount of H<sub>2</sub> from the measured increase of pressure, the Van-der-Waals equation was used (For more information see Appendix Section 6.4.1.1.).

Unluckily, this procedure did not prove to be successful, as it was noted that the increased pressure had a detrimental effect on the catalytic activity. To verify this observation, the autoclave was pressurised with additional nitrogen or hydrogen gas and indeed activities were found to be significantly lower, especially in the case of the applied hydrogen overpressure. (see Figure 7). Once the pressure was again released, catalytic activity improved significantly.

These findings show that the decrease in activity is caused by a chemical effect. At higher partial pressures, hydrogen presumably coordinates onto the active catalytic species, thus preventing the dehydrogenation reaction to take place. The successful hydrogenation of esters to alcohols with the related Fe-PNP catalyst has been reported in literature, which confirms the general ability of this type of complexes to catalyse hydrogenation reactions.<sup>[121]</sup> Consequently, the original setup had to be varied in order to obtain reliable reaction rates.

## Part I - Investigations for catalyst 1

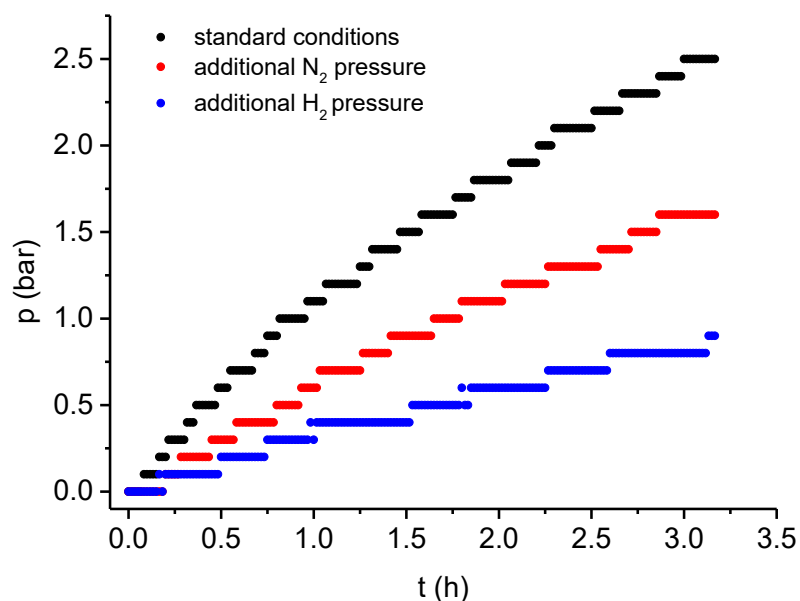


**Figure 7:** Influence of H<sub>2</sub> and N<sub>2</sub> pressure on the catalytic activity of **1**. Conditions: 8 M KOH, MeOH:H<sub>2</sub>O (9:1, 10 mL), 4.2 μmol **1**, 90 °C, approx. 6 bar H<sub>2</sub>/N<sub>2</sub> pressure, sealed autoclave setup).<sup>[118]</sup>

To overcome the reported problem, the influence of base was measured at 60 °C using the standard burette setup, since this temperature can be reached using a methanol-water solution that does not contain any additional salts. This modification was possible as it was shown before that the mechanism does not change with altering the temperature. Additionally, for measuring the activity for different base molarities at 90 °C, the autoclave setup was adjusted by implementing a pressure valve (Figure 8).



**Figure 8:** Modified autoclave setup.<sup>[118]</sup>

## Part I - Investigations for catalyst **1**

---

This design made it possible to leave a specified pressure on the system, whereas all exceeding pressure was released and the gas was captured by gas burettes connected to the autoclave exhaust via a condenser. It was chosen to use 0.6 bar on the autoclave because this enabled to investigate KOH molarities from 4 M to 8 M. The additional pressure on the system caused an expected attenuation in the catalysts' activities. Complex **1** reached a significantly lower TOF of approx.  $550 \text{ h}^{-1}$  under these conditions instead of  $1770 \text{ h}^{-1}$  in an open vessel. However, this effect is negligible as the relative activities and their correlation to the change in base molarities were in the focus of interest.

The results of the activity determination at different base molarities can be seen in Figure 9. With no additional base, the catalyst was not active at all. At  $60 \text{ }^\circ\text{C}$  a first-order dependency of the activity on the base molarity was observed. At the higher temperature of  $90 \text{ }^\circ\text{C}$ , catalytic activity stagnated with higher base concentrations, which means that saturation kinetics occurs. A possible explanation for this effect could be the mass-transport limiting loss of  $\text{H}_2$  at these high reaction rates, which were already observed and investigated by Dumeignil and Gauvin and co-workers.<sup>[122]</sup> This phenomenon had to be further examined, as well as the correlation between catalyst concentration and activity (see the following section).

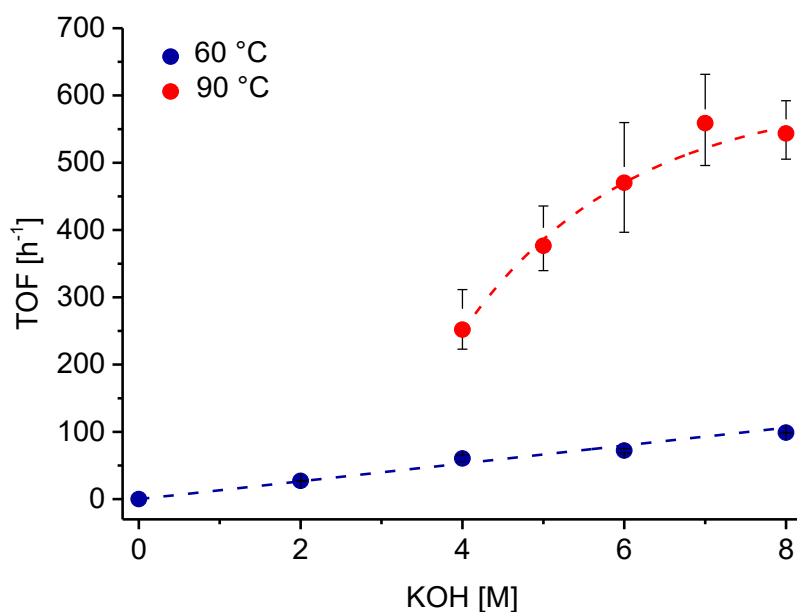


**Figure 9:** The influence of KOH concentration on the activity of catalyst **1** in methanol reforming at  $60 \text{ }^\circ\text{C}$  and  $90 \text{ }^\circ\text{C}$ . Conditions at  $60 \text{ }^\circ\text{C}$ : 10 mL MeOH:H<sub>2</sub>O (9:1) and **1** ( $8.41 \text{ } \mu\text{mol}$ ) using the "regular" burette setup. Conditions at  $90 \text{ }^\circ\text{C}$ : 20 mL MeOH:H<sub>2</sub>O (9:1) and **1** ( $8.41 \text{ } \mu\text{mol}$ ) in a leaking autoclave set to an over pressure of 0.6 bar. Lines are solely a guide for the eye.<sup>[118]</sup>

## Part I - Investigations for catalyst 1

---

### *Activity vs. catalyst concentration*

There are several cases mentioned in the literature about the increase of catalyst activity with decreasing catalyst loading. One example is the dehydrogenation of *iso*-propanol catalysed by the *in-situ* system generated from  $[\text{RuH}_2(\text{PPh}_3)_3\text{CO}]$  in combination with additional HPNPPr ligand reported by Beller and co-workers.<sup>[102]</sup> They observed a fourfold increase in activity when lowering the catalyst amount from 32 ppm to 4 ppm, but did not give possible explanations for this phenomenon. Also Spasyuk and Gusev observed a similar correlation for the Ru-PNN pincer catalysed ethanol dehydrogenation.<sup>[123]</sup> They suggested that a possible explanation could be dimerization processes of the catalyst, which occur at higher catalyst loadings.

Based on these findings, the relation between activity and catalyst concentration was measured. The result is a correlation below one, which is in agreement with the former reported observations (see Figure 10). To test for possible off-cycle dimerization processes, reactions at different catalyst loadings were performed and the reaction solution analysed by  $^{31}\text{P}$  NMR and mass spectrometry. Neither of the two methods gave any hints to the formation of Ru-dimers, which means that no comprehensive conclusion can be drawn concerning this issue.

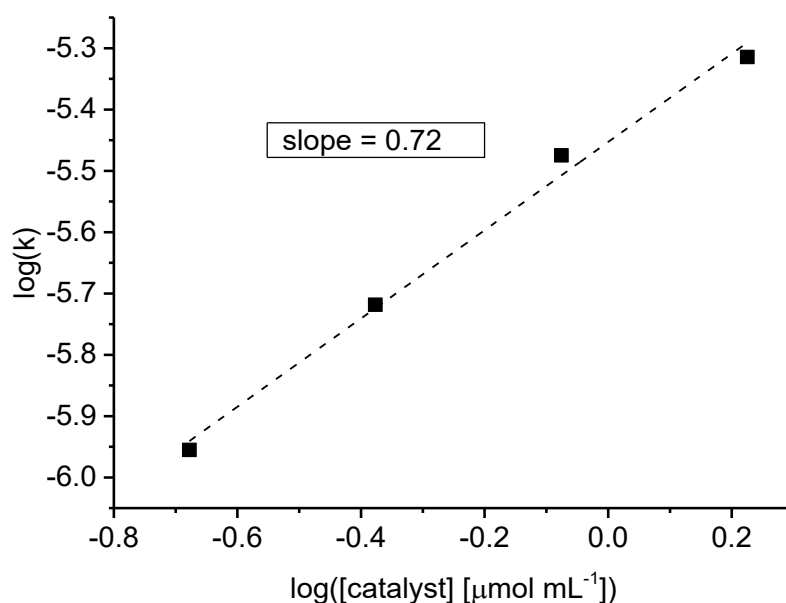


**Figure 10:** Catalytic activity of **1** vs. catalyst concentration. Conditions: 8 M KOH, MeOH:H<sub>2</sub>O (9:1, 10 mL), 2.1/4.2/8.4/16.8  $\mu\text{mol}$  **1**.<sup>[118]</sup>

## Part I - Investigations for catalyst 1

### *Investigations on the H<sub>2</sub> mass transfer*

Another possible explanation for both the observed saturation kinetics at higher molarities for catalyst **1** and the decline of catalytic activity with higher catalyst loading could be the limiting factor of hydrogen mass transfer, as described by Dumeignil, Gauvin and co-workers.<sup>[122]</sup> Thus, reactions were performed at different stirring rates of 100, 700 and 1200 rpm. From Figure 11 it is evident that this rate has a significant influence on the catalyst's activity. It is remarkable that increasing the stirring rate from 100 rpm to 1200 rpm caused a threefold rise in gas evolution. This effect can be explained by the reversibility of the hydrogenation/dehydrogenation reaction. At higher gas evolution rates the gas cannot escape fast enough due to limited hydrogen mass transfer, which leads to a higher saturation of the solution with hydrogen gas. This in turn causes the formation of inactive catalytic species as it was described before. Generally, these assumptions are in good accordance with the observed detrimental effect of additional N<sub>2</sub>, and even more so, H<sub>2</sub> pressure on the system.

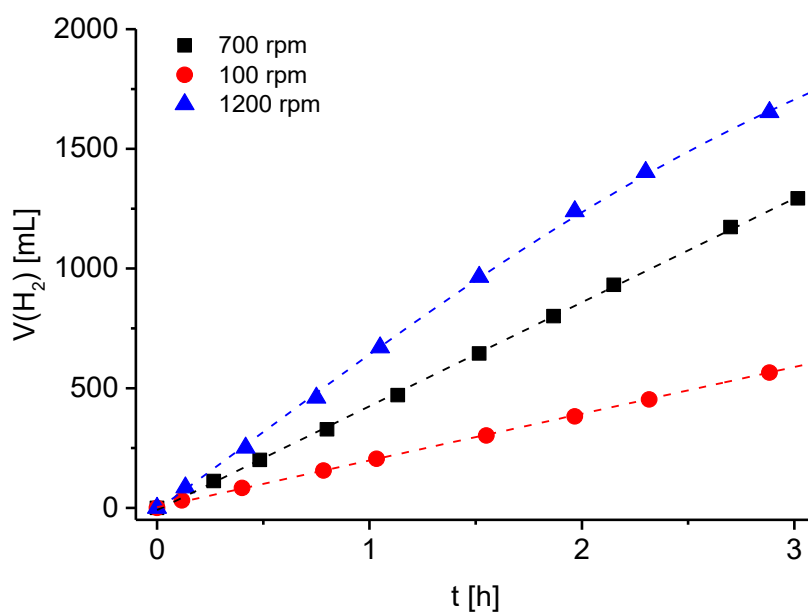


**Figure 11:** Dependency of hydrogen gas evolution on the stirring rate. Conditions: 8 M KOH, MeOH:H<sub>2</sub>O (9:1, 10 mL), 16.8 μmol **1**, 90 °C.<sup>[118]</sup>

The activity measurements described in this section have shown that the base actively takes part in the mechanism and substantially triggers catalytic activity. Subsequently, it was planned to get a better understanding of the observed macroscopic effects by performing microscopic studies on the actual catalytic species. The results of the NMR studies are depicted in detail in the following section.



## Part I - Investigations for catalyst 1

### 2.3.2.2. NMR studies

#### Stoichiometric investigations<sup>[124]</sup>

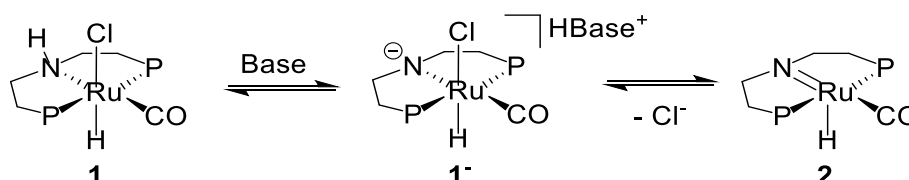
For a better comprehension of possible active intermediates and species, a range of catalyst intermediates were synthesized and analysed under aprotic conditions by Dr. Elisabetta Alberico.

#### Generation of the amido species **2**

The very first step was to verify the proposition that the active amido species **2** is generated by the dehydrochlorination of the pre-catalyst **1** (see Scheme 14). This was done by adding one equivalent of <sup>t</sup>BuOK to **1** leading to the formation of complex **2** as NMR analysis and the X-ray structure showed (For details on NMR experiments see Appendix Section 6.4.1.2.).

It is assumed that this step follows a conjugate base mechanism ( $S_N1CB$ ), which is common for a range of transition metal complexes bearing amine ligands.<sup>[125]</sup> In the case of the precursor, the acidity of the amino group is enhanced by the coordination to the ruthenium centre and the presence of the *trans*-coordinated, strongly  $\pi$ -accepting carbonyl ligand. The acidic proton of this N-H moiety is abstracted by the base, which leads to the stabilized anion **1<sup>-</sup>**. By the consecutive leaving of the chloride anion, the formal formation of the Ru-N double bond takes place.

**Scheme 14:** Dehydrochlorination of pre-cursor **1** with base. P = PPr<sub>2</sub>.<sup>[118]</sup>



The assumption of a reversible conjugate base mechanism was supported by the treatment of the *anti*-isomer of **1** with the weak base trimethylamine. As expected, isomerization between the *anti*- and the *syn*-isomer could be monitored by NMR measurements.

The reverse reaction, the addition of chloride to the amido complex **2**, could be shown to be kinetically irrelevant by the addition of 10 eq. of KCl to the standard reaction solution. Figure 12 clearly shows that the excess of chloride ions did not have a detrimental effect on the catalytic activity. This result is also indicative for the robustness of the catalytic system regarding the influence of coordinating anions.<sup>[122]</sup> In contrast, Beller and co-workers reported the negative effect of chloride sources on the catalytic activity of their Fe-PNP system for the hydrogenation of esters.<sup>[121]</sup>

## Part I - Investigations for catalyst 1

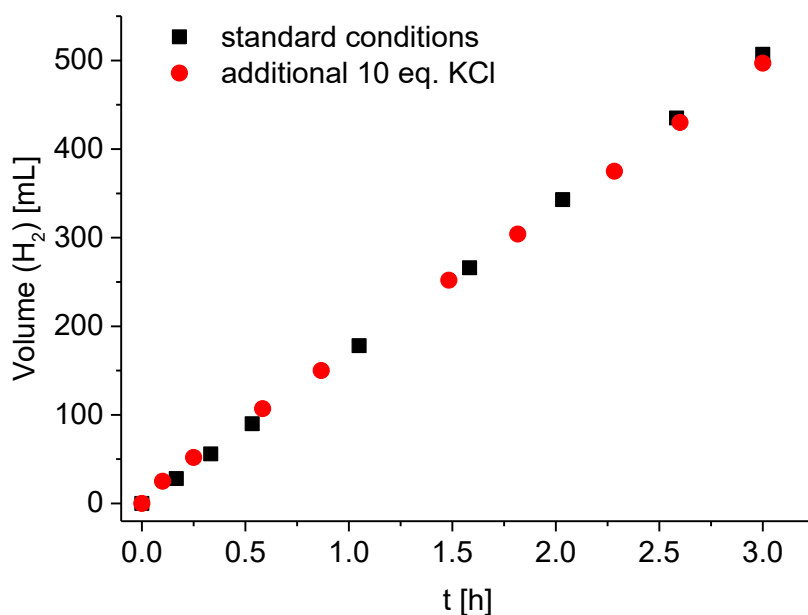
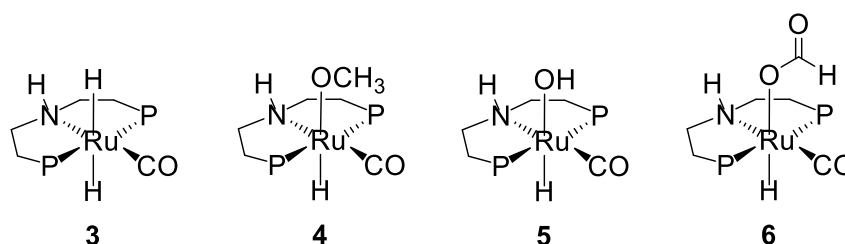


**Figure 12:** Comparison of hydrogen gas evolution under standard conditions (8 M KOH, MeOH:H<sub>2</sub>O (9:1, 10 mL), 4.2  $\mu$ mol **1**, 90 °C, black dots) and in the presence of 10 eq. of KCl (to the catalyst **1**, red dots) under otherwise identical conditions.<sup>[118]</sup>

### *Reactions of the amido species 2 with methanol, formic acid and water*

Starting from the active amido species **2**, it was aimed to let it react with methanol, water and formic acid as these are present in excess or accumulate during the reaction. For a better overview, the structures of the observed catalytic species are depicted in Scheme 15.

**Scheme 15:** Overview of related complexes of parent catalyst **1**. P = PPr<sub>2</sub>.



Already when adding two equivalents of methanol to **2**, the formation of the dihydride species **3** and a monohydride species was observed. The latter species was confirmed to be the methoxide complex **4** by the addition of <sup>13</sup>C-enriched methanol: The NMR spectrum at room temperature showed a single doublet, which could be assigned to Ru-O<sup>13</sup>CH<sub>3</sub> and free <sup>13</sup>CH<sub>3</sub>OH by decreasing the temperature as the single peak split into two well-resolved doublets. The methoxide species could not be isolated as by applying vacuum it reverted back to the amido complex **2**.

## Part I - Investigations for catalyst 1

---

Addition of formic acid to species **2** led to the formation of the Ru-formate **6**, which could be affirmed by a X-ray structure from crystals. No hydrogen gas evolved, nor was the dihydride species **3** formed.

The experiment of adding water to the amido species **2** resulted in the formation of the hydroxide species **5**. Comparable to the formation of the formate species, no gas evolution was visible, nor was the dihydride species **3** formed. Like the methoxide species, the hydroxide complex could not be isolated due to the reversion back to the amido complex **2**.

Generally, the chemical shifts of the monohydride complexes pre-catalyst **1**, methoxide species **4**, hydroxide species **5** and formate species **6** lie all in a very close range of 75 –77 ppm in the  $^{31}\text{P}$  NMR spectrum and in the range of –15 to –18 ppm in the  $^1\text{H}\{^{31}\text{P}\}$  NMR spectrum (See Table 4 p. XXI in the Appendix for details).

### *Reactions of the dihydride complex 3*

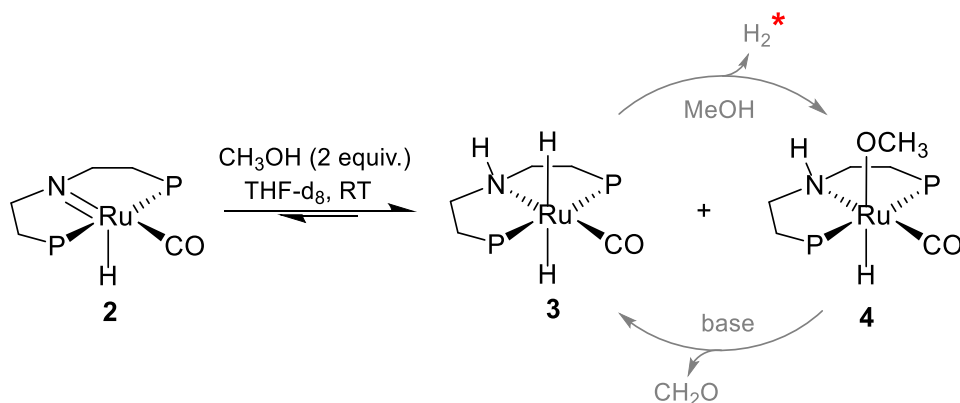
In the original report of the Ru-PNP catalysed methanol dehydrogenation, the solvent-mediated  $\text{H}_2$  release from the dihydride species had been proposed.<sup>[103]</sup> This assumption was confirmed by studies under aprotic conditions as the dihydride species **3** proved to be relatively stable and thermal treatment only led to a conversion of ca. 20% to the amido species **2** and consecutive release of hydrogen gas.

In contrast, when adding methanol to **3**, hydrogen gas evolved with the concomitant formation of the methoxide species **4**. As methanol is a comparably weak acid, a large excess was needed and after 50 eq. of methanol were added only 78% of the methoxide species were formed.<sup>[126]</sup> When leaving the solution under  $\text{H}_2$  atmosphere for several hours, the reformation of the dihydride complex could be observed. The low conversion from the dihydride complex **3** to the methoxide complex **4** and the back reaction support the theory of an equilibrium between these two species.

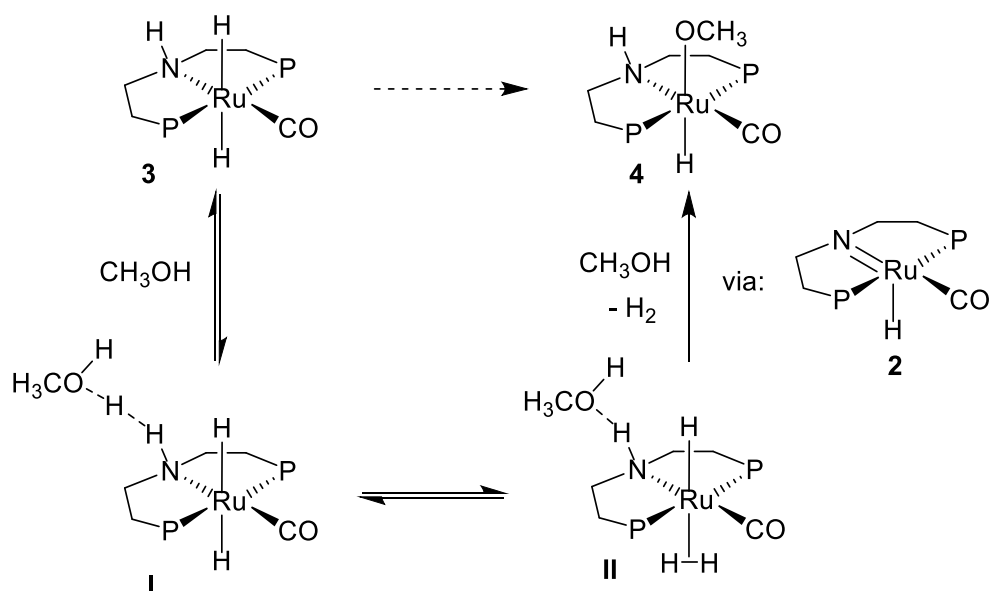
By performing further stoichiometric NMR experiments, the reversible equilibrium between the methoxide and the dihydride species could be shown (as shown in Scheme 16). This equilibrium is pushed forward to the side of the methoxide species by adding methanol to the dihydride complex, hereby generating hydrogen gas; and is driven more to the formation of the dihydride species by the addition of higher base amounts to the methoxide species, whereby formaldehyde is formed.

## Part I - Investigations for catalyst 1

**Scheme 16:** Equilibrium between **3** and **4** considering solvent-assisted H<sub>2</sub> evolution. P = P'Pr<sub>2</sub>.



\* solvent-assisted H<sub>2</sub> evolution:



## Part I - Investigations for catalyst 1

### *DFT calculations for the addition of protic species across the Ru-N bond*

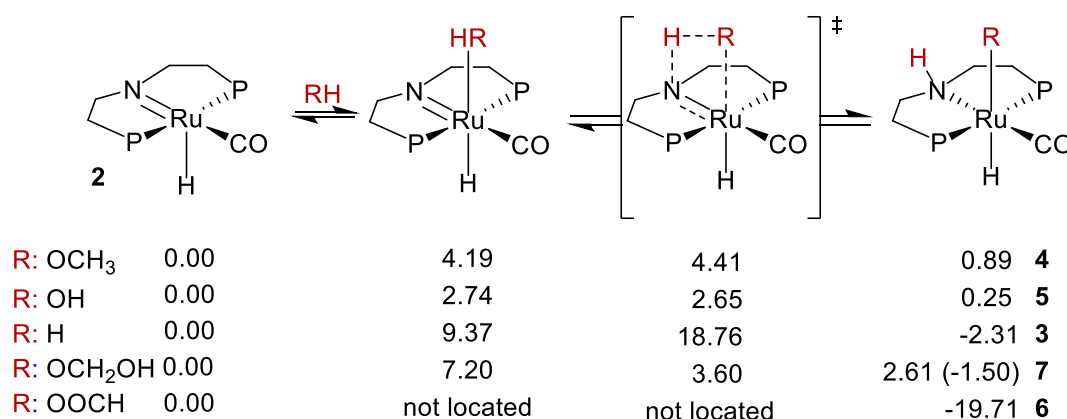
For the reactions that were investigated under aprotic conditions, theoretical calculations were performed by Dr. Haijun Jiao, leading to the energy values that are shown in Scheme 17. Methanol addition was calculated to have a relatively low energy barrier for the four-membered transition state of only 4.41 kcal mol<sup>-1</sup> and a very slightly endergonic value of 0.89 kcal mol<sup>-1</sup>. This agrees very well with the experimental result of an easy formation of the methoxide species and the straightforward reversion back to the amido species by applying vacuum.

For the addition of water across the Ru-N bond, the energy barrier is even lower with 2.65 kcal mol<sup>-1</sup> and the reaction is even less endergonic than the formation of the methoxide species, and also here the reversibility was experimentally observed. Also the formation of the gem-diolate complex should be rapid, as it was calculated to be exothermic by 1.50 kcal mol<sup>-1</sup> when taking hydrogen bonding into account.

In contrast, the energy difference between the amido species and the formate species is very high with a difference of 19.71 kcal mol<sup>-1</sup>, whereby the addition of formic acid to the amido species is highly exothermic. This confirms the experimental result of a straightforward and complete formation of the formate species.

DFT calculations show that the concerted addition of hydrogen across the Ru-N bond has an energy barrier of 18.76 kcal mol<sup>-1</sup> and is exergonic by -2.31 kcal mol<sup>-1</sup>, which supports the observation of only a fractional conversion to the amido complex **2** by heating the dihydride species **3** under aprotic conditions. This barrier was shown to be reduced by solvent effects to 13.71 kcal mol<sup>-1</sup>, which is in consonance with the formation of H<sub>2</sub> and the methoxide species by addition of methanol to **2**.

**Scheme 17:** Theoretical energies for the addition of protic species across the Ru-N bond. For the values shown in brackets for the gem-diolate species hydrogen bonding is considered. P = PPr<sub>2</sub>.<sup>[127-128]</sup>



## Part I - Investigations for catalyst 1

---

From the results of the stoichiometric experiments and the calculated energies, the following conclusions can be briefly summarised:

- The chemical shifts of the methoxide, hydride, formate and hydroxide species under aprotic conditions are very similar. They can be found in the range of 75-77 ppm in the  $^{31}\text{P}$  NMR.
- Calculations have shown that solvent-assisted liberation of hydrogen gas from the dihydride complex **3** is more likely than via a four-membered transition state.
- An equilibrium between the dihydride species **3** and the methoxide species **4** exists, which is influenced by the amount of methanol and base.
- The dihydride complex is stabilized by high base content.

Based on these experiments and supporting theoretical studies, the proposition that the methoxide complex is an off-cycle intermediate <sup>[103]</sup> could not be affirmed, and it is very likely that this monohydride species does play an active role in the mechanistic cycle. To test this theory, NMR studies under catalytic conditions were performed (see next section).

## Part I - Investigations for catalyst 1

### Investigations under catalytic conditions

#### *Studies of the reaction solution*

In the  $^{31}\text{P}$  NMR spectrum of catalyst **1** in a 9:1 MeOH:H<sub>2</sub>O solution containing 8 M KOH at room temperature two singlets at 88.9 ppm and 74.0 ppm were detected and in the  $^1\text{H}\{^{31}\text{P}\}$  NMR spectrum two corresponding broad singlets at -17.87 ppm and -6.92 ppm were observed (see Figures 13 and 14).

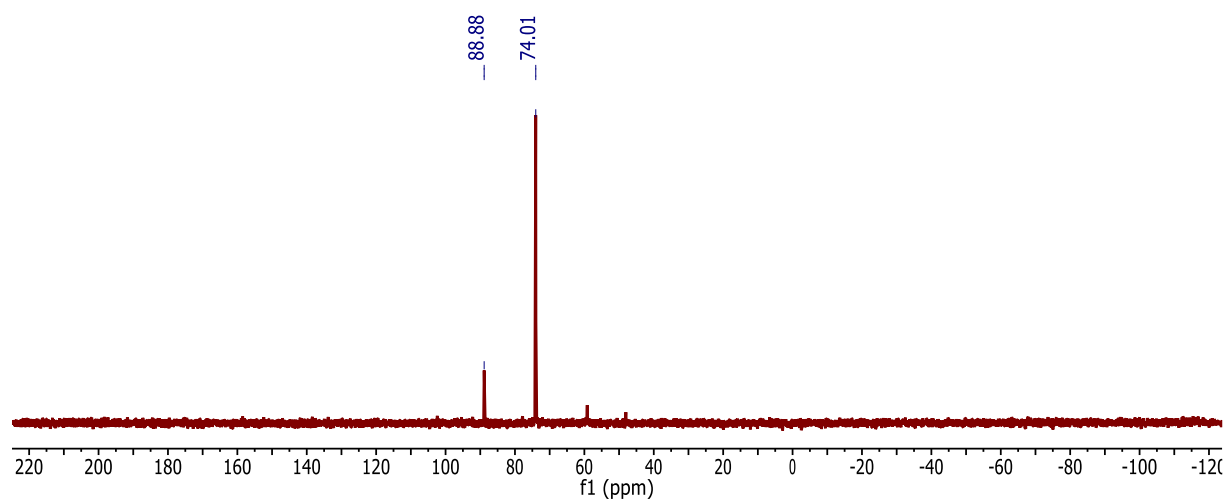


**Figure 13:**  $^{31}\text{P}$  NMR (162 MHz, 297 K, additional drops of  $\text{CD}_3\text{OH}$ ) of the reaction solution containing **1** (8.1 mg) in 1 mL 9:1 MeOH:H<sub>2</sub>O, 8 M KOH.

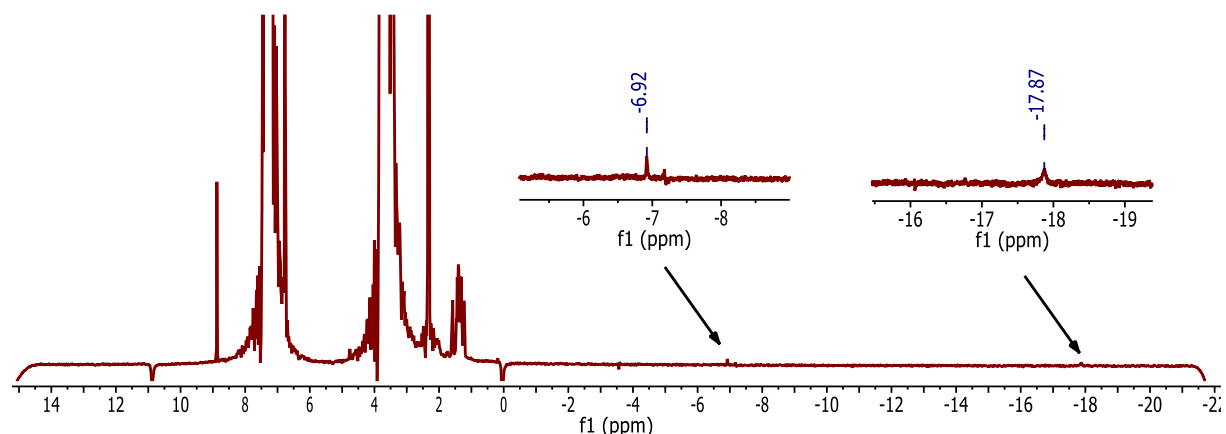


**Figure 14:**  $^1\text{H}$  NMR (400 MHz, 297 K, additional drops of  $\text{CD}_3\text{OH}$ ) of the reaction solution containing **1** (8.1 mg) in 1 mL 9:1 MeOH:H<sub>2</sub>O, 8 M KOH.

Based on the stoichiometric studies depicted in the previous part, the catalytic species with the low-field chemical shifts could be identified to belong to the dihydride complex **3**. The identification of the other species at higher chemical shifts was more complicated, as the hydroxide, methoxide or formate complex have very similar chemical shifts. Nevertheless, based on the following

## Part I - Investigations for catalyst 1

---

evidences, it is proposed that this monohydride species apparent under reaction conditions is the methoxide species **4**: In the  $^{31}\text{P}$  NMR spectrum of the reaction solution heated to 90 °C similar peaks as described before at 74.05 ppm and 88.43 ppm were observed (For details see Appendix Section 6.4.1.2.). After 30 minutes of reaction time, a third peak appeared at 74.63 ppm, which increased with elongated reaction time. As simultaneously free formate was detected in solution, it was concluded that the third peak belongs to the formate species. This fits very well with the assumption that the other peak with minimal higher-field chemical shift is indeed the methoxide species as the trans-effect of the –OMe ligand is slightly weaker than of the –COOH group.

During the reaction monitoring a white precipitate was formed, which was dissolved and based on which carbonate and hydrocarbonate were detected. Hence, it was proven that the parent catalyst is able to promote all three steps of the complete methanol reforming process. Throughout the reaction, no formaldehyde could be detected.

Further evidences that support the proposition that the main peak can be assigned to complex **4** are the shown equilibrium between the species **3** and **4**, the easy generation of the methoxide species from the amido species **2** and the fact that methanol is available in high excess. The other possible species, the hydroxide complex **5**, can be excluded as no rational mechanism can be developed to generate hydrogen from it and activity was shown to decrease with higher water contents. In contrast to the original theory that the methoxide species is an off-cycle intermediate<sup>[103]</sup>, these points strengthen the proposition that the methoxide complex **4** is indeed an important active species in the catalytic cycle as otherwise the high activity of this catalytic system would not fit the spectroscopic observations.

Another interesting aspect is that by changing from aprotic to the protic reaction conditions, the N-H peak disappears in the  $^1\text{H}$  NMR spectrum. This effect can be either caused due to hydrogen bonding or due to the deprotonation of the N-H moiety by the highly basic medium. The simplification of the multiplets to broad singlets and the up-field shift of the signals when changing from the aprotic to the protic reaction conditions indicate that the second effect is very likely (Tables **4** and **5** on page XXI of the Appendix).

Moreover, the calculation of the energies for the deprotonation of the ligand N-H backbone showed that this step is barrier-less and highly exergonic for both the dihydride and the methoxide species (Appendix page XXIV). The  $\text{pK}_a$  of the N-H moiety was calculated to be 9.09 and 8.24, respectively, which is significantly lower than the pH range of 10 to 13 under steady-state conditions.<sup>[103, 129]</sup> Thus, the deprotonation of the ligand backbone is an important aspect that has to be taken into account for the final mechanistic cycle.



## Part I - Investigations for catalyst 1

As formaldehyde was not detected at all under reaction conditions, it was assumed that the ruthenium-catalysed dehydrogenation step of the formaldehyde or the gem-diolate is very fast. Nevertheless, due to the highly basic conditions and/or the elevated temperature formaldehyde could also undergo other types of reactions, such as the Cannizzaro reaction or the thermally induced decomposition to formic acid, which are not catalysed by the aliphatic pincer complex.<sup>[130-131]</sup>

In order to test if the decomposition of formaldehyde caused by the basic reaction conditions or the elevated temperature attributes to a significant share to the overall hydrogen gas evolution, 0.2 mL of a 37% aqueous formaldehyde solution was added to the standard solution of 9:1 MeOH:H<sub>2</sub>O containing 8 M KOH at 90 °C. After three hours, only approximately 10 mL of hydrogen were released under these conditions, which is only a minor share of the theoretical amount of 50 mL hydrogen that would have been released by the complete decomposition of the formaldehyde. Thus, the amount of hydrogen that is generated from the thermal and/or basic decomposition of formaldehyde is negligible.

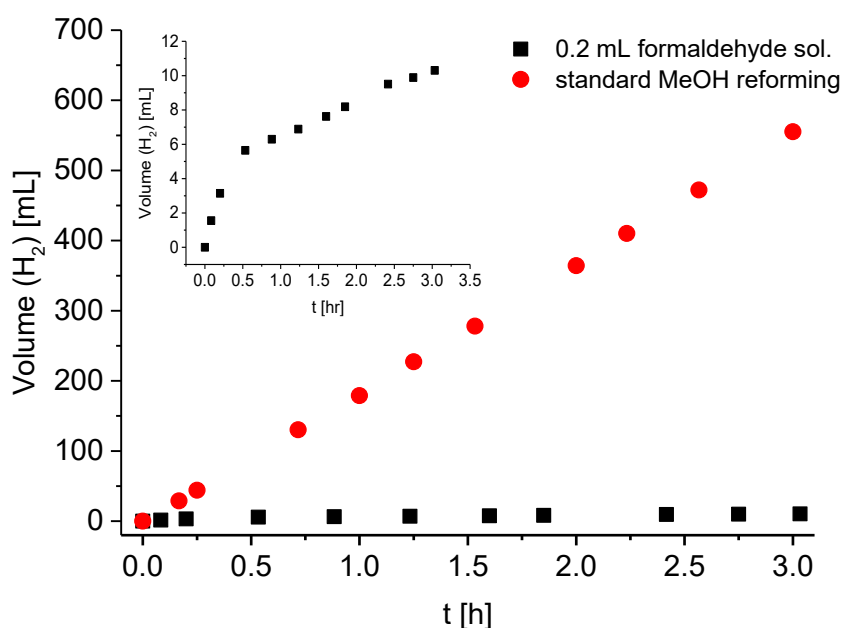


**Figure 15:** Comparison of hydrogen gas evolution caused by basic and thermal decomposition of formaldehyde with the standard gas evolution rate. Conditions standard MeOH reforming: 8 M KOH, MeOH:H<sub>2</sub>O (9:1, 10 mL), 4.2  $\mu$ mol **1**, 90 °C. Conditions for the decomposition of formaldehyde: 8 M KOH, MeOH:H<sub>2</sub>O (9:1, 10 mL), 0.2 mL 37% aqueous formaldehyde solution, 90 °C.<sup>[118]</sup>

To verify the result of the NMR monitoring that no formaldehyde is present under catalytic conditions, formaldehyde was tested for in the reaction solution by employing the Merck MColorTest, which gave a negative result. Therefore, it can be concluded that during the methanol dehydrogenation catalysed by **1** no formaldehyde accumulates during the reaction (For details see Appendix page XXIV).

## Part I - Investigations for catalyst 1

### *Influence of base on the catalytic species*

The next step was to investigate the influence of base on the catalytic species in a 9:1 MeOH:H<sub>2</sub>O solution.

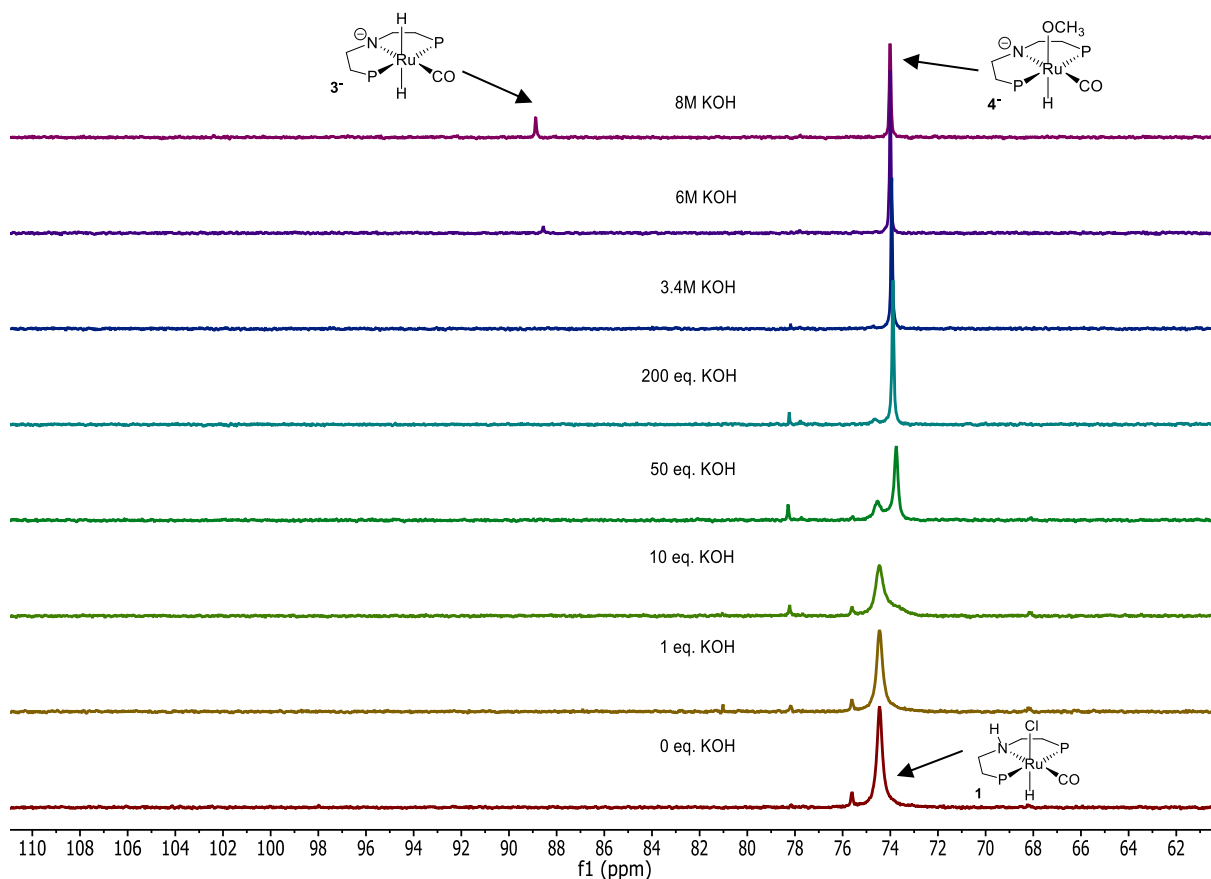


**Figure 16:** <sup>31</sup>P NMR (162 MHz, 297 K) of the reaction solution containing **1** (8.1 mg) in 1 mL 9:1 MeOH:H<sub>2</sub>O. Addition of increasing amounts of KOH. P = PPr<sub>2</sub>.<sup>[118]</sup>

Under neutral conditions, the pre-catalyst **1** was the prevalent species with a chemical shift of 74.16 ppm. By increasing the base amount to 10 eq. of KOH a second species appeared at a higher chemical shift, causing a broad tailing of the original peak. By comparison to the spectrum recorded previously under reaction conditions, this complex was determined to be the methoxide species **4**.

At 50 eq. KOH both complexes were detected until at 200 eq. of base the pre-catalyst vanished and only the methoxide species remained. Increasing the base amount further, a peak at a very low chemical shift of 88.99 ppm appeared, which could be assigned to the dihydride species **3**. By raising the base concentration to 8 M KOH the ratio between the methoxide and the dihydride species changed slightly to a higher proportion of the latter complex, although the methoxide species still remained the main catalyst complex. By the increasing addition of base, the dihydride species was stabilized and could therefore be detected by NMR.

## Part I - Investigations for catalyst 1

---

These observations are in agreement with the stoichiometric experiments, as also here a minimum of base was required to convert the pre-catalyst **1** and the equilibrium between the methoxide and the dihydride species was pushed towards the latter by the addition of base.

Based on the NMR experiments performed under reaction conditions, the following conclusions can be summarised:

- Under reaction conditions, the corresponding methoxide, hydride and to a minor extent the formate species were detected.
- The hydroxide complex was confirmed to be an ex-catalytic species.
- The methoxide species is very likely one of the main active catalytic species.

Eventually, to extend the findings that were obtained for the standard reaction time of three hours to longer investigation periods, the spectrum of spectroscopic investigations was broadened by *operando* Raman and GC measurements. These experiments were carried out in cooperation with the group of M. Haumann at the Friedrich-Alexander University Erlangen and are described in detail in the following section.

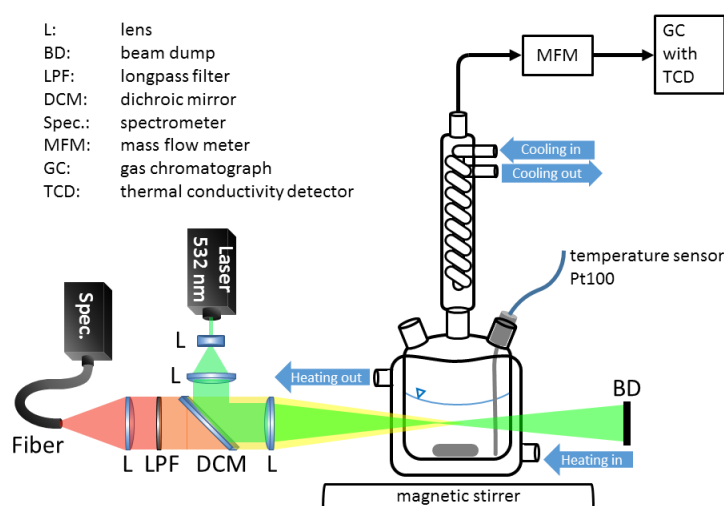
## Part I - Investigations for catalyst 1

### Operando Raman and GC investigations<sup>[132]</sup>

The aim of the combined *operando* Raman and GC setup was to perform longterm measurements, during which simultaneously the composition of the produced gases and changes in the reaction solution were monitored. The results described in this section are based on the experiments performed by Vinzent Strobel.

The reaction was carried out using the standard experimental setup of a double-walled vessel with additional temperature sensor. Instead of measuring the evolving gases by manual or automatic burettes, the gas flow was led via a mass flow meter to a GC unit, with which both hydrogen and carbon dioxide could be quantitatively measured (Scheme 18). More information about the experimental details are given in the Appendix Section 6.4.1.3.

**Scheme 18:** Schematic overview of the experimental setup for operando monitoring.<sup>[133]</sup>



An exemplary Raman spectrum of the reaction solution recorded for a duration of 7.5 hours is shown in Figure 17. In order to identify the chemical components in the liquid phase, the measured spectra were compared with Raman spectra of possible intermediates known in literature.<sup>[134]</sup>

In the spectrum, two bands for methanol between 800 and 1800  $\text{cm}^{-1}$  were identified, as well as a band that could be assigned to the symmetric stretch of the  $-\text{CO}$  group of formate, and a band at 1080  $\text{cm}^{-1}$  belonging to carbonate. The formate band appeared very soon after the start of the reaction and increased continuously during the progress of the reaction. In contrast, carbonate was detected only shortly before the reaction was stopped and concomitantly the Raman signal was disturbed by the coating of the inner reaction wall with white solid potassium carbonate (see Figure 18).

## Part I - Investigations for catalyst 1

---

Throughout the reaction, no band belonging to formaldehyde was identified. This can be related to the fast conversion of formaldehyde into formate, so that no measurable concentration can accumulate in the reaction solution during the course of the reaction. This finding is in agreement with the results of the *in-situ* NMR investigations.

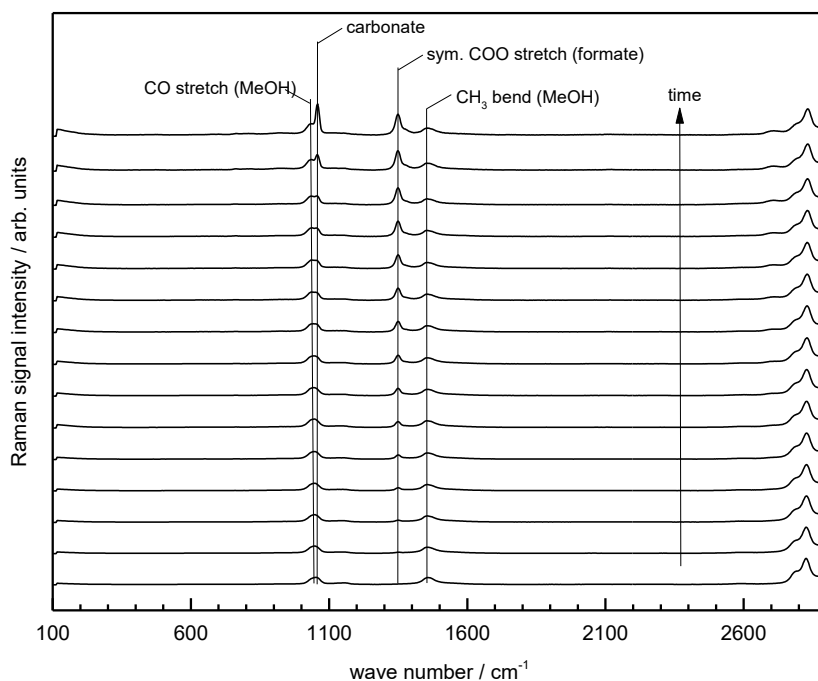


**Figure 17:** An exemplary Raman spectrum of the reaction solution recorded for a duration of 7.5 hours. Each spectrum represents an average of 30 minutes of recording.<sup>[135]</sup>

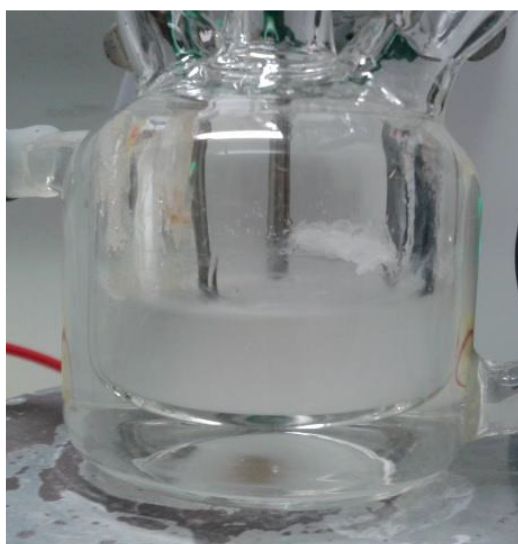


**Figure 18:** Coating of the inner wall of the reaction vessel with potassium carbonate.<sup>[135]</sup>

## Part I - Investigations for catalyst 1

The resulting diagrams from a longterm measurement of the reaction system containing 2 M KOH can be seen in Figure 19. During the first 22 hours the base got continuously consumed, which led to a steady decline in reaction temperature from 74.5 °C to 70.5 °C and a stabilised gas flow of approx. 0.75 mL/min. Simultaneously, the Raman signal for formate reached a peak after 10 hours and significantly lost in intensity afterwards. After the complete consumption of the KOH, both GC signals for carbon dioxide and hydrogen gas in a 3:1 ratio were detected. Thus, at this point of the reaction the final phase of full methanol reforming was reached.

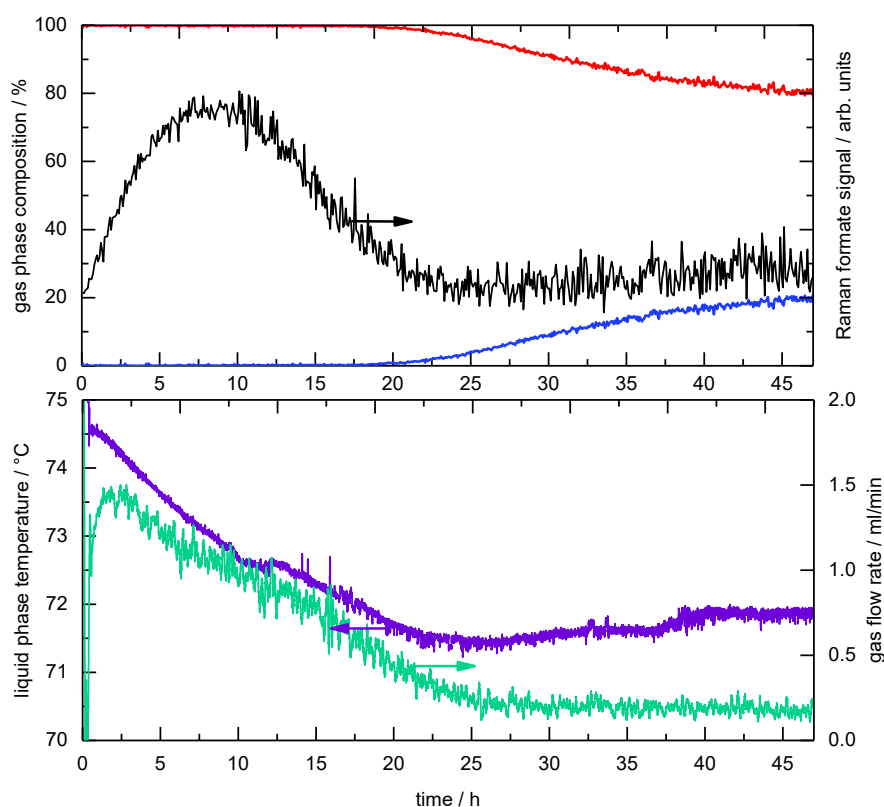


**Figure 19:** All experimental data obtained from a single run in the GC-Raman setup. Top: H<sub>2</sub> (red) and CO<sub>2</sub> (blue) concentrations measured by online GC, formate (black) intensity determined by Raman signal. Bottom: liquid phase temperature (purple) and the measured gas flow (green). Reaction conditions: 16 mL MeOH, 4 mL H<sub>2</sub>O, 16.8 μmol **1**, 2M KOH, T<sub>set</sub> = 95 °C (liquid phase at its boiling temperature at all times).<sup>[135]</sup>

These findings support the hypothesis that a certain amount of base is needed for efficient catalyst activity. When reaching the steady-state reforming phase, the efficiency of the system is stable, but at a very low turnover rate. In this regard the bell-shaped curve for the formate signal can be related to the ceasing of catalytic turnovers, as generally less of the product of the second dehydrogenation step is generated. Especially for future steps involving the upscaling of the system, the need of continuous make-up of the base with concomitant continuous generation of solid carbonate precipitate will have to be carefully considered.

## Part I - Mechanistic proposal for catalyst 1

---

### 2.3.3. Mechanistic proposal

Based on the performed activity measurements, the spectroscopical experiments and theoretical calculations, a better understanding of the active catalytic species and possible reaction pathways for the Ru-pincer catalyst **1** was developed. It was identified that the key steps involve the following transformations:

- The methoxide species **4** is formed from the highly active amido complex **2**.
- Under the basic reaction conditions, the prevalent species are anionic with a deprotonated N-H moiety of the ligand backbone.
- The C-H cleavage step leads to the formation of the dihydride species **3** from the methoxide species **4**.
- Hydrogen is liberated from the dihydride complex via a solvent-assisted pathway.

#### **2.3.3.1. Possible pathways for the key step involving C-H cleavage**

Still, a range of possibilities for the essential steps of the C-H cleavage and Ru-dihydride formation are possible, which are shown in Scheme 19 and which will be discussed in detail in this paragraph.

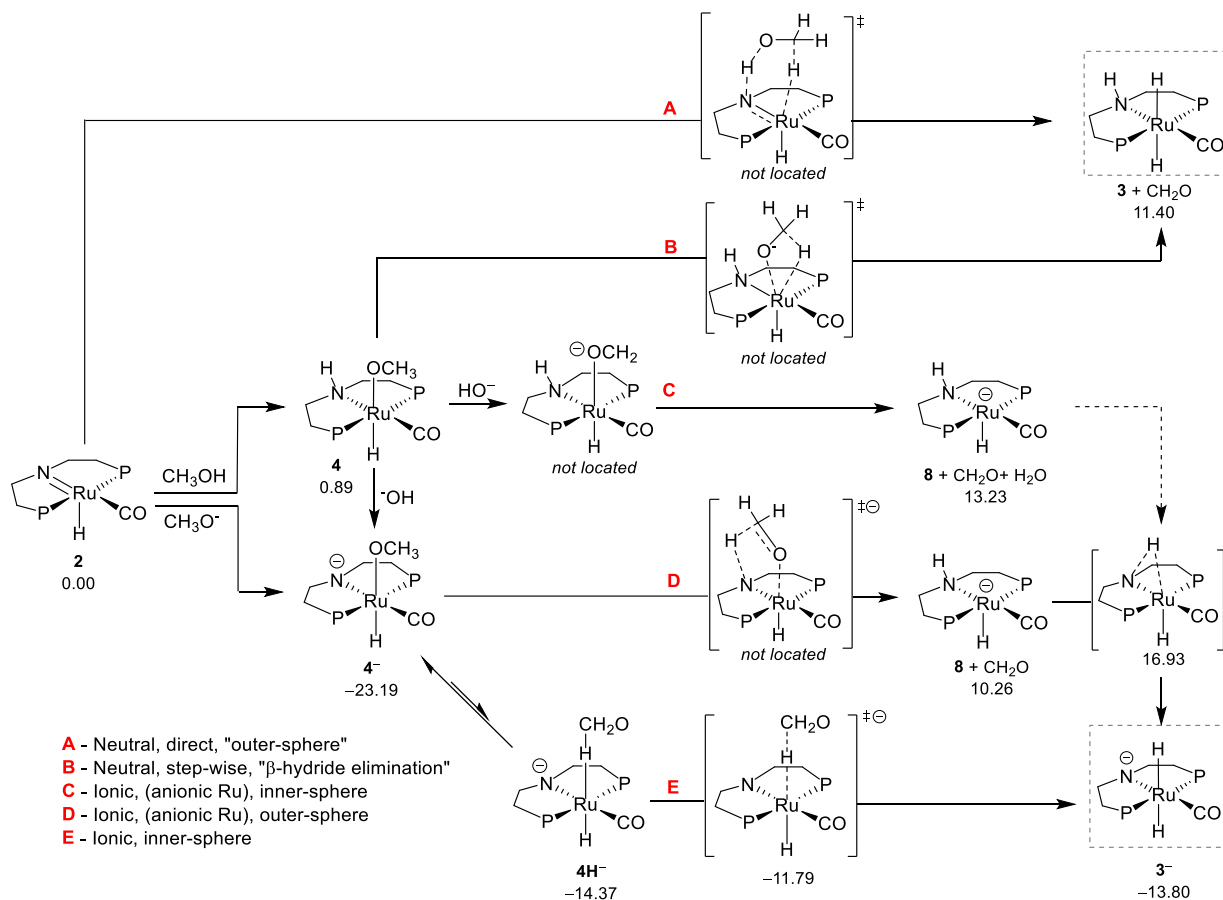
Pathway A depicts the originally postulated outer-sphere coordination of methanol to the amido species. This mechanism can be discarded, as no transition state could be located by calculations and it does not take into account the necessity of a high base concentration for efficient catalytic activity. Furthermore, the addition of formic acid did not result in the formation of the dihydride species nor was hydrogen gas evolved, which is further evidence that this pathway is not followed.

The second pathway, B, includes the formation of the methoxide complex as an active species. Following a non-classical  $\beta$ -hydride elimination, which was formerly proposed by Milstein and co-workers, the dihydride species is formed.<sup>[136]</sup> This step-wise mechanism neither involves any anionic species nor does it take the role of the base into account. Also here, the transition state could not be located.

In pathway C, the formation of the methoxide species is followed by the deprotonation of the -OMe moiety and the consecutive cleavage of formaldehyde. Both the energy of the deprotonated methoxide species was not found and the energy for the subsequent anionic Ru species was calculated to be comparably high. Therefore, it was concluded that also this pathway is not very likely.

## Part I - Mechanistic proposal for catalyst 1

**Scheme 19:** Possible mechanistic pathways for the key C-H cleavage step involving catalyst **1**. P = PPr<sub>2</sub>.<sup>[127-128]</sup>



Mechanism D is based on the direct coordination of methoxide to the amido species, leading to the anionic methoxide complex. The involvement of the methoxide rather than the protic methanol as substrate is indeed very likely under the highly basic reaction conditions. The intermediate of the consecutive C-H cleavage by an outer-sphere coordination could not be located, though, and the overall reaction from **4<sup>-</sup>** to the anionic species **8** would be very endergonic.

The final mechanism, pathway E, includes an ionic and inner-sphere route. Calculations show that the O-coordinated isomer of the deprotonated methoxide species **4<sup>-</sup>** is in equilibrium with the H-coordinated isomer **4H<sup>-</sup>**, which has been shown before for iron<sup>[106, 137]</sup> and iridium<sup>[136]</sup> catalysts. This equilibrium is pushed forward to **4H<sup>-</sup>** by the consecutive C-H cleavage, leading to the formation of formaldehyde and the deprotonated dihydride **3<sup>-</sup>**. Based on the reasonable energy values for the involved catalytic species, this last pathway appears as the most viable option.



## Part I - Mechanistic proposal for catalyst 1

### 2.3.3.2. Calculations for the ionic, inner-sphere pathway

The ensuing step was to verify if the energies for all three steps of the full methanol reforming following this ionic, inner-sphere pathway are consistent with the experimental results. These calculations were performed by Dr. Haijun Jiao.

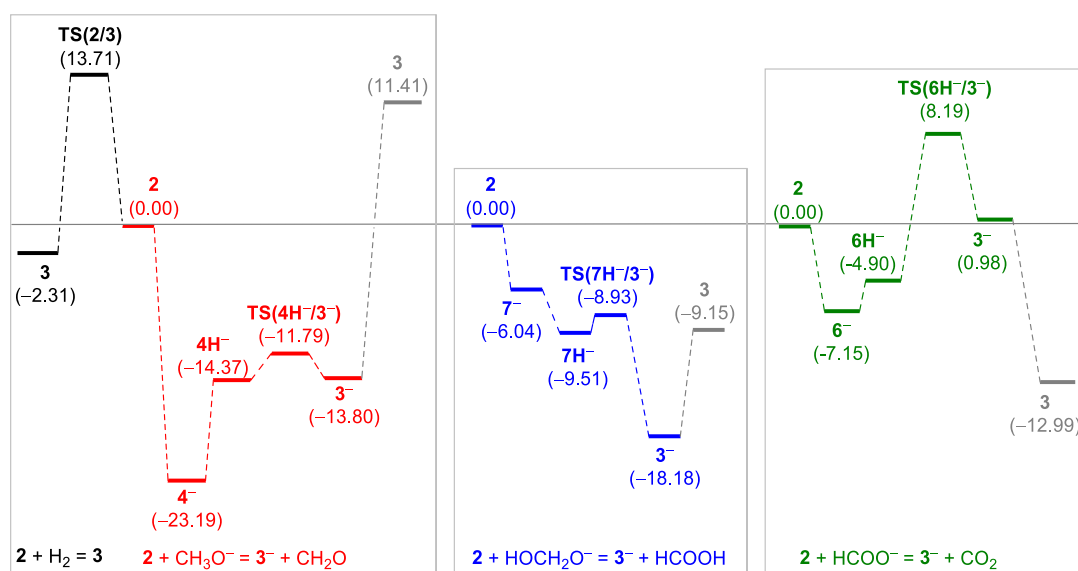
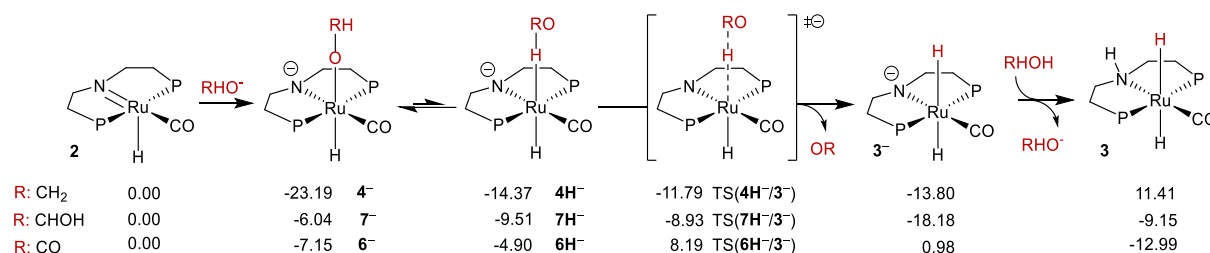


**Figure 20:** Potential energy surface for the anionic, inner-sphere pathway for the C-H cleavage step and Ru-dihydride formation. Energies are given in kcal mol<sup>-1</sup>. Protonations of 3<sup>-</sup> to 3 in each step are with CH<sub>3</sub>OH, HOCH<sub>2</sub>OH and HCOOH, respectively. P = P'Pr<sub>2</sub>.<sup>[118, 138]</sup>

According to the calculated energies, the species 4<sup>-</sup> and 3<sup>-</sup> (respectively 3 in case of the last mechanistic cycle starting from the formate species 6<sup>-</sup>) have the lowest energies and are the main resting states. This fits very well with the experimental investigations, as exactly these species were observed during the monitoring of the reaction.

For the dehydrogenation of the gem-diolate involving the step from 7<sup>-</sup> to 3<sup>-</sup> a highly exergonic energy of 12.14 kcal mol<sup>-1</sup> and a very low energy barrier was calculated. This is consistent with the fact that no formaldehyde was detected in solution and the proposition that the formaldehyde decomposition is the fastest step of the reaction cascade.

## Part I - Mechanistic proposal for catalyst **1**

---

In contrast, for the formate dehydrogenation, a relatively high energy barrier of 13.09 kcal mol<sup>-1</sup> was determined, which explains why formate accumulates during the reaction and the formate species is detected in situ. Finally, the methanol-promoted reaction of **2** with H<sub>2</sub> to form the dihydride complex **3** is exergonic by 2.31 kcal mol<sup>-1</sup> and has an energy barrier of 13.71 kcal mol<sup>-1</sup>, which is in accordance with the observed formation of the dihydride from the amido species under stoichiometric conditions.

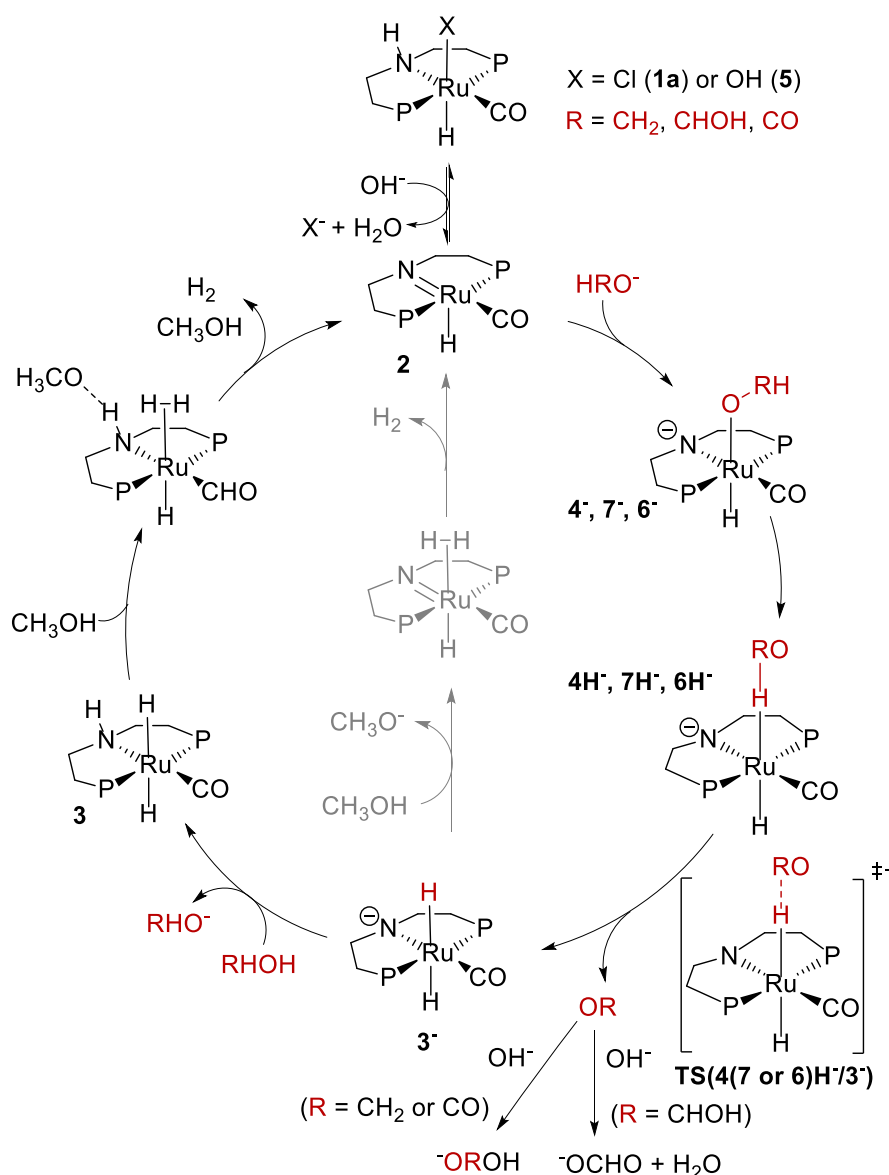
All these aspects let us be very confident in the proposition of this anionic, inner sphere pathways for the key C-H cleavage of the Ru-catalysed methanol dehydrogenation reaction.

## Part I - Mechanistic proposal for catalyst **1**

### 2.3.3.3. Final mechanistic cycle

In conclusion, we can propose the following mechanistic cycle for the aqueous-phase dehydrogenation of methanol catalysed by the aliphatic pincer catalyst **1**. This mechanism accounts for the role of the base and explains why high base amounts are needed for efficient catalytic activity.

**Scheme 20:** Proposed mechanistic cycle for the complete dehydrogenation of methanol employing Ru-pincer complex **1**. P = PPr<sub>2</sub>.<sup>[118]</sup>



The first role of the base is the dehydrochlorination of the pre-catalyst **1**, which leads to the formation of the highly active amido species **2** and is the initiative step to enter the mechanistic cycle. This is in agreement with the postulated mechanism before.

## Part I - Mechanistic proposal for catalyst 1

---

Base ensures that the substrates methanol, formaldehyde and formic acid are present in their deprotonated form, which attack the amido species leading to the formation of the negative Ru-amidate complexes **4<sup>-</sup>**, **6<sup>-</sup>** or **7<sup>-</sup>**. These species easily undergo isomerisation to form the H-coordinated complexes **4H<sup>-</sup>**, **6H<sup>-</sup>** or **7H<sup>-</sup>**. C-H cleavage takes place, leading to the formation of the deprotonated dihydride **3<sup>-</sup>** and the release of either formaldehyde, gem-diolate or carbon dioxide. Here, base plays again an essential role as the products are sequestered, which turns this key step thermodynamically more feasible and is a significant driving force of the reaction.

The cycle is either closed by the protonation of the amidate moiety of **3<sup>-</sup>** and the protonation of the hydride function by methanol, followed by the solvent-assisted hydrogen generation, or the direct protonation of the hydride and hydrogen cleavage (grey pathway).

This final step during which hydrogen is generated is actually hindered by the high basicity of the solution as protonation is made more difficult. This is the reason why a stabilization of the dihydride species at higher base concentrations was observed. Nevertheless, the general positive influence of base on the catalytic activity outweighs this attenuating effect.

In conclusion, this mechanistic proposal involving key anionic species explains in detail why an increase of catalytic turnover is reached with higher base concentration, which stands in contrast to the formerly postulated neutral, outer-sphere pathway. The saturation kinetics observed at higher base concentrations were shown to be related to mass-transfer issues.

## Part I - Investigations for catalyst **Me-1**

---

### 2.3.4. Investigations for catalyst **Me-1**

As the mechanism for the parent catalyst **1** could be fully elucidated, it was planned to obtain a similar understanding of the mechanistic pathway for the N-methylated derivative **Me-1**.

#### 2.3.4.1. *Base molarity-activity measurements*

Analogous to the Ru-pincer complex **1**, the base molarity-activity correlation was measured both at 60 °C and 90 °C, whereby for the higher temperature the modified autoclave setup described in Section 2.3.2.1. was employed. Unlike for catalyst **1**, a peak in rate was observed at 60 °C at 4 M KOH and a decline in activity at higher molarities for the **Me-1** catalyst. A comparable trend was noted for 90 °C as the activity continuously decreased with increasing KOH molarity. This tendency stands in stark contrast to the parent catalyst **1**, as here a positive correlation between base molarity and activity was noticed (see Figure 9). Still, a minimum amount of base is required for both catalysts as under neutral conditions no significant hydrogen gas evolution took place.

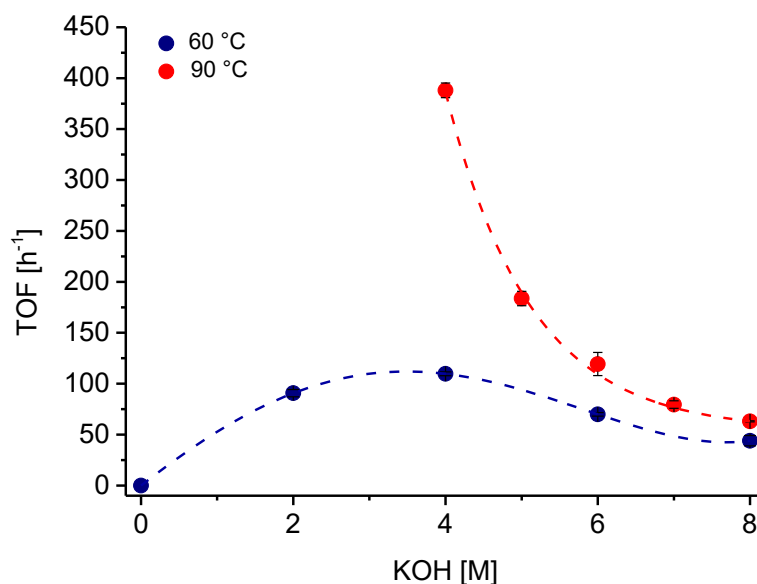


**Figure 21:** The influence of KOH concentration on the activity of catalyst **Me-1** at 60 °C and 90 °C. Conditions at 60 °C: 10 mL MeOH:H<sub>2</sub>O (9:1) and **Me-1** (8.41 μmol) using the “regular” burette setup. Conditions at 90 °C: 20 mL MeOH:H<sub>2</sub>O (9:1) and **Me-1** (16.82 μmol) in a leaking autoclave set to an over pressure of 0.6 bar. Lines are solely a guide for the eye.<sup>[118]</sup>

These contrasting tendencies in regard to the molarity-activity correlation support the assumption of different mechanistic effects for the two complexes. To get a better insight into the underlying microscopic reasons, stoichiometric and *in-situ* NMR studies were performed, which are described in the following section.

## Part I - Investigations for catalyst Me-1

### 2.3.4.2. NMR studies

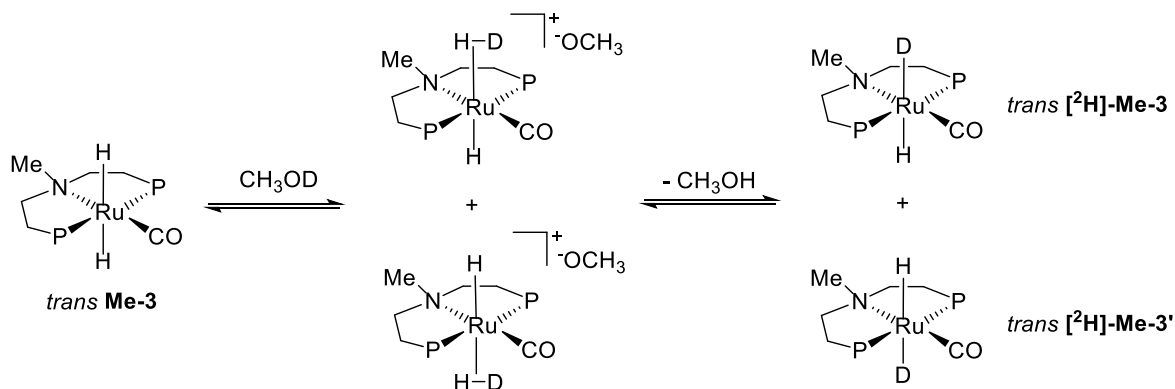
Firstly, stoichiometric studies were carried out by Dr. Elisabetta Alberico to characterize possible active catalytic species. Since with the methylated N-moiety of the ligand backbone it is not possible to generate the equivalent amido function of the complex **2**, investigations concentrated mainly on the formation of the dihydride species **Me-3** and possible reactions of it. A comprehensive table of all NMR data can be found in the Section 6.4.2.1. of the Appendix.

#### Stoichiometric investigations<sup>[139]</sup>

The addition of KOMe to the pre-catalyst **Me-1** led to the complete conversion to the dihydride complex **Me-3**. Compared to its unmethylated counterpart, the formation of **Me-3** from **Me-1** was found to be significantly more facile. Interestingly, no methoxide species could be detected.

As shown before, the protonation of the dihydride species by methanol is a key step in the mechanistic cycle.<sup>[126]</sup> To test for this transformation, **Me-3** was protonated using CH<sub>3</sub>OD, which led to the formation of the two monodeuterated isomers *trans* [<sup>2</sup>H]-**Me-3** and *trans* [<sup>2</sup>H]-**Me-3'** (Scheme 21). Both isomers were formed in equivalent amounts, which means that the orientation of the N-methyl group does not affect the H-D exchange as for the N-H moiety.<sup>[140]</sup>

Scheme 21: Protonation of *trans* **Me-3** by CH<sub>3</sub>OD. P = PPr<sub>2</sub>.



The addition of non-deuterated methanol to the dihydride complex did not lead to the release of hydrogen gas, nor was the methoxide species **Me-4** formed. Instead, a new species appeared, which was assumed to be either the *trans* **Me-3** species with additional hydrogen bonding to methanol or a cationic Ru-dihydrogen species. This result implies that the protonation of the methylated dihydride complex is significantly more impeded than it was the case for the unmethylated dihydride species.

**Me-3** was also treated with formic acid, whereby one equivalent of the acid was enough to reach quantitative conversion to the formate species **Me-6** and consecutive hydrogen gas evolution. Thermal treatment of the formate complex **Me-6** at 90 °C led to partial conversion back to the dihydride species **Me-3** after three hours.

## Part I - Investigations for catalyst Me-1

---

### Investigations under catalytic conditions

The subsequent step was to analyse which catalytic complexes are observed under reaction conditions and how they are influenced by the increasing base molarity.

#### ***Studies of the reaction solution***

In the  $^{31}\text{P}$  NMR of the highly basic methanol-water solution at room temperature containing catalyst **Me-1** three distinct species at 59.22 ppm, 75.76 ppm and 87.40 ppm were detected. They were assigned to the free oxidised HPNP $\text{Pr}$  ligand, the formate complex **Me-6** and the dihydride species *trans* **Me-3**, respectively.

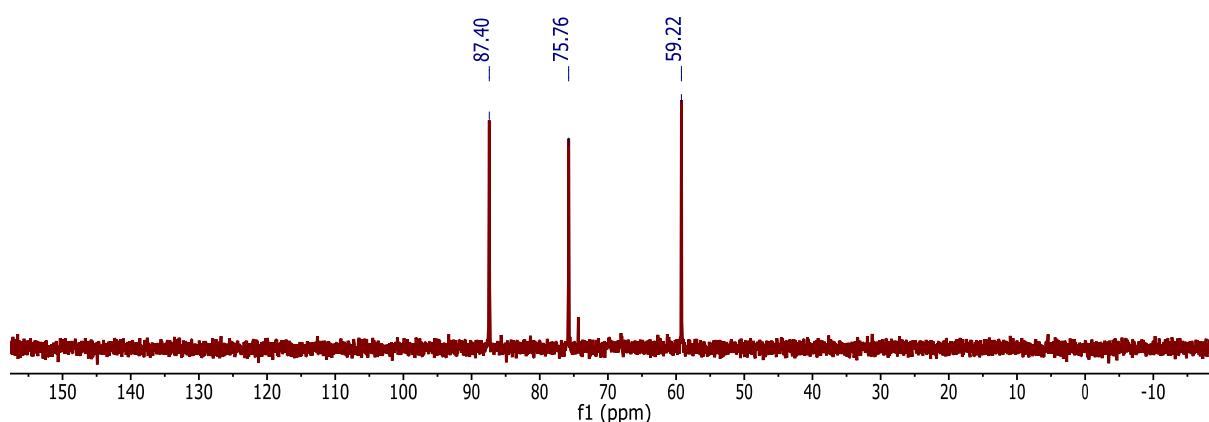


**Figure 22:**  $^{31}\text{P}$  NMR (162 MHz, 297 K, additional drops of  $\text{CD}_3\text{OH}$ ) of the reaction solution at room temperature containing **Me-1** (8.1 mg) in 1 mL 9:1 MeOH:H $_2$ O, 8 M KOH.

In the  $^1\text{H}\{^{31}\text{P}\}$  NMR spectrum only two triplets at -6.02 and -6.52 ppm were visible, which belong to the hydrides of the dihydride species. Due to the poor intensity and a relatively high signal-to-noise ratio, the hydride of the formate species could not be detected.

## Part I - Investigations for catalyst Me-1

---

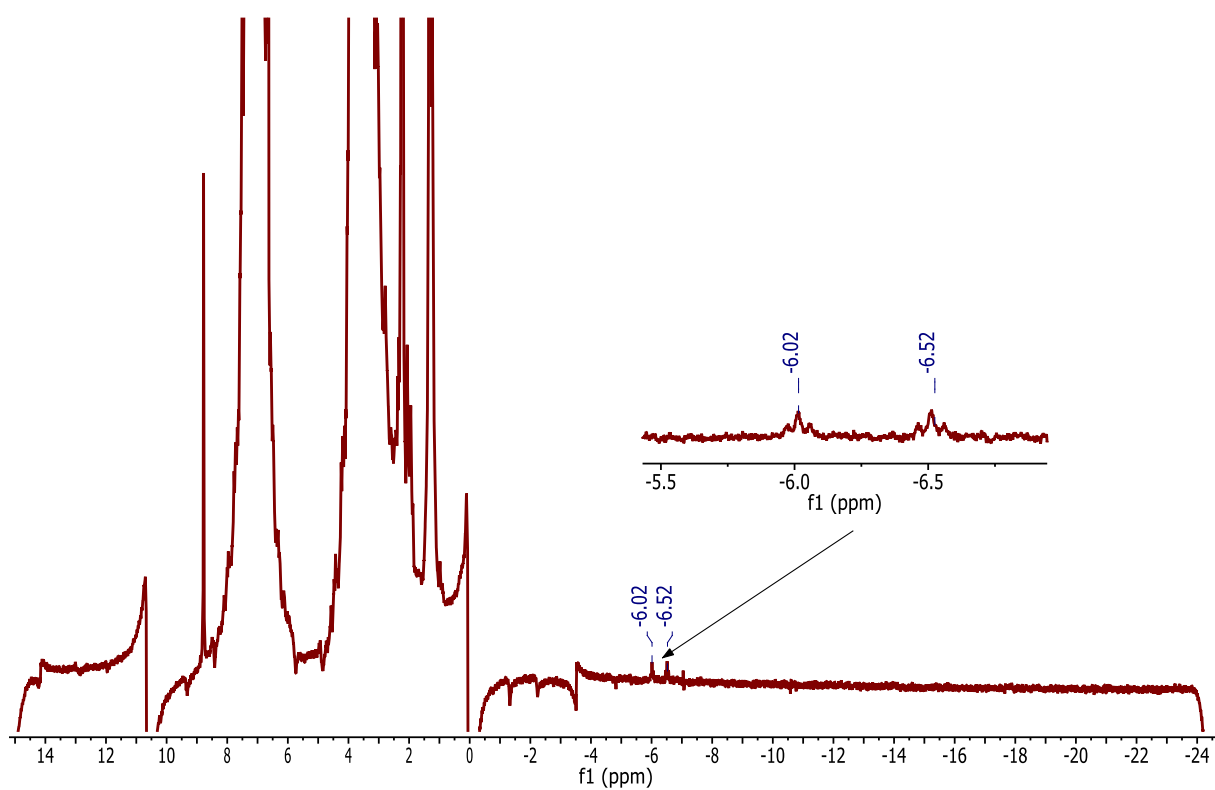


**Figure 23:**  $^1\text{H}\{^{31}\text{P}\}$  NMR (400 MHz, 297 K, additional drops of  $\text{CD}_3\text{OH}$ ) of the reaction solution containing **Me-1** (8.1 mg) in 1 mL 9:1 MeOH:H<sub>2</sub>O, 8 M KOH.



## Part I - Investigations for catalyst Me-1

### *Influence of base on the catalytic species*

To test for the influence of base on the catalytic species, increasing amounts of KOH were added to the reaction solution containing **Me-1** at room temperature.

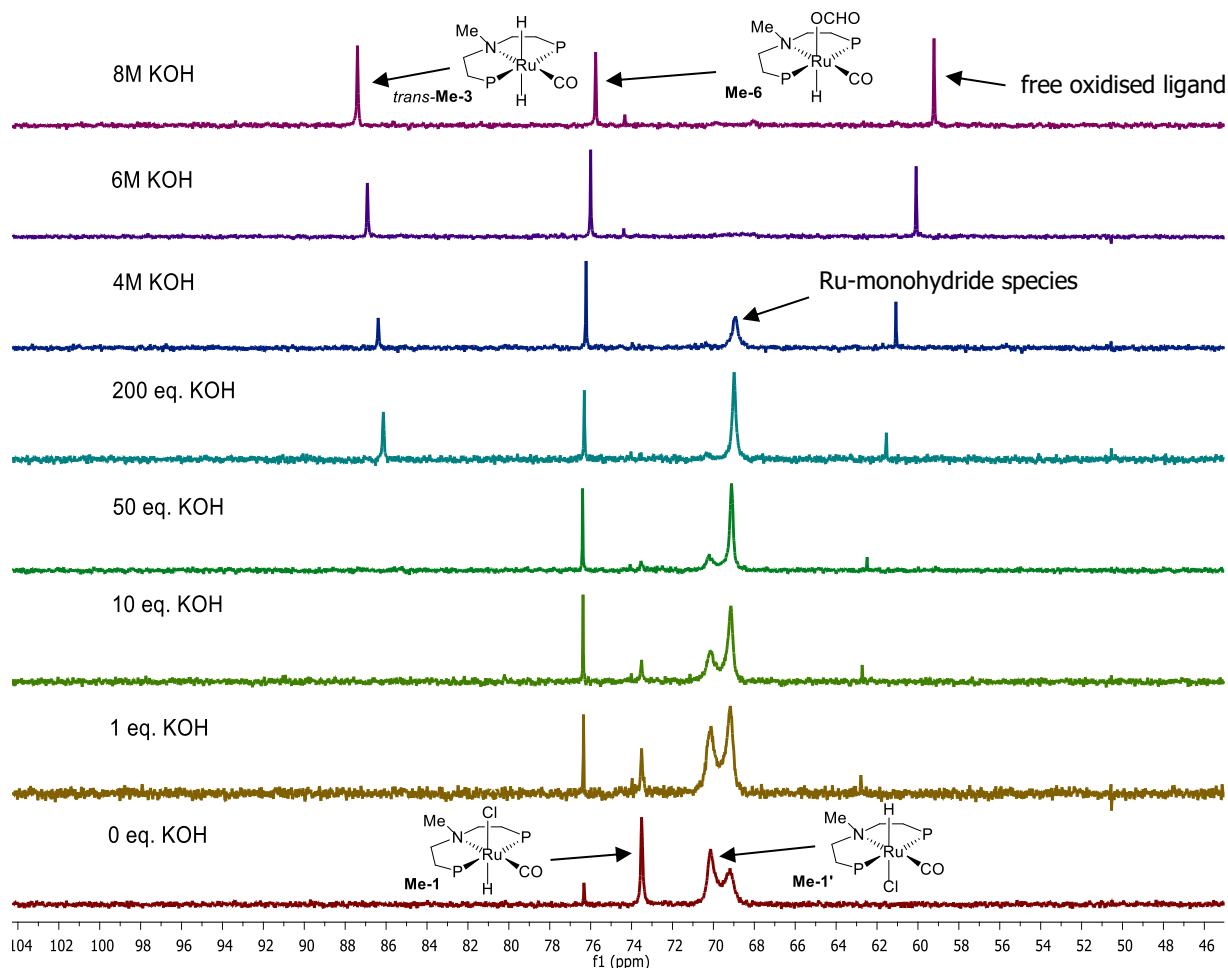


**Figure 24:**  $^{31}\text{P}$  NMR (162 MHz, 297 K) of the reaction solution containing **Me-1** (8.1 mg) in 1 mL 9:1 MeOH:H<sub>2</sub>O. Addition of increasing amounts of KOH. P = P'Pr<sub>2</sub>.<sup>[118]</sup>

Under neutral conditions, the two isomers of the starting complex, **Me-1** and **Me-1'**, which differ in the relative orientation of the hydride ligand to the orientation of the N-Me group, were detected. At 69.00 ppm a further monohydride species not unambiguously identifiable was visible. Nevertheless, it is fairly assumable that it could be the methoxide complex **Me-4**. This species disappeared after the base concentration reached 4 M. Under neutral conditions, the minor peak at 76.24 ppm belonging to the formate complex **Me-6** was apparent as well.

Already when adding 1 eq. of KOH it reached its maximum intensity, which did not change with increasing base concentration.

## Part I - Investigations for catalyst Me-1

---

The two isomers of the pre-catalyst were completely converted when reaching a base concentration of 200 eq. This was also the concentration at which the dihydride species *trans* **Me-3** at 86.16 ppm appeared. Finally, at 6 M and 8 M KOH three peaks were detected: the dihydride and the formate species and free oxidised HPNP<sup>Pr</sup> ligand.

The results of this NMR investigation are in agreement with the stoichiometric investigations as the dihydride species was shown to be one of the main resting states and was stabilized already at significant lower base concentrations compared to the dihydride of the unmethylated catalyst **3**. The second dominant species is the formate complex **Me-6**, and not the methoxide species **4**, as it is the case for the parent catalyst.

### 2.3.5. Mechanistic proposal

#### **2.3.5.1. Possible pathways for the key step involving C-H cleavage**

Analogous to the unmethylated parent catalyst, the key step of the dehydrogenation process is the generation of the dihydride complex **Me-3** from the methoxide, gem-diolate or formate complexes, respectively. Possible pathways for the conversion of the methoxide species **Me-4** to **Me-3** are exemplarily shown in Figure 22 on the next page.

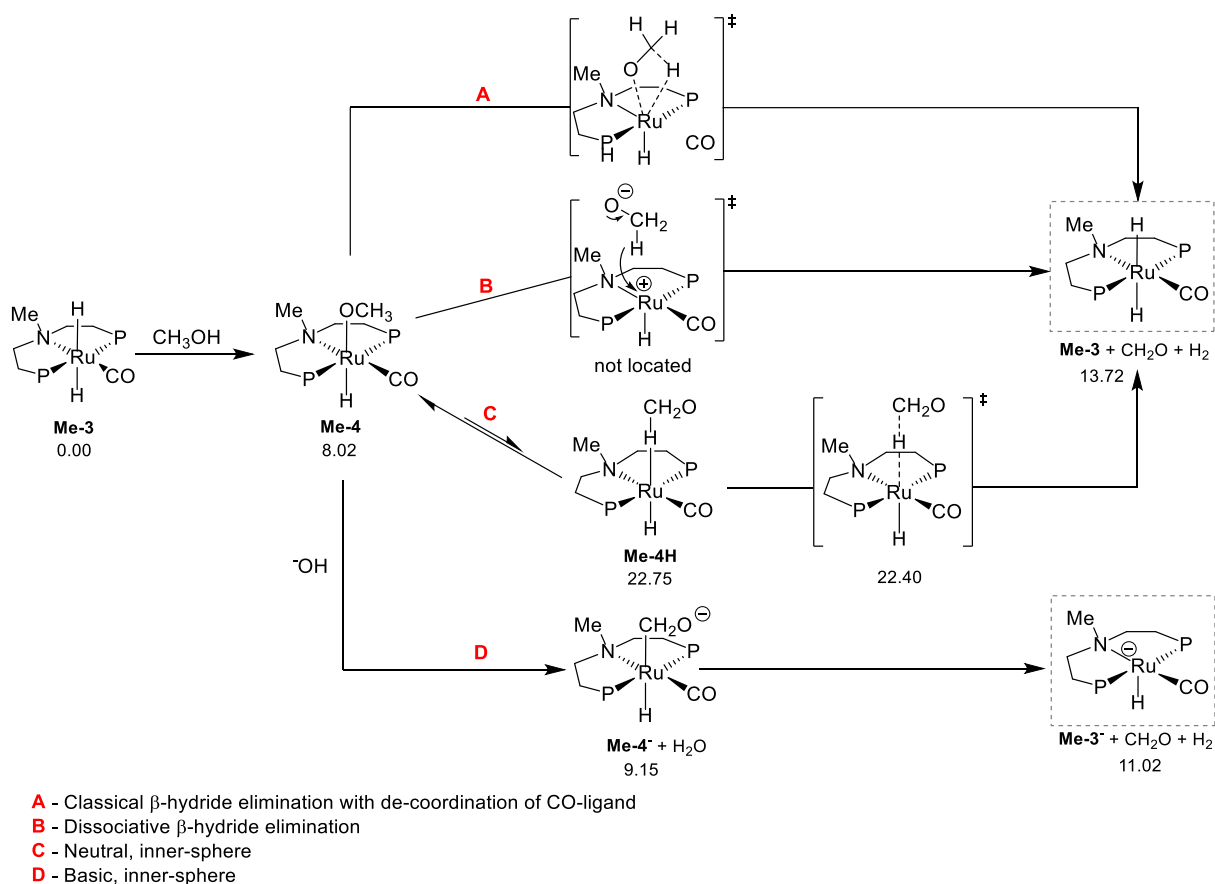
Pathway A depicts the classical  $\beta$ -hydride elimination pathway. Hereby, it is required that either the CO ligand or one of the phosphine ligands of the coordinatively saturated 18-electron complex **Me-4** undergo temporary decoordination.<sup>[141-148]</sup> Due to the high stability of these ligands, this pathway seems very unlikely, though. Another possibility is the dissociative  $\beta$ -hydride elimination, leading to a negative alkoxide ion and a positive ruthenium complex. The alkoxide dissociation should be accelerated in a polar medium like the highly basic methanol-water mixture. Still, as theoretical calculations could not locate a suitable transition state, pathway B can be discarded, too.

Assuming neutral conditions, a similar inner-sphere pathway as for the parent catalyst **1** can be taken into account (pathway C). Also for the **Me-1** complex, the isomerisation from the O-coordinated to the H-coordinated methoxide species takes place, leading to the formation of the dihydride species **Me-3** and formaldehyde. Calculations show that this pathway is a viable route for the key C-H cleavage step.

Finally, by considering the highly basic environment under reaction conditions, a fourth mechanism could be possible (pathway D). Here, the methoxide group gets deprotonated while being coordinated to the Ru centre, which then gives the formaldehyde and the anionic **Me-3<sup>-</sup>**.

## Part I - Mechanistic proposal for catalyst Me-1

**Scheme 22:** Possible mechanistic pathways for the key C-H cleavage step involving catalyst **Me-1**. P = P'Pr<sub>2</sub>.<sup>[138]</sup>



### 2.3.5.2. Calculations for the inner-sphere pathway

For the ionic, inner-sphere pathway the energies for all three dehydrogenation steps were calculated by Dr. Haijun Jiao (Figure 25). The first reaction cascade generating formaldehyde from methanol with concomitant hydrogen evolution is highly endothermic. Hereby, the protonation of the dihydride species **Me-3** by methanol is endothermic by 8.02 kcal mol<sup>-1</sup>. This fits very well the experimental observations that the addition of methanol to **Me-3** leads neither to the formation of **Me-4** nor to the evolution of hydrogen gas. The isomerisation from the O-coordinated to the H-coordinated methoxide species **Me-4H** is even more endothermic by 14.73 kcal mol<sup>-1</sup>. Thus, in contrast to the original catalyst **1**, the dehydrogenation of methanol is the least facile step in the reaction cycle.

The H-coordinated isomer of the gem-diolate species and the transition state leading to the formation of the dihydride **Me-3** could not be located. Nevertheless, the energies are significantly lower compared to the first dehydrogenation cycle. The last step, the dehydrogenation of formic acid to CO<sub>2</sub>, has the lowest energies and energy barriers. The generation of the formate complex **Me-6** from **Me-3** is exergonic by 7.77 kcal mol<sup>-1</sup> and the energy barrier is as low as 0.42 kcal mol<sup>-1</sup>. These values confirm the very easy generation of the formate complex and evolution of hydrogen

## Part I - Mechanistic proposal for catalyst Me-1

gas by the addition of only one equivalent of formic acid to the dihydride complex **Me-3**. With the very low energy of the formate complex, it is a reasonable species to detect in-situ.

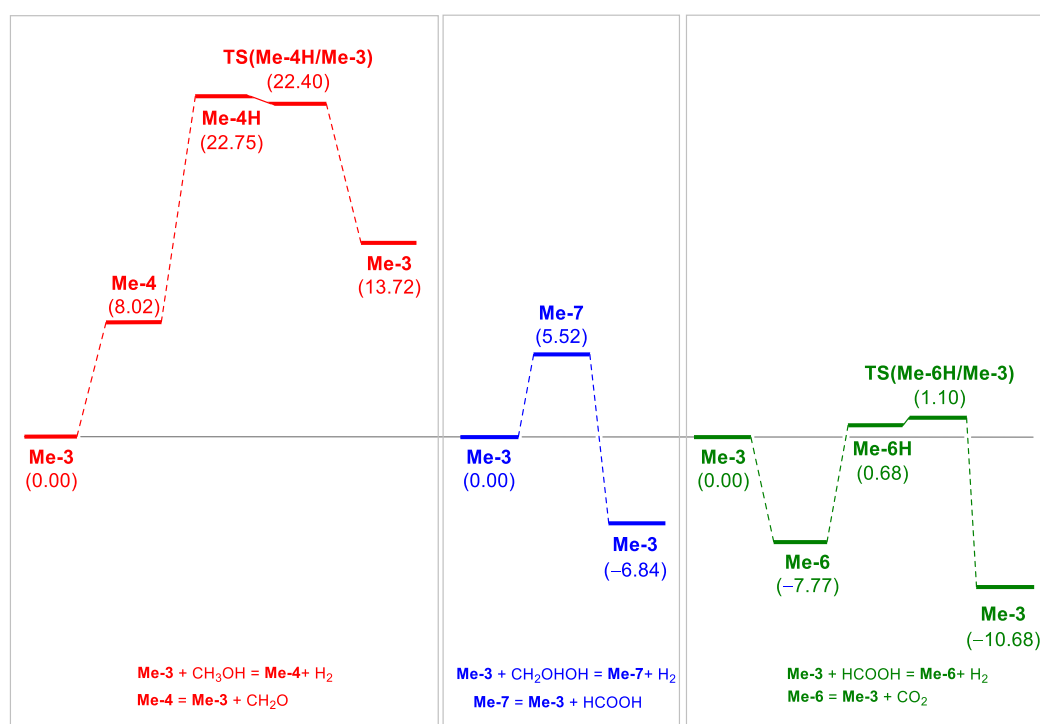
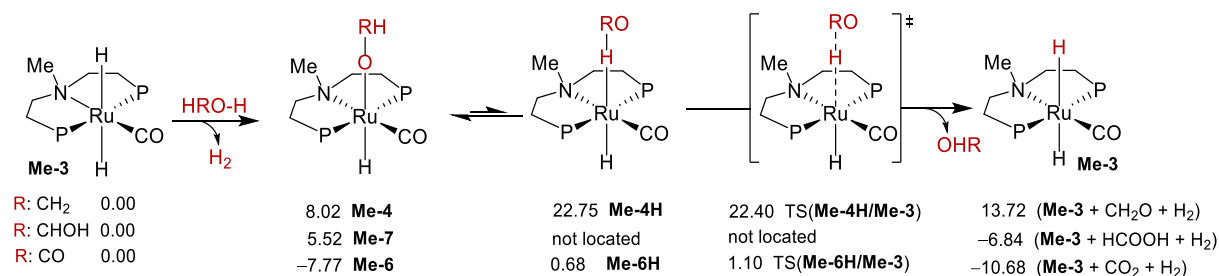


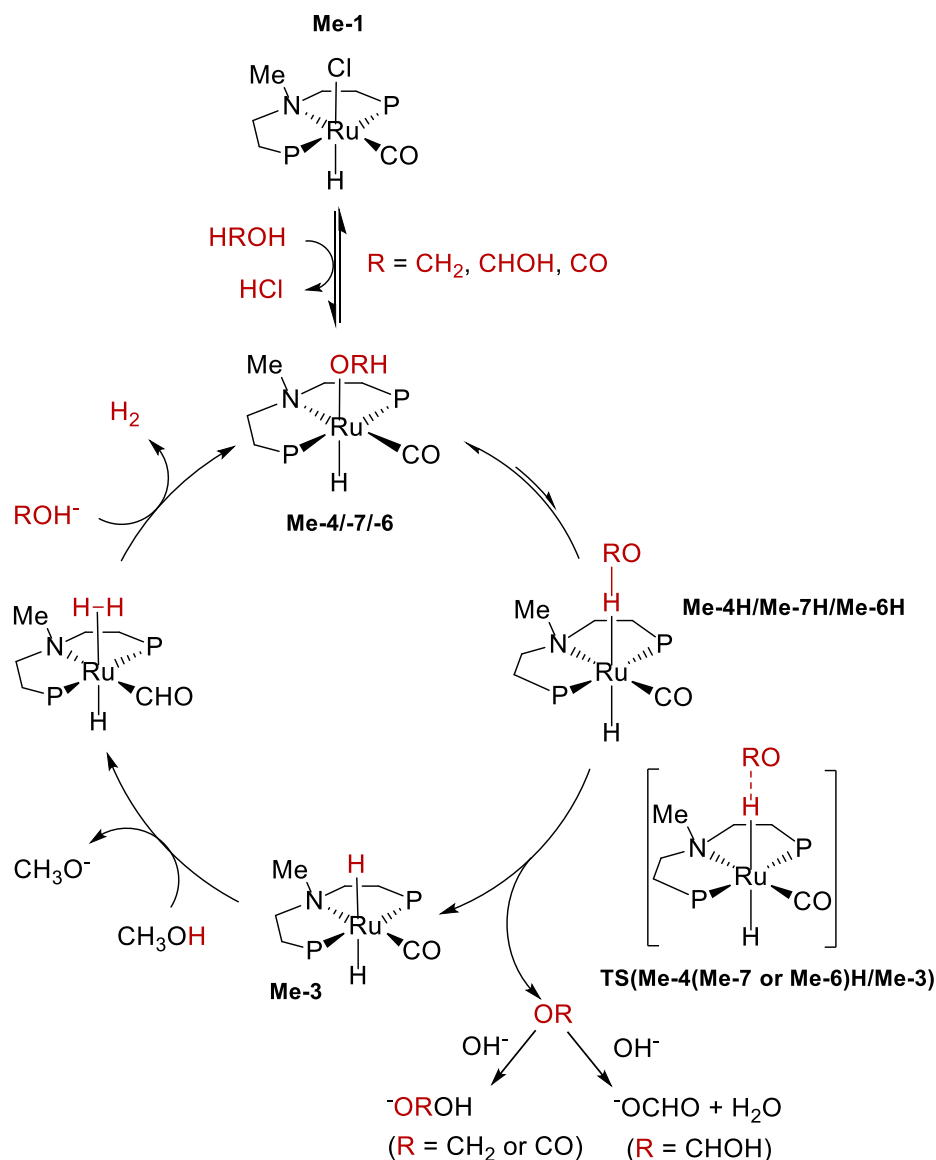
**Figure 25:** Potential energy surface for the inner-sphere pathway for the C-H cleavage step and Ru-dihydride formation. Energies are given in kcal mol<sup>-1</sup>. P = PPr<sub>2</sub>.<sup>[118, 138]</sup>

## Part I - Mechanistic proposal for catalyst Me-1

### 2.3.5.2. Final mechanistic cycle

In conclusion, the following inner-sphere pathway can be postulated for the N-methylated Ru pincer catalyst **Me-1** (Scheme 23).

**Scheme 23:** Proposed mechanistic cycle for the complete dehydrogenation of methanol employing Ru-pincer complex **Me-1**. P = PPr<sub>2</sub>.



The key steps are the isomerisation equilibrium between the O-coordinated and the H-coordinated monohydride species, which is pushed forward to the latter by the generation of formaldehyde, formic acid or CO<sub>2</sub>, respectively.

## Part I - Mechanistic proposal for catalyst Me-1

---

Analogous to the unmethylated parent catalyst **1**, the high base concentration enables the sequestration of these products, which is a strong driving force of the reaction. The formed dihydride complex **Me-3** is consecutively protonated by the protic methanol and the cycle is closed by the generation of hydrogen gas and the reformation of the above mentioned monohydride species **Me-4**, **Me-7** or **Me-6**. The bell-shaped correlation between catalytic activity and base concentration can be related to two competing tendencies.

Calculations have shown that the basic inner-sphere pathway is a well-possible alternative, which explains the increase of activity with the rising base concentration from 0 M to 4 M. The drop in activity with higher amounts of base can be rationalized by the higher stability of **Me-3** compared to its unmethylated counterpart **3** towards protonation. In a highly basic environment the ratio of  $\text{CH}_3\text{OH}/\text{CH}_3\text{O}^-$  is significantly decreased, which renders the last step of the mechanistic cycle significantly more difficult.

## Part I - Summary and outlook

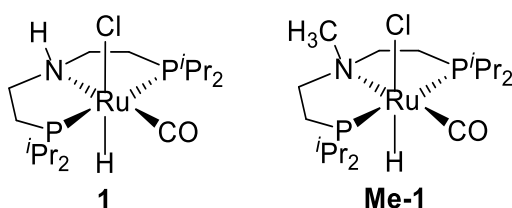
---

### 2.4. Summary and outlook for the ruthenium-catalysed dehydrogenation of methanol

The objective of this first part of the thesis was to acquire comprehensive understanding of the mechanism of the homogeneously Ru-PNP catalysed aqueous-phase reforming of methanol. A complete mechanistic cycle could be proposed for both the parent catalyst **1** and its methylated derivative **Me-1** based on the results from activity measurements, kinetic experiments, stoichiometric and *in-situ* NMR measurements and theoretical calculations. The following summary gives an overview of the most prominent results that were obtained:

- The methylated derivative **Me-1** reached 60% of the activity of its Ru-PNP parent catalyst for the methanol dehydrogenation reaction under the optimised conditions using a 9:1 MeOH:H<sub>2</sub>O solution containing 8 M KOH at 90 °C.

**Scheme 24:** Ru-PNP parent catalyst **1** and its methylated derivative **Me-1**.



- The ensuing kinetic investigations showed a striking difference in KIEs, whereby the value for **Me-1** was only slightly higher than one, which means that no significant cleavage of C-H, O-H or Ru-H bonds take place during the rate-limiting step(s).
- A linear temperature-activity relation means that the inflation of the temperature above the boiling point of the methanol-water mixture does not alter the mechanism and does not lead to a higher activity than caused by the rise in temperature, as it had been assumed before.
- A modified setup for the investigation of the molarity-activity correlation was developed due to the chemical attenuation of the catalyst's activity as hydrogen adds to the active catalyst species at higher partial hydrogen pressure.



## Part I - Summary and outlook

---



**Figure 26:** Modified autoclave setup.<sup>[118]</sup>

- At constant temperature, rates of reaction increased with increasing KOH concentrations for catalyst **1**, whereby at 90 °C saturation kinetics occurred at a base molarity above 6 M, which could be explained by the limiting factor of hydrogen mass transfer.
- One of the most essential aspects is that the mechanistic cycle is based on an inner-sphere, anionic pathway in which the ligand is not more active than acting as a strongly donating anionic ligand.
- The second important aspect is that the base is essential for catalytic activity, as it generates the active amido complex **2** by dehydrochlorination of the pre-catalyst via a conjugate base mechanism. Furthermore the high base concentration ensures that the deprotonated methoxide, gem-diolate and formate species are formed, for which C-H cleavage is facilitated. Finally base sequesters the dehydrogenation products, which is a significant driving force of the reaction.

Further mechanistic points that were elucidated are listed below:

- Generally, the anionic methoxide species **4<sup>-</sup>** is besides the anionic dihydride species **3<sup>-</sup>** one of the main active catalytic complexes in the cycle, which stands in contrast to its proposed role as an off-cycle intermediate.
- An equilibrium between these two complexes exists, which is influenced by the amount of methanol and base. Hereby, the dihydride complex is stabilised by high base content.
- The hydroxide complex **5** was confirmed to be an off-cycle intermediate.
- Hydrogen is liberated from the dihydride complex via a solvent-assisted pathway.
- For the methylated derivative both the neutral and the anionic inner-sphere pathways were determined to be viable routes, whereby during the latter the methoxide (gem-diolate or formate) group gets deprotonated while being coordinated to the Ruthenium centre.

## Part I - Summary and outlook

---

- The bell-shaped correlation between catalytic activity and base concentration for **Me-1** can be related to two competing tendencies: Firstly, base concentration up to 4 M enables the more effective anionic pathway. Secondly, at higher base molarities the higher stability of **Me-3** towards protonation compared to its unmethylated counterpart becomes decisive, which slows down catalytic activity.
- For catalyst **1**, formate dehydrogenation was found to be the least facile step, whereby for **Me-1** the conversion of methanol proved to be rate-determining.
- *Operando* Raman and GC investigations have shown that especially for future steps involving the upscaling of the system, the challenge of continuous make-up of the base with concomitant continuous generation of solid carbonate precipitate will have to be dealt with.

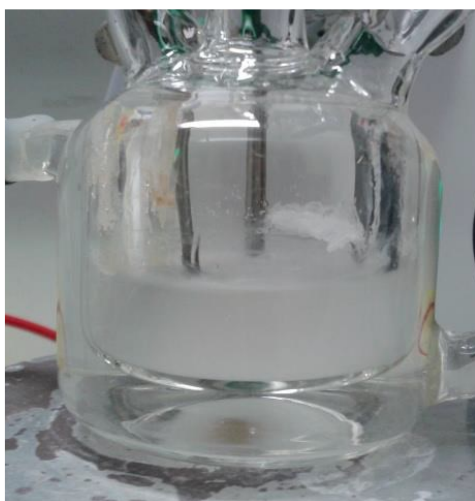


**Figure 27:** Coating of the inner wall of the reaction vessel with potassium carbonate.<sup>[135]</sup>

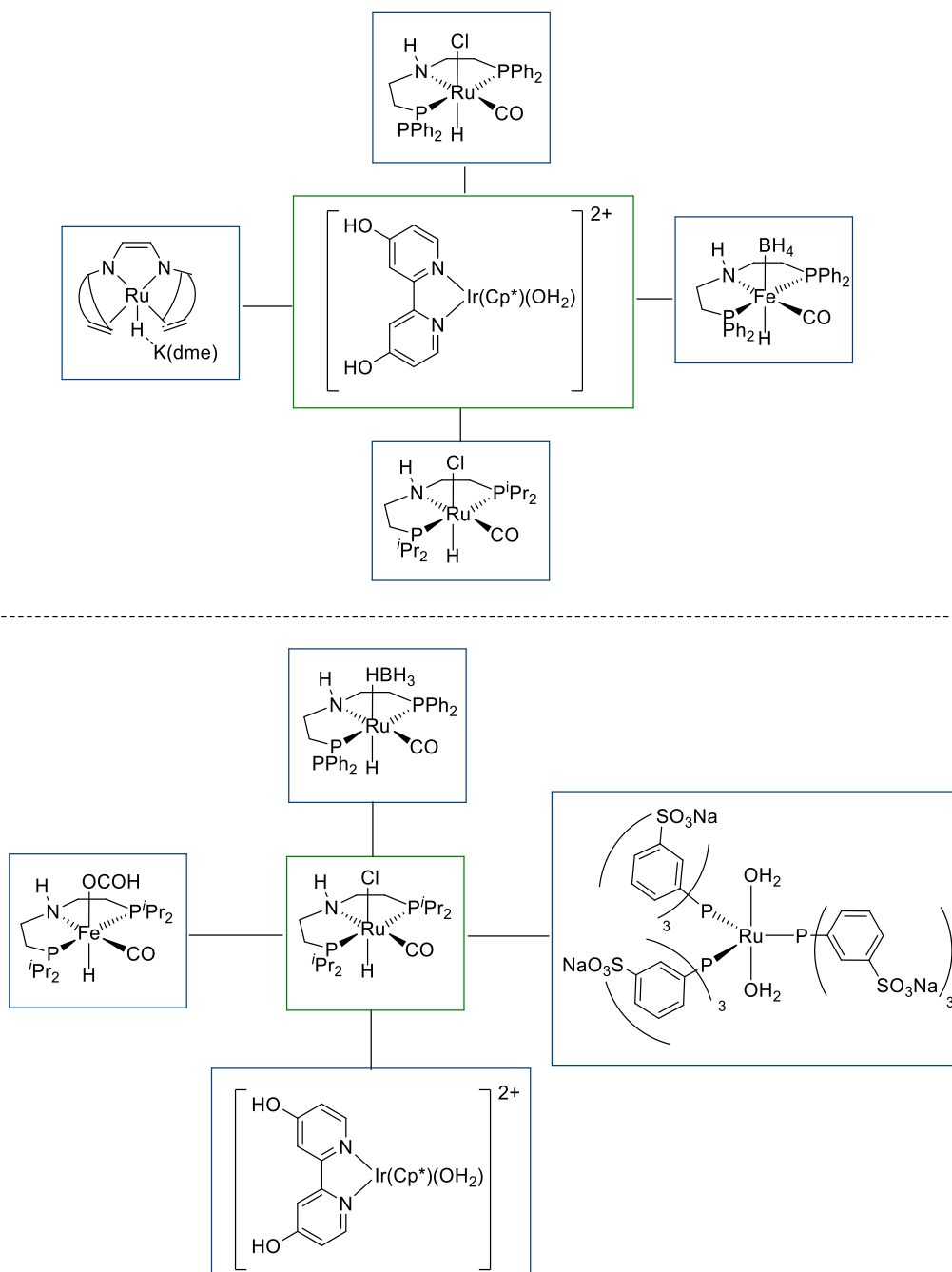
These findings are particularly valuable in respect to the development of novel type of catalysts that are active both at lower base concentrations and in the same temperature range for the aqueous-phase reforming of methanol. Generally, catalytic activity and stability of the Ru-PNP catalyst is adequate for further practical implementation, but the high amount of base and the hereby-caused accumulation of carbonate make this step not feasible at this point.

Different approaches to reach this objective can be envisioned. One option is the development of a bicatalytic system analogous to the one that was reported in 2014<sup>[111]</sup>, but with significantly higher activities. Ideally, the interaction of both catalysts would lead to synergistic effects, which pushes catalytic activity even further. To systematically test the optimal combination of two catalysts, an efficient method is to start from one complex known to effectively catalyse the dehydrogenation of methanol to formic acid and combine it with complexes or variation of these that have already been employed for the conversion of formic acid. Possible options for the latter

## Part I - Summary and outlook

case would be Iridium-based catalysts similar to the ones reported by Himeda and co-workers (Scheme 25).<sup>[149-152]</sup>

**Scheme 25:** Combination of possible catalysts that can be combined for a bicatalytic system. Upper part shows the combination of an active catalyst for formic acid dehydrogenation with well-known catalysts for methanol dehydrogenation, the lower part *vice versa*.



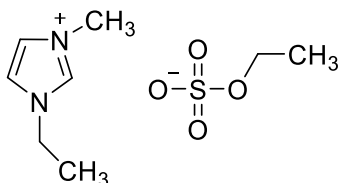
Another option is the reduction of the base amount without concomitant loss of catalytic activity by adding suitable solvents. The first attempts of this strategy have already been performed. By

## Part I - Summary and outlook

---

using the basic ionic liquid Ecoeng 212 (1-ethyl-3-methyl-imidazolium-ethylsulfate) it was hoped to enable a basic macroscopic environment (Scheme 26).

**Scheme 26:** Structure of the basic IL Ecoeng 212 (1-ethyl-3-methyl-imidazolium-ethylsulfate).



Unluckily, degradation issues occurred when a minimum amount of base was added to the reaction solution. Also the replacement of the base by the Lewis acid LiBF<sub>4</sub> that had been shown to trigger catalytic activity for the dehydrogenation of formic acid<sup>[153]</sup> did not prove to be successful.

A further strategy is the replacement of the base by carbonates: For complete methanol reforming, leading to the generation of one equivalent of CO<sub>2</sub> per three equivalents of hydrogen, long-term investigations showed that an equilibrium between hydroxide, (bi)carbonate and formate is reached and the pH value of the solution stays at approximately 10.<sup>[103]</sup> Based on these findings, two measurements were performed at a reduced temperature of 70 °C, whereby the first reaction solution contained only 2 M of KOH and the second one a mixture of 2 M KOH and 2 M K<sub>2</sub>CO<sub>3</sub> (For details see Section 6.4.3. of the Appendix). Also here no improvements of catalytic activity were observed.

In conclusion, despite the unsuccessful first attempts, several promising routes for improving the technical implementation of the Ru-PNP based system for the methanol dehydrogenation can be envisioned and are very likely to be put into practice in the not too distant future.

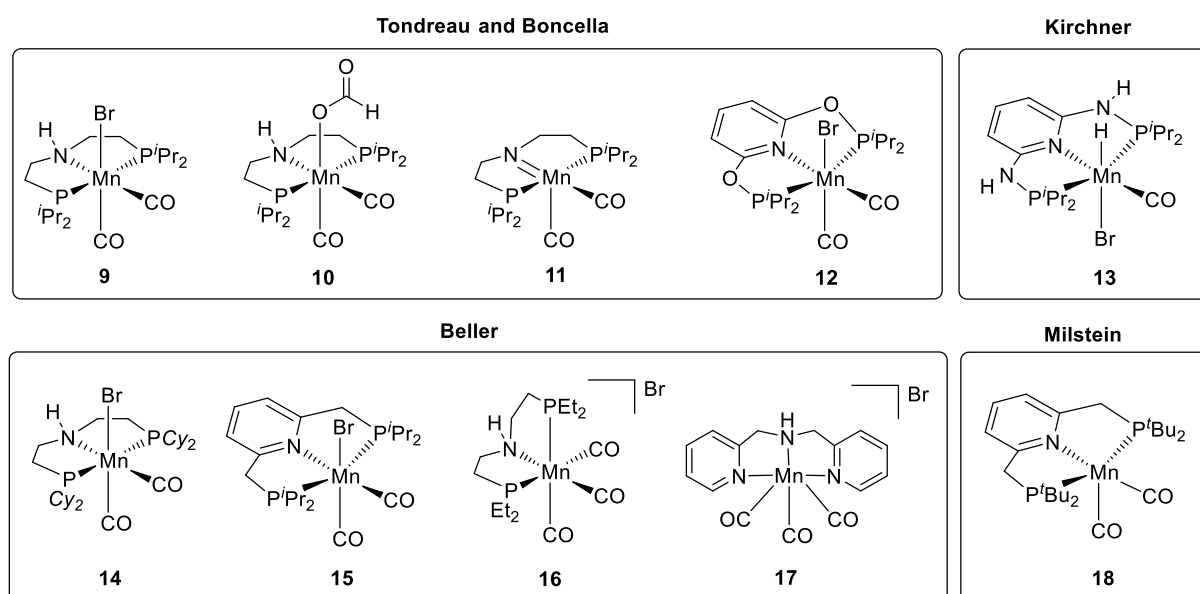
### 3. Part II: Manganese-catalysed dehydrogenation of methanol

#### 3.1. Introduction

Besides the already mentioned ruthenium catalyst systems, only a few examples using complexes based on the non-noble metal iron have been reported for the dehydrogenation of methanol. Very recently, manganese pincer catalysts have attracted increasing attention and have been employed for the first time for both hydrogenation and dehydrogenation reactions, though this metal is commonly used in oxidative conversions.<sup>[154-155]</sup> In nature, manganese occurs in abundance and is not only an essential trace element for living organisms, but is also present in many metalloproteins and enzymes.<sup>[156-157]</sup> Generally, this base metal is earth abundant, inexpensive due to its use for the iron and steel production and low toxic.<sup>[158-159]</sup>

Based on these favourable properties, the use of manganese pincer catalysts constitutes a viable option for replacing noble metal-based complexes. Examples of this type of catalysts that have been successfully applied for a range of chemical conversions are shown in Scheme 27.<sup>[160-166]</sup>

**Scheme 27:** Overview of manganese-based pincer catalysts.



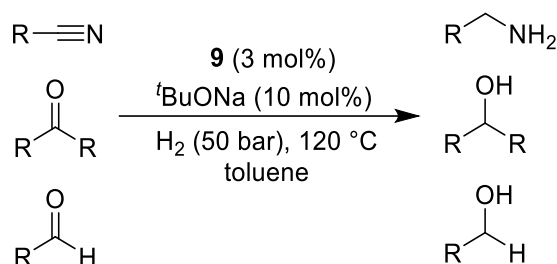
One of the firsts to report Mn-based pincer catalyst were A. Tondreau and J. Boncella, who synthesized i.a. the catalysts **9** and **12** by reacting the precursor  $\text{Mn}(\text{CO})_5\text{Br}$  with the respective HNPPr and PONOPPr ligands.<sup>[164]</sup> At around the same time Elongavan et al. successfully employed catalysts **9** and **14** for the hydrogenation of nitriles, ketones and aldehydes.<sup>[160]</sup> Various aromatic, heteroaromatic and also aliphatic nitriles were hydrogenated to the corresponding amines in good to excellent yields. Aliphatic ketones and also  $\alpha$ ,  $\beta$ -unsaturated aldehydes proved to be accessible

## Part II - Introduction

---

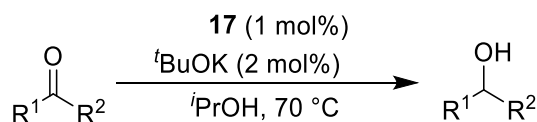
substrates. For mechanistic investigations, NMR and *ex-situ* IR measurements were performed, based on which a concerted outer-sphere mechanism for the nitrile hydrogenation was proposed. In contrast, the hydrogenation of benzaldehyde was calculated to follow a step-wise outer-sphere pathway.

**Scheme 28:** Hydrogenation of nitriles, ketones and aldehydes using Mn-catalyst **9**.



For the application in transfer hydrogenation of ketones with isopropanol as the hydrogen source, the *N,N,N*-Mn pincer complex **17** showed excellent activity.<sup>[116]</sup> A variety of aliphatic, aromatic and heteroaromatic ketones were successfully hydrogenated, although it was not possible to convert aldehydes under optimised reaction conditions.

**Scheme 29:** Transfer hydrogenation of ketones with Mn-catalyst **17**.

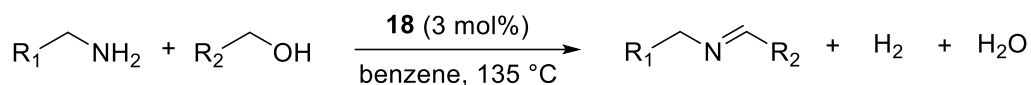


Additionally, deuterium experiments were carried out, which led to the conclusion that the hydrogen transfer proceeds through a Mn-monohydride species. Interestingly, the catalyst with methylated N-backbone of the ligand showed reasonable activity for the transfer hydrogenation of acetophenone. In this case, the deuterium labelling experiment resulted in a strong kinetic isotope effect, based on which it was assumed that different mechanistic pathways are visible and that the N-H moiety of the ligand backbone is not essential for the key C-H activation step.

The first dehydrogenation reactions were performed both by A. Tondreau and J. Boncella and Milstein and co-workers. Milstein reported the dehydrogenative coupling of alcohols and amines to imines under hydrogen gas evolution using the Mn catalyst **18**.<sup>[162]</sup>

## Part II - Introduction

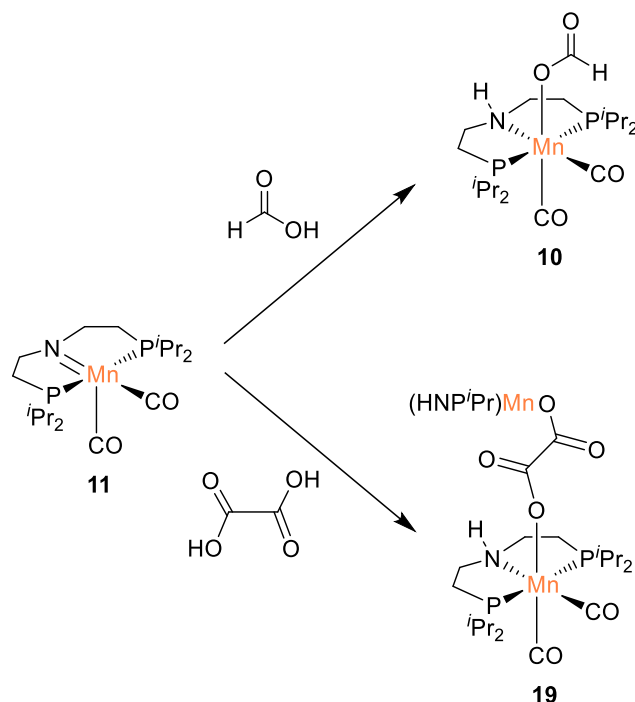
**Scheme 30:** Dehydrogenative coupling of alcohols and amines to imines using Mn-catalyst **18**.



A range of aromatic imines were synthesized in good to very good yields, and also an aliphatic imine proved to be an accessible product, although it was obtained in significantly lower conversion. For the dehydrogenation of the alcohol a bifunctional mechanism was postulated. This pathway involves the presumed concerted proton and hydride transfer from the alcohol to the active centre of the ligand backbone and the metal centre, respectively.

Boncella demonstrated the 1,2-addition of formic acid and oxalic acid to the Mn-amido complex **11**.<sup>[165]</sup> In the case of the latter substrate, the oxalate-bridged dimer **19** was formed. First tests proved that complex **11** catalyses the dehydrogenation of formic acid, although the turnovers were significantly lower than for related iron catalysts. Furthermore, significant amounts of water were detected, which means that not only the dehydrogenation but also the dehydration reaction took place. Interestingly, the use of the Lewis acid LiBF<sub>4</sub> completely shut down catalytic activity.

**Scheme 31:** 1,2-Addition of formic acid and oxalic acid to the Mn-amido complex **11**.



### 3.2. Objectives of project II

The recent achievements based on novel manganese catalysts were very promising, but also showed that significant advances can still be made. Especially in the field of dehydrogenation reactions only one Mn-containing catalyst has been applied so far, and both selectivity and activity should be significantly improved.

Based on our group's expertise in the dehydrogenation of alcohols and other hydrogen carriers, it is envisioned to develop an effective catalyst system based on this non-noble metal for the aqueous-phase reforming of methanol at low temperatures. Once a suitable catalyst is identified, further investigations are aspired both to optimise reaction conditions and to get a deeper understanding of the fundamental mechanism. To fulfil the second objective, it is planned to utilise our expertise in kinetic investigations combined with *ex-situ* and *in-situ* analytical methods that already proved to be very effective. Besides performing NMR measurements, it is envisioned to use IR methods to identify active catalytic intermediates, as this technique was shown to work very well for the identification of manganese pincer systems before.<sup>[164]</sup>

The mechanistic revelations are especially interesting when compared to the findings for the ruthenium catalyst. Both similarities and differences in the mechanism between the two systems can help to develop a better understanding of visible reaction pathways, which is one of the key steps in developing more efficient and preferably low-cost catalyst systems.



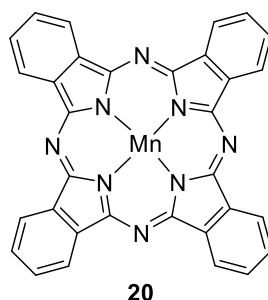
## Part II - Activity investigations

### 3.3. Results and discussion<sup>[167]</sup>

#### 3.3.1. Preliminary tests

To get a better understanding of the catalytic performance, several defined manganese complexes as well as precursors known from literature were tested by Maria Anderez-Fernandez, using the optimised conditions of a highly basic 9:1 MeOH:H<sub>2</sub>O solution at a reaction temperature of 90 °C from the Ru-pincer catalyst system. The employed catalysts are shown in Schemes 27 and 32.

**Scheme 32:** Structure of the Mn-porphyrine complex **20**.



Under these reaction conditions, a high sensitivity to light irradiation especially for the dissolved Mn complex **9** was observed, which led to a fast decline in its activity. This deactivation contrasts the complex's noted stability in crystalline form<sup>[160]</sup> and could be ascribed to the light-triggered cleavage of the HPNPPr ligand (see Figure 28). Interestingly, in the case of the related Ru- and Fe-PNP-pincer catalysts, this effect had not been noticed at all. Thus, to avoid irreproducibilities in the catalysts' performances, all ensuing experiments were carried out under rigorous exclusion of light.

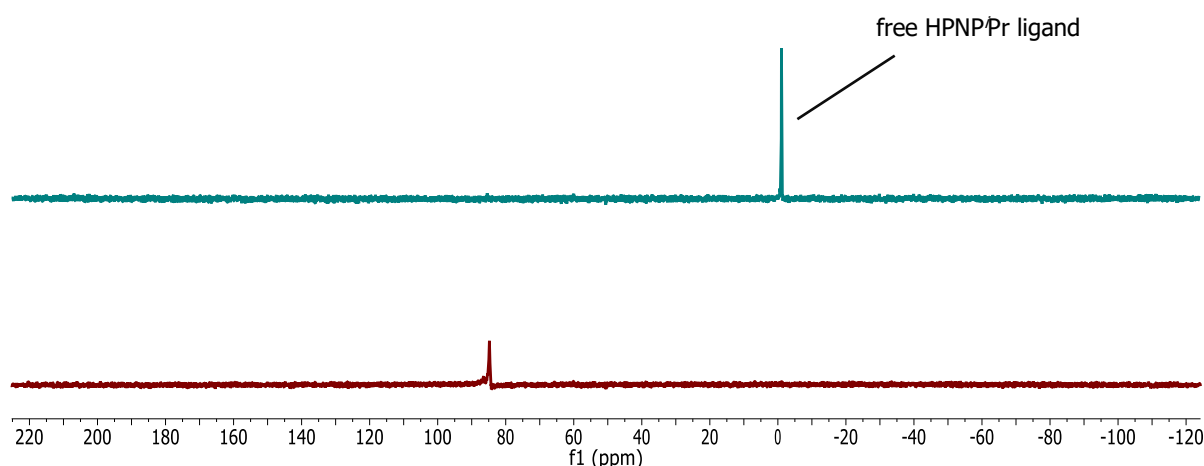


**Figure 28:** Influence of light on the catalytic activity of the Mn complex **9**. <sup>31</sup>P NMR (297 K, 162 MHz, 9:1 MeOH:H<sub>2</sub>O, a few drops of MeOD-d<sub>4</sub>). Bottom: **9** (10 mM) in 9:1 MeOH:H<sub>2</sub>O solution containing 8 M KOH. Top: After the exposure of **9** to a Luxeon LED light source for 30 min.<sup>[168]</sup>

## Part II - Activity investigations

Although the activities were significantly lower compared to the related iron- and ruthenium-based complexes, the aliphatic manganese pincer complex bearing ethyl groups **16**, the corresponding Pr catalyst **9** and the *in-situ* system consisting of the precursor Mn(CO)<sub>5</sub>Br with additional 10 equivalents of the HPNPPr ligand showed promising activities for the aqueous-phase methanol dehydrogenation. Hereby, productivities of 65, 54 and 68, respectively, were obtained after a reaction time of five hours (Table 1, entries 4, 1 and 8). In contrast, a range of the tested manganese complexes did not show significant activities, including the commercially available precursor Mn<sub>2</sub>(CO)<sub>10</sub> and the Mn-porphyrine complex **20**, as well as the pincer complex bearing cyclopentyl ligands **14** and catalyst **17**, which had been successfully employed before for the transfer hydrogenation of ketones<sup>[116]</sup> (Table 1, entries 7, 6, 2 and 5). The use of the Milstein-analogous complex **15** resulted in observable hydrogen gas evolution, but its performance fluctuated significantly and could not be well reproduced (see Part 6.5.1 Figure 70 in the Appendix).

**Table 1:** Testing of different Mn catalysts for the dehydrogenation of methanol.<sup>[169-170]</sup>

Entry	Catalyst	V <sub>5h</sub> [mL]	TON <sub>5h</sub>
1 <sup>[b]</sup>	9	11	54
2	14	-	-
3	15	9	41
4 <sup>[b]</sup>	16	13	65
5	17	-	-
6	20	-	-
7	Mn <sub>2</sub> (CO) <sub>10</sub>	-	-
8 <sup>[b]</sup>	Mn(CO) <sub>5</sub> Br + 10 eq. HPNPPr ligand	14	68

[a] Reaction conditions: MeOH:H<sub>2</sub>O (5 mL, ratio 9:1), 8 M KOH (molarity based on the total MeOH + H<sub>2</sub>O volume), catalyst (8.4 μmol, 1.68 mM); T<sub>set</sub>: 92°C; gas volumes were determined using manual or automatic gas burettes and were analysed by GC. Each molecule of hydrogen is counted as one turnover. All gas measurements were performed at least twice and corrected by blank values. [b] Standard deviation is less than 15%.

### 3.3.2. Optimisation reactions

Based on the results of the preliminary tests, the defined catalysts **9** and **16** seemed worth to be considered as promising candidates for more profound investigations. Due to the easy availability of the complex bearing isopropyl scaffolds and the observed activity of the *in-situ* system consisting of the precursor Mn(CO)<sub>5</sub>Br with additional 10 equivalents of the HPNPPr ligand, complex **9** was chosen for performing further optimisation experiments, which were carried out by Maria Anderez-Fernandez. Hereby, the use of additional solvents, the replacement of KOH by other bases or additives and the influence of the methanol-water ratio were investigated. (see Table 2). The attempts of substituting potassium hydroxide proved to be not successful, as the use of *t*BuOK or LiOH led to a reduction in activity of more than 50% and even to the entire seizure of gas evolution in the case of the latter. As it was observed by Boncella and co-workers in case of the

## Part II - Activity investigations

dehydrogenation of formic acid by the formate complex **10** [165], employing the Lewis acid LiBF<sub>4</sub> resulted in the complete deactivation of the catalyst **9** (Table 2, entries 6, 7 and 8).

As it had been noted before for the ruthenium-pincer complex **1**, the increase of the water-to-methanol ratio to 1:1 caused the breakdown of catalytic activity as well, which could be explained by the increasing formation of the inactive hydroxide species as ex-catalytic resting state. Consequently, omission of water as substrate led to a significant increase of activity compared to the 9:1 ratio of methanol and water used for the aqueous-phase reforming under standard conditions (Table 2 entries 11, 9 and 10). Also the addition of 10 equivalents of the HPNP<sup>Pr</sup> ligand caused a remarkable enhancement of the rate of hydrogen gas production (Table 2 entry 12).

**Table 2:** Influence of the different conditions on the activity of the Mn-catalyst **9**.<sup>[169-170]</sup>

Entry	Catalyst [ $\mu\text{mol}$ ]	MeOH [mL]	H <sub>2</sub> O [mL]	Additive	Solvent [mL]	T [°C]	VH <sub>2</sub> (5h) [mL]	TON (5h)
1	<b>9</b> (8.4)	9	1	KOH (8 M)	-	90	20	98
2	<b>9</b> (8.4)	4.5	0.5	KOH (8 M)	triglyme (5)	90	18	88
3	<b>9</b> (8.4)	4.5	0.5	KOH (8 M)	<i>t</i> -amyl alcohol (5)	90	23	114
4	<b>9</b> (8.4)	4.5	0.5	KOH (8 M)	toluene (5)	90	6	31
5	<b>9</b> (8.4)	4.5	0.5	KOH (8 M)	dioxane (5)	90	26	126
6	<b>9</b> (8.4)	4.5	0.5	<i>t</i> BuOK (8 M)	triglyme (5)	90	7	34
7	<b>9</b> (8.4)	4.5	0.5	LiOH (8 M)	triglyme (5)	90	-	-
8	<b>9</b> (8.4)	4.5	0.5	LiBF <sub>4</sub> (1 mM)	triglyme (5)	90	-	-
9	<b>9</b> (8.4)	5	-	KOH (8 M)	-	90	18	90
10	<b>9</b> (8.4)	4.5	0.5	KOH (8 M)	-	90	11	54
11	<b>9</b> (8.4)	2.5	2.5	KOH (8 M)	-	90	-	-
12	<b>9</b> (8.4)	4.5	0.5	KOH (8 M) HPNP <sup>Pr</sup> ligand (10 eq.)	-	90	25	121

Testing a range of solvents led to very diverging results. The addition of toluene had detrimental effects on the catalyst's activity and stability, whereas the use of dioxane and *t*-amyl alcohol led to an observable improvement of the catalytic rate. Triglyme caused a minor decrease in activity, whereby longer reaction times are necessary to evaluate the significance of the solvent's influence (Table 2 entries 4, 5, 3 and 2).

## Part II - Activity investigations

### 3.3.3. Longterm investigations

The addition of a solvent seemed a promising approach to increase the catalyst's activity and stability, therefore further tests investigating long-term effects were performed by Maria Anderez-Fernandez. Hereby, reactions were run for longer than 50 hours (Figure 29). Based on the results of the initial tests, triglyme and dioxane were chosen as solvents of choice and compared to the reaction system using methanol both as substrate and solvent.

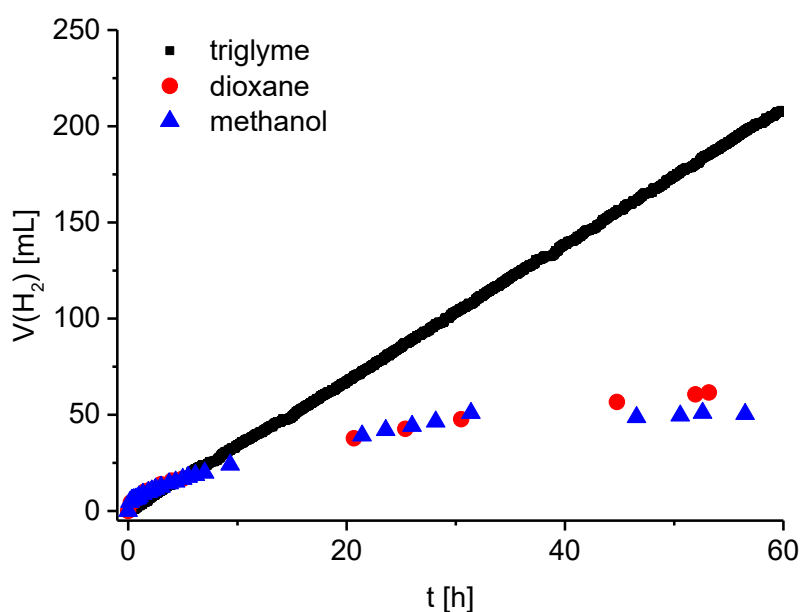


**Figure 29:** Testing of the long-term effects of the addition of solvents. Reaction cond.: MeOH:H<sub>2</sub>O (5 mL, ratio 9:1), 5 mL solvent, KOH (8 M; molarity based on the total MeOH + H<sub>2</sub>O volume), **9** (8.4 μmol, 0.84 mM), T<sub>set</sub> 92 °C. Reactions performed with dioxane and methanol as solvent were performed using the manual burette setup, while the reaction performed with the addition of triglyme was performed using the automatic burette setup.<sup>[168, 171]</sup>

Very interestingly and in contrast to the results of the measurements before, it was discovered that using triglyme as solvent had a significant long-term stabilising effect on the Mn-catalyst system. Hereby, the reaction continued with steady gas evolution even after 60 hours. In the cases of dioxane and methanol as solvents, activity surprisingly ceased after approximately 10 hours. Therefore, it can be concluded that although the use of dioxane and methanol leads to an increase in activity for the initial reaction period, triglyme has long-lasting stabilisation effects on the catalyst system. This could be due to the improved solubility of the base as well as the carbonate salts that are formed during the reaction. Generally, it was observed that the addition of triglyme resulted in improved homogeneity of the reaction solution compared to the other tested solvents. Consequently, triglyme was chosen as solvent of choice for the ensuing experiments.

As reaction conditions could be significantly improved, the next step was to investigate the differences in activity and stability of the defined Pr complex **9** and the precursor Mn(CO)<sub>5</sub>Br under

## Part II - Activity investigations

---

the optimised conditions using triglyme as solvent and adding 10 equivalents of the HPNP<sup>Pr</sup> ligand. The results of the long-term experiments performed for both systems are shown in Figure 30.

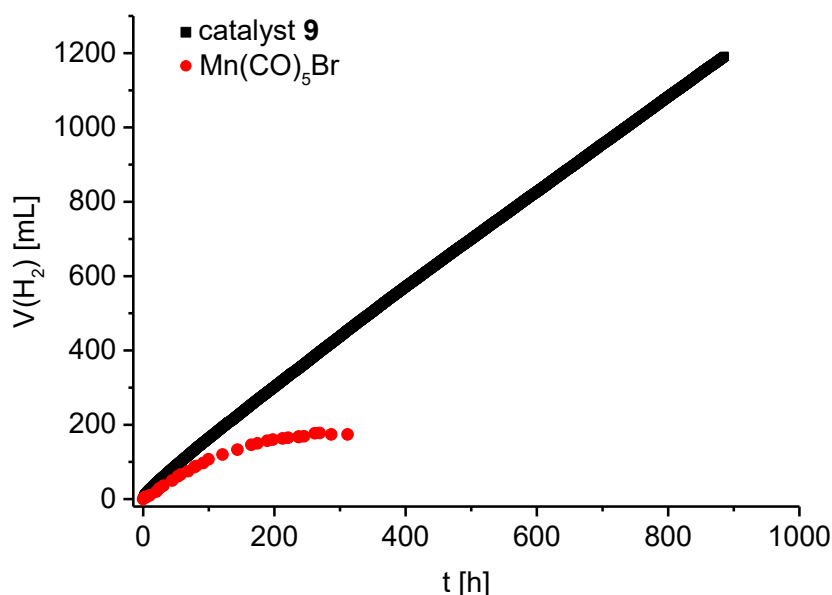


**Figure 30:** Longterm measurements. Reaction cond.: MeO/H<sub>2</sub>O (20 mL, ratio 9:1), triglyme (20 mL), KOH (8 M), Mn(CO)<sub>5</sub>Br or **9** plus 10 eq. HPNP<sup>Pr</sup> ligand (2.1 μmol, 0.05 mM); T<sub>set</sub> 92°C.<sup>[168, 172]</sup>

The outcome of these measurements were quite remarkable as the use of the defined catalyst resulted in a very steady gas evolution, which lasted for longer than a month. During that time a TON of more than 20,000 was reached and even after that period, catalytic activity was not observably diminished. Another aspect worth to be highlighted is that with this productivity the manganese catalyst exceeded the stability of the related Fe-<sup>Pr</sup> complex by far, whose activity ceased already after five days. The testing of the Ru-<sup>Pr</sup> catalyst **1** was stopped after 23 days, therefore no direct comparison can be made in this case.<sup>[103, 105]</sup>

In contrast, the *in-situ* system consisting of Mn(CO)<sub>5</sub>Br precursor plus additional HPNP<sup>Pr</sup> ligand, which had demonstrated promising activities for a reaction duration of five hours, showed a rapid decline in activity. Already after approximately four days a distinct diminishing of reactivity was observed and gas evolution finally completely ceased after twelve and a half days. Although triglyme showed a long-term stabilizing effect for the Mn-catalyst **9**, it was not sufficient for the reaction system based on the Mn(CO)<sub>5</sub>Br precursor. This trend of comparably high initial activity followed by a trend of deactivation after more than a week is not common for *in-situ* systems as they tend to show an initial activation phase.<sup>[173-174]</sup>

In order to get a better understanding of this interesting phenomenon and characterize possible catalytic intermediates, extensive analytic experiments including stoichiometric and *in-situ* studies were carried out, which will be described in detail in the following chapter.

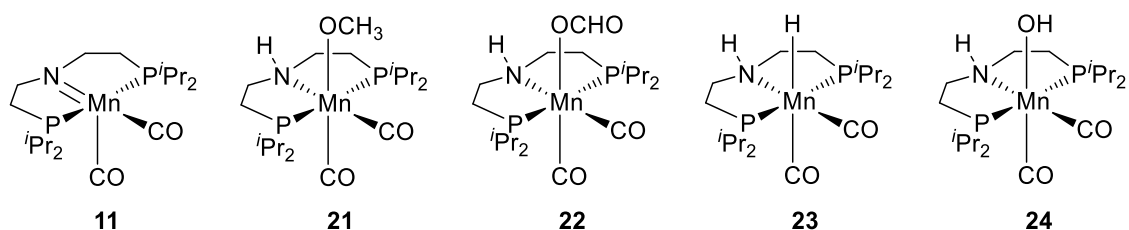
---

## Part II - Spectroscopic investigations

### 3.3.4. NMR investigations: Difference between defined Mn-catalyst and precursor

In analogy to the corresponding Ru-PNP catalyst system, the Mn-amido complex **11**, methoxide complex **21**, formate complex **22**, hydride complex **23** or the hydroxide complex **24** as off-cycle state – or due to the highly basic medium, the analogous deprotonated species – are likely intermediates to take part in the mechanistic cycle (Scheme 33).

**Scheme 33:** Overview of related complexes of Mn-parent catalyst **9**.



#### 3.3.4.1. Studies of the reaction solution

The first step was the analysis of the catalytic species that are observed under reaction conditions at room temperature. By dissolving the manganese catalyst **9** in the MeOH:H<sub>2</sub>O solution containing 8 M KOH two species with the chemical shifts  $\delta = 84.7$  (bs, major species) and  $86.5$  (bs, minor species) were detected in the <sup>31</sup>P NMR (see Figure 31). The possibility of being one of them the hydride complex **23** could be excluded as no signal in the hydride region in the <sup>1</sup>H NMR appeared, nor did the <sup>31</sup>P signals match the previously reported shift of 109.6 ppm for the hydride complex by Elangovan et. al.<sup>[160]</sup>

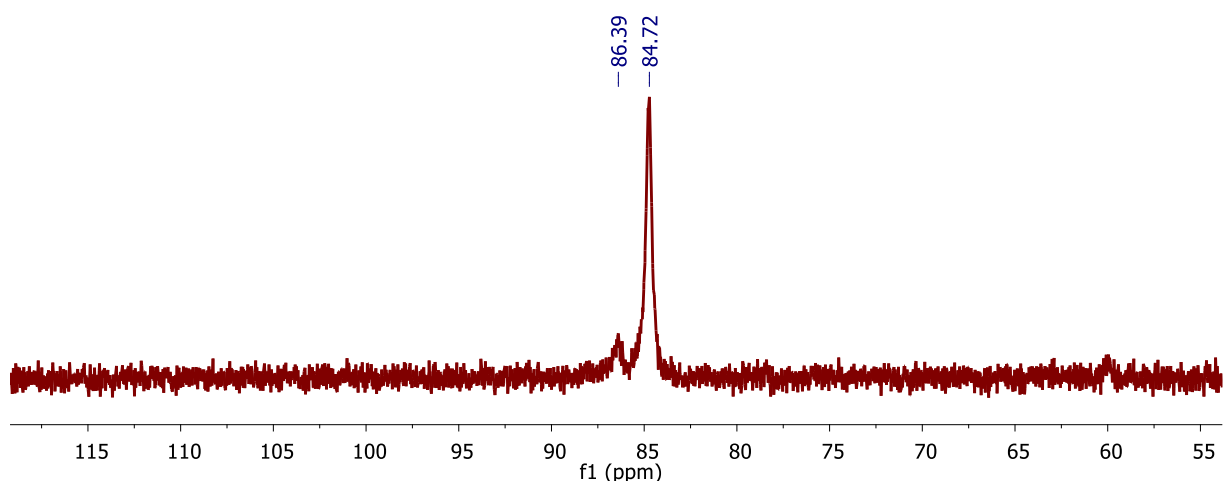


**Figure 31:** <sup>31</sup>P NMR of the reaction solution containing catalyst **9**. <sup>31</sup>P NMR (297 K, 162 MHz, 9:1 MeOH:H<sub>2</sub>O, a few drops of MeOD-d<sub>4</sub>). **9** (10 mM) in 9:1 MeOH:H<sub>2</sub>O solution containing 8 M KOH.<sup>[168]</sup>

## Part II - Spectroscopic investigations

In order to assess if the increase in reaction temperature leads to a change in the observed catalytic species, NMR spectra of the catalyst solution during a heating-up and subsequent cooling-down procedure were recorded. Hereby, both the defined complex **9** and the *in-situ* system based on the  $\text{Mn}(\text{CO})_5\text{Br}$  precursor plus additional HPNP<sup>Pr</sup> ligand were investigated.

### 3.3.4.2. Influence of reaction temperature on the defined Mn-catalyst

During the first experiment, the reaction solution containing 10 mM of the Mn-pincer complex was stepwise heated up to 90 °C and cooled down afterwards in a gas-tight NMR Schlenk tube (Figure 32). Generally, no new peaks appeared and also the ratio between the two existing peaks did not change significantly. When the temperature was increased to 70 °C, peaks for hydrogen and formate were detected (for details see Section 6.5.1.1. of the Appendix), which confirms that the methanol reforming proceeds beyond the very first step. The deterioration in the spectra's quality can be related to the increase in the signal-to-noise ratio caused by the growing rate of gas evolution.

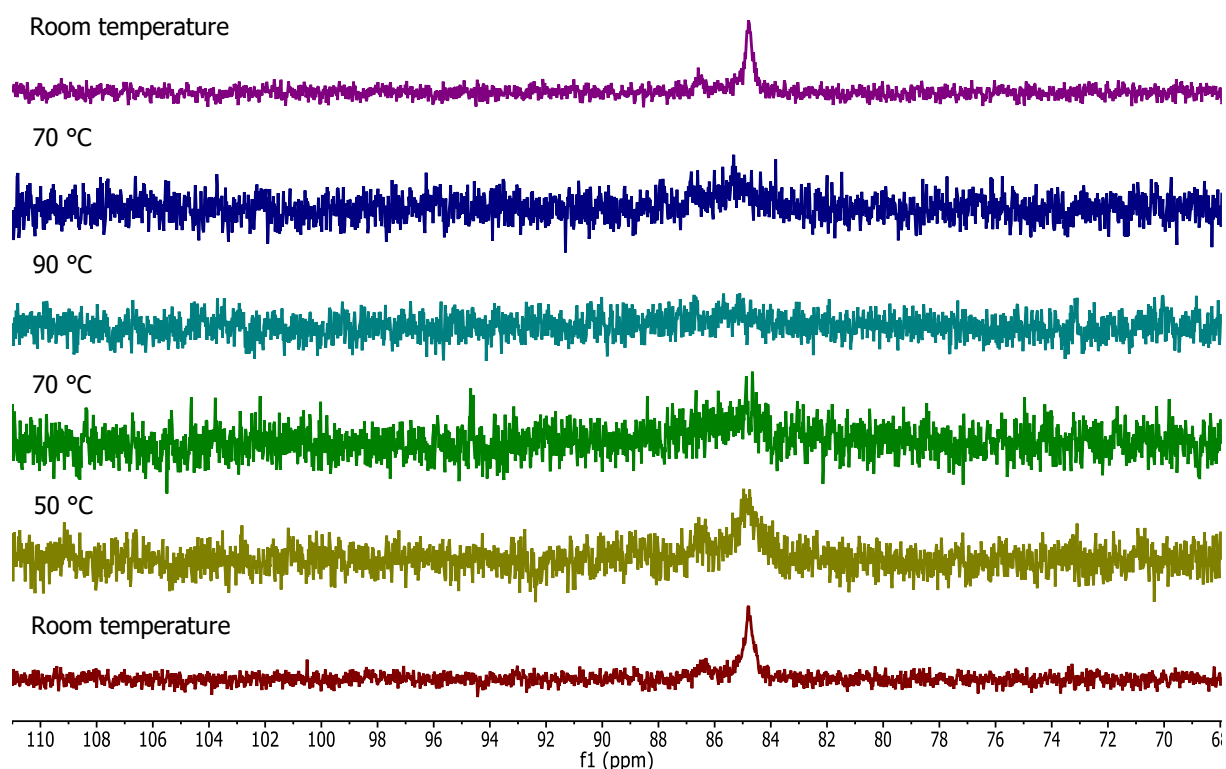


**Figure 32:** Influence of temperature on the active catalytic species of complex **9**.  $^{31}\text{P}$  NMR (varied temperature, 162 MHz, 9:1 MeOH:H<sub>2</sub>O, 8 M KOH, a few drops of MeOD- $d_4$ ). Reaction solution contains 24 mg (10mM) of catalyst **9**. Reaction solution was heated up in a gas-tight NMR vial in steps from room temperature to 50 °C, 70 °C and 90 °C and afterwards let cool down to 70 °C and back to room temperature.<sup>[168]</sup>

## Part II - Spectroscopic investigations

### 3.3.4.3. Influence of reaction temperature on the precursor $\text{Mn}(\text{CO})_5\text{Br}$

The analogous experiment was performed for the precursor  $\text{Mn}(\text{CO})_5\text{Br}$  and additional 10 eq. of the HPNPPr ligand, which were dissolved in the highly basic methanol-water reaction solution.

The main peaks detected were free and free oxidised HPNPPr ligand. Very interestingly, when reaching 70 °C, the formation of a peak at 84.84 ppm in the  $^{31}\text{P}$  NMR spectrum could be observed, which is analogous to the main peak of the dissolved defined catalyst in the reaction solution. At this temperature also peaks that could be assigned to formate and hydrogen, respectively, became visible in the  $^1\text{H}$  NMR spectrum (Figures 73 and 74 in the Section 6.5.1.1. of the Appendix). Due to the experimental setup, the temperature programme was stopped at that point to avoid higher rates of hydrogen gas evolution. Generally, the spectra for the *in-situ* system showed a significantly better signal-to-noise ratio compared to the spectra of the defined catalyst, which can be related to the lower amount of gas that was formed in case of the  $\text{Mn}(\text{CO})_5\text{Br}$  system.

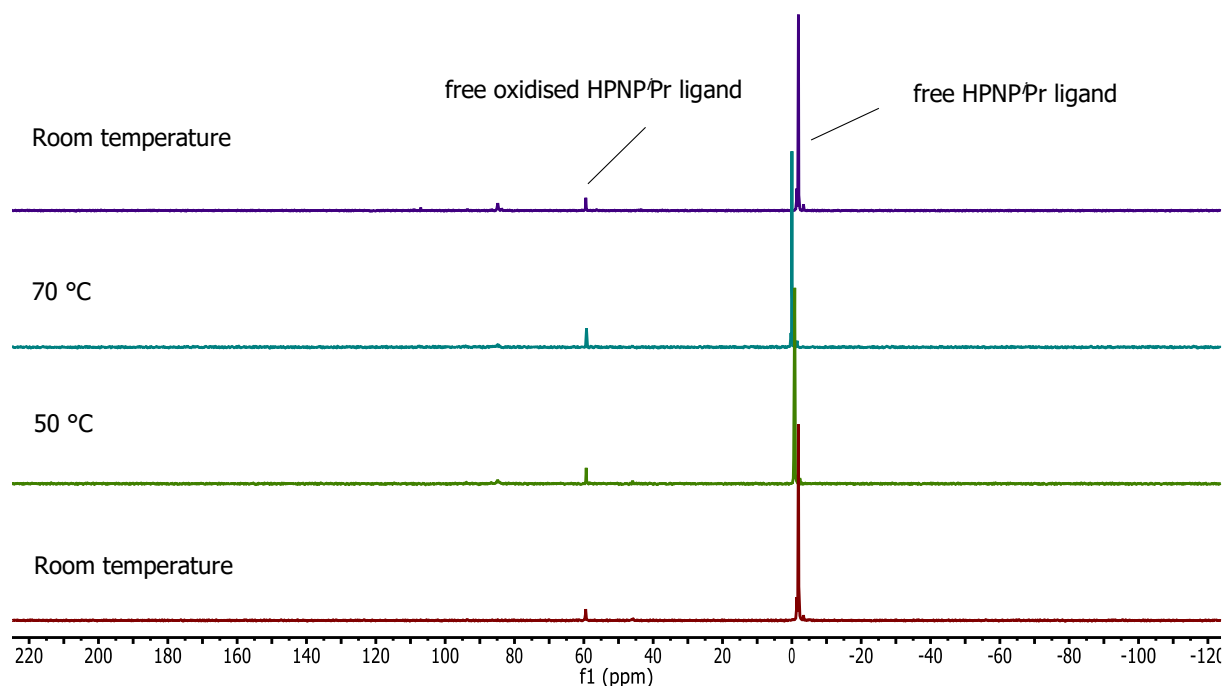


**Figure 33:** Influence of temperature on the active catalytic species of the *in-situ* system.  $^{31}\text{P}$  NMR (varied temperature, 162 MHz, 9:1 MeOH:H<sub>2</sub>O, 8 M KOH, a few drops of MeOD-d<sub>4</sub>). Reaction solution contains 24 mg of precursor  $\text{Mn}(\text{CO})_5\text{Br}$  + 10 eq. ligand. Reaction solution was heated up in a gas-tight NMR vial in steps from room temperature to 50 °C, 70 °C and 90 °C and afterwards let cool down to 70 °C and back to room temperature.<sup>[168]</sup>

To identify the species that were observed for the defined Mn-pincer system and the *in-situ* system, further *ex-situ* IR investigations under reaction conditions and stoichiometric NMR experiments were performed using the Mn-PNP catalyst **9**.



## Part II - Spectroscopic investigations

### 3.3.5. IR and NMR investigations on the defined Mn-catalyst **9**

The previously reported work by Elongovan et al. had shown that *ex-situ* IR experiments are a viable method for analysing related complexes of Mn-parent catalyst **9**.<sup>[160]</sup> For these measurements, reactions were performed with a significant higher catalyst loadings of 10 mM and samples of the reaction solution were taken in intervals, allowed to cool down and measured at room temperature. For details on the experimental procedure see the Section 6.5.2. of the Appendix.

#### 3.3.5.1. Influence of base on the catalytic species

Similar to the investigations performed for the Ru-PNP complex **1**, the influence of increasing amounts of base on the catalytic species of the manganese catalyst **9** was investigated in cooperation with Steffen Fischer. Hereby, the amount of KOH in the 9:1 MeOH:H<sub>2</sub>O solution containing **9** was stepwise raised and samples were measured by IR spectroscopy. Under the initial neutral conditions, two distinct bands at 1925 and 1843 cm<sup>-1</sup> were observed, which were assigned to the symmetric and asymmetric C-O frequencies of the starting complex **9**. Already the addition of 0.5 eq. of KOH led to the appearance of further bands at slightly lower wavenumbers (1910 and 1825 cm<sup>-1</sup>), which caused a broadening of the original bands. At 10 eq. of KOH full conversion to this new species was reached and the spectrum did not change even after the final concentration of 8 M KOH was obtained (see Figure 34).

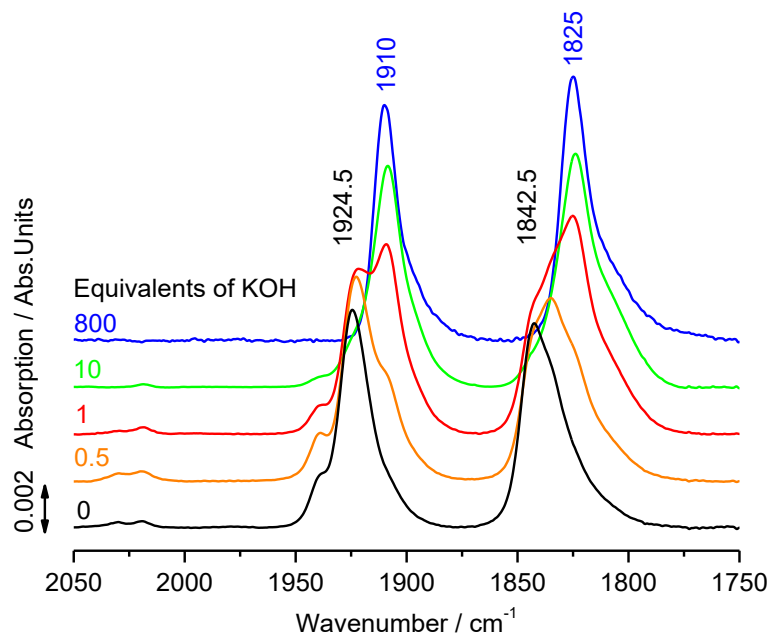


**Figure 34:** IR measurements of the active catalytic species in dependence on base molarity. Reaction conditions: MeOH:H<sub>2</sub>O (1 mL, ratio 9:1), **9** (10 μmol, 10 mM), room temperature.<sup>[168, 175]</sup>

The next step aimed to assign the observed bands to a specific catalytic species. This was hoped to achieve by performing stoichiometric NMR experiments and comparing NMR and IR spectra recorded under the same conditions. These NMR experiments were carried out by generating the

## Part II - Spectroscopic investigations

amido complex **11** from the original complex **9** by the addition of three equivalents of NaO*t*Bu in deuterated benzene. Subsequently, the amido species was reacted with methanol, water or formic acid to generate possible intermediates in the catalytic cycle such as the methoxide **21**, hydroxide **24** or formate **22** complexes (see Schemes 33 and 34).

### 3.3.5.2. Stoichiometric NMR studies

Addition of water to the *in-situ* generated amido complex led to the appearance of a peak at 86.74 ppm in the  $^{31}\text{P}$  NMR spectrum and confirmed that the minor peak observed in the NMR spectrum of the reaction solution containing pre-catalyst **9** (see Figure 31) can be attributed to the hydroxide species **24**. The slight low-field shift compared to the parent complex can be explained by the trans-effect of the hydroxide group.

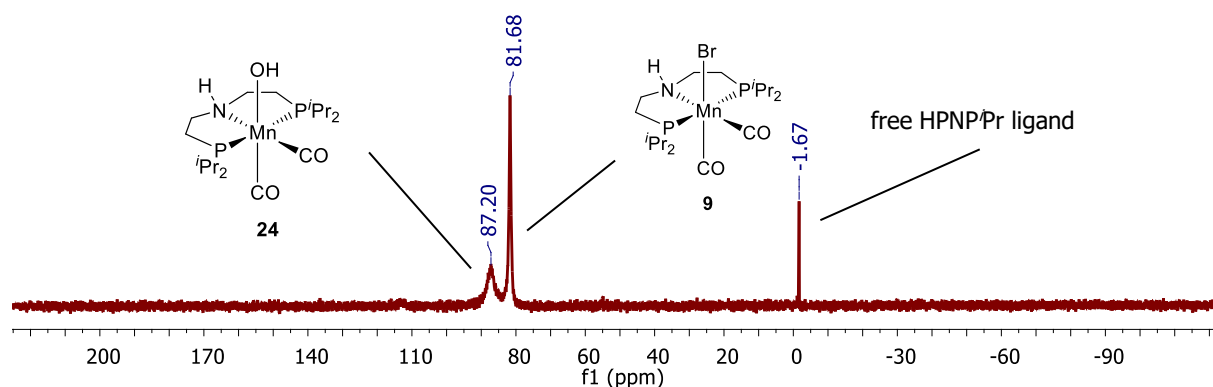


**Figure 35:** Addition of 10 eq. of  $\text{H}_2\text{O}$  to amido species **11**.  $^{31}\text{P}$  NMR (296 K, 121.5 MHz,  $\text{C}_6\text{D}_6$ ): The spectrum was recorded after stirring for 1 hour.<sup>[168]</sup>

The analogous experiments of adding methanol and formic acid resulted in the appearance of broad peaks in the  $^{31}\text{P}$  NMR with very similar chemical shifts of 84.97 ppm and 85.97 ppm, respectively, which are comparable to the shift of the major peak observed under reaction conditions (Figures 36 and 37).

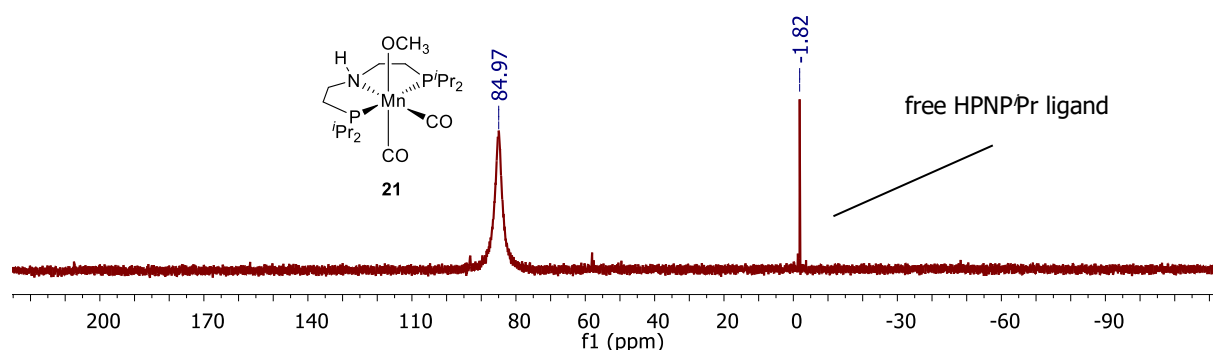


**Figure 36:** Addition of 10 eq. of MeOH to amido species **11**.  $^{31}\text{P}$  NMR (296 K, 121.5 MHz,  $\text{C}_6\text{D}_6$ ): The spectrum was recorded after stirring for 1 hour.<sup>[168]</sup>

## Part II - Spectroscopic investigations

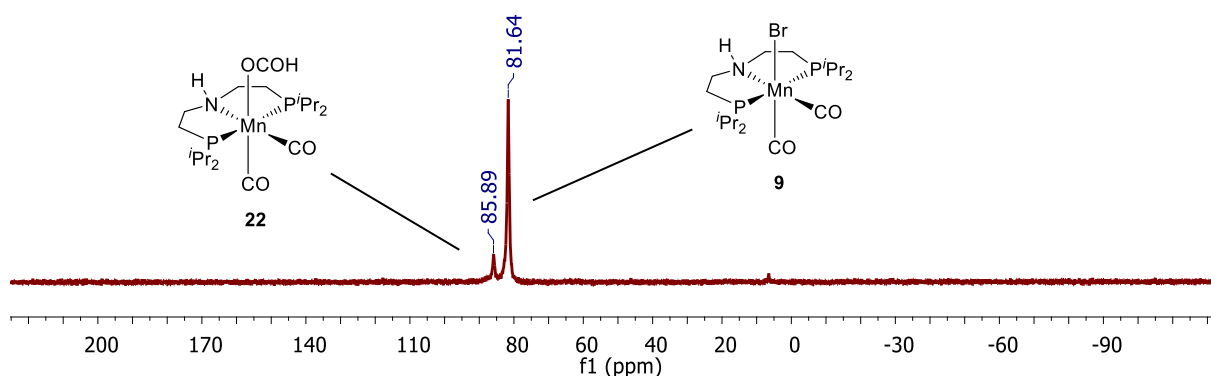


**Figure 37:** Addition of 10 eq. of formic acid to amido species **11**.  $^{31}\text{P}$  NMR (296 K, 121.5 MHz,  $\text{C}_6\text{D}_6$ ): The spectrum was recorded after stirring for 1 hour.<sup>[168]</sup>

In order to be able to unambiguously differentiate between the methoxide and formate complex, further NMR experiments were performed. Hereby,  $^{13}\text{C}$ -enriched methanol was added to the *in-situ* generated amido complex **11** leading to the appearance of a carbon signal at 26.56 ppm, which could be assigned to the  $-\text{OCH}_3$ -group of the Mn-methoxide complex **21**. In contrast, no signal in the low-field region of 170 ppm was detected, which was reported by Boncella and co-workers to belong to the Mn-formate complex **22**<sup>[165]</sup> (Figures 38 and 39). Unluckily, the attempt of correlating the signals arising from the dissolution of the Mn-pincer complex **9** in a basic methanol-water solution to this spectrum proved to be unsuccessful due to the complex's poor solubility: The low signal-to-noise ratio made it impossible to assign any  $^{13}\text{C}$  signals (Figure 40).

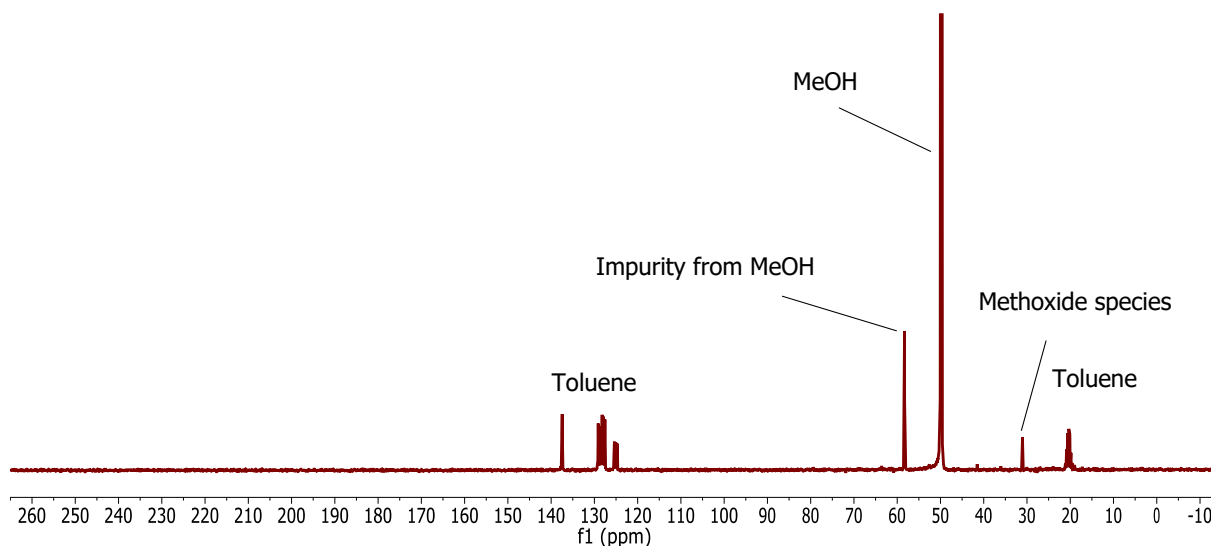


**Figure 38:**  $^{13}\text{C}$  NMR (296 K, 75.5 MHz, toluene- $\text{d}_8$ ). Addition of 10 eq. of  $^{13}\text{C}$ -MeOH to amido species **11**. Spectrum was recorded after stirring for 1 hour. The amido species was generated *in-situ* by adding 3 eq. of NaOtBu to the Mn complex **9**.

## Part II - Spectroscopic investigations

---

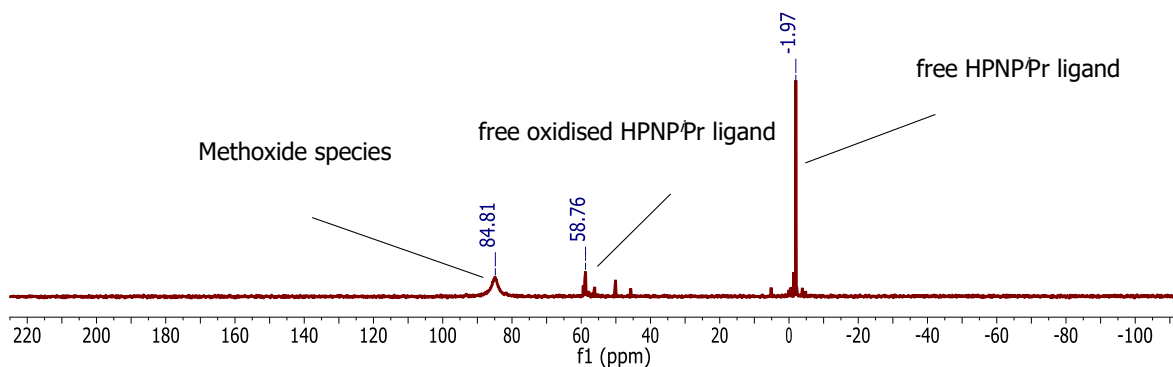


**Figure 39:** Addition of 10 eq. of  $^{13}\text{C}$ -MeOH to amido species **11**.  $^{31}\text{P}$  NMR (296 K, 75.5 MHz, toluene- $d_8$ ): Spectrum was recorded after stirring for 1 hour.

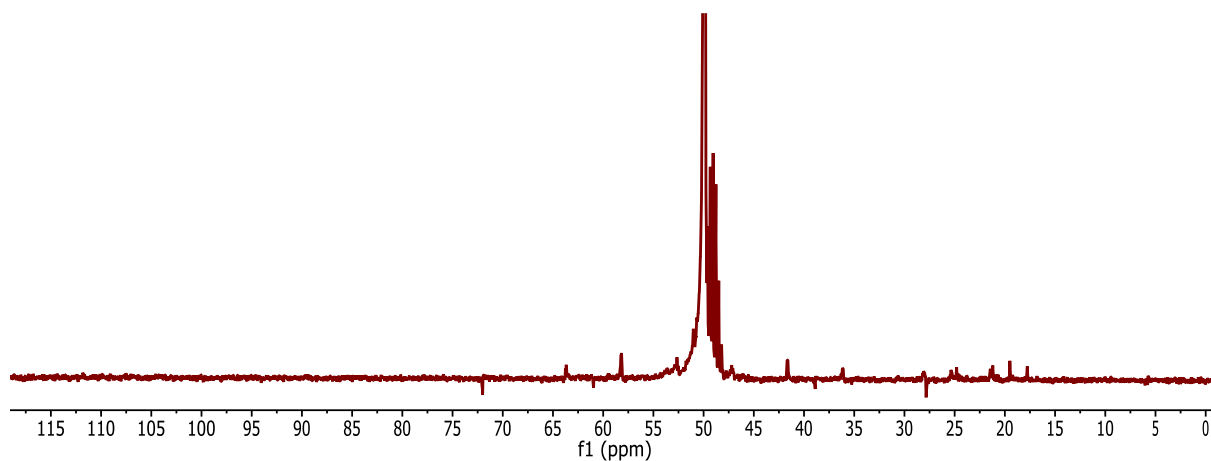


**Figure 40:** Dissolution of pre-catalyst **9** in a basic methanol-water solution.  $^{13}\text{C}$  NMR (296 K, 75.5 MHz, in 9:1 MeOH:H $_2$ O, additional drops of MeOD- $d_3$ ). Reaction solution containing 10 mM **9** and 2 M KOH.

Hence, it was not possible to clearly identify the main catalyst species that was observed in reaction solution by experimental means. However, the approach of comparing theoretical calculated IR bands of a number of possible catalytic intermediates to the measured IR spectrum proved to be futile. The results of these calculations are described in detail in the following section.

## Part II - Spectroscopic investigations

### 3.3.5.3. Theoretical calculations of the IR spectrum

Figures 41 and 42 show the results of the DFT-calculated IR spectra for a range of catalytic intermediates performed by Steffen Fischer. The calculated bands for the bromide species fit very well with the experimental observed bands that were assigned to belong to this species (see Figure 34). The bands of the other complexes, precisely the amido, methoxide, hydroxide, hydride, formate and the methoxide species, lie all in a very narrow range between 1925 and 1825  $\text{cm}^{-1}$ . The shift to lower wavenumbers when exchanging the bromide ligand by these ligands can be explained by the increased backdonation from the metal to the  $\pi$ -antibonding orbitals of the C-O bond as the latter are better  $\sigma$  donors.

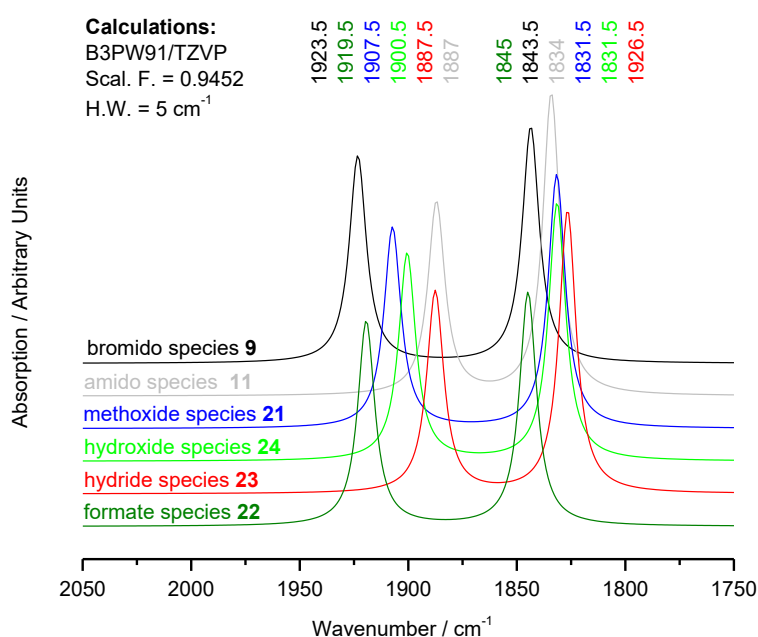


**Figure 41:** DFT-calculated IR spectra for a range of Mn species.<sup>[168, 176]</sup>

The question if the main species is the methoxide or the formate complex can be answered when extending the spectrum to wavenumbers up to 1500  $\text{cm}^{-1}$  (Figure 42): In this range, the formate complex shows a distinct band at approximately 1550  $\text{cm}^{-1}$ , which is related to the C-O frequency of the formate group. As this band was not observed during the IR experiment of adding stepwise KOH to the reaction solution, it can be deduced that the main species is indeed the methoxide complex.

The broad tailing of the bands at 1910 and 1825  $\text{cm}^{-1}$  observed in the IR spectrum of the reaction solution (Figure 34) can be very well explained by the appearance of the hydroxide complex as the minor species, since the shifts of the bands for this species fit extremely well the calculated absorption range.

## Part II - Spectroscopic investigations

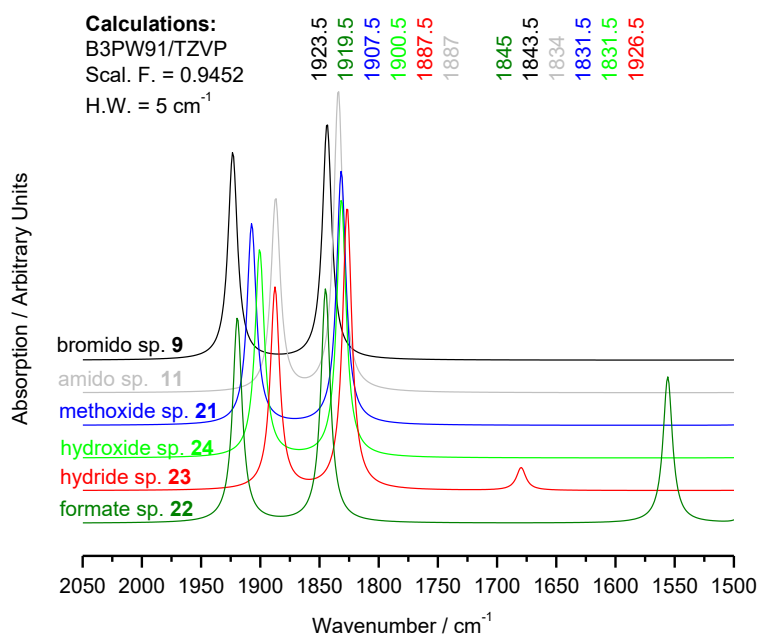


**Figure 42:** DFT-calculated IR spectra for a range of Mn species with an extended scaling of the x-axis up to 1500 cm<sup>-1</sup>.<sup>[168, 176]</sup>

Calculations were not only performed for the protonated species, but also for the anionic complexes, which gave very similar absorption bands. As the same highly basic protic conditions are used as for the Ru-pincer catalyst system, it is reasonable to assume that the active catalytic species are indeed deprotonated at the N-ligand backbone.

In the course of the analytical investigations described in this section, the anionic methoxide species **21**<sup>-</sup> was revealed to be the main resting state of the catalytic cycle. Furthermore, it was postulated that the hydroxide complex **24**<sup>-</sup> is very likely an off-cycle resting state. In contrast to the Ru-PNP catalyst, no hydride species was detected under reaction conditions.

Generally, the experiment investigating the influence of base on the catalytic species at room temperature resulted in a very clear IR spectrum with distinct bands in contrast to the NMR spectra obtained by the investigations performed under reaction conditions. Therefore, a further IR experiment was carried out in order to clarify the temperature influence on the active catalytic species, which is depicted in detail in the ensuing section.

## Part II - Spectroscopic investigations

### 3.3.5.4. Influence of temperature on the catalytic species

To clarify the temperature influence on the catalytic species, the reaction solution containing 10 mM of the manganese-pincer catalyst **9** was heated from room temperature to 90 °C (Figure 43) and samples were measured at intervals by IR spectroscopy in cooperation with Steffen Fischer.

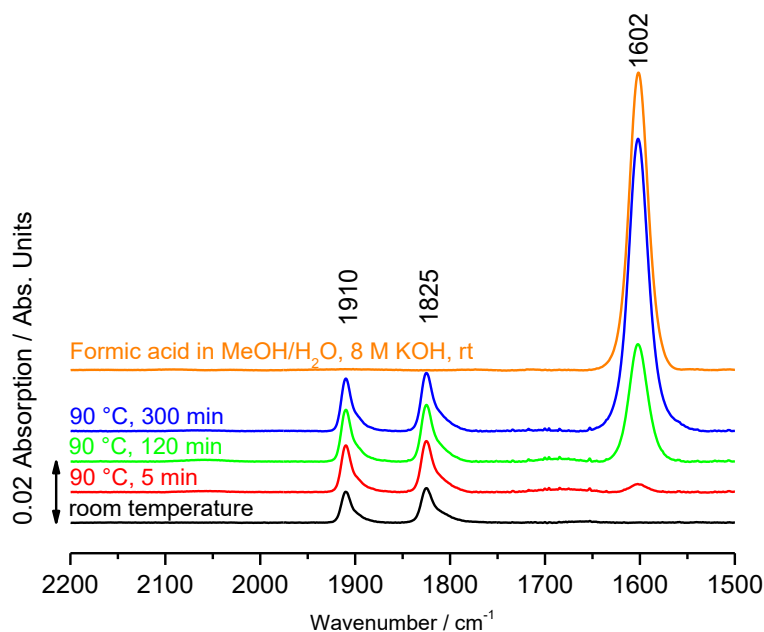


**Figure 43:** Reaction monitoring by IR. Reaction conditions: MeOH:H<sub>2</sub>O (10 mL, ratio 9:1), 8 M KOH, **9** (100 μmol, 10 mM), room temperature – 90°C.<sup>[168, 175]</sup>

As in the previous investigation, two bands at 1910 cm<sup>-1</sup> and 1825 cm<sup>-1</sup> were observed, whereby especially the latter showed a very broad tailing at lower wavenumbers. In accordance to the conclusions derived from the preceding measurements, the main bands were assigned to the anionic methoxide species **21**<sup>-</sup> and the minor bands hidden as tailing to the hydroxide species **24**<sup>-</sup>.

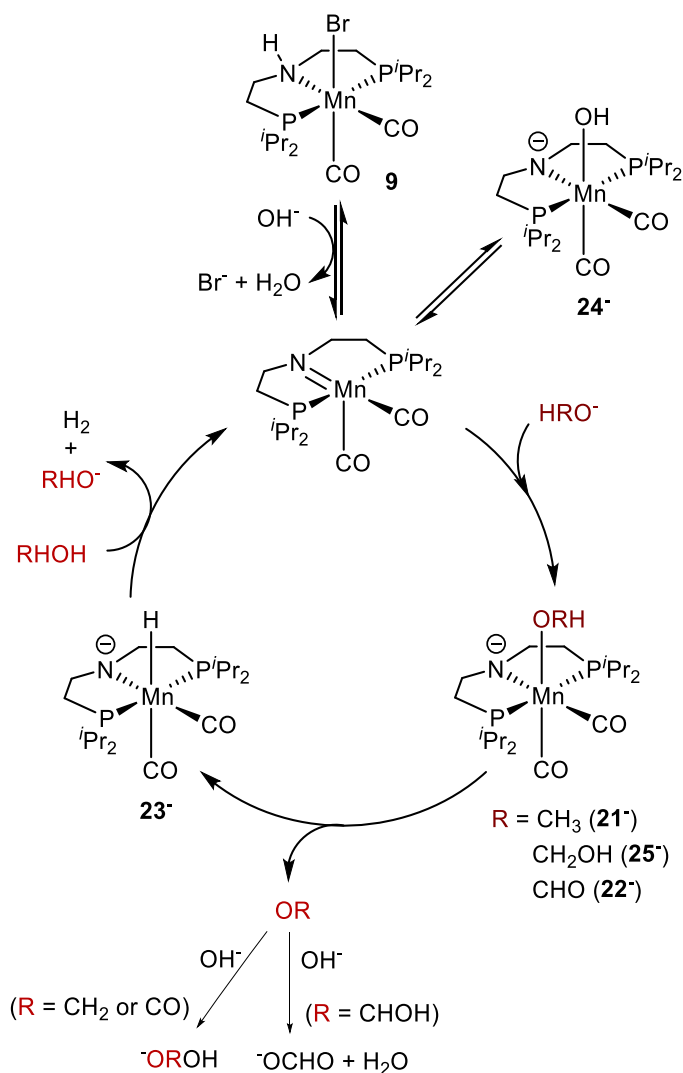
Additionally, a band at approximately 1600 cm<sup>-1</sup> was detected after the reaction solution had been heated to 90 °C for five minutes. It gradually increased during the progress of the reaction and at the end of the monitoring experiment its intensity was significantly higher compared to the bands assigned to the catalytic species. Accordingly, this band at low wave numbers was determined to belong to the intermediate product formate by adding formic acid to the basic reaction solution.

## Part II - Mechanistic proposal

### 3.3.6. Mechanistic proposal

Based on the results of the stoichiometric NMR experiments and *ex-situ* IR studies, and additional supporting DFT calculations, the mechanistic cycle shown in Scheme 34 could be proposed.

**Scheme 34:** Proposed mechanistic cycle for the complete dehydrogenation of methanol employing Mn-pincer complex **9**.



Initially, the active amido species **11** is generated by the base-mediated dehydrobromination of pre-catalyst **9** or by the dehydration of the off-cycle hydroxide complex **24<sup>-</sup>**. By coordination of methoxide, gem-diolate or formate, the anionic hydride species **21<sup>-</sup>**, **22<sup>-</sup>**, or **25<sup>-</sup>** are formed. They undergo the key C-H cleavage step to form formaldehyde, formic acid and  $\text{CO}_2$ , respectively, and the hydride species **23<sup>-</sup>**. Similar to the Ru-PNP catalyst system, the high base concentration ensues the sequestration of the formed products, which renders this process thermodynamically highly favourable. In the last step of the mechanistic cycle the hydride coordinated to the Mn-centre is protonated, which leads to the formation of hydrogen and the regeneration of the active catalyst.



## Part II - Dehydrogenation of further relevant substrates

### 3.3.7. Dehydrogenation of further relevant substrates

The attempt of determining the amount of carbon dioxide trapped as carbonate in the highly basic reaction solution at the end of the long-term reaction was not successful. This was probably due to the decomposition of the additional triglyme, which led to the formation of insoluble degradation products prior the release of CO<sub>2</sub>. Therefore, further dehydrogenation reactions of paraformaldehyde and formic acid were carried out by Maria Anderez-Fernandez in order to prove that complex **9** actively promotes hydrogen generation from these intermediate products of the full methanol dehydrogenation process. Furthermore, ethanol was chosen to be tested as an important C<sub>2</sub>-substrate.

**Table 3:** Dehydrogenation of C<sub>1</sub>- and C<sub>2</sub>-substrates with Mn complex **9**.<sup>[169-170]</sup>

Entry	Substrate	VH <sub>2</sub> (5h) [mL]	TON (5h)
1 <sup>[a]</sup>	EtOH	33	163
2 <sup>[b,d]</sup>	Paraformaldehyde	32	80
3 <sup>[c,d]</sup>	Formic acid	73	283

<sup>[a]</sup> Reaction cond.: EtOH/H<sub>2</sub>O (5 mL, ratio 9:1), KOH (0.04 mol, 8 M), **9** (8.4 μmol, 1.68 mM); T<sub>set</sub>: 92°C.

<sup>[b]</sup> Reaction cond.: *t*BuOH (36mL), H<sub>2</sub>O (4mL), KOH (0.05 M), paraformaldehyde (4 mmol, 0.1 M), **9** (16.72 μmol, 0.418 mM); T<sub>set</sub>: 81°C.

<sup>[c]</sup> Reaction cond.: PC (5mL), 11 mol FA/10 mol DMOA (5mL), **9** (5.3 μmol, 0.53 μM); T<sub>set</sub>: 60°C.

<sup>[d]</sup> Concomitant production of CO<sub>2</sub> (ratio H<sub>2</sub>/CO<sub>2</sub> 1:1, analysed by GC)

By the outcome of the experiments using optimised reaction protocols, it was demonstrated that the Mn catalyst **9** actively promoted the dehydrogenation of the tested C<sub>1</sub>- and C<sub>2</sub>-substrates. For ethanol as substrate the same conditions as for the methanol dehydrogenation were applied, which resulted in a TON of 163 after a reaction time of five hours (Table 3, entry 1). Dehydrogenation of paraformaldehyde in a slightly basic *t*BuOH solution at 81°C a TON of 80 was obtained (Table 3, entry 2). Following a formic acid dehydrogenation protocol<sup>[177]</sup>, which included the addition of DMOA as base, the manganese catalyst showed significantly higher activity, reaching a TON of 283 (Table 2, entry 3). When reacting formic acid with the Mn-amido complex **11**, Boncella and Tondreau<sup>[165]</sup> reported that dehydration occurred as non-negligible side reaction. In our case, no significant amount of carbon monoxide was detected in the gas phase, which would hint at the occurrence of the dehydration reaction.

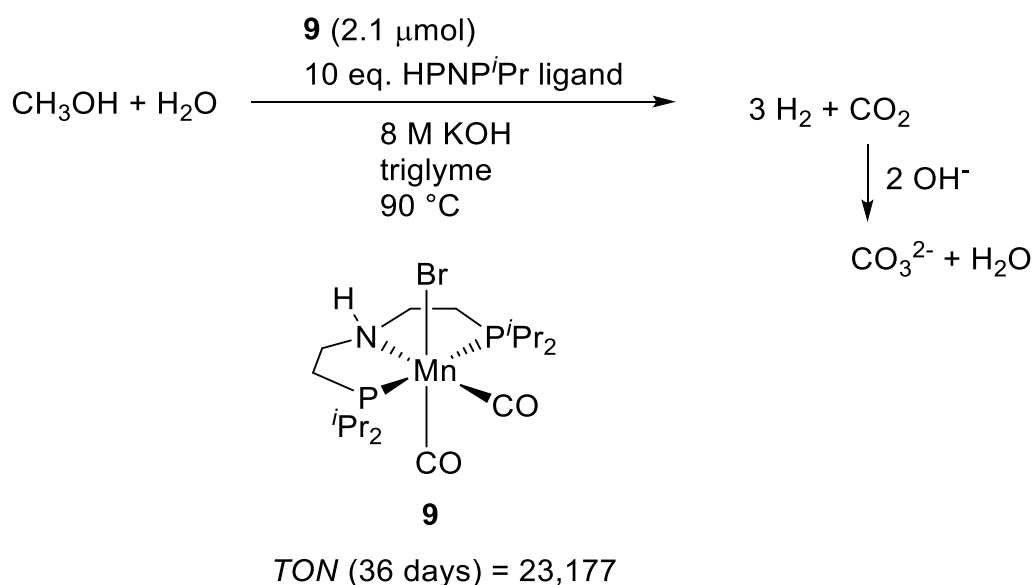
On the basis of these results, it was demonstrated that catalyst **9** shows good activity for the dehydrogenation of methanol, formaldehyde and formic acid and is thus generally able to promote the complete aqueous-phase reforming of methanol.

### 3.4. Summary and outlook for the manganese-catalysed dehydrogenation of methanol

In conclusion, it was shown for the first time that a pincer complex based on the easily available and non-toxic base metal manganese catalyses the aqueous-phase reforming of methanol. By combining methodology to optimise reaction parameters, long-term activity measurements and extensive analytical investigations, a highly stable catalyst system was developed. Furthermore, essential mechanistic aspects were elucidated, which are crucial in advancing specific catalyst designs tailored to the specific reaction conditions. The following summary gives an overview of the most essential points that were ascertained:

- Among a variety of different Mn-based catalysts, the Mn-PNP pincer catalyst **9** was identified to show significant activity for the methanol dehydrogenation under the basic reaction conditions adapted from the Ru-PNP catalyst system.
- A high sensitivity to light irradiation of this catalyst was noted, which could be ascribed to the light-triggered cleavage of the HPNP<sup>i</sup>Pr ligand.
- Optimization experiments showed that the combination of additional triglyme and 10 eq. of HPNP<sup>i</sup>Pr ligand caused a long-term stabilizing effect.
- Under these optimized conditions, an impressive TON of more than 20,000 was reached and catalyst **9** was still active after one month. This stability is even more remarkable, as the analogous iron-pincer complex already deactivated after five days.

**Scheme 35:** Optimised conditions for the methanol dehydrogenation using Mn catalyst **9**.



## Part II - Summary and outlook

---

- In contrast to the defined complex, the activity of the  $\text{Mn}(\text{CO})_5\text{Br}$  precursor plus additional HPNP<sup>t</sup>Pr ligand ceased after 300 hours.
- It was demonstrated that under the highly basic reaction conditions, the prevalent catalytic species are deprotonated analogous to the Ru-PNP catalyst complexes.
- Based on the combination of NMR and IR investigations and theoretical calculations, the anionic methoxide complex **21**<sup>-</sup> was identified to be one of the main catalytic species. Already by the addition of 10 equivalents of KOH, the pre-catalyst is converted and the methoxide and hydroxide species are formed, whereby the latter was determined to be an off-cycle intermediate.
- By the successful dehydrogenation of formaldehyde and formic acid, it was demonstrated that the Mn-catalyst **9** is generally able to promote the complete aqueous-phase reforming of methanol.

Generally, it can be concluded that these promising results show that a molecularly-defined non-noble metal catalyst can be successfully applied for the hydrogen generation from methanol. The manganese complex **9** is a good example for the very high stability and robustness of these types of catalysts, which is also of importance for future applications. Nevertheless, for practical purposes, the general activity still has to be improved.

The last point is one of the crucial aspects that are necessary to investigate further. Possible methods would be the synthesis of manganese catalysts with similar ligand scaffolds, which are as stable as this particular catalyst, but are more active and do not show sensitivity towards light irradiation. For reducing the amount of base, the efforts that are made for the Ru-PNP-catalyst-based system can be applied to the analogous Mn systems as well. A third option is the expansion of the catalyst scaffold to further non-noble metals, such as cobalt or nickel. Especially a range of recent reports of the successful implementation of cobalt-based catalysts for hydrogenation reactions render this base metal very promising.<sup>[178-179]</sup> Based on the concept of reversibility, it is very likely that these catalysts are also active for the dehydrogenation of methanol.

### 4. Conclusion and outlook

In the course of this PhD thesis, a thorough understanding of the essential mechanistic interactions for the most active catalyst system up to date for the homogeneously catalysed aqueous-phase reforming of methanol has been established. Furthermore, the range of non-noble-metal complexes employed for this type of reaction was extended by the first Mn-based catalyst.

Both of these accomplished objectives are important steps for the successful development and application of bifunctional catalysts for the hydrogen generation from methanol. These advances are not only relevant from the chemical perspective, but also when viewed in broader context: The dehydrogenation of chemical substrates, such as methanol, constitutes one decisive part in the overall model of an alternative energy system based on renewable energy sources and energy carriers as key means of storage.

This transition of our current, fossil-based to a renewable-based system is in progress and is accepted by the majority of people as an urgent topic that has to be dealt with in our modern times. To tackle "the single biggest challenge our civilization has ever had to face" (David King, UK Government's Chief Science Advisor until 2007), political, economic, scientific and social forces have to be combined to make the most possible advances in the period of time that is left before the point of no return has been reached. Hereby, the latest insights into the warming of the global oceans have shown that this point could be sooner than anticipated.

I am convinced that science has the power and the obligation to make an essential contribution to the solution of this global challenge and hope that our generation will actively take part in shaping the state we will leave the earth to our future descendants.

## Bibliography

---

### 5. Bibliography

- [1] Sustainable Development Goals, by The United Nations, <http://www.un.org/sustainabledevelopment/sustainable-development-goals> (accessed 2017-01-20).
- [2] B. Obama, *The Audacity of Hope: Thoughts on Reclaiming the American Dream*, Crown/Three Rivers Press, New York, **2006**.
- [3] J. A. Tainter, *Environmental Innovation and Societal Transitions* **2011**, *1*, 89–95.
- [4] C. Wilson, A. Grubler, *Lessons from the History of Technology and Global Change for the Emerging Clean Technology Cluster*, IIASA Interim Report, **2011**, <http://pure.iiasa.ac.at/9833>, (accessed 2017-01-05).
- [5] BP, *Statistical Review of World Energy*, **2015**, <http://www.bp.com/en/global/corporate/energy-economics/statistical-review-of-world-energy/2015-in-review.html>, (accessed 2017-01-05).
- [6] Three Gorges Corp. generates 191 bln kwh of electricity, by China News Service, <http://www.ecns.cn/business/2016/01-05/194619.shtml> (accessed 2017-01-07).
- [7] Three Gorges breaks world record for hydropower generation, by China News Service, [http://news.xinhuanet.com/english/china/2015-01/01/c\\_127352471.htm](http://news.xinhuanet.com/english/china/2015-01/01/c_127352471.htm) (accessed 2017-01-07).
- [8] K. S. Deffeyes, *Beyond Oil: The View from Hubbert's Peak*, Hill and Wang, New York, **2005**, pp. 1–224.
- [9] N. Armaroli, V. Balzani, *Angew. Chem. Int. Ed.* **2007**, *46*, 52–66.
- [10] S. Sorrell, *Renewable and Sustainable Energy Reviews* **2015**, *47*, 74–82.
- [11] A. Gasparatos, C. N. H. Doll, M. Esteban, A. Ahmed, T. A. Olang, *Renewable and Sustainable Energy Reviews* **2017**, *70*, 161–184.
- [12] N. Armaroli, V. Balzani, *Chemistry – An Asian Journal* **2011**, *6*, 768–784.
- [13] B. Obama, *Science* **2017**, 1–5.
- [14] *Energy production and storage: inorganic chemical strategies for a warming world*, R. H. Crabtree, Wiley-VCH, **2010**, pp. 1–2.
- [15] Monthly atmospheric carbon dioxide levels 1950 until today, by NASA's Jet Propulsion Laboratory, <http://climate.nasa.gov/vital-signs/carbon-dioxide> (accessed 2017-01-05).
- [16] Annual global land and ocean temperature anomalies, by NOAA National Centers for Environmental information, <https://www.ncdc.noaa.gov/cag/time-series/global> (accessed 2017-01-05).
- [17] *Fifth Assessment Report*, Intergovernmental panel on climate change **2009**, <http://www.ipcc.ch/report/ar5/index.shtml>, (accessed 2017-01-23).
- [18] *Climate Change Science - An Analysis of some Key Questions*, Committee on the Science of Climate Change, National Academy Press, Washington D.C., **2011**.
- [19] Paris Agreement, by United Nations Treaty Collection, [https://treaties.un.org/pages/ViewDetails.aspx?src=TREATY&mtdsg\\_no=XXVII-7-d&chapter=27&clang=\\_en](https://treaties.un.org/pages/ViewDetails.aspx?src=TREATY&mtdsg_no=XXVII-7-d&chapter=27&clang=_en) (accessed 2017-01-23).
- [20] World Energy Outlook Executive Summary 2010, by International Energy Agency, [www.worldenergyoutlook.org/media/weo2010.pdf](http://www.worldenergyoutlook.org/media/weo2010.pdf) (accessed 2017-01-23).
- [21] Capacity for renewable energy in India hits 42,850 mw; surpasses capacity of hydel projects by ET Bureau, <http://economictimes.indiatimes.com/industry/energy/power/capacity-for-renewable-energy-in-india-hits-42850-mw-surpasses-capacity-of-hydel-projects/articleshow/52680042.cms> (accessed 2016-01-23).
- [22] Projects, by the Energy Foundation China, <http://www.efchina.org/> (accessed 2017-01-23).
- [23] Gesetz für den Ausbau erneuerbarer Energien by Bundesministerium der Justiz und für Verbraucherschutz.
- [24] *Zeitreihen zur Entwicklung der erneuerbaren Energien in Deutschland*, Bundesministerium für Wirtschaft und Energie **2016**, [http://www.erneuerbare-energien.de/EE/Navigation/DE/Service/Erneuerbare\\_Energien\\_in\\_Zahlen/Zeitreihen/zeitreihen.html](http://www.erneuerbare-energien.de/EE/Navigation/DE/Service/Erneuerbare_Energien_in_Zahlen/Zeitreihen/zeitreihen.html) (accessed 2016-01-23).

## Bibliography

---

- [25] *Erneuerbare Energien. Systemtechnik, Wirtschaftlichkeit, Umweltaspekte.*, M. Kaltschmitt, W. Streicher, A. Wiese, Springer Vieweg, Berlin/Heidelberg, **2013**, pp. 47–138.
- [26] N. Armaroli, V. Balzani, *Energy Environ. Sci.* **2011**, *4*, 3193–3222.
- [27] G. Gahleitner, *Int. J. Hydrogen Energy* **2013**, *38*, 2039–2061.
- [28] G. A. Olah, A. Goepfert, G. K. S. Prakash, *Beyond Oil and Gas: The Methanol Economy*, Wiley-VCH, Weinheim, **2006**, pp. 133–134.
- [29] F. A. d. Bruijn, B. Rietveld, R. W. v. d. Brink, *Catalysis for Renewables*, Wiley-VCH, Weinheim, **2007**, pp. 299–336.
- [30] H. Zhang, P. K. Shen, *Chem. Rev.* **2012**, *112*, 2780–2832.
- [31] X.-Z. Yuan, H. Wang, *Handbook of Combustion, Vol. 1*, Wiley-VCH, Weinheim, **2010**, pp. 333–355.
- [32] S. Mekhilef, R. Saidur, A. Safari, *Renewable and Sustainable Energy Reviews* **2012**, *16*, 981–989.
- [33] N. Armaroli, V. Balzani, *ChemSusChem* **2011**, *4*, 21–36.
- [34] G. A. Olah, *Angew. Chem. Int. Ed.* **2005**, *44*, 2636–2639.
- [35] J. Emsley, *Nature's Building Blocks: An A-Z Guide to the Elements*, Second ed., Oxford University Press, New York, **2011**.
- [36] A. F. Dalebrook, W. Gan, M. Grasemann, S. Moret, G. Laurenczy, *Chem. Commun.* **2013**, *49*, 8735–8751.
- [37] U. Eberle, M. Felderhoff, F. Schüth, *Angew. Chem. Int. Ed.* **2009**, *48*, 6608–6630.
- [38] N. Brückner, K. Obesser, A. Bösmann, D. Teichmann, W. Arlt, J. Dungs, P. Wasserscheid, *ChemSusChem* **2014**, *7*, 229–235.
- [39] K. Müller, K. Stark, B. Müller, W. Arlt, *Energy & Fuels* **2012**, *26*, 3691–3696.
- [40] M. Yadav, Q. Xu, *Energy Environ. Sci.* **2012**, *5*, 9698–9725.
- [41] Y. Kim, E.-K. Lee, J.-H. Shim, Y. W. Cho, K. B. Yoon, *J. Alloys Compd.* **2006**, *422*, 283–287.
- [42] A. Remhof, O. Friedrichs, F. Buchter, P. Mauron, A. Züttel, D. Wallacher, *Phys. Chem. Chem. Phys.* **2008**, *10*, 5859–5862.
- [43] T. B. Marder, *Angew. Chem. Int. Ed.* **2007**, *46*, 8116–8118.
- [44] F. H. Stephens, V. Pons, R. Tom Baker, *Dalton Trans.* **2007**, 2613–2626.
- [45] R.-F. Lu, G. Boethius, S.-H. Wen, Y. Su, W.-Q. Deng, *Chem. Commun.* **2009**, 1751–1753.
- [46] A. Moores, M. Poyatos, Y. Luo, R. H. Crabtree, *New J. Chem.* **2006**, *30*, 1675–1678.
- [47] Y. Okada, E. Sasaki, E. Watanabe, S. Hyodo, H. Nishijima, *Int. J. Hydrogen Energy* **2006**, *31*, 1348–1356.
- [48] D. E. Schwarz, T. M. Cameron, P. J. Hay, B. L. Scott, W. Tumas, D. L. Thorn, *Chem. Commun.* **2005**, 5919–5921.
- [49] P. Makowski, A. Thomas, P. Kuhn, F. Goettmann, *Energy Environ. Sci.* **2009**, *2*, 480–490.
- [50] LOHC storage technologies, by hydrogenous technologies, <http://www.hydrogenous.net/de> (accessed 2017-01-23).
- [51] M. Markiewicz, Y. Q. Zhang, A. Bosmann, N. Bruckner, J. Thoming, P. Wasserscheid, S. Stolte, *Energy Environ. Sci.* **2015**, *8*, 1035–1045.
- [52] A. Boddien, F. Gärtner, M. Nielsen, S. Losse, H. Junge, in *Comprehensive Inorganic Chemistry II, Vol. 6*, Elsevier, Oxford, **2013**, pp. 587–588.
- [53] G. A. Olah, *Angew. Chem. Int. Ed.* **2013**, *52*, 104–107.
- [54] F. Asinger, *Methanol, Chemie- und Energierohstoff.*, Akademie-Verlag, Berlin, **1987**.
- [55] Icons made by Yannick Lung, Visual Pharm, Sergei Kokota and RNS Fonts. Retrieved from [www.flaticon.com](http://www.flaticon.com) (2016-12-05)
- [56] J. Han, I.-s. Kim, K.-S. Choi, *J. Power Sources* **2000**, *86*, 223–227.
- [57] P. J. de Wild, M. J. F. M. Verhaak, *Catal. Today* **2000**, *60*, 3–10.
- [58] J. Agrell, M. Boutonnet, I. Melián-Cabrera, J. L. G. Fierro, *Applied Catalysis A: General* **2003**, *253*, 201–211.
- [59] J. Agrell, M. Boutonnet, J. L. G. Fierro, *Applied Catalysis A: General* **2003**, *253*, 213–223.
- [60] D. R. Palo, R. A. Dagle, J. D. Holladay, *Chem. Rev.* **2007**, *107*, 3992–4021.
-

## Bibliography

---

- [61] *Membrane Reactors for Hydrogen Production Processes*, M. D. D. Falco, L. Marrelli, G. Iaquaniello, Springer Verlag, London, **2011**, pp. 3–5.
- [62] A. Iulianelli, P. Ribeirinha, A. Mendes, A. Basile, *Renewable and Sustainable Energy Reviews* **2014**, *29*, 355–368.
- [63] C.-Z. Yao, L.-C. Wang, Y.-M. Liu, G.-S. Wu, Y. Cao, W.-L. Dai, H.-Y. He, K.-N. Fan, *Applied Catalysis A: General* **2006**, *297*, 151–158.
- [64] H.-M. Yang, P.-H. Liao, *Applied Catalysis A: General* **2007**, *317*, 226–233.
- [65] R. D. Cortright, R. R. Davda, J. A. Dumesic, *Nature* **2002**, *418*, 964–967.
- [66] J. W. Shabaker, R. R. Davda, G. W. Huber, R. D. Cortright, J. A. Dumesic, *J. Catal.* **2003**, *215*, 344–352.
- [67] E. Furimsky, *Industrial & Engineering Chemistry Research* **2013**, *52*, 17695–17713.
- [68] G. W. Huber, J. A. Dumesic, *Catal. Today* **2006**, *111*, 119–132.
- [69] T. Nozawa, Y. Mizukoshi, A. Yoshida, S. Hikichi, S. Naito, *Int. J. Hydrogen Energy* **2017**, *42*, 168–176.
- [70] A. Tanksale, Y. Wong, J. N. Beltramini, G. Q. Lu, *Int. J. Hydrogen Energy* **2007**, *32*, 717–724.
- [71] M. B. Valenzuela, C. W. Jones, P. K. Agrawal, *Energy & Fuels* **2006**, *20*, 1744–1752.
- [72] G. Rothenberg, *Catalysis: Concepts and Green Applications*, Wiley-VCH, Weinheim, **2008**, pp. 10–12.
- [73] M. Nielsen, in *Hydrogen production and remediation of carbon and pollutants* (Eds.: E. Lichtfouse, J. Schwarzbauer, D. Robert), Springer, Heidelberg, **2015**, pp. 5–6.
- [74] C. Gunanathan, D. Milstein, *Science* **2013**, *341*, 249–262.
- [75] J. B. Arterburn, M. Pannala, A. M. Gonzalez, R. M. Chamberlin, *Tetrahedron Lett.* **2000**, *41*, 7847–7849.
- [76] J. S. M. Samec, J.-E. Bäckvall, P. G. Andersson, P. Brandt, *Chem. Soc. Rev.* **2006**, *35*, 237–248.
- [77] R. Cohen, C. R. Graves, S. T. Nguyen, J. M. L. Martin, M. A. Ratner, *J. Am. Chem. Soc.* **2004**, *126*, 14796–14803.
- [78] H. Grützmacher, *Angew. Chem. Int. Ed.* **2008**, *47*, 1814–1818.
- [79] K. Chernichenko, Á. Madarász, I. Pápai, M. Nieger, M. Leskelä, T. Repo, *Nat. Chem.* **2013**, *5*, 718–723.
- [80] D. W. Stephan, *Org. Biomol. Chem.* **2008**, *6*, 1535–1539.
- [81] H. Guan, M. Iimura, M. P. Magee, J. R. Norton, G. Zhu, *J. Am. Chem. Soc.* **2005**, *127*, 7805–7814.
- [82] R. M. Bullock, *Chem. Eur. J.* **2004**, *10*, 2366–2374.
- [83] M. P. Magee, J. R. Norton, *J. Am. Chem. Soc.* **2001**, *123*, 1778–1779.
- [84] K. Rossen, *Angew. Chem. Int. Ed.* **2001**, *40*, 4611–4613.
- [85] M. D. Fryzuk, P. A. MacNeil, *Organometallics* **1983**, *2*, 355–356.
- [86] M. D. Fryzuk, P. A. MacNeil, S. J. Rettig, *J. Am. Chem. Soc.* **1987**, *109*, 2803–2812.
- [87] Y. Blum, Y. Shvo, *J. Organomet. Chem.* **1985**, *282*, C7–C10.
- [88] M. Yamakawa, H. Ito, R. Noyori, *J. Am. Chem. Soc.* **2000**, *122*, 1466–1478.
- [89] K.-J. Haack, S. Hashiguchi, A. Fujii, T. Ikariya, R. Noyori, *Angew. Chem. Int. Ed.* **1997**, *36*, 285–288.
- [90] R. Noyori, M. Yamakawa, S. Hashiguchi, *J. Org. Chem.* **2001**, *66*, 7931–7944.
- [91] H. B. Charman, *J. Chem. Soc. B* **1970**, *584*, 584–587.
- [92] H. B. Charman, *Nature* **1966**, *212*, 278–279.
- [93] H. B. Charman, *Journal of the Chemical Society B: Physical Organic* **1967**, 629–632.
- [94] A. Dobson, S. D. Robinson, *Inorg. Chem.* **1977**, *16*, 137–142.
- [95] D. J. Cole-Hamilton, D. Morton, I. Utuk, M. Paneque-Sosa, M. Lopez-Poveda, *J. Chem. Soc. Dalton Trans.* **1989**, *489*, 489–495.
- [96] D. Morton, D. J. Cole-Hamilton, *J. Chem. Soc. Chem. Commun* **1988**, 1154–1156.
- [97] J. Zhang, M. Gandelman, L. J. W. Shimon, H. Rozenberg, D. Milstein, *Organometallics* **2004**, *23*, 4026–4033.
-

## Bibliography

---

- [98] K. J. Szabo, in *Organometallic Pincer Chemistry, Vol. 40* (Eds.: G. v. Koten, D. Milstein), Springer Verlag, Berlin Heidelberg, **2013**, p. 204.
- [99] J. Zhang, G. Leitus, Y. Ben-David, D. Milstein, *J. Am. Chem. Soc.* **2005**, *127*, 10840–10841.
- [100] E. Balaraman, E. Khaskin, G. Leitus, D. Milstein, *Nat. Chem.* **2013**, *5*, 122–125.
- [101] M. Kass, A. Friedrich, M. Drees, S. Schneider, *Angew. Chem. Int. Ed.* **2009**, *48*, 905–907.
- [102] M. Nielsen, A. Kammer, D. Cozzula, H. Junge, S. Gladiali, M. Beller, *Angew. Chem. Int. Ed.* **2011**, *50*, 9593–9597.
- [103] M. Nielsen, E. Alberico, W. Baumann, H. J. Drexler, H. Junge, S. Gladiali, M. Beller, *Nature* **2013**, *495*, 85–90.
- [104] R. E. Rodríguez-Lugo, M. Trincado, M. Vogt, F. Tewes, G. Santiso-Quinones, H. Grützmacher, *Nat. Chem.* **2013**, *5*, 342–347.
- [105] E. Alberico, P. Sponholz, C. Cordes, M. Nielsen, H.-J. Drexler, W. Baumann, H. Junge, M. Beller, *Angew. Chem. Int. Ed.* **2013**, *52*, 14162–14166.
- [106] E. A. Bielinski, M. Förster, Y. Zhang, W. H. Bernskoetter, N. Hazari, M. C. Holthausen, *ACS Catal.* **2015**, 2404–2415.
- [107] J. Campos, L. S. Sharninghausen, M. G. Manas, R. H. Crabtree, *Inorg. Chem.* **2015**, 5079–5084.
- [108] K.-i. Fujita, R. Kawahara, T. Aikawa, R. Yamaguchi, *Angew. Chem. Int. Ed.* **2015**, *54*, 9057–9060.
- [109] L. E. Heim, D. Thiel, C. Gedig, J. Deska, M. H. G. Prechtel, *Angew. Chem. Int. Ed.* **2015**, *54*, 10308–10312.
- [110] P. Hu, Y. Diskin-Posner, Y. Ben-David, D. Milstein, *ACS Catal.* **2014**, 2649–2652.
- [111] A. Monney, E. Barsch, P. Sponholz, H. Junge, R. Ludwig, M. Beller, *Chem. Commun.* **2014**, *50*, 707–709.
- [112] X. Yang, *ACS Catal.* **2014**, *4*, 1129–1133.
- [113] M. Lei, Y. Pan, X. Ma, *Eur. J. Inorg. Chem.* **2015**, *2015*, 794–803.
- [114] The results described in this section of the thesis are based on the work published by E. Alberico, A. J. J. Lennox, L. K. Vogt et al. in *J. Am. Chem. Soc.* **2016**, *138*, 14890–14904.
- [115] The results described in this section were performed by L. K. Vogt in the course of her master's thesis. For experimental details the reader is kindly referred to this work.
- [116] M. Perez, S. Elangovan, A. Spannenberg, K. Junge, M. Beller, *ChemSusChem* **2017**, *10*, 83–86.
- [117] A. N. Marziale, A. Friedrich, I. Klopsch, M. Drees, V. R. Celinski, J. Schmedt auf der Günne, S. Schneider, *J. Am. Chem. Soc.* **2013**, *135*, 13342–13355.
- [118] This figure is taken from the work published by E. Alberico, A. J. J. Lennox, L. K. Vogt et al. in *J. Am. Chem. Soc.* **2016**, *138*, 14890–14904.
- [119] M. S. Gomez-Gallego, M.A., *Chem. Rev.* **2011**, *111*, 4857–4963.
- [120] D. A. Dougherty, E. V. Anslyn, *Modern Physical Organic Chemistry* University Science Books, Sausalito, California, **2006**, pp. 421–430.
- [121] S. Werkmeister, K. Junge, B. Wendt, E. Alberico, H. Jiao, W. Baumann, H. Junge, F. Gallou, M. Beller, *Angew. Chem. Int. Ed.* **2014**, 8722–8726.
- [122] L. Zhang, G. Raffa, D. H. Nguyen, Y. Swesi, L. Corbel-Demilly, F. Capet, X. Trivelli, S. Desset, S. Paul, J.-F. Paul, P. Fongarland, F. Dumeignil, R. M. Gauvin, *J. Catal.* **2016**, *340*, 331–343.
- [123] D. Spasyuk, D. G. Gusev, *Organometallics* **2012**, *31*, 5239–5242.
- [124] The results of the stoichiometric NMR investigations shown in this section (except Figure 12) are based on the work performed by Elisabetta Alberico.
- [125] R. B. Jordan, *Mechanismen anorganischer und metallorganischer Reaktionen*, C. Elschenbroich, F. Hensel, H. Hopf, Teubner Studienbücher, Stuttgart, **1994**, pp. 59–60.
- [126] M. Besora, A. Lledos, F. Maseras, *Chem. Soc. Rev.* **2009**, *38*, 957–966.
- [127] The results of the theoretical calculations shown in this scheme are based on the work performed by Haijun Jiao.
- [128] This scheme is taken from the work published by E. Alberico, A. J. J. Lennox, L. K. Vogt et al. in *J. Am. Chem. Soc.* **2016**, *138*, 14890–14904.
-



## Bibliography

---

- [129] The proton affinity (PA) of each complex was calculated and compared to a calibration curve that was populated with known pK<sub>a</sub>s and calculated PAs.
- [130] E. C. Ashby, F. Doctorovich, C. L. Liotta, H. M. Neumann, E. K. Barefield, A. Konda, K. Zhang, J. Hurley, D. D. Siemer, *J. Am. Chem. Soc.* **1993**, *115*, 1171–1173.
- [131] S. Kapoor, F. A. Barnabas, M. C. Sauer, D. Meisel, C. D. Jonah, *The Journal of Physical Chemistry* **1995**, *99*, 6857–6863.
- [132] The results described in this section of the thesis are based on the work published by V. Strobel, J. J. Schuster, A. S. Braeuer, L. K. Vogt, H. Junge, M. Haumann, *React. Chem. Eng.*, **2017**, Accepted Manuscript. Experiments were performed by V. Strobel.
- [133] This scheme is taken from the work published by V. Strobel, J. J. Schuster, A. S. Braeuer, L. K. Vogt, H. Junge, M. Haumann, *React. Chem. Eng.*, **2017**, Accepted Manuscript.
- [134] A. Wokaun, *B. Schrader: Infrared and Raman Spectroscopy - Methods and Applications, Vol. 100*, Wiley-VCH, Weinheim, **1996**.
- [135] This figure is taken from the work published by V. Strobel, J. J. Schuster, A. S. Braeuer, L. K. Vogt, H. Junge, M. Haumann, *React. Chem. Eng.*, **2017**, Accepted Manuscript.
- [136] O. Blum, D. Milstein, *J. Organomet. Chem.* **2000**, *593–594*, 479–484.
- [137] T. Zell, B. Butschke, Y. Ben-David, D. Milstein, *Chem. Eur. J.* **2013**, *19*, 8068–8072.
- [138] The results of the theoretical calculations shown in this figure are based on the work performed by Haijun Jiao.
- [139] The results of the stoichiometric NMR investigations shown in this section are based on the work performed by Elisabetta Alberico.
- [140] A. Friedrich, M. Drees, J. Schmedt auf der Günne, S. Schneider, *J. Am. Chem. Soc.* **2009**, *131*, 17552–17553.
- [141] L. Canovese, F. Visentin, G. Chessa, P. Uguagliati, C. Santo, G. Bandoli, L. Maini, *Organometallics* **2003**, *22*, 3230–3238.
- [142] A. Choualeb, A. J. Lough, D. G. Gusev, *Organometallics* **2007**, *26*, 5224–5229.
- [143] G. R. Fulmer, W. Kaminsky, R. A. Kemp, K. I. Goldberg, *Organometallics* **2011**, *30*, 1627–1636.
- [144] R. Lindner, B. van den Bosch, M. Lutz, J. N. H. Reek, J. I. van der Vlugt, *Organometallics* **2011**, *30*, 499–510.
- [145] D. Meyerstein, *Coord. Chem. Rev.* **1999**, *185–186*, 141–147.
- [146] G. L. Moxham, H. Randell-Sly, S. K. Brayshaw, A. S. Weller, M. C. Willis, *Chem. Eur. J.* **2008**, *14*, 8383–8397.
- [147] D. Vuzman, E. Poverenov, L. J. W. Shimon, Y. Diskin-Posner, D. Milstein, *Organometallics* **2008**, *27*, 2627–2634.
- [148] C.-Q. Zhao, M. C. Jennings, R. J. Puddephatt, *Dalton Trans.* **2008**, 1243–1250.
- [149] J. F. Hull, Y. Himeda, W.-H. Wang, B. Hashiguchi, R. Periana, D. J. Szalda, J. T. Muckerman, E. Fujita, *Nat. Chem.* **2012**, *4*, 383–388.
- [150] J. Kothandaraman, M. Czaun, A. Goeppert, R. Haiges, J.-P. Jones, R. B. May, G. K. S. Prakash, G. A. Olah, *ChemSusChem* **2015**, *8*, 1442–1451.
- [151] K. Sordakis, A. Tsurusaki, M. Iguchi, H. Kawanami, Y. Himeda, G. Laurenczy, *Chem. Eur. J.* **2016**, *22*, 15605–15608.
- [152] A. Thevenon, E. Frost-Pennington, G. Weijia, A. F. Dalebrook, G. Laurenczy, *ChemCatChem* **2014**, *6*, 3146–3152.
- [153] E. A. Bielinski, P. O. Lagaditis, Y. Zhang, B. Q. Mercado, C. Würtele, W. H. Bernskoetter, N. Hazari, S. Schneider, *J. Am. Chem. Soc.* **2014**, 10234–10237.
- [154] R. J. Gritter, G. D. Dupre, T. J. Wallace, *Nature* **1964**, *202*, 179–181.
- [155] G. Wu, Y. Gao, F. Ma, B. Zheng, L. Liu, H. Sun, W. Wu, *Chem. Eng. J.* **2015**, *271*, 14–22.
- [156] D. W. Christianson, *Prog. Biophys. Mol. Biol.* **1997**, *67*, 217–252.
- [157] K. Wieghardt, *Angew. Chem. Int. Ed.* **1989**, *28*, 1153–1172.
- [158] H. Hasan, *Manganese*, The Rosen Publishing Group, New York, **2008**.
-

## Bibliography

---

- [159] S. E. Olsen, M. Tangstand, T. Lindstad, *Production of Manganese Ferroalloys*, Tapir Akademisk Forlag, Trondheim, **2007**, p. 15.
- [160] S. Elangovan, C. Topf, S. Fischer, H. Jiao, A. Spannenberg, W. Baumann, R. Ludwig, K. Junge, M. Beller, *J. Am. Chem. Soc.* **2016**, *138*, 8809–8814.
- [161] M. Mastalir, M. Glatz, N. Gorgas, B. Stöger, E. Pittenauer, G. Allmaier, L. F. Veiros, K. Kirchner, *Chem. Eur. J.* **2016**, *22*, 12316–12320.
- [162] A. Mukherjee, A. Nerush, G. Leitus, L. J. W. Shimon, Y. Ben David, N. A. Espinosa Jalapa, D. Milstein, *J. Am. Chem. Soc.* **2016**, *138*, 4298–4301.
- [163] M. Perez, S. Elangovan, A. Spannenberg, K. Junge, M. Beller, *ChemSusChem* **2016**, 83–86.
- [164] A. M. Tondreau, J. M. Boncella, *Polyhedron* **2016**, *116*, 96–104.
- [165] A. M. Tondreau, J. M. Boncella, *Organometallics* **2016**, *35*, 2049–2052.
- [166] J. Neumann, S. Elangovan, A. Spannenberg, K. Junge, M. Beller, *Chem. Eur. J.* **2017**, doi: 10.1002/anie.201610182.
- [167] The results described in this section of the thesis are based on the work published by M. Anderez-Fernandez, L. K. Vogt S. Fischer et al. in *Angew. Chem. Int. Ed.* **2017**, *56*, 559–562.
- [168] This figure is taken from the work published by M. Anderez-Fernandez, L. K. Vogt S. Fischer et al. in *Angew. Chem. Int. Ed.* **2017**, *56*, 559–562.
- [169] The results shown in this table are based on the work performed by M. Anderez-Fernandez.
- [170] This table is taken from the work published by M. Anderez-Fernandez, L. K. Vogt S. Fischer et al. in *Angew. Chem. Int. Ed.* **2017**, *56*, 559–562.
- [171] The results shown in this figure are based on the work performed by M. Anderez-Fernandez.
- [172] The results shown in this figure are based on the work performed by M. Anderez-Fernandez and Wei Zhou.
- [173] A. Boddien, B. Loges, H. Junge, F. Gärtner, J. R. Noyes, M. Beller, *Adv. Synth. Catal.* **2009**, *351*, 2517–2520.
- [174] A. Boddien, F. Gartner, R. Jackstell, H. Junge, A. Spannenberg, W. Baumann, R. Ludwig, M. Beller, *Angew. Chem. Int. Ed.* **2010**, *49*, 8993–8996.
- [175] The results shown in this figure are based on the work performed in cooperation with Steffen Fischer.
- [176] The results of the theoretical calculations shown in this figure are based on the work performed by Steffen Fischer.
- [177] S. Enthaler, A. Brück, A. Kammer, H. Junge, E. Irran, S. Gülak, *ChemCatChem* **2015**, *7*, 65–69.
- [178] T. J. Korstanje, J. Ivar van der Vlugt, C. J. Elsevier, B. de Bruin, *Science* **2015**, *350*, 298–302.
- [179] A. Z. Spentzos, C. L. Barnes, W. H. Bernskoetter, *Inorg. Chem.* **2016**, *55*, 8225–8233.
- [180] E. Alberico, A. J. J. Lennox, L. K. Vogt, H. Jiao, W. Baumann, H.-J. Drexler, M. Nielsen, A. Spannenberg, M. P. Checinski, H. Junge, M. Beller, *J. Am. Chem. Soc.* **2016**, *138*, 14890–14904.
- [181] The results shown in this table are based on the work performed by Elisabetta Alberico.
- [182] The results shown in this figure are based on the work performed by Elisabetta Alberico.
- [183] S. K. Luther, J. J. Schuster, A. Leipertz, A. Braeuer, *The Journal of Supercritical Fluids* **2013**, *84*, 146–154.
- [184] The results of the theoretical calculations explained in this section are based on the work performed by Haijun Jiao.
- [185] The results of the theoretical calculations explained in this section are based on the work performed by Steffen Fischer.
-

## Appendix

---

### 6. Appendix

<b>6. APPENDIX.....</b>	<b>I</b>
6.1. TECHNIQUES, SOLVENTS AND REAGENTS .....	II
6.2. ANALYTICAL METHODS .....	III
6.2.1. <i>NMR spectroscopy</i> .....	III
6.2.2. <i>IR spectroscopy</i> .....	III
6.2.3. <i>Elemental analysis</i> .....	III
6.2.4. <i>Mass spectrometry</i> .....	III
6.2.5. <i>Gas chromatography</i> .....	III
6.3. GENERAL EXPERIMENTAL DETAILS .....	IX
6.3.1. <i>Measurements of catalytic activity</i> .....	IX
6.4. PART I: RUTHENIUM-CATALYSED DEHYDROGENATION OF METHANOL .....	XIV
6.4.1. <i>Investigations for catalyst <b>1</b></i> .....	XIV
6.4.2. <i>Investigations for catalyst <b>Me-1</b></i> .....	XXVIII
6.4.3. <i>Preliminary tests</i> .....	XXX
6.4.4. <i>Details on theoretical calculations</i> .....	XXXII
6.5. PART II: MANGANESE-CATALYSED DEHYDROGENATION OF METHANOL .....	XXXIV
6.5.1. <i>Preliminary tests</i> .....	XXXIV
6.5.2. <i>Dilution effects</i> .....	XXXV
6.5.1. <i>NMR investigations</i> .....	XXXVI
6.5.2. <i>Details on performed IR experiments</i> .....	XXXVII
6.5.3. <i>Computational studies</i> .....	XXXVIII

## Appendix

---

Some parts of the experimental details described in the appendix are obtained from the work published by E. Alberico, A. J. J. Lennox, L. K. Vogt, H. Jiao, W. Baumann, H.-J. Drexler, M. Nielsen, A. Spannenberg, M. P. Checinski, H. Junge and M. Beller in *J. Am. Chem. Soc.* **2016**, *138*, 14890–14904, from the work published by M. Anderez-Fernandez, L. K. Vogt, S. Fischer, W. Zhou, H. Jiao, M. Garbe, S. Elangovan, K. Junge, H. Junge, R. Ludwig, M. Beller, *Angew. Chem. Int. Ed.* **2017**, *56*, 559–562 and the work published by V. Strobel, J. J. Schuster, A. S. Braeuer, L. K. Vogt, H. Junge and M. Haumann in *React. Chem. Eng.*, **2017**, which was accepted as manuscript at the time of finishing this thesis. For details that are beyond the limit of this appendix, the reader is kindly referred to these works.

### 6.1. Techniques, solvents and reagents

All reactions were performed under argon atmosphere with exclusion of air using standard Schlenk techniques. Formic acid (FA), N,N-dimethyl-n-octylamine (DMOA), propylene carbonate (PC), dioxane, tert-amyl alcohol, and triglyme were refluxed and distilled following standard procedures and stored under argon atmosphere. Heptane, toluene, tetrahydrofuran (THF), diethylether, EtOH and MeOH were dried by passing through a column of anhydrous alumina using a solvent purification system equipment from *Innovative Technology* and stored under argon atmosphere. Water was degassed by bubbling argon overnight. Deuterated organic solvents were distilled over Na/benzophenone ketyl (THF-d<sub>8</sub>, C<sub>6</sub>D<sub>6</sub> and toluene-d<sub>8</sub>) or CaH<sub>2</sub> (CD<sub>2</sub>Cl<sub>2</sub>). CD<sub>3</sub>OD and CD<sub>3</sub>OH were used as received and stored under argon. KOH and LiOH were used and stored as received.

The following substances were purchased from various suppliers and were stored under argon atmosphere:

- n-Butyllithium solution, 2.5 M in hexanes (Sigma-Aldrich)
- Bis-2-chloroethyl amine hydrochloride (Alfa Aesar)
- N-methyl-bis-2 chloroethyl amine hydrochloride (Sigma-Aldrich)
- Diisopropylphosphine, 10 wt% in hexane (Acros Organics)
- Chlorohydridotris(triphenylphosphine)ruthenium(II) (Strem Chemicals)
- Dichloro(1,5-cyclooctadiene)ruthenium(II) (Sigma-Aldrich)
- Ethylenebis(diphenylphosphine) (Sigma-Aldrich)
- Bromopentacarbonylmanganese(I) (Sigma-Aldrich)
- Lithium tetrafluoroborate (Sigma-Aldrich)
- Potassium *tert*-butoxide (Sigma-Aldrich)
- Sodium *tert*-butoxide (Sigma-Aldrich)
- Potassium hexafluorophosphate (Sigma-Aldrich)

### 6.2. Analytical methods

#### 6.2.1. NMR spectroscopy

$^1\text{H}$  NMR spectra were obtained at 300 MHz (Bruker AV-300) or 400 MHz (Bruker AV-400).  $^{13}\text{C}\{^1\text{H}\}$  NMR spectra were obtained at 75 MHz or 101 MHz.  $^{31}\text{P}\{^1\text{H}\}$  NMR spectra were obtained at 121 MHz or 162 MHz. NMR chemical shifts are reported in ppm downfield from tetramethylsilane and were referenced to the residual proton resonance and the natural abundance  $^{13}\text{C}$  resonance of the solvents.  $^{31}\text{P}$  NMR chemical shifts are reported in ppm downfield from  $\text{H}_3\text{PO}_4$  and referenced to an external 85% solution of phosphoric acid. Abbreviations used in the reported NMR experiments: b, broad; s, singlet; d, doublet; t, triplet; q, quartet; m, multiplet.

#### 6.2.2. IR spectroscopy

IR-spectroscopy measurements were performed on a Vertex-80-FTIR spectrometer (BRUKER) with a MCT detector. The sample solutions were filled in a sealed IR-cell with  $\text{CaF}_2$  windows and an optical path length of 0.012 mm, which was purged with argon prior to use. The temperature of the cell was controlled by a thermostat at 25 °C. The spectra were taken with 256 scans and a resolution of 1  $\text{cm}^{-1}$ .

#### 6.2.3. Elemental analysis

Elemental analyses were recorded by the analytic department of the Leibniz Institute for Catalysis with a Flash EA 1112 analyzer by Thermo Quest or with a C/H/N/S-micro analyzer TruSpec-932 by Leco.

#### 6.2.4. Mass spectrometry

Mass spectra were recorded on a MAT 95XP ThermoFisher Mass Spectrometer using electrospray ionization mode.

#### 6.2.5. Gas chromatography

GC measurements were carried out using a gas chromatograph HP6890 by Hewlett Packard (Agilent). After having injected the gas sample into the gas chromatograph it is divided onto two columns. Low-molecular organic compounds are led over a capillary column of the type HP-PLOT Q (length: 30 m, inner diameter: 530  $\mu\text{m}$ , film thickness: 40  $\mu\text{m}$ ) and are detected by a flame ionization detector (FID) (GC a). For analyzing the content of the gases hydrogen, oxygen, argon, nitrogen, carbon monoxide, carbon dioxide and methane in the sample, they are led over a molecular sieve column (Carboxen 1000) of the type Supelco 1-2392U (length: 5 m, inner diameter: 530  $\mu\text{m}$ , film thickness: 10  $\mu\text{m}$ ) and are detected by a thermal conductivity sensor (TCS) (GC b). For the quantitative analysis an external calibration with calibration gases is done. The gas

## Appendix

---

integration was calibrated using certified gas mixtures from commercial suppliers (Linde and Air Liquide) with the following gas vol%:

GC a):

H<sub>2</sub>: 1%, 10%, 25%, 50%, 100%

CO: 10 ppm, 100 ppm, 250 ppm, 1000 ppm, 1%, 10%

CO<sub>2</sub>: 1%, 50%

CH<sub>4</sub>: 1%

GC b):

H<sub>2</sub>: 1%, 10%, 25%, 50%, 100%

CO: 1 ppm, 20 ppm, 75 ppm, 100 ppm, 250 ppm, 1000 ppm, 1%, 10%

CO<sub>2</sub>: 1%, 50%

CH<sub>4</sub>: 1%

The systems allow for the determination of H<sub>2</sub>, Ar, CH<sub>4</sub>, CO and CO<sub>2</sub> within the ranges:

H<sub>2</sub> ≥ 0.5 vol% – 100 vol%

CO ≥ 10 ppm [GC a)], CO down to 1 ppm [GC b)]

CO<sub>2</sub> ≥ 100 ppm – 100 vol% [GC a)], down to 1 ppm [GC b)]

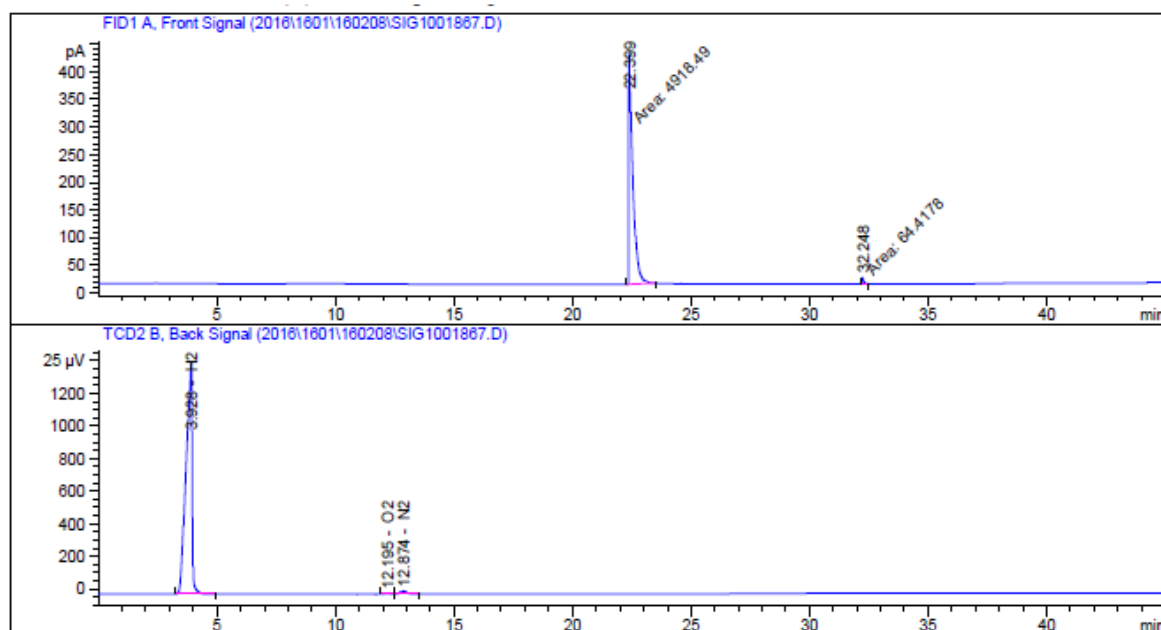
CH<sub>4</sub> ≥ 1 ppm [GC b)]

GC analysis provides the relative composition of the different components of the collected gas. H<sub>2</sub>, CO<sub>2</sub>, CO, and CH<sub>4</sub> amounts were determined and their ratios established.

## Appendix

### 6.2.5.1. Exemplary GC spectra

#### Dehydrogenation of methanol



=====  
External Standard Report  
=====

Sorted By : Signal  
Calib. Data Modified : 2/29/2016 12:51:40 PM  
Multiplier : 1.0000  
Dilution : 1.0000  
Use Multiplier & Dilution Factor with ISTDs

Signal 1: FID1 A, Front Signal

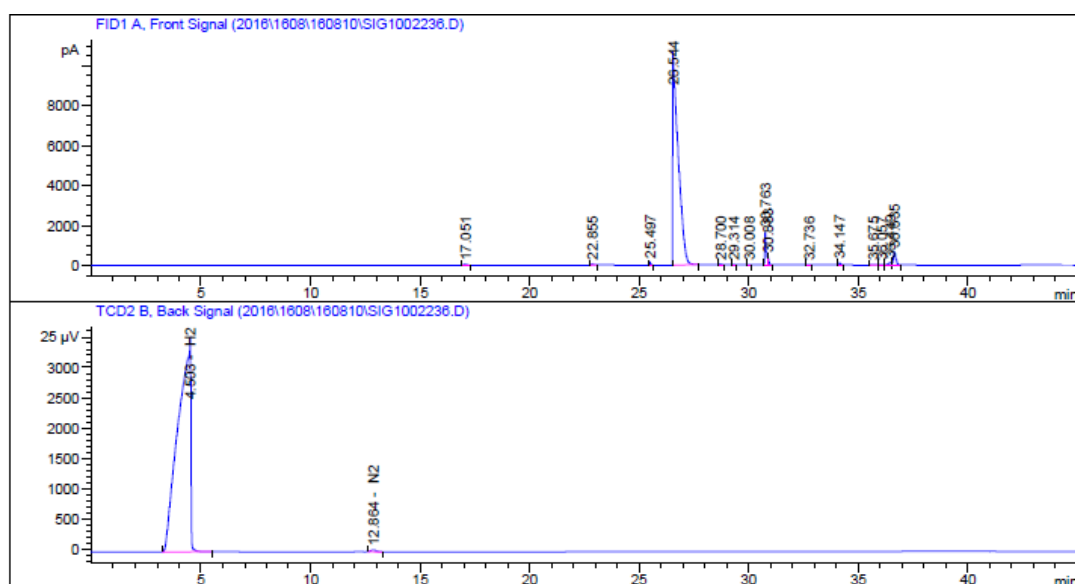
Signal 2: TCD2 B, Back Signal

RetTime [min]	Type	Area [25 $\mu$ V*s]	Amt/Area	Amount [% Vol.]	Grp	Name
3.928	BB	2.55032e4	3.07808e-4	7.85010	H2	
12.195	BV	68.25850	2.88802e-3	1.97132e-1	O2	
12.874	VB	358.66495	3.12725e-3	1.12164	N2	
16.400		-	-	-	CO	
30.100		-	-	-	CH4	
36.800		-	-	-	CO2	
Totals :				9.16887		

**Figure 44:** GC spectrum for the dehydrogenation of methanol.

# Appendix

## Dehydrogenation of ethanol



External Standard Report

Sorted By : Signal  
 Calib. Data Modified : 8/9/2016 2:30:06 PM  
 Multiplier : 1.0000  
 Dilution : 1.0000  
 Use Multiplier & Dilution Factor with ISTDs

Signal 1: FID1 A, Front Signal

Signal 2: TCD2 B, Back Signal

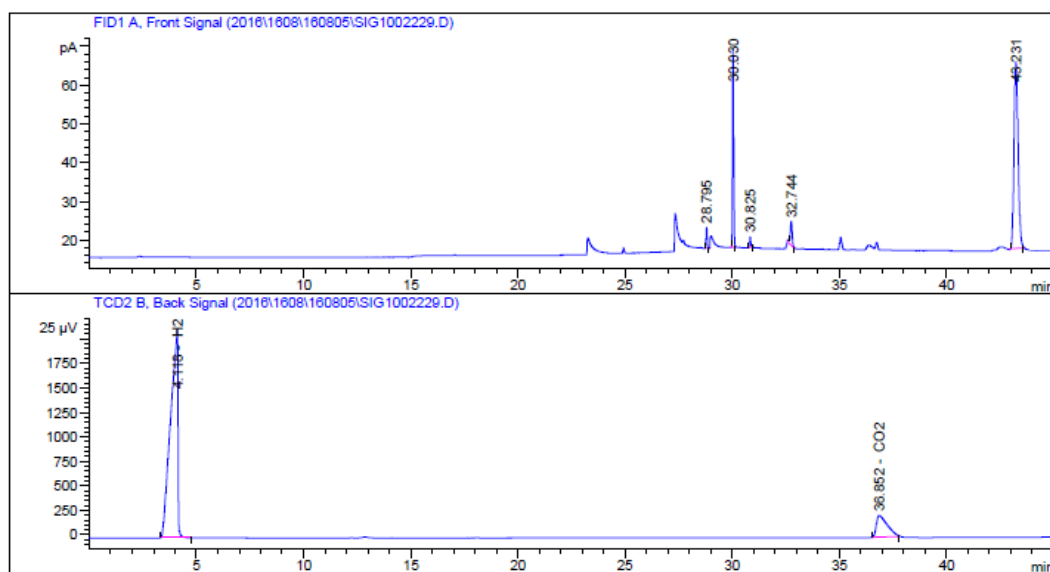
RetTime [min]	Type	Area [25 µV*s]	Amt/Area	Amount [% Vol.]	Grp	Name
4.503	BB	1.35661e5	3.28151e-4	44.51733		H2
12.000		-	-	-		O2
12.864	BB	520.86621	3.12854e-3	1.62955		N2
16.400		-	-	-		CO
29.068		-	-	-		CH4
36.090		-	-	-		CO2
Totals :				46.14688		

Figure 45: GC spectrum for the dehydrogenation of ethanol.<sup>[168]</sup>



# Appendix

## Dehydrogenation of formic acid



External Standard Report

Sorted By : Signal  
Calib. Data Modified : 8/5/2016 3:44:15 PM  
Multiplier : 1.0000  
Dilution : 1.0000  
Use Multiplier & Dilution Factor with ISTDs

Signal 1: FID1 A, Front Signal

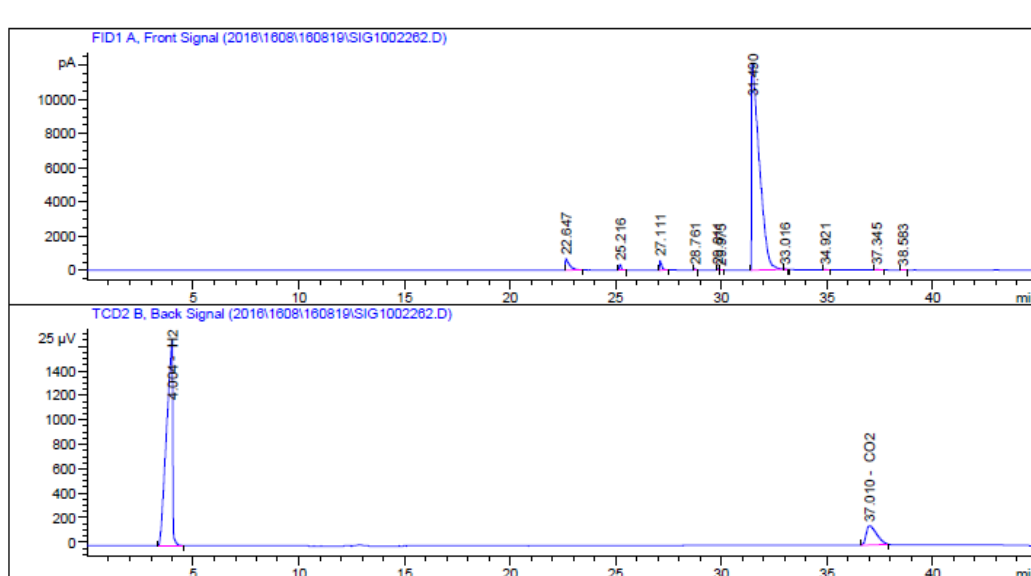
Signal 2: TCD2 B, Back Signal

RetTime [min]	Type	Area [25 µV*s]	Amt/Area	Amount [% Vol.]	Grp	Name
4.118	BB	5.07765e4	3.10680e-4	15.77522		H2
12.000		-	-	-		O2
12.832		-	-	-		N2
16.400		-	-	-		CO
29.068		-	-	-		CH4
36.852	BB	7774.96191	1.72772e-3	13.43296		CO2
Totals :				29.20818		

Figure 46: GC spectrum for the dehydrogenation of formic acid.<sup>[168]</sup>

## Appendix

### Dehydrogenation of paraformaldehyde



=====  
External Standard Report  
=====

Sorted By : Signal  
Calib. Data Modified : 9/6/2016 2:16:00 PM  
Multiplier : 1.0000  
Dilution : 1.0000  
Use Multiplier & Dilution Factor with ISTDs

Signal 1: FID1 A, Front Signal

Signal 2: TCD2 B, Back Signal

RetTime [min]	Type	Area [25 µV*s]	Amt/Area	Amount [% Vol.]	Grp	Name
4.004	BB	3.36513e4	3.08388e-4	10.37767		H2
12.115		-	-	-		O2
12.780		-	-	-		N2
16.408		-	-	-		CO
29.400		-	-	-		CH4
37.010	BB	5351.93799	1.71845e-3	9.19703		CO2

Totals : 19.57470

**Figure 47:** GC spectrum for the dehydrogenation of paraformaldehyde.<sup>[168]</sup>

## Appendix

### 6.3. General experimental details

#### 6.3.1. Measurements of catalytic activity

Measurements of catalytic activity were performed with manual and automatic burettes and in an autoclave setup. The corresponding experimental setups are shown in the Figures 47, 48 and 49. After every reaction, a gas-phase GC was made to verify the formation gaseous products.

##### **6.3.1.1. Details on experiments performed with manual and automatic burettes**

The reaction room is a double-walled three-necked reaction vessel connected to two scaled gas burettes filled with water via a Dimroth condenser. The temperature of the vessel is controlled by a cryostat.

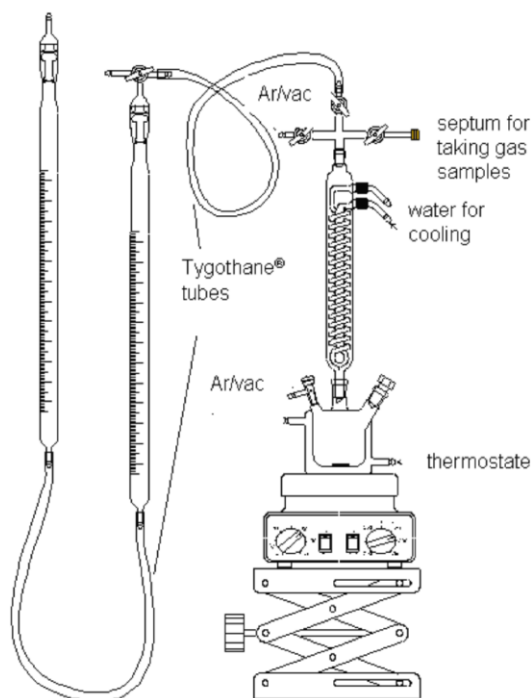


**Figure 48:** Setup of the manual burette equipment.<sup>[168]</sup>

The automatic burette equipment was developed at the Leibniz Institute for Catalysis together with MesSen Nord GmbH. A detailed description of the equipment is provided in H.-J. Drexler, A. Preetz, T. Schmidt, D. Heller in *The Handbook of Homogeneous Hydrogenation*, Vol. 1 (Eds.: J. G. De Vries, C. J. Elsevier), Wiley-VCH, Weinheim, **2007**, pp. 257–293.

## Appendix

---

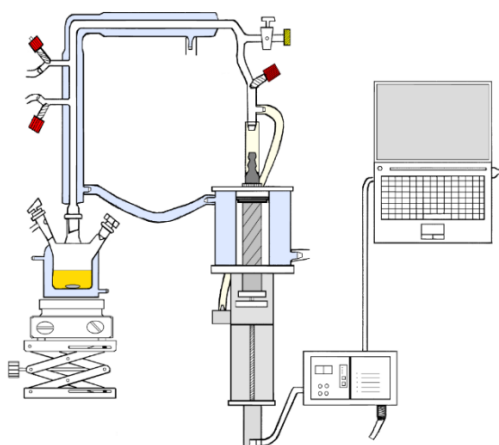


**Figure 49:** Setup of the automatic burette equipment.

### General procedure for the dehydrogenation of methanol

KOH (8 M, 0.08 mol) and a 9:1 MeOH/H<sub>2</sub>O (8 mL/1 mL) solution were placed in the three-necked reaction vessel heated up under argon flow to the set temperature. The reaction was started by adding a stock solution of the catalyst **1a** or **Me-1** (4.20  $\mu$ mol in 1 mL MeOH).

### General procedure for the dehydrogenation of ethanol

A solution (5mL) of EtOH and H<sub>2</sub>O in a ratio 9:1 (volume) containing KOH (2.2444 g, 40 mmol) was heated to 92°C and the system was equilibrated for 20 min. Afterwards, catalyst **9** (4.18 mg, 8.4  $\mu$ mol) was added in a Teflon crucible, setting this point as the starting point for measuring the evolved gas volume.

### General procedure for the dehydrogenation of formic acid

A solution of formic acid and DMOA (11:10 molar ratio mixture, 5mL) was added to PC (5mL). The mixture was heated to the desired temperature of 60°C and the system was equilibrated for 20 min. Catalyst **9** (2.64 mg, 5.3  $\mu$ mol) was added in a Teflon crucible, which marked the starting point for measuring the evolved gas volume.

### General procedure for the dehydrogenation of paraformaldehyde

Paraformaldehyde (120 mg, 0.004 mol) was added to a mixture of *t*BuOH (36 mL) and KOH solution (4 mL), obtaining a final composition of 9:1 *t*BuOH/H<sub>2</sub>O, 0.05M KOH, 0.1 M paraformaldehyde. To this reaction mixture, the catalyst **9** (8.28 mg, 16.72  $\mu$ mol) was added. This mixture was heated and the reaction monitoring was started when the set temperature of 81°C was reached.

## Appendix

---

### 6.3.1.2. Details on experiments performed with the autoclave setup



**Figure 50:** Setup of the autoclave equipment.<sup>[118]</sup>

#### General procedure for the dehydrogenation of methanol

KOH was placed in an autoclave (100 mL) and after having flushed the system several times with argon, MeOH (17 mL), H<sub>2</sub>O (2 mL) and a stock solution of the catalyst, **1** or **Me-1** (8.41 μmol in 1 mL MeOH), resulting in a MeOH/H<sub>2</sub>O 9/1 solution, were added under the protection of argon. The measurement was started once the temperature of the reaction solution reached the desired reaction temperature. During the reaction the pressure and the temperature of the reaction solution and of the gas phase and in the autoclave were monitored.

## Appendix

---

### 6.3.1.3. Calculation of TON and TOF

The measured gas volumes were corrected by a blank value (gas evolution measured in a reaction performed using same conditions but no catalyst added). The catalyst's productivity can be expressed in terms of a turnover number (TON), which is calculated by equation (7):

$$TON = \frac{V_{obs} - V_{blank}}{(V_{m,H_2,25^\circ C} + V_{m,CO_2,25^\circ C}) \cdot n_{cat}} \quad (7)$$

where  $V_{obs}$  and  $V_{blank}$  are the gas volume measured in the catalytic reaction and blank reaction, respectively. The calculation of  $V_{m,H_2,25^\circ C}$  was carried out using the Van der Waals equation (8):

$$V_{m,H_2,25^\circ C} = \frac{RT}{p} + b_{H_2} - \frac{a_{H_2}}{RT} = 24.48 \frac{L}{mol} \quad (8)$$

Parameters that were used for this equation:

$$\begin{aligned} R &= 8.3145 \text{ m}^3 \text{ Pa mol}^{-1} \text{ K}^{-1} \\ p &= 101,325 \text{ Pa} \\ T &= 298.15 \text{ K} \\ a_{H_2} &= 24.7 \cdot 10^{-3} \text{ Pa m}^6 \text{ mol}^{-2} \\ b_{H_2} &= 26.6 \cdot 10^{-6} \text{ m}^3 \text{ mol}^{-1} \end{aligned}$$

The calculation of  $V_{m,CO_2,25^\circ C}$  was carried out using Van der Waals equation (9):

$$V_{m,CO_2,25^\circ C} = \frac{RT}{p} + b_{CO_2} - \frac{a_{CO_2}}{RT} = 24.36 \frac{L}{mol} \quad (9)$$

Parameters that were used for this equation:

$$\begin{aligned} R &= 8.3145 \text{ m}^3 \text{ Pa mol}^{-1} \text{ K}^{-1} \\ p &= 101,325 \text{ Pa} \\ T &= 298.15 \text{ K} \\ a_{CO_2} &= 36.5 \cdot 10^{-2} \text{ Pa m}^6 \text{ mol}^{-2} \\ b_{CO_2} &= 42.7 \cdot 10^{-6} \text{ m}^3 \text{ mol}^{-1} \end{aligned}$$

## Appendix

---

The equation (7) could be simplified when no CO<sub>2</sub> was released in the gas phase (MeOH and EtOH dehydrogenation) as it is shown in the equation (10):

$$TON = \frac{V_{obs} - V_{blank}}{V_{m,H_2,25^\circ C} \cdot n_{cat}} \quad (10)$$

The catalyst's activity, which can be expressed by the turnover frequency (TOF), was calculated by equation (11):

$$TON = \frac{TOF}{t} \quad (11)$$

### 6.4. Part I: Ruthenium-catalysed dehydrogenation of methanol

#### 6.4.1. Investigations for catalyst **1**

##### 6.4.1.1. *Base- and temperature-activity dependency*

###### Temperature-activity measurements

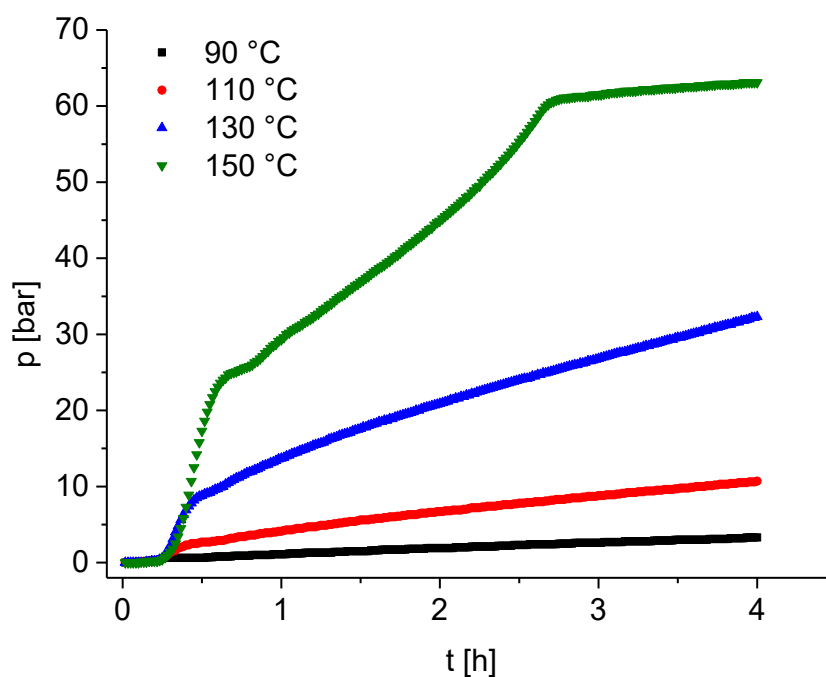


**Figure 51:** Correlation between catalytic activity and temperature. Measurements performed in the sealed autoclave setup. Conditions: 8 M KOH, MeOH:H<sub>2</sub>O (9:1, 10 mL), 4.2  $\mu$ mol **1**.



## Appendix

---

### Temperature-molarity measurements

Based on the measured pressure  $p$  and the temperature of the gas in the autoclave  $T$ , the moles of the generated hydrogen gas  $n_{H_2}$  were determined. Generally,  $n_{H_2}$  can be calculated by the equation for the molar volume:

$$n_{H_2} = \frac{V_{AC}}{V_{m,H_2}} = \frac{V_{AC}}{\frac{RT}{p} + b - \frac{a}{RT}} \quad (12)$$

$$\text{with } V_{AC} = 134 \text{ mL} \quad (13)$$

For the calculation of the molar volume of the hydrogen gas  $V_{m,H_2}$  at a certain pressure and temperature, the already mentioned Van-der-Waals equation (8) was used.

$V_{AC}$  is the abbreviation for the volume of the gas room of the autoclave and the following method was used for its determination: The sealed autoclave was pressurised with nitrogen gas  $V_{N_2}$ . After noting the pressure value  $p_{N_2}$  the gas was released and the amount of released gas was determined by a connected gas burette.

$$V_{AC} = n_{N_2} \cdot V_{m,N_2} = \frac{V_{N_2}}{V_{m,N_2,25^\circ C}} \left( \frac{R}{p_{N_2}} \cdot T + b - \frac{a}{R} \cdot \frac{1}{T} \right) \quad (14)$$

Parameters that were used for this equation:

$$R = 8.3145 \text{ m}^3 \text{Pa mol}^{-1} \text{K}^{-1}$$

$$T = 298.15 \text{ K}$$

$$a_{N_2} = 140.8 \cdot 10^{-3} \text{ Pa m}^6 \text{ mol}^{-2}$$

$$b_{N_2} = 39.1 \cdot 10^{-6} \text{ m}^3 \text{ mol}^{-1}$$

$$V_{m,N_2,25^\circ C} = 22.402 \text{ L mol}^{-1}$$

## Appendix

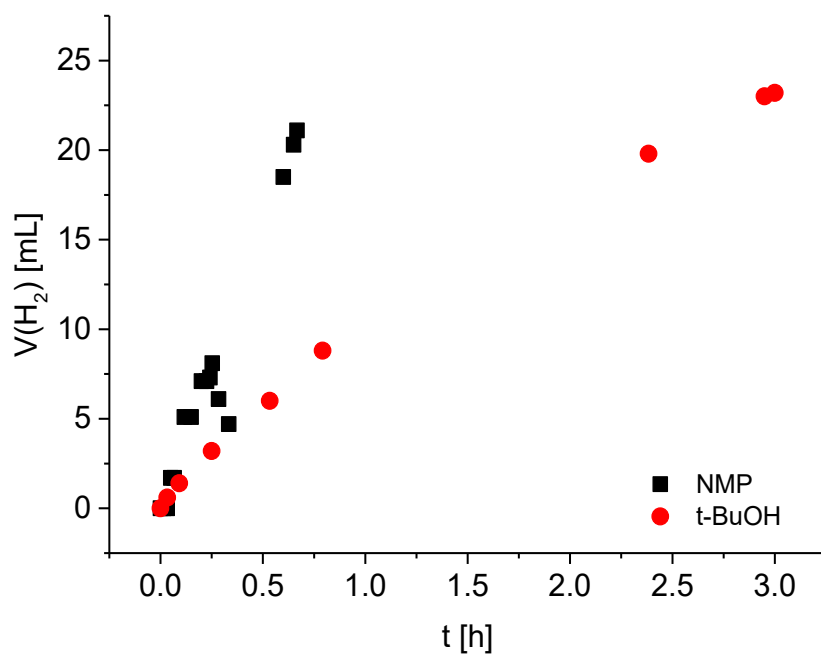


**Figure 52:** Testing of different solvents for reduction of base. Conditions: 1 M KOH, MeOH:H<sub>2</sub>O (9:1, 1.2 mL), 4 mL solvent (NMP or *t*-BuOH), 4.2  $\mu\text{mol}$  **1**, 65 °C.

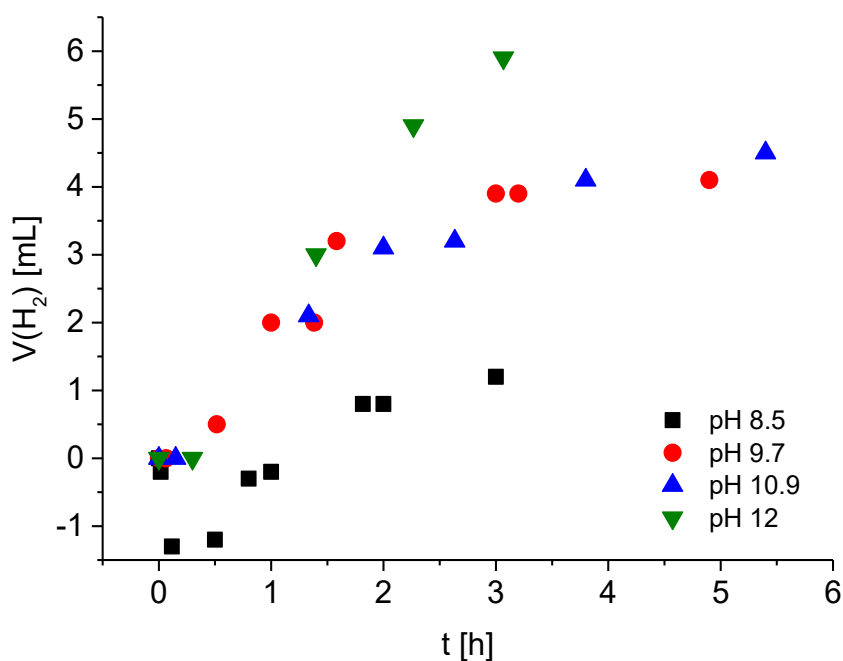


**Figure 53:** Testing of pH-buffered solutions for the reduction of base. Conditions: MeOH:H<sub>2</sub>O (buffered aqueous solution with a defined pH value) (1:1, 15 mL), 8.4  $\mu\text{mol}$  **1**, 70 °C.

## Appendix

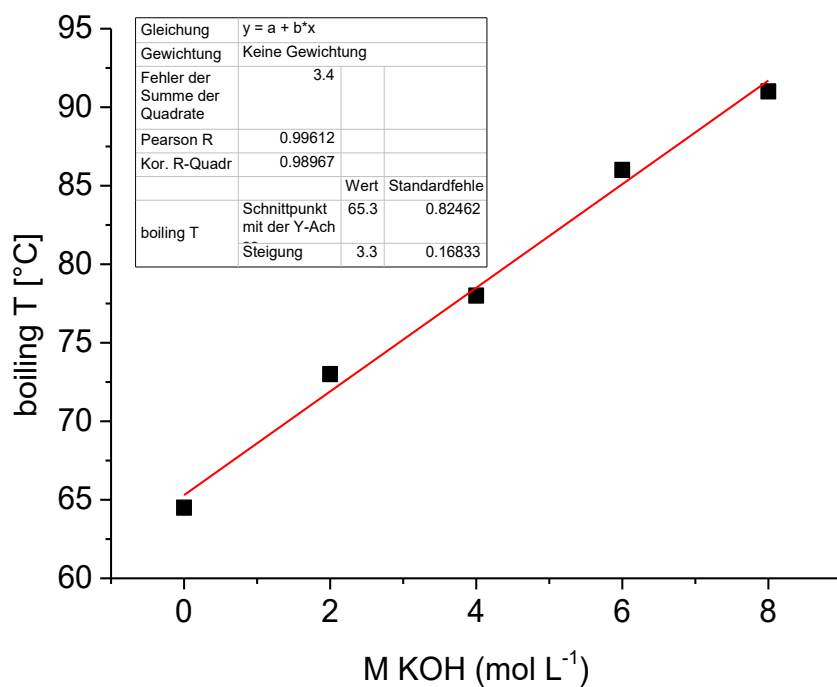


**Figure 54:** Correlation between base molarity and boiling temperature of the 9:1 MeOH:H<sub>2</sub>O reaction solution.

Experiments performed for investigating difference in catalytic activity between measurements performed in the manual burette and in the autoclave setup:

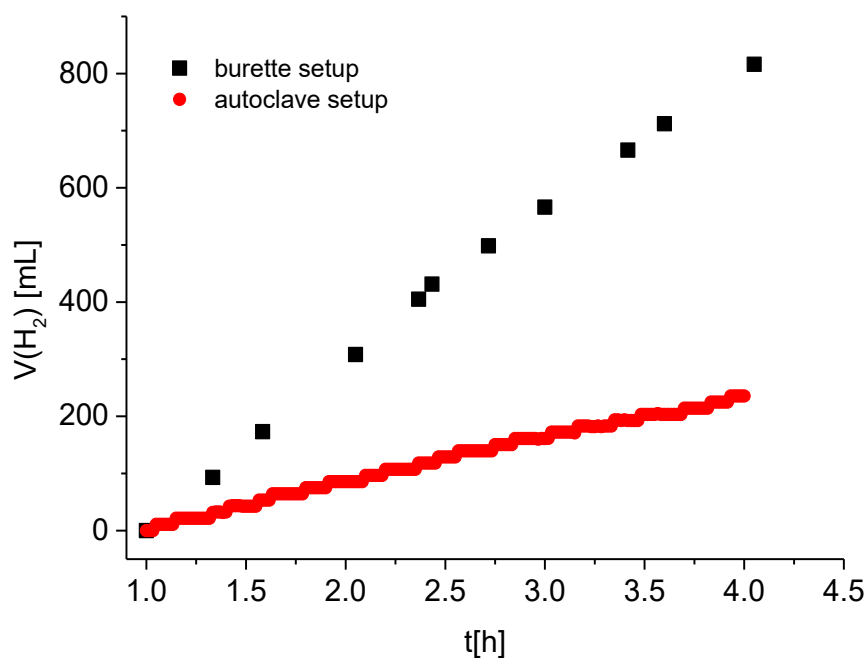
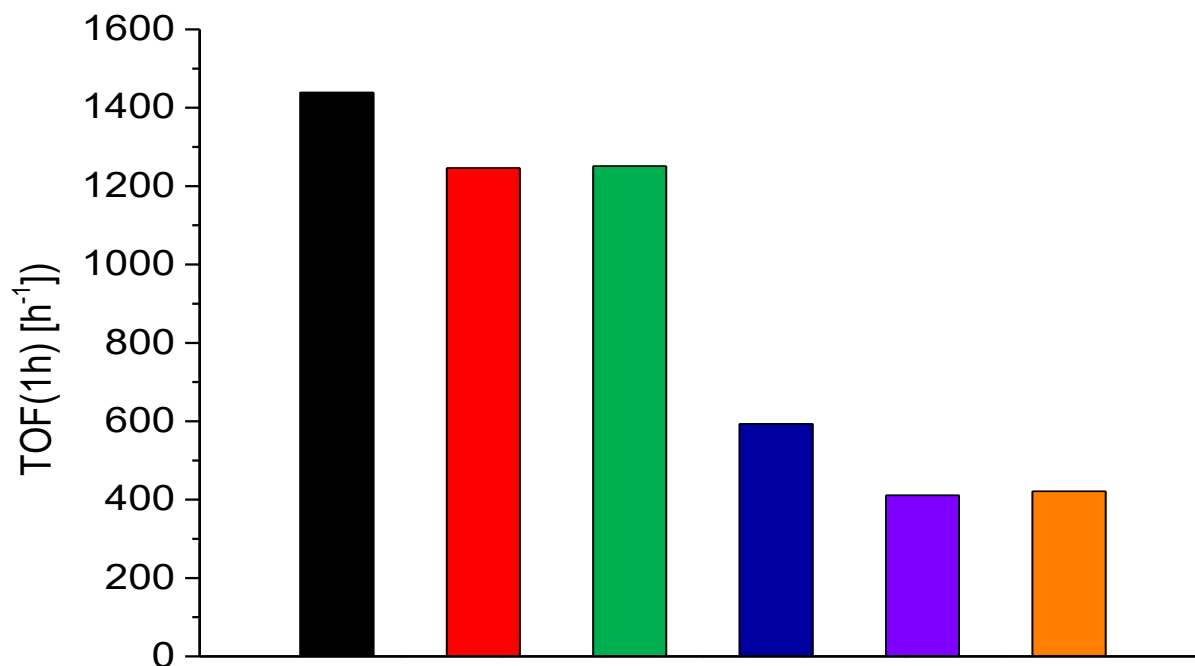


**Figure 55:** Difference in catalytic activity between manual burette and autoclave setup. Volumes of gas for the autoclave setup calculated from the measured increase in pressure based on the equations shown before. Reaction conditions: 8 M KOH, MeOH:H<sub>2</sub>O (9:1, 20 mL), 8.4 μmol **1**, 90 °C.

## Appendix

Several test experiments were performed to exclude physical or handling reasons for the observed differences.

**Scheme 36:** Experiments performed to investigate different catalytic activities between burette and autoclave setup.



Reaction setup	burette	burette	ac-burette	ac-burette	ac	ac
Reaction system	open	open	open	open	closed	closed
Reaction vessel	Glass vessel	Glass vessel	Teflon inlay	Teflon inlay	Teflon inlay	Teflon inlay
Heating system	01	02	02	02	02	02
Stirring [rpm]	700	700	700	300	700	300

**Heating system:** (minor) influence

**Reaction vessel:** no influence

**Stirring:** major influence  
for open system

**Stirring:** minor influence  
for closed system

## Appendix

---

Explanation:

- b: Burette measurement with glass reaction vessel
- ac-burette: Autoclave vessel connected to the burette
- ac: Standard autoclave measurement

Conditions:

- MeOH:H<sub>2</sub>O (9:1, 10 mL), 8.4  $\mu\text{mol}$  **1**, 90 °C.

Conclusions:

- The type of reaction vessel and heating system could be excluded to cause significant lower catalytic activity for autoclave setup compared to burette setup.
- The stirring velocity had only a major influence for the burette setup, as the solution was more efficiently degassed and therefore higher gas evolution rates were achieved.
- For the autoclave setup the stirring rate had no comparable influence.

→ Since all physical reasons for the differences in activity could be excluded, it is very probable that this effect is caused by a chemical reason.

### Development of an alternative autoclave setup

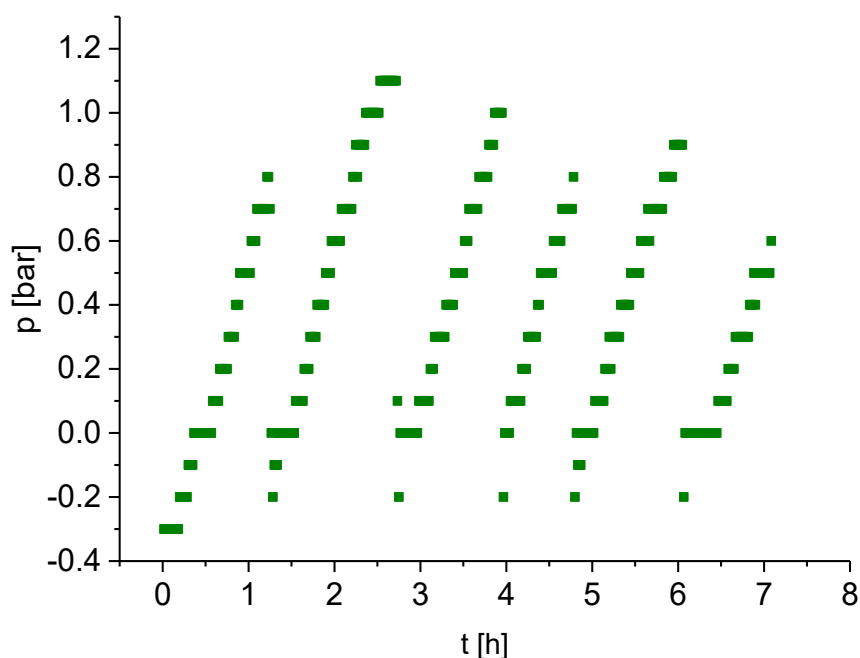


**Figure 56:** Measurements of increase in pressure by the evolution of hydrogen gas. Setup in a closed autoclave, pressure is let to increase to 0.4 bar, at which point the gas is released. Conditions: 8 M KOH, MeOH:H<sub>2</sub>O (9:1, 20 mL), 8.4  $\mu\text{mol}$  **1**, 90 °C, 300 rpm.

## Appendix

---

This procedure did not prove to be successful as the employed pressure sensor turned out to be unsuitable for this low pressure range as the error margin lies in the range of 0.3 bar. Therefore the method of letting the hydrogen pressure increase and release the gas afterwards leads to reproducibility problems (see Figure 54).

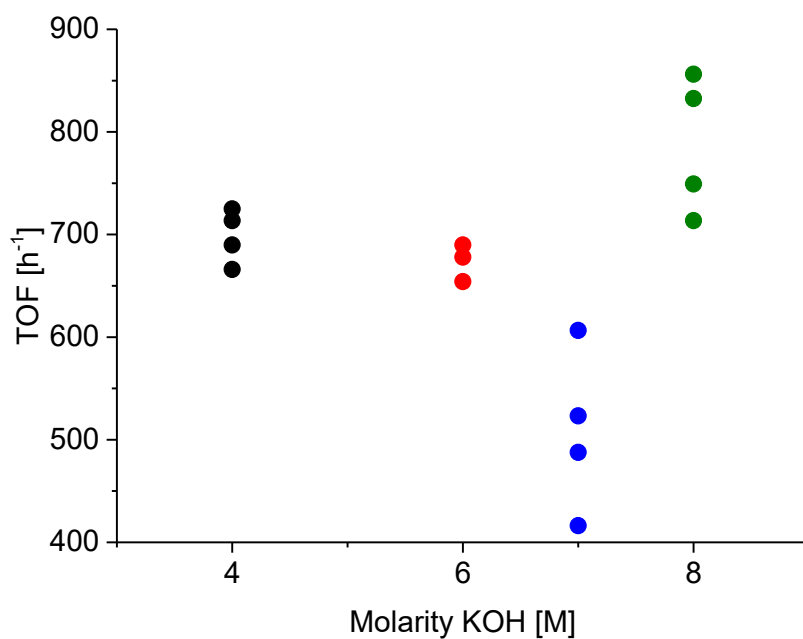


**Figure 57:** Calculated TOF based on the increase in pressure measured in the closed autoclave setup. For conditions: see Figure 53.

In conclusion, the modified setup based on the autoclave connected to the burettes via a pressure valve was used (For details see Figure 8).

## Appendix

### 6.4.1.2. NMR studies

For details on the performed stoichiometric NMR investigations, the reader may refer to the supporting information of the JACS article.<sup>[180]</sup>

**Table 4:** NMR data for the PNP-pincer complex **1** and related complexes in deuterated solvents.<sup>[181]</sup>

Complex	<sup>1</sup> H					<sup>31</sup> P		solvent
	$\delta(\text{NH})$ [ppm]	$J$ [Hz]	$\delta(\text{RuH}_1)$ [ppm]	$\delta(\text{RuH}_2)$ [ppm]	$J_{\text{HH}}$ [Hz]	$J_{\text{HP}}$ [Hz]	$\delta(\text{P})$ [ppm]	
<i>Syn-1a</i>	bt, 4.1	11.8	t, -15.7	-	-	19.2	s, 75.8	THF-d <sub>8</sub>
<i>Anti-1a</i>	bt, 3.8	11.8	t, -16.0	-	-	17.9	s, 76.3	THF-d <sub>8</sub>
Amido complex <b>2</b>	-	-	bt, -19.0	-	-	17.1	bs, 93.8	THF-d <sub>8</sub>
Dihydride complex <b>3</b>	bt, 3.7	11.5	td, -6.7	td, -6.8	4.5	19.2	s, 91.8	dioxane-d <sub>8</sub>
Methoxide complex <b>4</b>	nd	-	t, -17.8	-	-	20.0	s, 75.3	THF-d <sub>8</sub>
Hydroxide complex <b>5</b>	bs, 2.9	-	t, -16.5	-	-	18.4	s, 76.6	THF-d <sub>8</sub>
Ru-formate complex <b>6</b>	bt, 8.61	-	td, -18.1	-	2.3	18.2	s, 76.9	THF-d <sub>8</sub>

**Table 5:** NMR data for the PNP-pincer complex **1** and related complexes in the 9:1 MeOH:H<sub>2</sub>O reaction solution containing 8 M KOH.

Complex	<sup>1</sup> H					<sup>31</sup> P		solvent
	$\delta(\text{NH})$ [ppm]	$J$ [Hz]	$\delta(\text{RuH}_1)$ [ppm]	$\delta(\text{RuH}_2)$ [ppm]	$J_{\text{HH}}$ [Hz]	$J_{\text{HP}}$ [Hz]	$\delta(\text{P})$ [ppm]	
Species 1	-	-	s, - 18.17	-	-	-	74.05	9:1 MeOH:H <sub>2</sub> O, 8 M KOH
Species 2	-	-	s, -7.20	-	-	-	88.64	9:1 MeOH:H <sub>2</sub> O, 8 M KOH

## Appendix

### Studies of the reaction solution

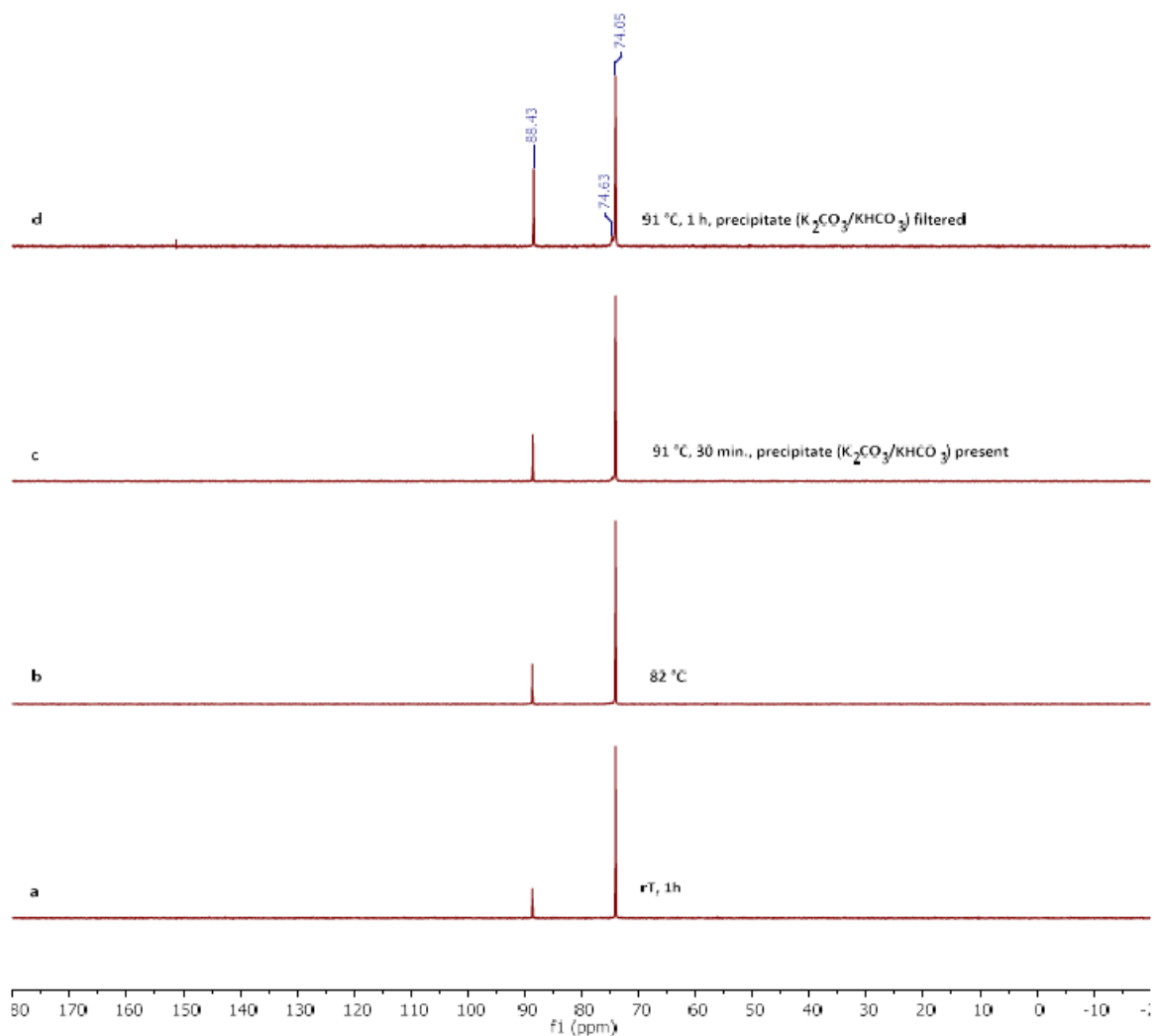


**Figure 58:**  $^{31}\text{P}$  NMR spectra (162 MHz, 297 K, MeOH/H<sub>2</sub>O 9:1 KOH 8M, one drop of CD<sub>3</sub>OH) of the reaction mixture arising from aqueous methanol reforming with **1**: Spectra were recorded at room temperature, the values reported in the spectra refer to the temperature of the solution at the time of sample withdrawal.<sup>[118, 182]</sup>



## Appendix

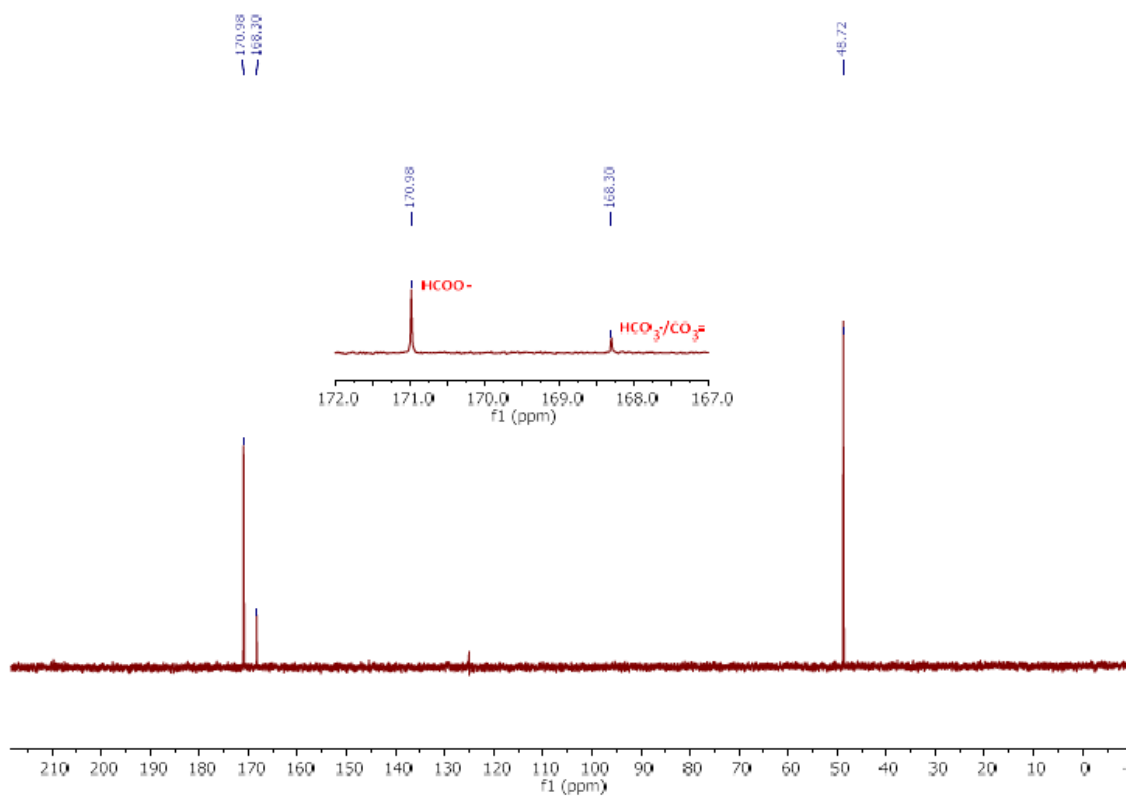


**Figure 59:**  $^{13}\text{C}$  NMR (75 MHz,  $\text{D}_2\text{O}$ , 298 K) of the precipitate formed during aqueous methanol reforming with **1**, after isolation and dissolution in  $\text{D}_2\text{O}$ .<sup>[118, 182]</sup>

## Appendix

*DFT calculations for the deprotonation of the ligand backbone N-H moiety*

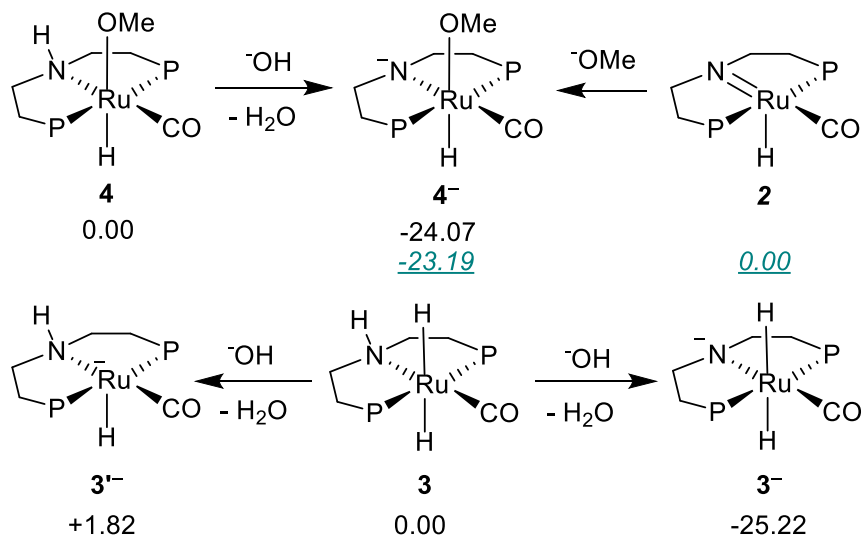


**Figure 60:** DFT calculated energies (kcal mol<sup>-1</sup>) for the formation of anionic complexes. P = PPr<sub>2</sub>.<sup>[118, 138]</sup>

### *Testing for formaldehyde (Merck MColorstest)*

The Merck MColorstest is a colorimetric test based on the reaction of formaldehyde with 4-amino-3-hydrazino-5-mercapto-1,2,4-triazole to form a purple-red tetrazine. The formaldehyde concentration is measured semi-quantitatively by visual comparison of the colour of the measurement solution with the colour fields of a colour card.

A 9:1 MeOH:H<sub>2</sub>O solution containing 4.2 μmol **1**, 8 M KOH and 0.2 mL of a 37% aqueous formaldehyde solution resulted in the appearance of a deep red colour, which equals a formaldehyde concentration of more than 1.5 mg/L. After the MeOH reforming reaction was performed for three hours, the reaction solutions (9:1 MeOH:H<sub>2</sub>O, 8 M KOH) containing the standard amount of **1** (4.2 μmol) and the fourfold amount of **1** (16.8 μmol) were subjected to the Merck formaldehyde test. Both tests resulted in a highly yellow colour, which equals a concentration of 0 mg/L formaldehyde.

## Appendix

---

### 6.4.1.3. *Operando Raman and GC investigations*<sup>[132]</sup>

#### Experimental setup

For a longterm measurement, the reactor was charged with a defined amount of KOH pellets and purged with argon flow. The reactor temperature was set to the desired temperature and the reflux chiller was set to 5 °C. The temperature of the reaction solution was measured with a Pt100 temperature probe. After having added the 9:1 MeOH:H<sub>2</sub>O solution the reactor was equilibrated for at least 15 min. Complete degassing and equilibrium were reached when the MFM indicated a mass flow of zero mL min<sup>-1</sup>. During this preparation time the Raman sensor was adjusted for maximum intensity with the focus point in the well-stirred part of the liquid phase above the stirrer bar. The catalyst was dissolved in 2mL of the methanol-water mixture and added to the reactor, which was the starting point of the reaction.

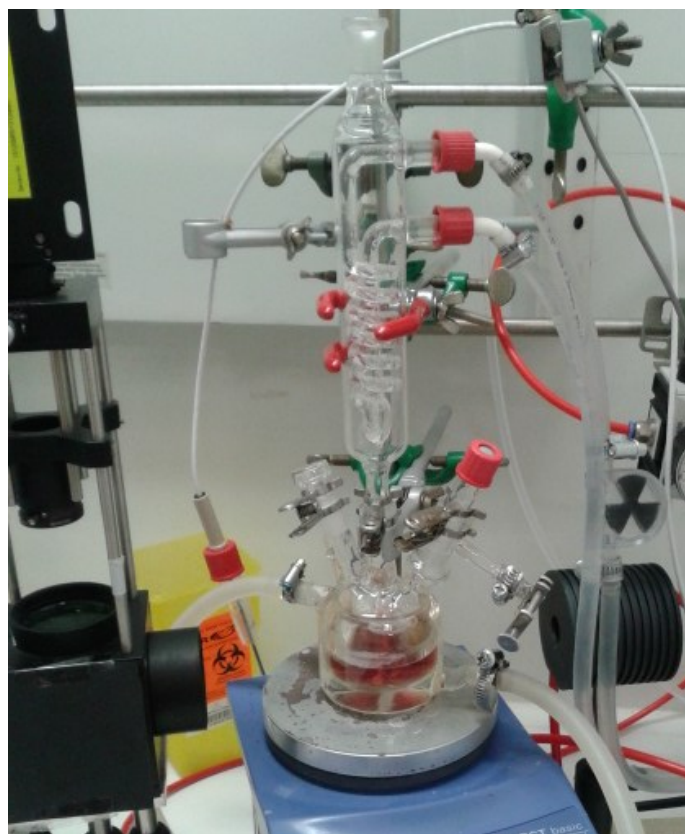


**Figure 61:** Setup for the operando Raman and GC investigation.<sup>[135]</sup>

## Appendix

---

### Analytcs and Calibration

The gas phase was analyzed by an Agilent Technologies 7820A gas chromatograph equipped with a GS-GASPRO 30m\*0.32mm capillary column and thermal conductivity detector (TCD). Due to the low expected gas emission, the complete gas stream was led through the GC's sample loop. A 1:1 volumetric mixture of argon and helium was used as carrier gas in the GC to maximize CO<sub>2</sub> signal in the TCD.

The GC was calibrated solely for the ratio of hydrogen and carbon dioxide. The mass flow of the emitted gas phase was detected by the MFM. Though originally calibrated for pure hydrogen, the actual mass flow could be calculated *a posteriori* with correction factors from Fluidat® and the known CO<sub>2</sub>:H<sub>2</sub> ratio from the GC measurements.

A self-developed Raman sensor by the group of A. Braeuer was used.<sup>[183]</sup> Hereby, the laser, installed at the top of the sensor, emitted light with an output power of 250 mW at a wavelength of 532 nm. The laser beam was widened by means of a Galilean telescope system, reflected at a dichroic mirror and focused into the liquid phase inside the glass reactor. There, the laser light was scattered elastically and inelastically in all room directions. The backscattered part of these measurement signals were collected and collimated by the focusing lens. While the elastically scattered light was suppressed at the dichroic mirror and a subsequent long pass filter, the desired inelastically scattered Raman signals were focused onto a glass fiber bundle and guided to the spectrometer (QE Pro, Ocean Optics Inc., Dunedin, FL, USA). The spectrometer was equipped with an entrance slit of 25 μm and a grating of 1800 lines mm<sup>-1</sup>. In the detected wavelength region, the optical resolution was 0.23 nm or 5.8 – 8.0 cm<sup>-1</sup>, respectively.

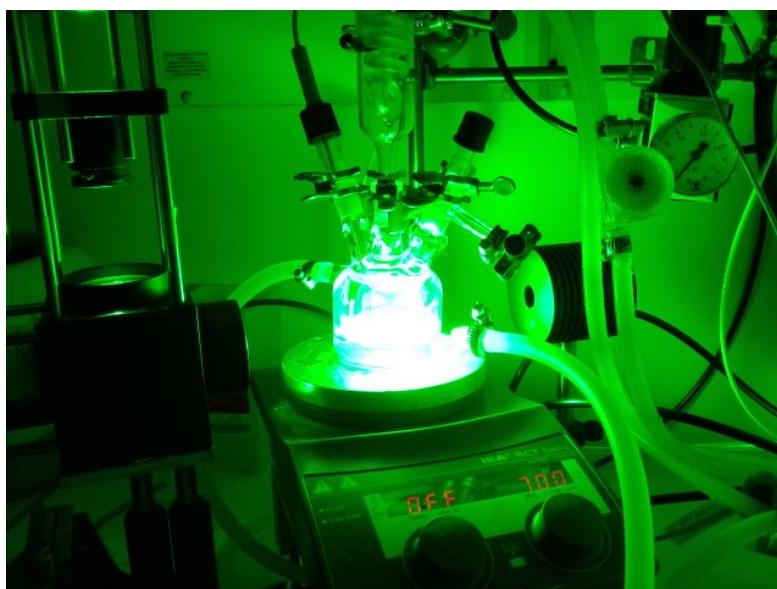


**Figure 62:** Recording of the operando Raman spectra.<sup>[135]</sup>

## Appendix

---

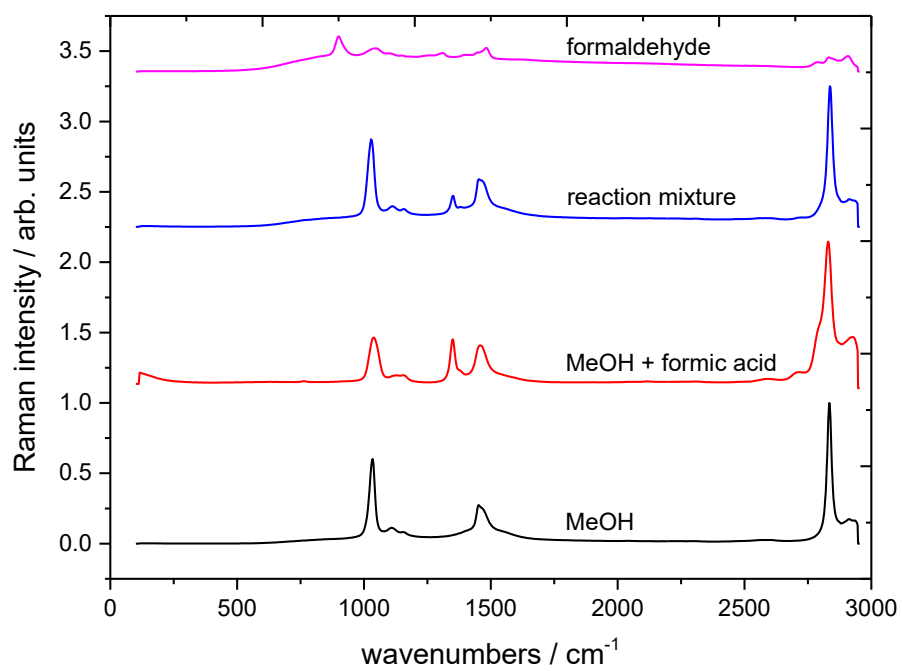


**Figure 63:** Comparison of Raman spectra for formaldehyde, methanol and the reaction solution.<sup>[135]</sup>

## Appendix

### 6.4.2. Investigations for catalyst **Me-1**

#### 6.4.2.1. NMR studies

**Table 6:** NMR data for the methylated PNP-pincer complex **Me-1** and related complexes in deuterated solvents.<sup>[181]</sup>

Complex	$\delta$		$^1\text{H}$				$^{31}\text{P}$	
	$\delta(\text{NCH}_3)$ [ppm]	$\delta(\text{RuH}_2)$	$J_{\text{HH}}$ [Hz]	$J_{\text{HP}}$ [Hz]	$\delta(\text{RuH}_2)$ [ppm]	$J_{\text{HH}}$ [Hz]	$J_{\text{HP}}$ [Hz]	$\delta(\text{P})$ [ppm]
<b>Me-1a</b>	-	s, 2.1	-	18.2	-	-	-	s, 71.6
<b>Me-1a'</b>	-	s, 1.9	-	18.2	-	-	-	s, 74.2
<i>Trans</i> <b>Me-3</b>	-	s, 2.0	3.8	20.0	m, -5.7	3.2	18.5	s, 89.6
<i>Cis</i> <b>Me-3</b>	-	nd	5.2	18.6	td, -7.13	5.2	21.7	s, 86.8
<b>Me-6</b>	m, 9.1	s, 1.9	-	19.4	-	-	-	s, 70.6
<b>Me-6'</b>	m, 9.0	s, 1.9	-	18.7	-	-	-	s, 73.0
<i>trans</i> [ $^2\text{H}$ ]- <b>Me-3</b>	-	t, -5.64	-	18.1	-	-	-	-
<i>trans</i> [ $^2\text{H}$ ]- <b>Me-3'</b>	-	t, -5.96	-	20.0	-	-	-	-

Solvent for all complexes: toluene- $d_8$ .

#### Studies of the reaction solution

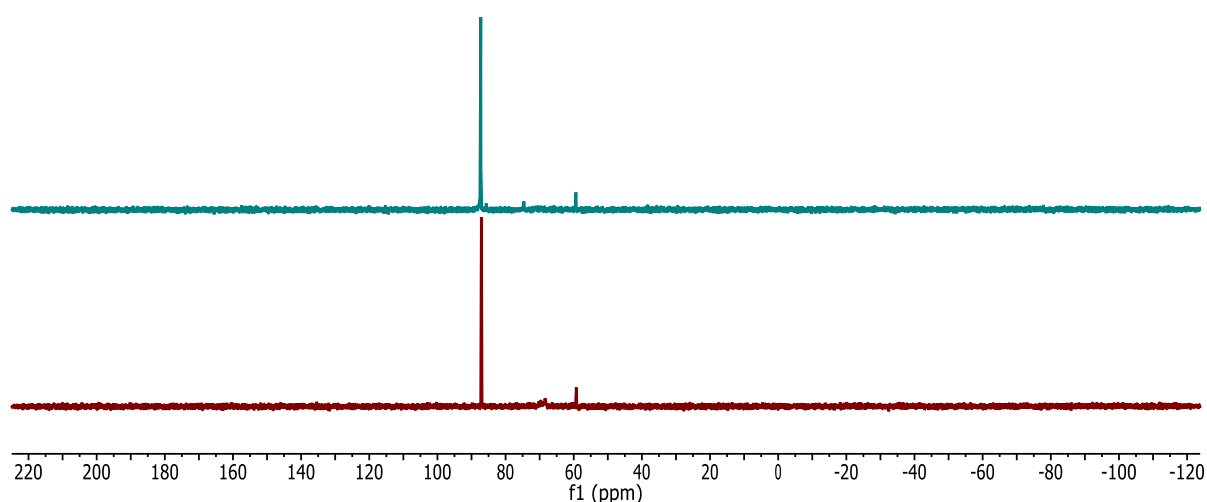


**Figure 64:**  $^{31}\text{P}$  NMR (162 MHz, 297 K) of the reaction solution containing **Me-1** (5 mg) in 0.7 mL 9/1 MeOH/H<sub>2</sub>O, 8 M KOH. Reaction solution was heated up in a gas-tight NMR vial. The lower spectrum of the reaction solution was measured at room temperature. The upper spectrum was measured at room temperature, after the solution had been heated up from room temperature to 90 °C and afterwards let cooled down to room temperature again.

## Appendix

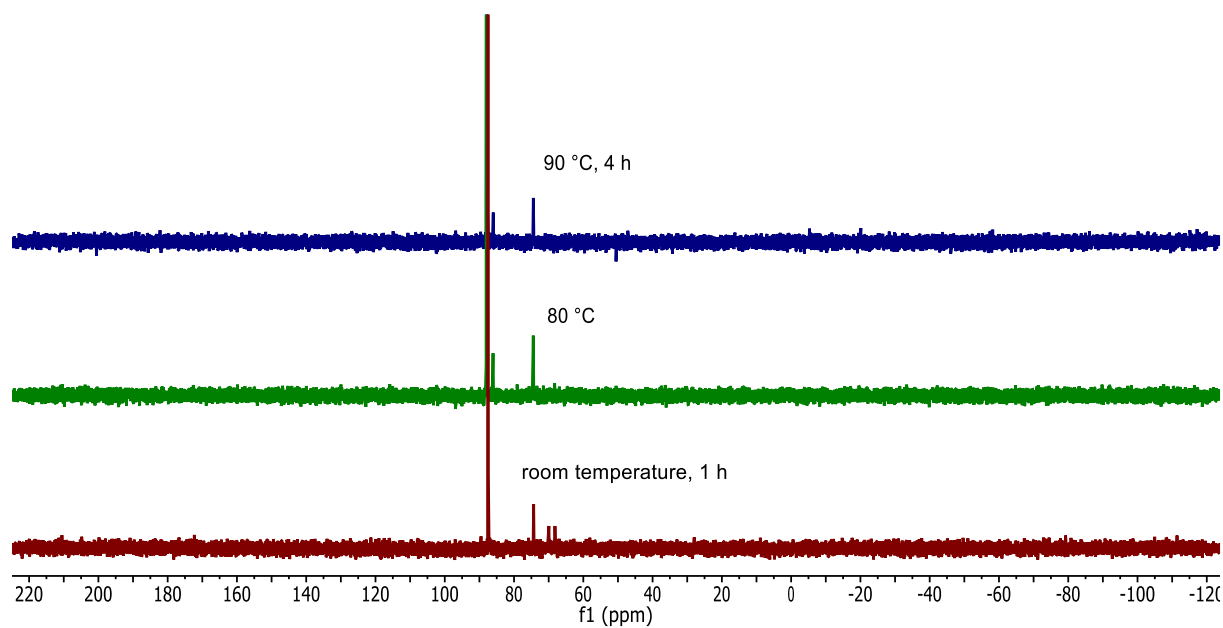


**Figure 65:**  $^{31}\text{P}$  NMR (162 MHz, 297 K, additional drops of  $\text{CD}_3\text{OH}$ ) of the reaction solution containing **Me-1** (100 mg) in 5 mL 9/1 MeOH/H<sub>2</sub>O, 8 M KOH.

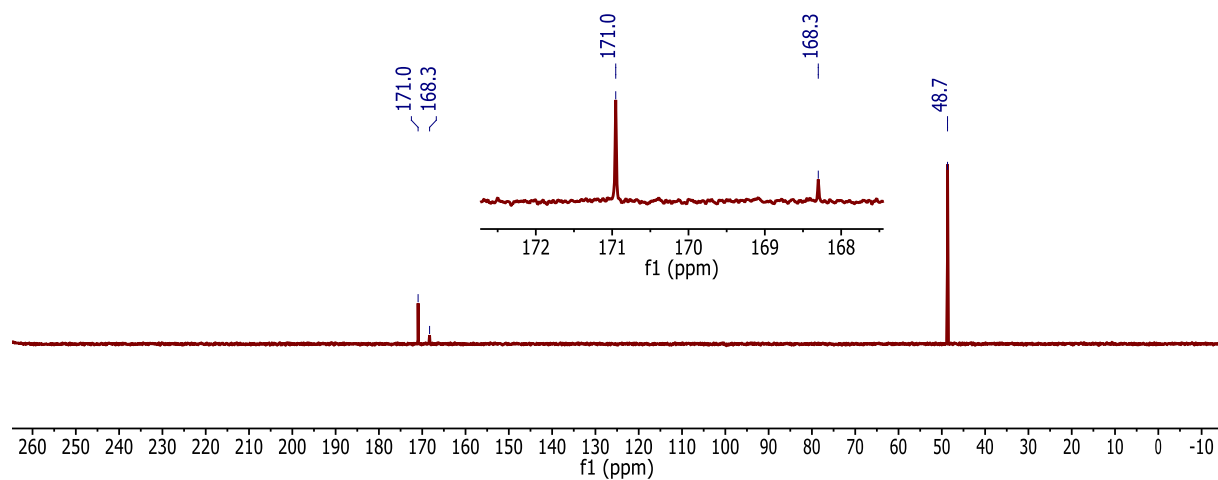


**Figure 66:**  $^{13}\text{C}$  NMR (75 MHz, 295 K,  $\text{D}_2\text{O}$ ) solid dissolved in  $\text{D}_2\text{O}$ .<sup>[118]</sup>

## Appendix

### 6.4.3. Preliminary tests

#### 6.4.3.1 Testing of a basic ionic liquid as additional solvent

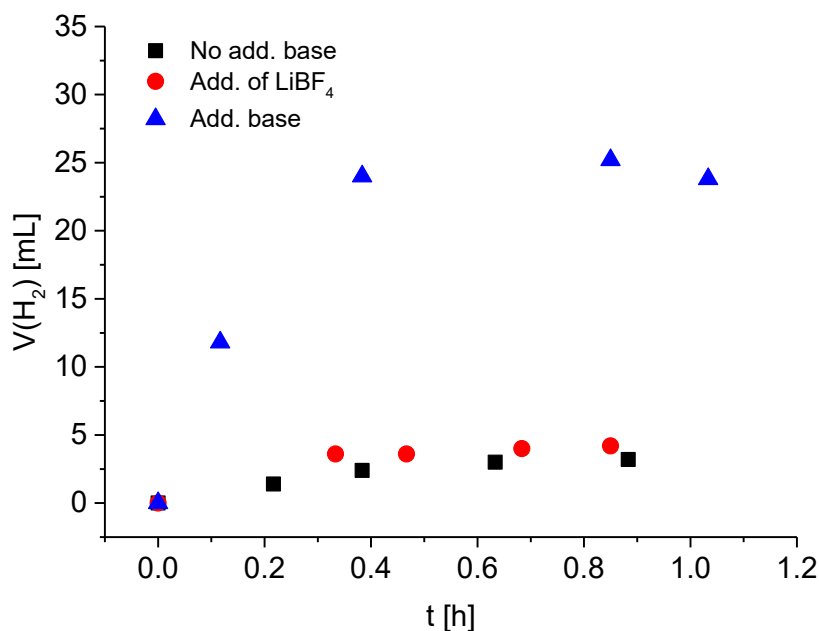


**Figure 67:** Testing of the IL Ecoeng 212 as additional solvent. Conditions: MeOH:H<sub>2</sub>O (9:1, 1 mL), 4 mL Ecoeng 212, 17.6  $\mu$ mol **1**, 70 °C. Addition of 100 eq. of LiBF<sub>4</sub> and 2 M KOH. After the addition of base, the former clear solution turned red-brownish under visible gas evolution.

#### 6.4.3.2 Testing of a bicatalytic system

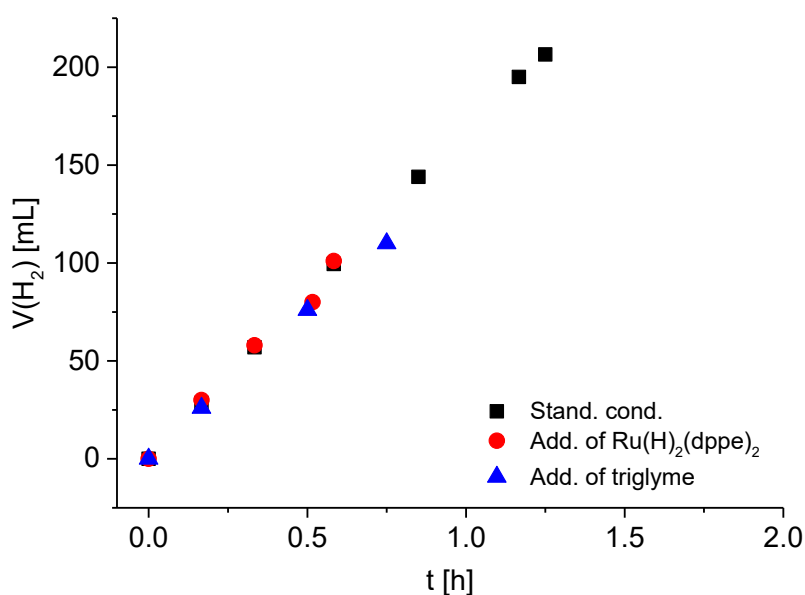


**Figure 68:** Testing of a bicatalytic system. Conditions: MeOH:H<sub>2</sub>O (9:1, 10 mL), 8 M KOH, 4.2  $\mu$ mol **1**, 90 °C. Addition of 4.2  $\mu$ mol Ru(H)<sub>2</sub>(dppe)<sub>2</sub> led to a milky white solution. Addition of 4 mL triglyme improved solubility slightly.



6.4.3.3 Replacement of KOH by  $K_2CO_3$

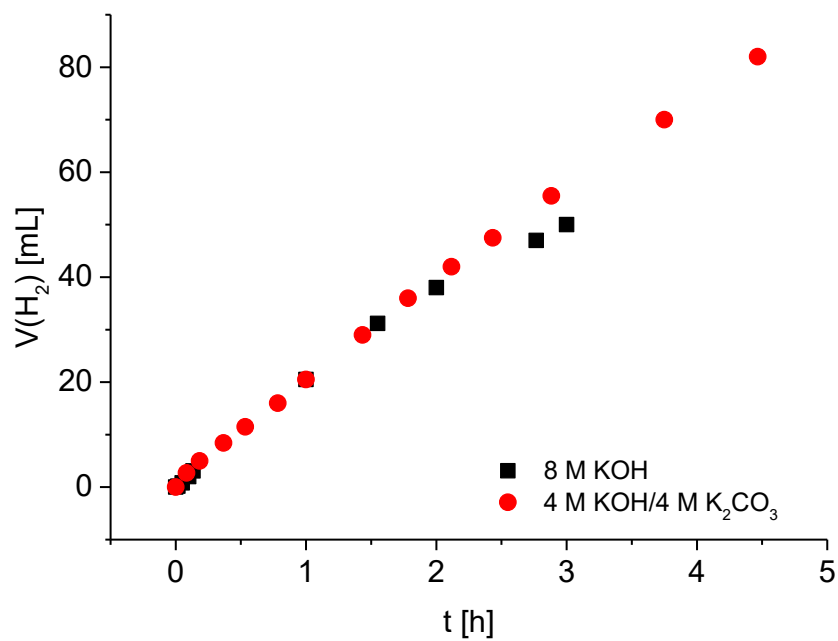


**Figure 69:** Replacement of KOH by  $K_2CO_3$ . Conditions: MeOH:H<sub>2</sub>O (9:1, 10 mL), 4.2  $\mu$ mol **1**, 70 °C. Black dots: Use of 8 M KOH. Red dots: Use of 4 M KOH and 4 M  $K_2CO_3$ .

## Appendix

---

### 6.4.4. Details on theoretical calculations<sup>[184]</sup>

To explicitly list all data would be beyond the limit of this thesis. For detailed information the reader may refer to the supporting information of the JACS article.<sup>[180]</sup>

In this section essential details on the computational methodology including energetic data and Cartesian coordinates are given.

(a) All calculations were carried out using the Gaussian 09 program<sup>1</sup>. All structures were optimized at the B3PW91<sup>2</sup> level of DFT with the TZVP<sup>3</sup> basis set (LANL2DZ for Ru<sup>4</sup>). Each optimized structure was characterized either as energy minimum without imaginary frequencies or transition state with only one imaginary frequency by frequency calculations; and the imaginary model connects the initial and the final states. The thermal corrections to Gibbs free energy at 298 K from the frequency analysis are added to the total electronic energy, and we therefore used the corrected Gibbs free energy ( $\Delta G$ ) at 298 K for our energetic discussion and comparison. We also carried out self-consistent reaction field (SCRF) structure optimizations and frequency calculations at the B3PW91 level using the polarizable continuum model (PCM)<sup>5</sup> and methanol as solvent to estimate the solvation influence.

(b) To validate our computational methodology, the following thermal exchange reactions between complexes **3** and **2** (**3** = **2** + H<sub>2</sub>) were carried out: Heating complex **3** (62 mM) in dioxane-d<sub>8</sub> to 100 °C for 50 min in a sealed NMR tube furnished only 20% of the dehydrogenated Ru-amido complex **2**, in parallel with H<sub>2</sub> evolution. H<sub>2</sub> was then shown to add back onto **2** to form **3** within a few hours. This reveals that complex **3** is thermodynamically more stable than complex **2**; and the dehydrogenation reaction should be endergonic.

-----  
<sup>1</sup> Gaussian 09, Revision D.01, Frisch, M. J.; Trucks, G. W.; Schlegel, H. B.; Scuseria, G. E.; Robb, M. A.; Cheeseman, J. R.; Scalmani, G.; Barone, V.; Mennucci, B.; Petersson, G. A.; Nakatsuji, H.; Caricato, M.; Li, X.; Hratchian, H. P.; Izmaylov, A. F.; Bloino, J.; Zheng, G.; Sonnenberg, J. L.; Hada, M.; Ehara, M.; Toyota, K.; Fukuda, R.; Hasegawa, J.; Ishida, M.; Nakajima, T.; Honda, Y.; Kitao, O.; Nakai, H.; Vreven, T.; Montgomery, J. A., Jr.; Peralta, J. E.; Ogliaro, F.; Bearpark, M.; Heyd, J. J.; Brothers, E.; Kudin, K. N.; Staroverov, V. N.; Kobayashi, R.; Normand, J.; Raghavachari, K.; Rendell, A.; Burant, J. C.; Iyengar, S. S.; Tomasi, J.; Cossi, M.; Rega, N.; Millam, J. M.; Klene, M.; Knox, J. E.; Cross, J. B.; Bakken, V.; Adamo, C.; Jaramillo, J.; Gomperts, R.; Stratmann, R. E.; Yazyev, O.; Austin, A. J.; Cammi, R.; Pomelli, C.; Ochterski, J. W.; Martin, R. L.; Morokuma, K.; Zakrzewski, V. G.; Voth, G. A.; Salvador, P.; Dannenberg, J. J.; Dapprich, S.; Daniels, A. D.; Farkas, Ö.; Foresman, J. B.; Ortiz, J. V.; Cioslowski, J.; Fox, D. J. Gaussian, Inc., Wallingford CT, 2009.

<sup>2</sup> Becke, A. D. *J. Chem. Phys.* **1993**, *98*, 5648-5652.

<sup>3</sup> Schaefer, A.; Huber, C.; Ahlrichs, R. *J. Chem. Phys.* **1994**, *100*, 5829-5835.

<sup>4</sup> Hay, P. J.; Wadt, W. R. *J. Chem. Phys.* **1985**, *82*, 299-310.

<sup>5</sup> Tomasi, J.; Mennucci, B.; Cammi, R. *Chem. Rev.* **2005**, *105*, 2999-3094.

## Appendix

---

That H<sub>2</sub> was then shown to add back onto complex **2** to form complex **3** within a few hours also shows that the reaction should be exergonic and has a lower barrier than the forward reaction. The ratio of 20 : 80 between complex **2** and **3** under heating roughly shows that the free energy changes should be in the range of 1-1.5 kcal/mol.

In our previous work<sup>6</sup>, we computed the concerted thermal exchange reaction between complex **3** and complex **2** (**3** = **2** + H<sub>2</sub>) at B3PW91, B3LYP and BP86 levels of theory. We found that the B3PW91 computed thermodynamic parameters are in best agreement with our experimental results, i.e. the exchange reaction is endergonic by 2.31 kcal/mol and the thermal reaction free energy barrier is 21.07 kcal/mol. The low endergonic property of 2.31 kcal/mol implies a possible equilibrium under the reaction conditions and is also in rough agreement with the deduced value from our experiment. In addition, the back reaction has a lower barrier of 18.76 kcal/mol and is exergonic by 2.31 kcal/mol, in agreement with our experimental observation. In addition, we also reported that including solvation effect raises the barrier of the exchange reaction from 21.07 to 26.15 kcal/mol; and the reaction becomes more endergonic (6.55 kcal/mol), implying that there will be no possible equilibrium under the reaction conditions.

We also computed this exchange reaction at the M06 and wB97XD levels of theory in order to test the methods including van der Waals dispersion correction. At the WB97XD level, the computed barrier is 24.42 kcal/mol and higher than at B3PW91 and most interestingly the reaction becomes highly endergonic by 7.40 kcal/mol, implying the suppression of the possible equilibrium under the reaction conditions. At the M06 level, the computed barrier is 21.22 kcal/mol and the reaction is endergonic by 1.70 kcal/mol, close to those at the B3PW91 level. This exchange reaction was calculated to be much more endergonic according to Yang<sup>7,8</sup> using the M06-SCRF (11.8 kcal/mol) as well as to Gusev et al.<sup>9,10</sup> using mPW1K-SCRF (18.8 kcal/mol) and at PBE0-SCRF (15.4 kcal/mol) or Lei et al.<sup>11</sup> using wB97X-D-SCRF (7.6 kcal/mol); all these data do not support the possible equilibrium

---

<sup>6</sup> Jiao, H.; Junge, K.; Alberico, E. A.; Beller, M. *J. Comput. Chem.* **2016**, *37*, 168-176.

<sup>7</sup> Yang, X. *ACS Catal.* **2014**, *4*, 1129–1133.

<sup>8</sup> Yang, X. *ACS Catal.* **2013**, *3*, 2684–2688. For closely related references: (a) Yang, X. *ACS Catal.* **2012**, *2*, 964–970. (b) Yang, X. *ACS Catal.*, **2011**, *1*, 849–854.

<sup>9</sup> Bertoli, M.; Choualeb, A.; Lough, A. J.; Moore, B.; Spasyuk, D.; Gusev, D. G. *Organometallics* **2011**, *30*, 3479-3482.

<sup>10</sup> For closely related references: (a) Spasyuk, D.; Smith, S.; Gusev, D. G. *Angew. Chem., Int. Ed.* **2012**, *51*, 2772–2775. (b) Spasyuk, D.; Gusev, D. G. *Organometallics* **2012**, *31*, 5239–5242.

<sup>11</sup> Lei, M.; Pan, Y.; Ma, X. *Eur. J. Inorg. Chem.* **2015**, *5*, 794-803.

## 6.5. Part II: Manganese-catalysed dehydrogenation of methanol

### 6.5.1. Preliminary tests

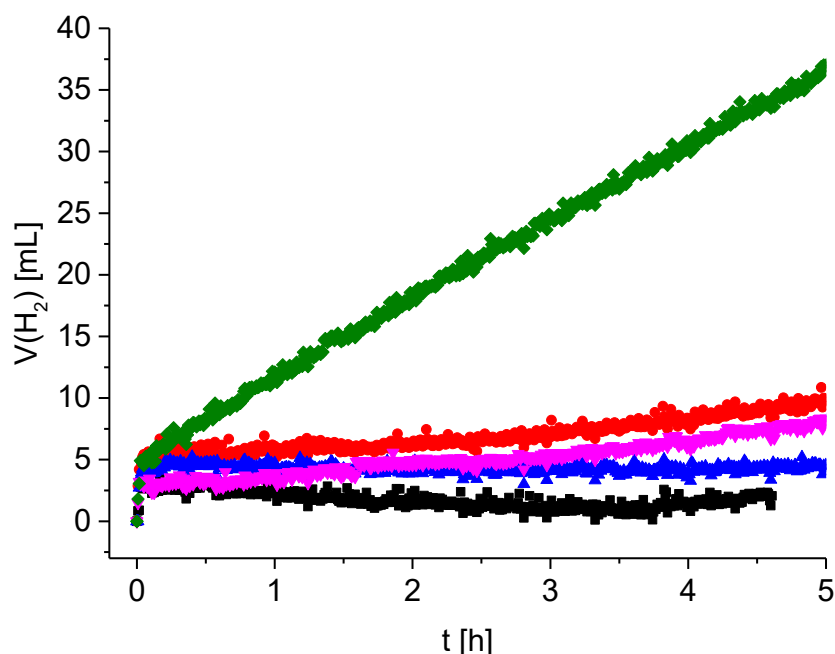


**Figure 70:** Activity measurements using a variation of Milstein's catalyst **15**. Conditions: MeOH:H<sub>2</sub>O (9:1, 5 mL), 8 M KOH, 8.4 μmol **15**, 90 °C.<sup>[171]</sup>

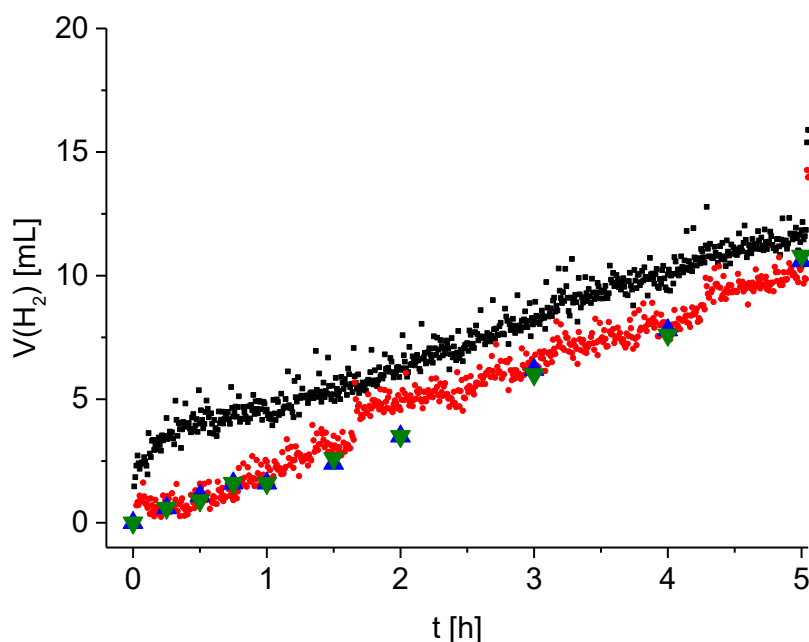


**Figure 71:** Activity measurements using Mn-Pr catalyst **9**. Conditions: MeOH:H<sub>2</sub>O (9:1, 5 mL), 8 M KOH, 8.4 μmol **9**, 90 °C. Manual and automatic burettes were used.<sup>[171]</sup>

### 6.5.2 Dilution effects

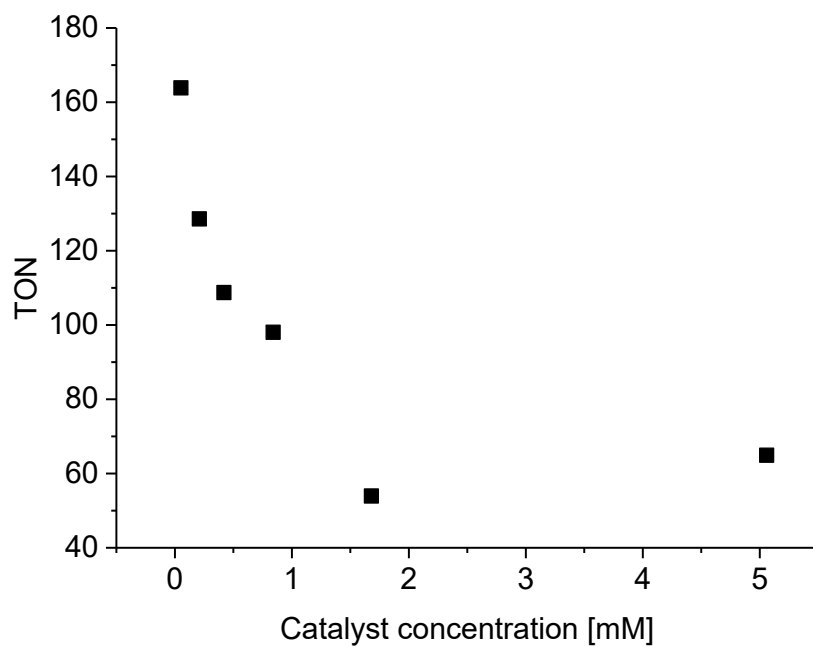


**Figure 72:** Correlation between catalyst concentration and productivity of **9**. Conditions: MeOH:H<sub>2</sub>O (9:1, 5 mL), 8 M KOH, 90 °C.<sup>[171]</sup>

## Appendix

### 6.5.1. NMR investigations

#### 6.5.1.1. Influence of reaction temperature on the defined Mn-catalyst and the precursor $\text{Mn}(\text{CO})_5\text{Br}$

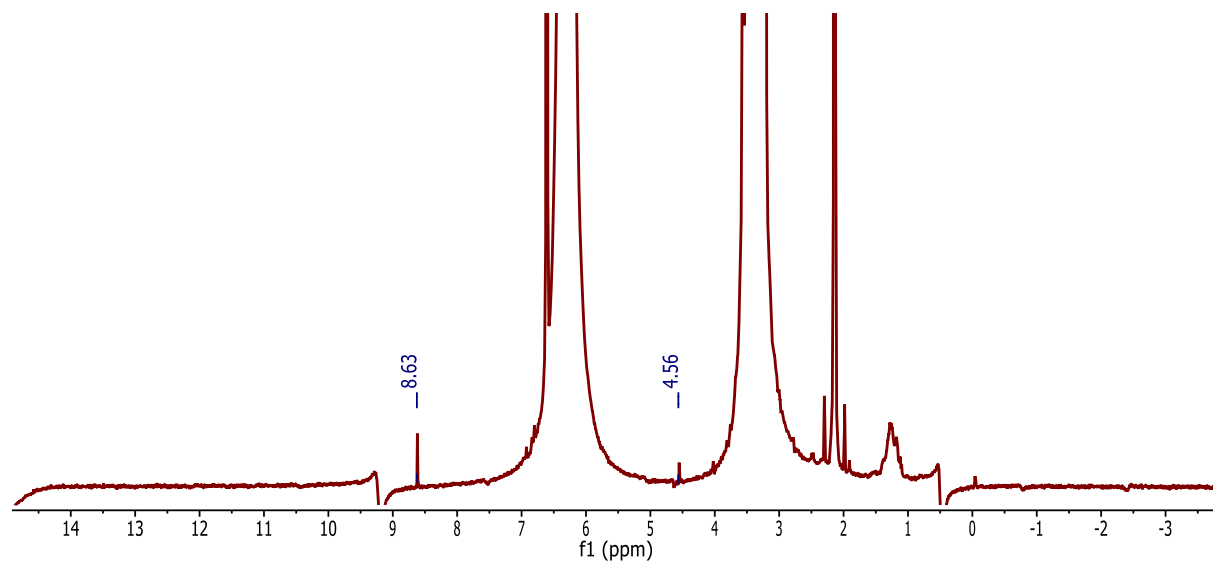


**Figure 73:**  $^1\text{H}$  NMR (400 MHz, 343 K) of the reaction solution containing catalyst **9** (20 mg) in 2 mL 9/1 MeOH/ $\text{H}_2\text{O}$ , 8 M KOH.

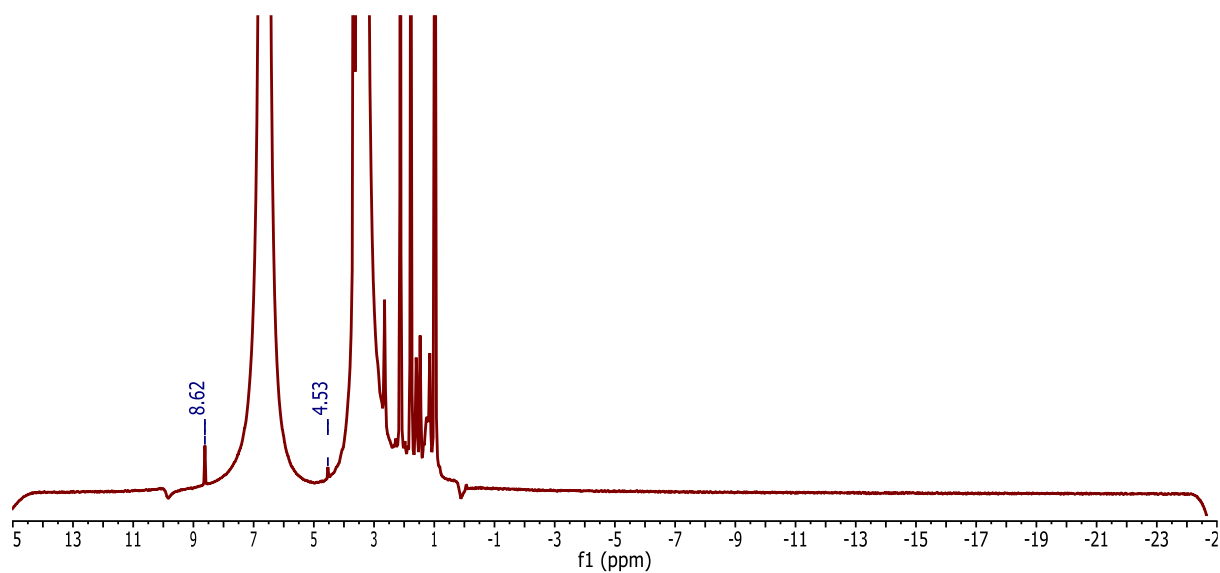


**Figure 74:**  $^1\text{H}$  NMR (400 MHz, 343 K) of the reaction solution containing  $\text{Mn}(\text{CO})_5\text{Br}$  (20 mg) with 10 eq. HPNP/Pr ligand in 2 mL 9/1 MeOH/ $\text{H}_2\text{O}$ , 8 M KOH.

## Appendix

---

### 6.5.2. Details on performed IR experiments

#### ***6.5.2.1. Addition of KOH to 9:1 MeOH/H<sub>2</sub>O solution containing Mn<sup>-i</sup>Pr catalyst 9***

To a 9:1 MeOH/H<sub>2</sub>O solution containing 10 mM Mn<sup>-i</sup>Pr catalyst in a Schlenk flask sequentially 0.5/1/10/800 eq. KOH were added (by the addition of a 8 M aqueous KOH sol.) and each time samples were taken and IR spectra were measured. Simultaneously, the same procedure was performed without catalyst in order to obtain IR background spectra.

#### ***6.5.2.2. Reaction monitoring***

The 9:1 MeOH/H<sub>2</sub>O solution containing 10 mM Mn<sup>-i</sup>Pr catalyst and 8 M KOH in a Schlenk flask with condenser was stirred for 1 hour before 0.5 mL sample was taken and measured by IR and NMR spectroscopy. The solution was heated to 90 °C and another sample was taken after the solution was stirred for 5 min at that temperature. Subsequent samples were taken after 120 min and 300 min. For referencing purposes, formic acid was added to a 9:1 MeOH/H<sub>2</sub>O solution containing 8 M KOH and measured. A reference solution without catalyst was measured for all samples for background.

## Appendix

---

### 6.5.3. Computational studies<sup>[185]</sup>

In our previous studies we have computed the structures, stabilities and catalytic properties of a set of PNP-ligand-based transition metal pincer complexes (M = Fe, Ru, Os, Mn, and Ir) in the hydrogenation and dehydrogenation reactions, where we have validated different density functional methods on the basis of experimental evidences. It is found that the B3PW91<sup>1</sup> density functional theory method in conjugation with the all-electron TZVP basis set<sup>2</sup> (LANL2DZ<sup>3</sup> for Ru, Os, and Ir) has the best agreement between computation and experiment in structures and energies. In this study, we have used the same models and methods for investigating the methanol water reforming reactions; i.e.; all stationary structures were optimized and subsequently characterized at the B3PW91/TZVP level either as energy minimums without imaginary frequencies or transition states with only one imaginary frequency by frequency calculations; and the imaginary model connects the initial and the final states. The thermal corrections to Gibbs free energy at 298 K from the frequency analysis are added to the total electronic energy, and we therefore used the corrected Gibbs free energy ( $\Delta G$ ) at 298 K for our energetic discussion and comparison. All calculations have been carried out by using the Gaussian09 program package<sup>4</sup>.

With the availability of the experimental recorded IR spectra for the bromide complex **9**, we scaled the computed harmonic CO stretching frequencies. We obtained an average scaling factor of 0.9452 for the CO stretching frequencies; this factor can be used to scale all CO frequencies of other complexes for the discussion of their changes upon the change of the reaction condition. The scaled IR spectra with a band width of 5 cm<sup>-1</sup> are plotted in Figures 40 and 41.

---

<sup>1</sup> Perdew, J. P. *Phys. Rev. B* **1986**, *33*, 8822-8824.

<sup>2</sup> Schaefer, A.; Huber, C.; Ahlrichs, R. *J. Chem. Phys.* **1994**, *100*, 5829-5835.

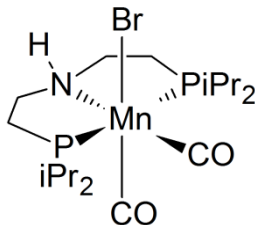
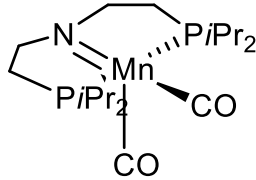
<sup>3</sup> P. J. Hay, W. R. Wadt, *J. Chem. Phys.* **1985**, *82*, 299-310.

<sup>4</sup> Frisch J. *et al.*, Gaussian 09, Revision C.01, Gaussian, Inc., Wallingford CT, 2010.

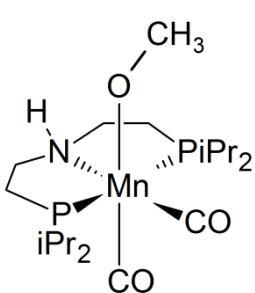
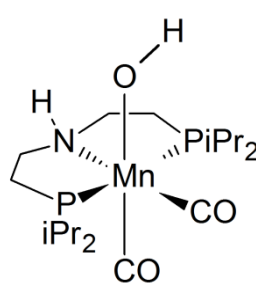


## Appendix

**Table 7:** B3PW91 Computed Cartesian Coordinates.

							
C	0.354934	0.107189	-0.123069	C	-0.048981	-0.048328	-0.012012
P	0.085728	0.061594	1.758605	P	0.077279	0.028203	1.871529
C	1.899079	-0.060683	2.281626	C	1.935037	0.000224	2.173721
Mn	-1.459973	1.385021	2.891743	Mn	-1.378545	1.294730	3.100802
C	-0.975485	2.950655	2.182769	C	-1.351464	2.642149	1.930242
O	-0.638908	3.968923	1.756577	O	-1.334583	3.515137	1.163463
P	-3.276075	2.182352	4.116617	P	-3.217833	2.094683	4.197130
C	-4.675879	3.243590	3.389307	C	-4.676200	2.809031	3.233102
N	-2.206832	-0.521538	3.545086	N	-1.977826	-0.389047	3.752633
C	-1.231593	-1.620699	3.508446	C	-1.225172	-1.634884	3.612628
C	-0.549633	-1.649975	2.148671	C	-0.491140	-1.690106	2.286094
C	-0.345333	1.677587	4.215078	C	-0.177525	2.071157	4.112886
O	0.412043	1.932052	5.061624	O	0.612937	2.512569	4.843641
C	-4.076232	0.584520	4.655857	C	-3.999448	0.527220	4.815258
C	-3.001042	-0.485080	4.781055	C	-2.930614	-0.549580	4.849993
C	-3.072691	3.098788	5.757525	C	-3.114999	3.207918	5.711489
Br	-3.129045	0.891053	0.944958	H	-4.493846	0.662106	5.779781
H	-2.853436	-0.646764	2.760474	H	-4.767508	0.255672	4.088387
H	-4.636246	0.693579	5.587380	H	-2.407489	-0.537272	5.819742
H	-4.781512	0.294828	3.874873	H	-3.413942	-1.536370	4.786018
H	-2.324658	-0.271549	5.611380	H	-1.186269	-1.986104	1.497659
H	-3.461088	-1.464567	4.972358	H	0.328628	-2.412112	2.287919
H	-1.281853	-1.909278	1.381930	H	-1.908076	-2.495424	3.680922
H	0.241460	-2.402936	2.120743	H	-0.514268	-1.752160	4.446211
H	-1.727256	-2.581541	3.705142	H	2.345744	-0.618506	1.365811
H	-0.508144	-1.454720	4.309550	C	2.561925	1.394274	2.104543
H	2.326991	-0.757628	1.550331	C	2.282512	-0.652377	3.511598
C	2.600027	1.287442	2.123177	H	0.345248	-1.042475	-0.259285
C	2.145870	-0.650440	3.667382	C	-1.511572	0.017082	-0.450857
H	1.419253	-0.127752	-0.232807	C	0.774931	0.991860	-0.765816
C	-0.434219	-0.938386	-0.906895	H	-4.152163	3.493863	5.927864
C	0.119971	1.505466	-0.690674	C	-2.550687	2.464519	6.922008
H	-4.105148	3.325019	6.051682	C	-2.290955	4.470791	5.453275
C	-2.446045	2.285009	6.886410	H	-5.539794	2.620723	3.883911
C	-2.332344	4.419055	5.552604	C	-4.605072	4.307720	2.954361
H	-4.987727	3.867051	4.234452	C	-4.872749	2.038187	1.928009
C	-4.166229	4.166482	2.284205	H	-1.591451	-0.234450	-1.512840
C	-5.895763	2.454861	2.919841	H	-2.154325	-0.669869	0.103107
H	-2.440377	2.887728	7.799997	H	-1.911506	1.023558	-0.316568
H	-3.011156	1.377550	7.108659	H	0.587947	0.893185	-1.839556

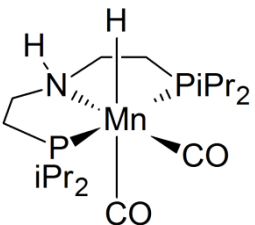
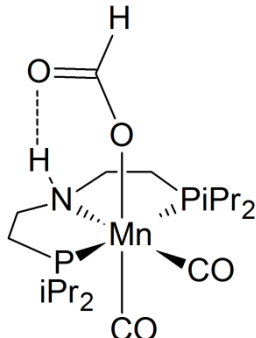
## Appendix

H	-1.413115	2.010026	6.675541	H	0.499796	2.009472	-0.480065
H	-2.289049	4.972825	6.495217	H	1.847183	0.865892	-0.611800
H	-1.306357	4.250301	5.220730	H	3.366854	-0.633001	3.656472
H	-2.822838	5.061146	4.818607	H	1.833409	-0.108190	4.345016
H	-4.966850	4.849583	1.984107	H	1.964409	-1.694128	3.571157
H	-3.316340	4.771853	2.602584	H	3.652444	1.304518	2.123975
H	-3.860747	3.591691	1.409448	H	2.291019	1.944991	1.204998
H	-6.641761	3.153412	2.528439	H	2.266636	1.996297	2.963807
H	-5.633921	1.763160	2.117527	H	-2.398940	5.156480	6.299423
H	-6.370381	1.896061	3.729584	H	-1.231807	4.231403	5.357831
H	3.665783	1.181863	2.346660	H	-2.592226	5.005020	4.553457
H	2.516541	1.682319	1.108850	H	-2.491524	3.147356	7.774866
H	2.190271	2.030812	2.809223	H	-3.166618	1.616639	7.225182
H	3.224760	-0.721006	3.837296	H	-1.539744	2.101474	6.725075
H	1.734922	-0.030004	4.462959	H	-5.462045	4.603066	2.341110
H	1.743247	-1.660422	3.767512	H	-4.640519	4.903623	3.866996
H	0.424446	1.526361	-1.741733	H	-3.702026	4.573045	2.400272
H	-0.935257	1.774552	-0.635152	H	-5.820716	2.328095	1.464830
H	0.690743	2.272309	-0.164925	H	-4.072422	2.265304	1.221723
H	-0.198273	-0.837508	-1.970808	H	-4.888231	0.955767	2.069921
H	-0.180563	-1.959872	-0.615127				
H	-1.509072	-0.791979	-0.789033				
							
C	0.035914	0.019196	0.188783	C	-0.029107	0.001628	-0.019364
O	-0.078317	0.021907	1.340282	O	-0.048123	0.006723	1.139373
Mn	0.157223	0.016382	-1.586763	Mn	0.069452	-0.002778	-1.792808
C	-1.599247	0.112947	-1.673768	P	-0.048790	-2.293663	-2.078573
O	-2.762716	0.185749	-1.666525	C	1.383534	-3.477993	-1.749078
P	0.138711	-2.299040	-1.889940	C	1.771266	-3.474893	-0.271406
C	0.711205	-2.443355	-3.659109	O	-1.937992	-0.074663	-2.227685
C	0.268470	-1.209901	-4.430076	C	1.828409	0.044127	-1.663369
N	0.626397	-0.005043	-3.676736	O	2.986570	0.070943	-1.534769
C	0.373285	1.231350	-4.422158	P	-0.179808	2.280783	-2.099906
C	0.951748	2.411381	-3.657883	C	-1.679838	3.208100	-1.400913
P	0.398708	2.320618	-1.878368	C	-2.037613	2.693444	-0.007890
C	-1.053910	3.529079	-1.852451	N	-0.066718	-0.013185	-3.928429
C	-1.700296	3.575424	-0.469315	C	0.348684	1.220939	-4.602339
C	1.224493	-3.529744	-0.928924	C	-0.362421	2.400259	-3.957221
C	1.432195	-3.075531	0.514060	C	1.165765	3.559259	-1.761844
C	2.555057	-3.863099	-1.598384	C	2.432276	3.352948	-2.588540
C	-1.460440	-3.307891	-1.903252	C	1.496447	3.633138	-0.272565
				C	0.399703	-1.234215	-4.593635
				C	-0.250581	-2.438831	-3.931328

## Appendix

C	-2.439428	-2.944141	-3.015828	C	-1.476709	-3.309036	-1.352651
C	-2.136655	-3.269141	-0.534036	C	-2.713450	-3.381550	-2.245971
C	1.659621	3.371744	-0.925669	C	-1.858544	-2.810132	0.039919
C	3.030380	3.465828	-1.590266	C	-2.910967	3.187754	-2.304661
C	1.791146	2.898131	0.519802	C	2.604929	-3.227755	-2.630084
C	-2.099652	3.296536	-2.940407	H	-2.525147	-0.067538	-1.471144
O	2.220490	-0.022964	-1.738308	H	-1.092636	-0.034967	-3.864804
H	1.623061	-0.049410	-3.401482	H	0.154980	-3.376263	-4.318210
H	0.681686	3.361260	-4.125364	H	-1.319674	-2.424771	-4.145577
H	2.039523	2.332320	-3.660442	H	1.488545	-1.273375	-4.512177
H	-0.705945	1.334647	-4.558303	H	0.150932	-1.211865	-5.664569
H	0.824441	1.177414	-5.423711	H	-1.426759	2.335976	-4.185722
H	1.801638	-2.474612	-3.638576	H	0.004857	3.352123	-4.346973
H	0.358220	-3.360607	-4.136823	H	0.109286	1.177199	-5.674770
H	0.742856	-1.199286	-5.422153	H	1.434116	1.310608	-4.513884
H	-0.812488	-1.206977	-4.589101	H	0.716067	4.513253	-2.065765
H	-1.119093	-4.333707	-2.090412	H	-1.342280	4.246492	-1.305050
H	0.626895	-4.447812	-0.910670	H	0.982817	-4.467989	-2.001583
H	-0.588022	4.503212	-2.048225	H	-1.068850	-4.321268	-1.250410
H	1.220193	4.375521	-0.916832	H	-3.748379	3.664021	-1.785094
H	3.121955	-4.543640	-0.955737	H	-2.755895	3.738969	-3.234405
H	2.423065	-4.361054	-2.560995	H	-3.196430	2.162160	-2.547731
H	3.168129	-2.973325	-1.752064	H	-2.823241	3.318832	0.427093
H	1.937430	-3.864078	1.080515	H	-2.410566	1.669895	-0.058637
H	2.048784	-2.178521	0.560542	H	-1.190976	2.695510	0.678711
H	0.492654	-2.852093	1.020890	H	3.133083	4.168825	-2.385890
H	-3.303276	-3.614531	-2.966390	H	2.936079	2.419833	-2.335905
H	-2.814681	-1.925912	-2.920156	H	2.235186	3.359297	-3.662510
H	-1.999389	-3.063151	-4.007821	H	2.264998	4.392069	-0.097701
H	-3.030577	-3.900020	-0.540473	H	0.629440	3.901929	0.333078
H	-1.483750	-3.636169	0.259928	H	1.882277	2.679662	0.094242
H	-2.447648	-2.256052	-0.273370	H	2.570846	-4.200315	-0.093452
H	-2.512198	4.308891	-0.460890	H	2.138824	-2.494182	0.038167
H	-2.124965	2.607308	-0.197480	H	0.936647	-3.743064	0.378388
H	-0.991850	3.864309	0.308945	H	3.369111	-3.980132	-2.411258
H	-2.865383	4.075673	-2.873061	H	2.373751	-3.306341	-3.694256
H	-1.673480	3.354142	-3.944064	H	3.048840	-2.249491	-2.443704
H	-2.603158	2.336511	-2.829886	H	-2.576288	-3.499847	0.494609
H	2.416366	3.598775	1.082044	H	-1.004565	-2.726236	0.712265
H	0.830226	2.826099	1.030135	H	-2.327035	-1.826798	-0.015156
H	2.259939	1.916234	0.564042	H	-3.512740	-3.907799	-1.714629
H	3.710337	4.025050	-0.940322	H	-3.068383	-2.379691	-2.496629
H	3.462130	2.477019	-1.752682	H	-2.528199	-3.930578	-3.171485
H	2.993769	3.990158	-2.547269				
C	3.219662	-0.188398	-0.800123				
H	3.729795	-1.165676	-0.882673				
H	4.016656	0.569612	-0.906939				
H	2.871016	-0.118272	0.243427				

## Appendix

			
C	-0.080998	-0.123630	-0.029963
P	0.031809	0.045145	1.850488
C	1.911417	0.128136	2.068578
Mn	-1.366187	1.327179	3.066834
C	-0.917518	2.864183	2.317870
O	-0.655977	3.865866	1.792006
P	-3.212947	2.105216	4.093043
C	-4.666380	2.894310	3.176786
N	-2.157475	-0.591733	3.665601
C	-1.133688	-1.648175	3.704333
C	-0.419493	-1.703107	2.365340
C	-0.270094	1.512643	4.461673
O	0.462889	1.682894	5.353229
C	-4.038462	0.543656	4.725405
C	-2.979920	-0.533774	4.884219
C	-3.128506	3.223147	5.618226
H	-2.348193	1.173116	1.819961
H	-2.774342	-0.782093	2.880615
H	-4.583352	0.704711	5.656882
H	-4.773041	0.232521	3.977703
H	-2.313609	-0.300580	5.717592
H	-3.442332	-1.510075	5.089201
H	-1.092114	-2.110358	1.606145
H	0.447022	-2.363694	2.406866
H	-1.585493	-2.621173	3.945716
H	-0.436104	-1.396601	4.506198
H	2.332906	-0.344128	1.172578
C	2.382659	1.582133	2.133998
C	2.418586	-0.627374	3.296006
H	0.529107	-1.005923	-0.264438
C	-1.507031	-0.371213	-0.510415
C	0.507869	1.081942	-0.760824
H	-4.134289	3.647303	5.729603
C	-2.778045	2.473457	6.902411
C	-2.127784	4.361077	5.404622
H	-5.498962	2.837852	3.890485
C	-4.425362	4.363136	2.832587
C	-5.049691	2.124835	1.917264
H	-1.509251	-0.514647	-1.595347
			
C	-0.256542	-0.016746	0.078903
Mn	-0.090234	-0.007714	1.858944
O	2.032828	0.079611	1.656828
C	3.018836	0.119602	2.453741
O	-0.424974	-0.026165	-1.063751
C	-1.843724	-0.078108	1.969940
O	-3.005888	-0.124220	1.994797
P	-0.042989	2.300169	2.142103
C	-1.561488	3.401373	1.960126
C	-2.098655	3.347588	0.531054
N	0.251621	0.004387	3.969442
C	-0.091205	-1.234418	4.673512
C	0.550160	-2.415866	3.958854
P	0.146699	-2.304601	2.140852
C	1.498079	-3.286162	1.233680
C	1.827248	-2.653125	-0.117068
C	0.358552	2.440946	3.957870
C	-0.185729	1.212753	4.674383
C	1.215418	3.395844	1.232599
C	2.458314	3.747984	2.046117
C	-1.276961	-3.525743	1.950298
C	-2.405609	-3.357388	2.963069
C	-1.809892	-3.511230	0.519259
C	1.594051	2.798993	-0.121828
C	-2.670955	3.145016	2.976193
C	2.762802	-3.527005	2.053770
H	1.284131	0.044834	3.866910
H	0.235984	-3.366910	4.395398
H	1.633545	-2.340797	4.065526
H	-1.180193	-1.330369	4.701468
H	0.262758	-1.193833	5.713075
H	1.445039	2.449295	4.058599
H	-0.025632	3.364529	4.397106
H	0.173263	1.200632	5.712916
H	-1.278727	1.222032	4.705550
H	-1.170000	4.409532	2.145064
H	0.668173	4.327605	1.053072
H	-0.806304	-4.499465	2.135820

## Appendix

H	-1.962346	-1.259679	-0.066687	H	1.034866	-4.261811	1.049969
H	-2.145696	0.480564	-0.271390	H	3.111661	4.384626	1.441967
H	0.385827	0.953435	-1.840614	H	2.218782	4.299989	2.957153
H	-0.004062	2.004923	-0.478539	H	3.034792	2.864563	2.326137
H	1.573630	1.210086	-0.568678	H	2.253831	3.490364	-0.655443
H	3.501697	-0.495780	3.380701	H	2.112314	1.848163	0.004109
H	1.975573	-0.238211	4.214813	H	0.722980	2.619716	-0.753892
H	2.229977	-1.701281	3.246216	H	-3.465173	3.884104	2.832386
H	3.476015	1.618887	2.097825	H	-3.119504	2.159255	2.857070
H	1.999211	2.194231	1.318099	H	-2.322974	3.246163	4.006012
H	2.064014	2.047632	3.067714	H	-2.930120	4.049489	0.418091
H	-2.204655	5.079913	6.226556	H	-1.341759	3.614709	-0.209169
H	-1.106941	3.977110	5.393392	H	-2.470303	2.350770	0.286184
H	-2.283060	4.902401	4.471649	H	-2.580214	-4.278594	0.399111
H	-2.702807	3.185928	7.729576	H	-2.260448	-2.547039	0.276575
H	-3.529393	1.733641	7.184595	H	-1.029425	-3.711827	-0.217394
H	-1.810628	1.974356	6.820633	H	-3.139254	-4.156602	2.818800
H	-5.274683	4.750503	2.261660	H	-2.053142	-3.429477	3.993789
H	-4.319309	4.988779	3.719168	H	-2.929199	-2.409762	2.841441
H	-3.531267	4.486152	2.217075	H	2.551965	-3.278176	-0.648279
H	-5.958863	2.555923	1.486456	H	0.946918	-2.553885	-0.753924
H	-4.252985	2.180779	1.174458	H	2.252879	-1.658124	0.014717
H	-5.246759	1.067106	2.104340	H	3.478776	-4.092208	1.449657
				H	3.248795	-2.595039	2.346549
				H	2.569955	-4.107845	2.957898
				H	4.006959	0.165649	1.952189
				O	2.997209	0.112448	3.696826